UNIVERSITÉ DU QUÉBEC À TROIS-RIVIÈRES

CONCEPTION ET DÉVELOPPEMENT DE CATALYSEURS MOLÉCULAIRES
À BASE DE DIAMINOTRIAZINE POUR LA PRODUCTION
D'HYDROGÈNE PAR LA LUMIÈRE

*DESIGN AND DEVELOPMENT OF DIAMINOTRIAZINE BASED MOLECULAR
CATALYSTS FOR LIGHT-DRIVEN HYDROGEN PRODUCTION*

THÈSE PRÉSENTÉE
COMME EXIGENCE PARTIELLE DU
DOCTORAT EN SCIENCES DE L'ÉNERGIE ET DES MATÉRIAUX

PAR
SANIL RAJAK

MARS 2021

Université du Québec à Trois-Rivières

Service de la bibliothèque

UNIVERSITÉ DU QUÉBEC À TROIS-RIVIÈRES

DOCTORAT EN SCIENCES DE L'ÉNERGIE ET DES MATÉRIAUX (PH. D.)

Direction de recherche :

Adam Duong	Directeur de recherche

Jury d'évaluation de la thèse :

Adam Duong	Directeur de recherche
Phuong Nguyen-Tri	Président de jury
Olivier Lebel	Évaluateur externe
Gustavo Emilio Ramirez Caballero	Évaluateur externe

Thèse soutenue le 26 février 2021

"Energy is this invisible link that connects everything;

the materials provide us the evidence".

-DuongLab

Summary

Chemistry of polypyridine ligands is an active and important field of research as polypyridines are one of the most versatile chelating ligands for transitions metal ions, generating diverse molecular architectures with useful physical properties. A vast literature is reported on metal complexes of polypyridines and their applications in supramolecular functional devices, catalysis, liquid crystals, artificial photosynthesis, and host-guest interactions. Although, there are several reports on polypyridine chemistry, the development in this area is limited due to the low yield and synthetic inaccessibility associated with polypyridines. Furthermore, their crystal structures cannot be predicted because they lack functional groups that conduct self-assembly.

With the depletion of fossil fuels and the phenomenon of global warming, the necessities for the development of clean and sustainable energy resources are imperative. Hydrogen is a clean, environmentally benign, and sustainable energy carrier as water is the only product of its combustion. Hydrogen as a fuel possesses high energy output relative to its mass. However, molecular hydrogen is very rare in the Earth's atmosphere *c.a.* 1 ppm by volume. Therefore, it needs to be produced from suitable sources. Sunlight-triggered hydrogen evolution reaction (HER) has proven to be an interesting solution to harvest the abundant and inexhaustible power of solar energy in the form of chemical bonds in hydrogen.

A typical hydrogen evolution reaction is based on visible light-induced sensitization of photosensitizers from which the electrons are transferred to the photo catalytic centre to produce hydrogen with the help of a sacrificial electron donor (SED). Ruthenium and cobalt molecular complexes are the most widely studied and reported complexes as photosensitizers (PSs) and photocatalysts (PCs) respectively. For efficient electron transfer, the PS and the PC must be in close proximity. Direct contact in the form of covalent or coordination bonds can increase the benefits, but such systems are usually difficult and expensive to synthesize. Sometimes, weaker contacts have also proven to be effective. Nevertheless, the design and development of efficient

and non-expensive molecular catalysts and the modification of the catalysts by low-cost ligand design remains the principal focus of research in this area.

Our work demonstrates a simple and inexpensive technique to prepare molecular photocatalysts (PCs). The strategy used to prepare these PCs is based on the concept of metallotectons. Metallotectons are molecular complexes that can form supramolecular networks by ligands possessing standard patterns of coordination like bipyridine, terpyridine and quarterpyridine, and ligands containing functional groups that can form strong hydrogen bonds. Such type of ligands are called as tectoligands. In our study, we have used ligands which are bipyridine-like, terpyridine-like and quaterpyridine-like. These ligands possess diaminotriazinyl groups (DAT), that allow them to self-assemble with several transition metal ions by coordination and hydrogen bonds. The most attractive feature of the diaminotriazine group is that, it can be introduced in a single step. To the best of our knowledge, these molecular complexes are the first examples of coordination chemistry based molecular catalysts for the hydrogen evolution reaction (HER). In addition to their interesting catalytic properties, these molecular complexes also have ability to self-assemble *via* hydrogen bonds to produce fascinating supramolecular networks.

Keywords: coordination chemistry, molecular catalysts, hydrogen-bonding, diaminotriazinyl (DAT) groups, metallotectons, supramolecular networks, crystal growth, X-ray diffraction, visible light radiation, photocatalysts (PCs), photosensitizers (PSs), hydrogen evolution reactions (HER), homogeneous catalysis, energy conversion and energy storage.

Résumé

La chimie des ligands polypyridines est un domaine de recherche actif et important, car ces molécules sont l'un des chélateurs les plus polyvalents pour les ions métalliques, générant diverses architectures moléculaires aux propriétés utiles. Une vaste littérature est rapportée sur les complexes métalliques de polypyridines et leurs applications dans les dispositifs fonctionnels supramoléculaires, la catalyse, les cristaux liquides, la photosynthèse artificielle et les interactions hôte-invité. Bien qu'il existe plusieurs rapports sur la chimie des polypyridines, le développement dans ce domaine est limité en raison du faible rendement et de l'inaccessibilité synthétique associés aux polypyridines. De plus, leurs structures ne sont pas prévisibles du fait du manque de groupes fonctionnels qui permettent une association bien définie.

Avec l'épuisement des combustibles fossiles et le phénomène du réchauffement climatique, la nécessité d'un développement de ressources énergétiques propres et durables est impérative. L'hydrogène est un vecteur d'énergie propre et respectueux de l'environnement car l'eau est le seul produit de sa combustion. L'hydrogène en tant que carburant possède une grande densité énergétique par rapport à sa masse. Cependant, l'hydrogène moléculaire est très rare dans l'atmosphère terrestre, c.a. 1 ppm en volume. Par conséquent, il doit être produit à partir de sources appropriées. La réaction d'évolution d'hydrogène déclenchée par la lumière du soleil (HER) s'est avérée être une solution intéressante pour récolter la puissance abondante et inépuisable de l'énergie solaire sous la forme de liaisons chimiques dans l'hydrogène.

Une réaction typique de dégagement d'hydrogène est basée sur la sensibilisation induite par la lumière visible des photosensibilisateurs à partir de laquelle les électrons sont transférés vers le centre photocatalytique pour produire de l'hydrogène à l'aide d'un donneur d'électrons sacrificiel (SED: sacrificial electron donor). Les complexes moléculaires de ruthénium et de cobalt sont les complexes les plus largement étudiés et rapportés comme photosensibilisateurs (PS) et photocatalyseurs (PC) respectivement. Pour un transfert d'électrons efficace, le PS et le PC doivent

être à proximité. Un contact direct sous la forme de liaisons covalentes ou de coordination peut augmenter les avantages, mais de tels systèmes sont généralement difficiles et coûteux à synthétiser. Parfois, des contacts plus faibles se sont également avérés efficaces. La conception et le développement de catalyseurs moléculaires efficaces et peu coûteux et la modification des catalyseurs par la conception de ligands à faible coût restent le principal objectif de la recherche dans ce domaine.

Notre travail démontre une technique simple et peu coûteuse pour préparer des photocatalyseurs moléculaires (PC). Au cours de cette thèse, nos activités de recherche seront ciblées sur la préparation des PC basés sur la diaminotriazine (DAT) et les études de l'autoassemblage par les liaisons de coordination et hydrogène. Les métallotectons sont des complexes moléculaires qui peuvent être utiles pour la photocatalyse mais aussi pour former des réseaux supramoléculaires lorsque les ligands sont fonctionnalisés adéquatement. Les complexes de coordinations que nous préparerons seront basés à partir des modèles standard de coordination avec les ligands de types bipyridine (bpy), la terpyridine (tpy) et la quarterpyridine (qtpy). Dans notre étude, nous proposons préparer des ligands mimant les polypyridines en remplaçant une ou plusieurs pyridines par des groupements diaminotriazines (DATs). Les ligands avec les DATs sont appelés des tectoligands car ils peuvent coordonner les ions métalliques et s'autoassembler par liaisonss hydrogène. La caractéristique la plus intéressante du DAT est qu'il peut être introduit en une seule étape avec quasiment tous les groupements fractionnels (phényle, phénantroline, anthracène, etc.). À notre connaissance, ces types de complexes n'ont jamais été utilisés auparavant comme catalyseurs moléculaires pour la réaction de dégagement d'hydrogène (HER: Hydrogen Evolution Reaction). En plus de leurs propriétés catalytiques intéressantes, ces métallotectons ont également la capacité de s'auto-assembler via des liaisons hydrogène pour produire des réseaux supramoléculaires fascinants.

Mots clés: chimie de coordination, catalyseurs moléculaires, liaisons hydrogène, groupement diaminotriazinyle (DAT), métallotectons, réseaux supramoléculaires, croissance cristalline, diffraction des rayons X, rayonnement lumineux visible, photocatalyseurs (PC), photosensibilisateurs (PS), réactions d'évolution d'hydrogène (HER), catalyse homogène, conversion d'énergie et stockage d'énergie.

Table of Contents

Chapter 1: Introduction

Chapter 4: Mimicking 2, 2′:6′, 2″:6″, 2‴-Quaterpyridine Complexes for the Light-Driven Hydrogen Evolution Reaction: Synthesis, Structural, Thermal and Physicochemical Characterizations

Chapter 5: Design of a [FeFe] Macrocyclic Metallotecton for Light-Driven Hydrogen Evolution Reaction

Chapter 6: Amidine/Amidinate Cobalt Complexes: One-Pot Synthesis, Mechanism and Photocatalytic Application for Hydrogen Production

Chapter 7: Conclusions and Perspectives

List of Tables

Lists of Charts

List of Schemes

List of Figures

metallotecton **9**. (b) Racemic pairs of metallotecton held together by four N–H···N hydrogen bonds of type **1** and multiple hydrogen bonds involving bridging nitrates to form the two-dimensional (2D) sheet. (c) View showing sheets packed together to form the three-dimensional structure. For clarity, layers are marked in red and blue.

oxygen atoms in red, nitrogen atoms in blue and nickel atoms in cyan. (a) Alternating arrangement of complex **9** and its enantiomer joined together by hydrogen bonding of DAT groups according to motif **I** and by free N−H···O$_{nitrate}$ to generate chains (b) Chains are maintained together by hydrogen bonding involving bridging nitrates to form the three-dimensional structure. For clarity a chain is marked in green.

Article 3: Mimicking 2, 2':6', 2":6", 2'''-Quaterpyridine Complexes for the Light-Driven Hydrogen Evolution Reaction: Synthesis, Structural, Thermal and Physicochemical Characterizations

of the molecular structure of **2**. (b) View showing the hydrogen bonding between macrocycles. For more clarity, methanol and nitrates are omitted.

List of Abbreviations

Å :	Ångström
A:	Absorbance
a.u.	Arbitrary unit
ATR	Attenuated total reflectance
bpy:	Bipyridine
BFDH:	Bravais-Friedel-Donnay-Harker
DNA:	Deoxyribonucleic acid
Anal. :	Analysis
° C:	Degree Celsius
cm:	Centimeter
calcd:	Calculated
CRR:	Carbon dioxide reduction reaction
$CDCl_3$	Deuterated chloroform
CV:	Cyclic voltammetry
D or d:	Density
d:	Doublet (in NMR)
DAT:	2,4-diamino-1,3,5-triazine
dmg:	Dimethylglyoxime
DMF:	Dimethylformamide
DMSO:	Dimethyl sulfoxide
DMSO-d_6:	Deuterated dimethyl sulfoxide
DSC:	Differential scanning calorimetry
ε:	Molar absorptivity
E:	Potential
EA:	Elemental analysis
equiv:	Equivalence
ESI:	Electron-spray ionization
ESI:	Electronic Supporting Information
EtOAc:	Ethyl acetate

Et$_2$O:	Diethyl ether
FTIR:	Fourier-transform infrared spectroscopy
Fw:	Formula weight
FWHM:	Full width at half maximum
g:	Gram
GC:	Gas Chromatography
GoF:	Goodness-of-fit
h:	Hour
HBF$_4$:	Tetrafluoroboric acid
HER:	Hydrogen evolution reaction
Hz:	Hertz
HRMS:	High-resolution mass spectrometry
I:	Intensity (X-rays)
I :	Current
IR:	Infrared
J:	Coupling constant
K:	Kelvin
λ:	Wavelength
LED:	Light-Emitting Diode
kcal:	Kilocalorie
kJ:	Kilojoule
M:	Molar
μm:	Micrometer
m:	Multiplet (in NMR)
m/z:	Mass-to-charge ratio
mg:	Milligram
MHz:	Megahertz
mL:	Milliliter
MLCT:	Metal Ligand Charge Transfer
mm:	Millimeter
mM:	Millimolar

mmol:	Millimole
mol:	Mole
mp:	Melting point
MS:	Mass Spectrometry
mW:	Milliwatt
NMR:	Nuclear Magnetic Resonance
ORTEP:	Oak Ridge Thermal Ellipsoid Program
ox:	Oxidation
PS:	Photosensitizer
PC:	Photocatalyst
PXRD:	Powder X-ray diffraction
pyDAT:	Pyridine diaminotriazine
pzDAT	Pyrazine diaminotriazine
q:	Quartet (in NMR)
qtpy:	Quaterpyridine
R1:	Factor of agreement on the observed reflections
red:	Reduction
RT:	Room Temperature
s:	Singlet (in NMR)
SCE :	Saturated Calomel Electrode
SCXRD:	Single Crystal X-ray Diffraction
SEM:	Scanning Electronic Microscopy
SED:	Sacrificial Electron Donor
sh:	shoulder (for UV-Vis or Infrared Spectroscopy)
STA:	Simultaneous Thermal Analysis
t:	Triplet (in NMR)
T:	Temperature
TBAP:	Tetrabutylammonium hexafluorophosphate
TEA:	Triethylamine
TEOA:	Triethanolamine
tpy:	Terpyridine

TGA :   Thermogravimetric analysis

THF: Tetrahydrofuran

TON: Turnover number

TOF: Turnover Frequency

UV-Vis: Ultraviolet and Visible Spectroscopy

V: Volt

W: Watt

ωR: Weighted tuning factor

w/v: Weight by volume

ν: Frequency (of infrared vibration)

$\tilde{\nu}$:   Frequency in terms of wavenumber (of infrared vibration)

Achievements as a Ph. D Student

During my Ph. D, I published 8 research articles, 5 as 1st author and 3 as 2nd author all-in world-renowned journals with high impact factors. The article published in *Inorg. Chem* was also selected for a supplementary cover art. I also received best poster award at the 9th annual conference of centre québécois sur les matériaux fonctionnels (CQMF) in 2016 held at École de Technologie Supérieure, Montreal, Quebec, Canada. I also received twice the second prize in Concours D'affiches Scientifiques in 2017 & 2019, held at the Université du Québec à Trois-Rivières, Québec, Canada.

List of articles published

1. **Rajak, S.**; Mohan, M.; A. Tremblay, A.; Maris, T.; Leal do Santos, S.; Venancio, E. C.; Ferreira Santos, S.; Duong, A., Programmed molecular construction: Driving the self-assembly by coordination and hydrogen bonds using 6-(Pyridin-2-yl)-1, 3, 5-triazine-2, 4-diamine with M(NO$_3$)$_2$ salts. *ACS omega* **2019,** *4* (2), 2708-2718

2. **Rajak, S.**; Schott, O.; Kaur, P.; Maris, T.; Hanan, G. S.; Duong, A., Synthesis, crystal structure, characterization of pyrazine diaminotriazine based complexes and their systematic comparative study with pyridyl diaminotriazine based complexes for light-driven hydrogen production. *Polyhedron* **2020,** *180*, 114412

3. **Rajak, S.**; Schott, O.; Kaur, P.; Maris, T.; Hanan, G. S.; Duong, A., Mimicking 2, 2′: 6′, 2″: 6″, 2‴-quaterpyridine complexes for the light-driven hydrogen evolution reaction: synthesis, structural, thermal and physicochemical characterizations. *RSC advances* **2019,** *9* (48), 28153-28164

4. **Rajak, S.**; Schott, O.; Kaur, P.; Maris, T.; Hanan, G. S.; Duong, A., Design of a [FeFe] macrocyclic metallotecton for light-driven hydrogen evolution reaction. *International Journal of Hydrogen Energy* **2020,** *45* (4), 2699-2708

5. **Rajak, S.**; Chair, K.; Rana, L. K.; Kaur, P.; Maris, T.; Duong, A., Amidine/Amidinate Cobalt Complexes: One-Pot Synthesis, Mechanism, and Photocatalytic Application for Hydrogen Production. *Inorganic Chemistry* **2020**, *59* (20), 14910-14919

6. Duong, A.; **Rajak, S.**; Tremblay, A. A.; Maris, T.; Wuest, J. D., Molecular organization in crystals of bis (diaminotriazinyl)-substituted derivatives of benzene, pyridine, and pyrazine. *Crystal Growth & Design* **2018**, *19* (2), 1299-1307

7. Mohan, M.; **Rajak, S.**; Tremblay, A. A.; Maris, T.; Duong, A., Syntheses of mono and bimetallic cyamelurate polymers with reversible chromic behaviour. *Dalton Transactions* **2019**, *48* (20), 7006-7014

8. Garcia, L. M.; **Rajak, S.**; Chair, K.; Godoy, C. M.; Silva, A. J.; Gomes, P. V.; Sanches, E. A.; Ramos, A. S.; De Souza, R. F.; Duong, A.; Neto, A., Conversion of methane into methanol using the [6, 6'-(2, 2'-bipyridine-6, 6'-diyl) bis (1, 3, 5-triazine-2, 4-diamine)](nitrato-O) copper (II) complex in a solid electrolyte reactor fuel cell type. *ACS omega* **2020**, *5* (26), 16003-16009

Acknowledgement

The present thesis is the outcome of four and a half years of research work. These projects would not have been accomplished without the help and support of all the people that have accompanied me in this long journey. I am extremely grateful to all my educators in every part of my academic and industrial carrier. My intellectual and personal development has been a result of every teacher and professor with whom I have had interacted, starting from Bachelor of Science (B.Sc.) to Master of Science (M.Sc.) followed by working as a Trainee Chemist for a year, at BASF-The Chemical company and then during my Doctor of Philosophy (Ph.D.).

This thesis is the climax of an ideal working relationship with my supervisor, Prof. Dr. Adam Duong to whom I am eternally grateful. His unconditional support during my Ph. D. created a path towards my development as a research scientist. I have always been very fond of research and Ph. D. was my dream course which I decided to pursue during my Bachelor of Science (B.Sc.) degree. I would like to thank Prof. Duong for supporting me personally, for being behind me like an elder brother, for pushing me to excel in each and every task, for giving me the confidence, strength and hope whenever I was sick, weak or felt drifted astray. It would have not been possible to carry out the research work and make it into a final dissertation without his guidance and encouragement. I am also very grateful for his contribution in the form of countless advice on several revisions of this dissertation and the manuscripts enclosed. He also taught me a lot about how to conduct research, write articles, give presentations, and participate in large collaborative projects. I will forever remember and appreciate his efforts and endeavours for my betterment. I am very thankful to the government of Canada for providing me the prestigious Queen Elizabeth Scholarship to pursue a Ph.D. in Québec, Canada. This outstanding scholarship not only funded my education and living but also helped me improve my leadership and community engagement skills. It also helped me learn French language. Its carrier guidance sessions were also very beneficial. I would like to thank my family, my Mom, Dad, and my Brother for their constant financial support

Chapter 1

Introduction

1. Context: The Global Energy Consumption

Energy is the primary requirement to obtain any kind of service in our present reliant world. According to the British petroleum statistical review of world's energy report 2019, ~ 85 % of energy is produced from fossil fuels (oils, natural gas, and coals), ~ 4 % from nuclear fuels, ~ 4 % from non-fossil resources such as biofuels and waste, and about ~ 7 % is produced from renewable energy resources such as hydro, wind, solar, thermal and geothermal energies etc. as shown in Figure 1.[1] Currently, the world's fossil fuels energy demand amounts to about 1066 barrels of oil, 108,000 cubic metres of natural gas and 250 tonnes of coal per second, which means that each person living on earth needs at least 2 litres of oil each day.[2]
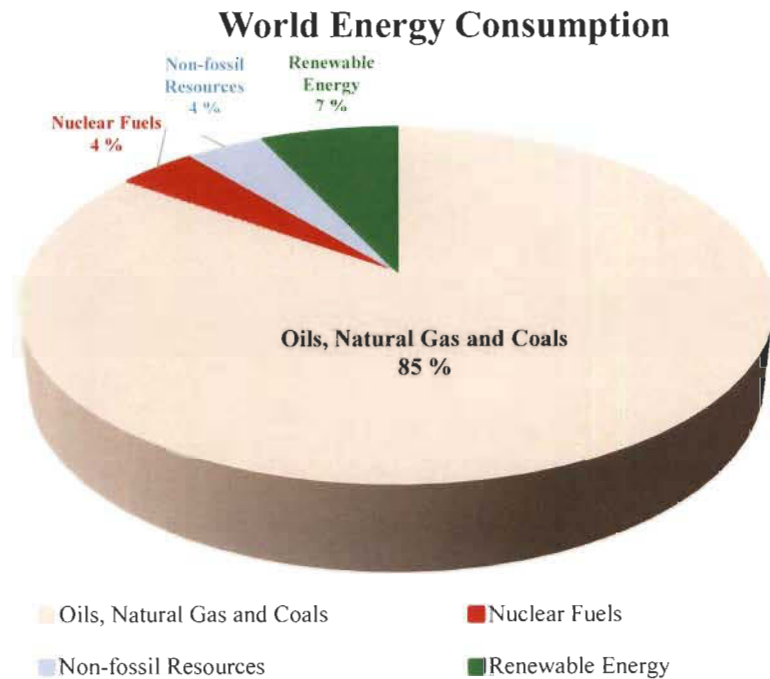
Figure 1. The British petroleum statistical review of world energy report 2019.

Figure 2. An average American family, surrounded by the barrels of oil they consume annually, in this 1970's picture.[3]

By mid-2000s, the world's energy consumption is expected to increase by 50 %.[4] To satisfy the growing energy demands with increasing industrialization, economic growth and rising global population, oil is envisaged to be the primary energy source. Nearly 80 % of oil is used to power the world transportation systems, while the remaining 20 % is used for petrochemicals, asphalt, lubricants, heat, and electricity, in the order of their priorities.[5] Fossil fuels have built the standard of modern and wealthy people as compared to the lives of our ancestors. It has also added disparity and inequity in our society since almost half of the global energy supply is consumed by wealthy countries and only 3 % is consumed by poorer nations while the rest of the 47 % energy is consumed by nations that are neither rich nor poor. The research in energy is the perfect area where chemistry can play an important role in establishing new ideas, concepts, materials and methods to be applied for the productive energy conversion and storage followed by their effective distribution and efficient utilization.[6]

2. Problem: Fossil Fuels and their Effect on Environment

Ever since the dawn of mankind, humans have used biomass such as the organic material obtained from plants and animals as their main energy resource. Biomass has been used to satisfy three basic needs: food, energy and valuable materials. Biomass can produce energy in the form of heat and electricity and can also be used for the production of biogas and liquid biofuels. Currently, fossil fuels such as coal, oils and natural gas form the basis of the world's economy, although it is well known that they are regional, limited and will not last forever. Coal reserves by far are the largest in quantity, among the fossil fuels, as they may cover the present world energy demand for approximately 110 more years, as compared to 52 years each, for oil and natural gas, respectively. Therefore, in order to meet the energy demands of the current and the future generations, we should develop processes to transform biomass into biofuels however, this process is likely to compete with the agricultural food production.[2, 7] Due to the burning of fossil fuels, there is a huge increase in air pollution accompanied with the release of a large amount to green house gases such as water vapor (H_2O), carbon dioxide (CO_2), methane (CH_4), nitrous oxide (N_2O) and ozone (O_3) into the atmosphere.[8] Greenhouse gases are gases that absorb and emit radiant energy within the thermal infrared range. Greenhouse gases confine the heat absorbed by solar radiation on a global scale and accelerates the phenomenon of global warming. Without the presence of excess greenhouse gases, the average temperature of the Earth's surface would be about -18 °C, instead of the present average of 15 °C. Since the beginning of the Industrial Revolution in 1750, human activities have resulted in a 45 % increase in the atmospheric concentration of carbon dioxide, from 280 ppm to 415 ppm in 2019 (see the keeling curve in Figure 3 below). The majority of the carbon dioxide (CO_2) emission comes from the combustion of fossil fuels, deforestation, changes in land use, soil erosion with an additional contribution from agriculture. However, the leading source of methane (CH_4) emission in our atmosphere is from animal agriculture.[9, 10]
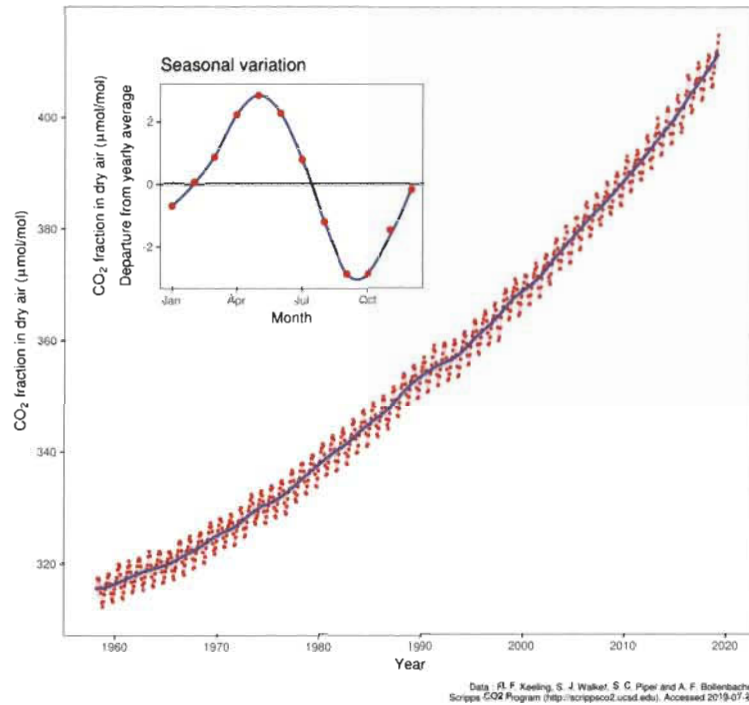
Figure 3. Keeling Curve: Atmospheric concentrations of CO_2 measured at the Mauna Loa observatory.

Since we know that fossil fuels are finite and regional, it is quite challenging to assure that our energy demands can be met, despite the possible political strains and other problems pertaining to energy supplies. The melting of ice caps and glaciers due to global warming caused by the emission of greenhouse gases has resulted in a rise in the sea level. Nevertheless, mankind now must face the consequences arising from this fossil fuels dependence. The intergovernmental panel on climate change recently reported the importance of the necessity to decrease CO_2 emission to zero level on a global scale before the next century. All these discussions clearly make the development of clean, sustainable, and carbon-neutral energy technologies as one of the most urgent challenges all over the world. We need to phase-out fossil fuels on account of the numerous drawbacks associated with them. The prompt termination of their use is, however, not suitable because, our infrastructures and lifestyles strongly depend on them, and the absence of an

5

equivalent amount of alternative energy resources, would cause the world's economy to collapse. By waiting for the progress in the development and exploitation of renewable energy resources, we have entered into an era of energy crisis.[8, 11, 12]

3. Possible Solutions: Renewable Energy Resources

There are three main categories of energy resources, (i) fossil fuels, (ii) renewable, and (iii) nuclear energy resources. Fossil fuels are currently providing almost 85 % of global energy needs and it is clear that burning large amount of fossil fuels is posing serious problems to life on earth. It is therefore necessary to develop alternative energy resources which are clean, renewable and sustainable. The energy collected from renewable resources, which are naturally replenishable on a human timescale, is called renewable energy. Renewable energy resources can be used to produce energy repeatedly: for example, solar energy, wind energy, biomass energy, geothermal energy, etc (see Figure 4). At present, renewable resources provide energy in four main areas, (1) electricity generation, (2) air and water heating or cooling, (3) transportation, and (4) rural (off-grid) energy services.[13, 14]

Solar Energy   **Wind Energy**

Bio Energy   **Hydro Energy**   **Geothermal Energy**

Figure 4. Different types of renewable energy resources: solar energy, wind energy, biomass energy, hydro energy, and geothermal energy, etc.

Renewable energy sources have the potential to provide energy with zero or almost zero emission of both greenhouse gases and air pollutants. There are three key technology changes in the sustainable energy development strategies, (i) energy savings on demand, (ii) improved efficiency in the energy production, and (iii) replacement of fossil fuels by renewable energy resources. Influenced by the energy savings and their efficiencies, renewable energy must be implemented on the large scale into our current energy systems. The most abundant and renewable energy on our planet is solar energy. The energy of solar illumination on Earth every hour is greater than the global energy consumption for an entire year. Hence, the conversion, storage and utilization of solar energy is a promising solution for the energy problems we are currently facing.[15]

(a)   (b)

Solar Energy to Electrical Energy   **Solar Energy to Chemical Energy**
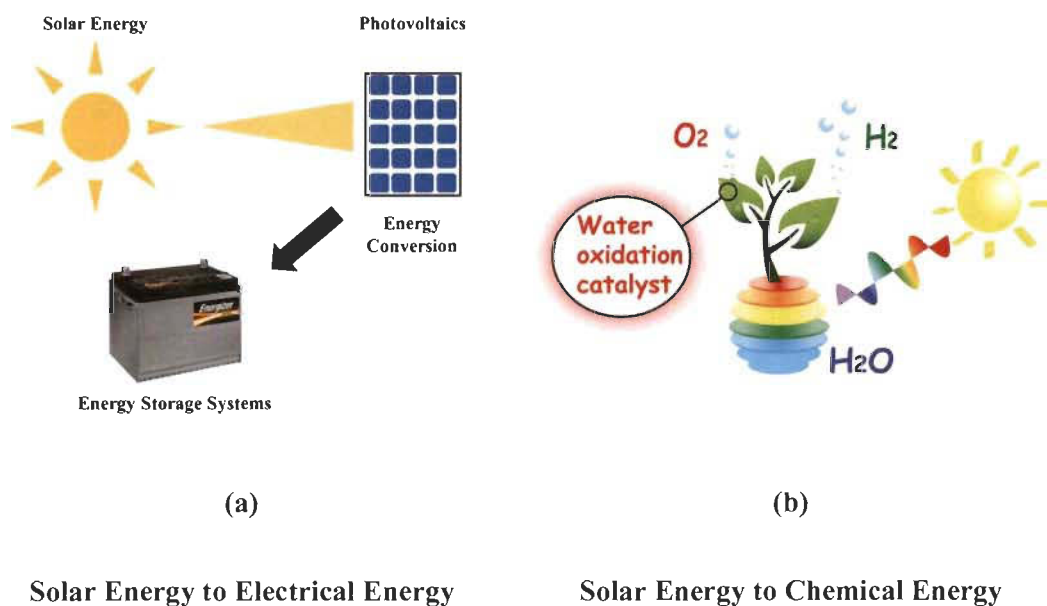
Figure 5. Solar energy conversion and storage, (a) Solar energy to electrical energy, (b) Solar energy to chemical energy.

Solar energy carrier consists of photons moving at the speed of light. Basically, solar energy can be used, by converting it into electrical energy with the help of photovoltaic devices. Generally, these devices are light absorbers that undergo charge separation to generate separated electrons and holes when light is incident on them. These photogenerated electrons and holes can be collected to produce potential and current *viz.* electricity, which is one of the most important necessities in our daily life. Nevertheless, electricity cannot be stored on a large scale because, the energy density of batteries is low. Thus, instead of collecting the photo-generated electrons and holes for electricity, they can be used to power chemical reactions. Hence the harvested solar energy can be transformed into chemical energy (solar fuels), stored in the form of chemical bonds. This process is inspired by and it imitates the function of natural photosynthesis and is commonly called artificial photosynthesis.[11, 15]

Photosynthesis is the process through which plants and some microorganisms convert solar energy into chemical energy. Photosynthesis is derived from Greek word, phos, which means "light" and synthesis, which means "putting together". Substantially, oxygen is released as a by-product during the process. Photosynthesis is mainly responsible for producing and maintaining the oxygen content of the Earth's atmosphere. The chemical energy *viz.* carbohydrates, obtained by the conversion of carbon dioxide (CO_2) and water (H_2O) with the help of sunlight can be released later to fuel organism activities. For several thousands of years, plants and microorganisms on Earth have provided oxygen and food for the aerobic life cycle by the process of photosynthesis. Photosynthesis occurs by the combined effort of photosystem I (PSI) and photosystem II (PSII). Triggered by sunlight, water (H_2O) is firstly oxidized in PSII into oxygen (O_2), releasing four protons and four electrons. The protons and electrons are then transferred to PSI *via* cytochrome b6f, where these electrons and protons are finally consumed to produce carbohydrates, by carbon dioxide (CO_2) reduction reaction (CRR).[16-19] A simple schematic diagram of the natural photosynthesis process is shown in Figure 6.
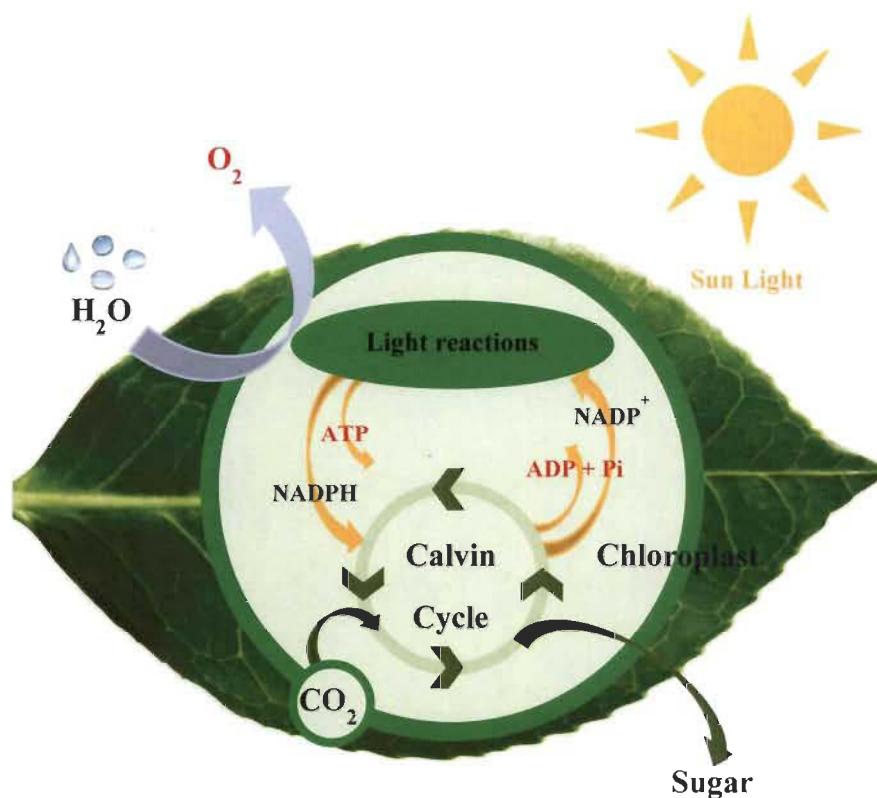
Figure 6. A schematic diagram of natural photosynthesis process.

The photosystems and photosynthesis are very complex processes and it is difficult to imitate their structures and components. Nevertheless, their functions and chemical processes can be mimicked, and nowadays practically, solar energy can be converted into chemical energy (solar fuels). There are three main techniques by which solar energy can be converted to chemical energy: (i) by photo electrocatalytic reactions, (ii) by photocatalytic reactions and (iii) by using the electricity generated from solar cells to drive electrocatalytic reactions. The first two techniques are direct whereas the third technique is an indirect way of conversion. The production of hydrogen by the process of water splitting and the reduction of carbon dioxide to produce carbon neutral fuels are the most widely investigated reactions in artificial photosynthesis.[11]

Technically, hydrogen would be an exceptional solution for the current energy crisis. The ideology of depending on hydrogen to obtain energy was first proposed by Jules Verne in 1874, when he

published his novel L'lle mystriéuse (The Mysterious Island). In the novel, the author claimed that, "Water will be the coal of the future". He further proposed that water made up of hydrogen and oxygen will be used as a fuel and will provide infinite source of heat and light of which even coal is not capable.[20] The curiosity towards the use of hydrogen as a fuel arose in the 1970s when people started getting concerned about the depletion of fossil fuels and the effect of global warming. During the last three decades, several scientists and government bodies have proposed hydrogen economy as a means to solve the problems associated with the use of fossil fuels. The idea is very interesting because, (i) hydrogen can be used directly in internal combustion engines (ICEs) and in fuel cells to generate mechanical and electrical energy, respectively, (ii) the combustion of molecular hydrogen with oxygen in ICEs and the combination of molecular hydrogen and oxygen in fuel cells produces heat and electricity, respectively, (iii) the only by-product produced by its usage is water whereas the combustion of fossil fuels produces carbon dioxide and several other atmospheric pollutants. Therefore, the problems based on energy and environment can be simultaneously solved by replacing fossil fuels with hydrogen.[21, 22] Hydrogen is the most plentiful element in the cosmos and is the third most abundant element on Earth's surface in the form of molecules with other elements. Under normal conditions, molecular hydrogen (H_2) exists in gaseous form and is invisible, non-toxic and light in nature. However, molecular hydrogen is very rare on Earth (about 1 ppm by volume). It escapes the earth's atmosphere due to its light weight and due of its high reactivity. Besides, hydrogen is always combined with other elements. Hydrogen is highly flammable, and it mixes well with air and can form explosive mixtures at high concentrations. In air, it burns at concentrations between 4 % to 75 %. Due to its small size, it has the potential to diffuse through most materials thus making them brittle for example, it can easily diffuse through steel and make it brittle, this phenomenon is called as hydrogen embrittlement.[23] The efficient storage of large amount of hydrogen has also been a difficult assignment as the volumetric energy density of H_2 is very low compared to the other fuels. Uncompressed hydrogen occupies 11,250 L kg^{-1} at room temperature and when pressurized at 35.5

MPa/ 350 atm in a steel tank, it occupies 56 L kg^{-1}. It liquifies at -253 °C (20 K) and liquified hydrogen occupies 14.1 L kg^{-1}. Hydrogen has a very high energy content relative to its mass, 120 MJ kg^{-1}, compared to 44.4 MJ kg^{-1} for gasoline. Therefore, the search for efficient and cost-effective methods for the production and storage of H$_2$ is one of the most challenging contemporary tasks. Molecular hydrogen cannot be obtained spontaneously from water, additional energy must be provided for its production. Therefore, hydrogen is an energy carrier and not an alternative fuel.[24, 25] Nowadays, about 50 million tonnes of hydrogen is produced yearly worldwide.[26] It is mostly used as a feedstock in the chemical and petrochemical industries to mainly produce ammonia and lighter hydrocarbons, respectively. Hydrocracking is a process in which hydrocarbon molecules of petroleum are broken into simpler molecules, like gasoline or kerosene, by the addition of hydrogen under high pressure in the presence of a catalyst. Due to the increased oil prices, the rate of hydrogen used for hydrocracking is growing. Practically, only a small amount of hydrogen is distributed to the end users.[27] Currently, almost 95 % of hydrogen is produced by steam reforming of fossil fuels which besides hydrogen produces carbon dioxide, while the remaining 5 % of hydrogen is produced by electrolysis and thermolytic water splitting, which are much costlier processes (Figure 7).

(a) (b)

Sources of hydrogen production **Hydrogen consuming sectors**
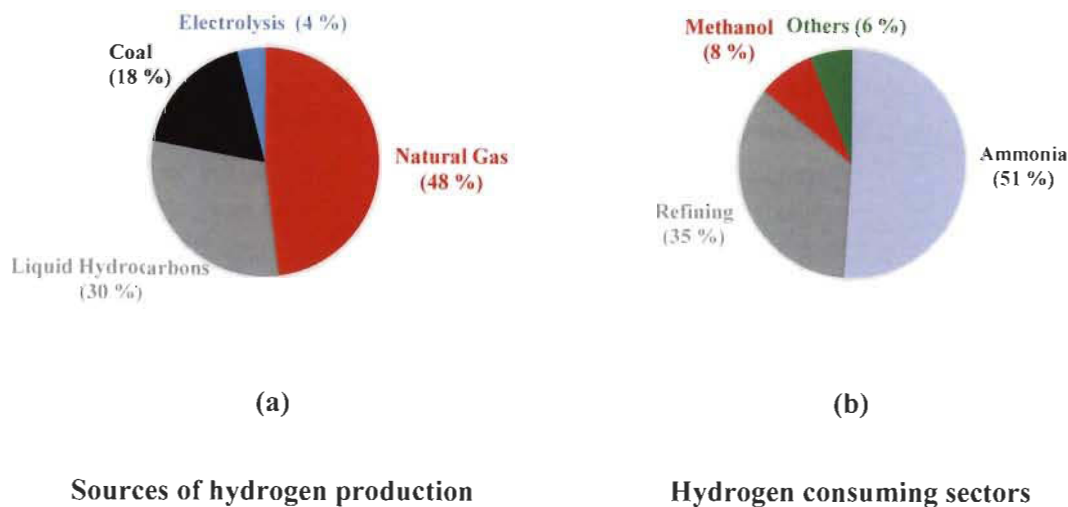
Figure 7. (a) Current sources of hydrogen production all over the world, (b) Main hydrogen consuming sectors.

3.1. Design of Catalytic Materials for Energy Applications

At present, there are three main type of materials considered as most promising for applications in energy conversion and storage. These are (i) catalytic materials, (ii) electronic materials and (iii) porous materials. Examples of these materials are provided in Figure 8. Materials such as molecular complexes, metal-organic frameworks (MOFs), covalent organic frameworks (COFs), and hydrogen-bonded organic frameworks are widely recognized to have catalytic, electronic and porous properties. They can be efficiently used in the preparation of (i) renewable fuels, (ii) solar energy conversion and storage, (iii) gas storage tanks, (iv) electrodes for batteries and many other sectors. The synthetic procedures to prepare these materials are simple and well known and they consist of linking organic building blocks *via* coordination, covalent and hydrogen bonds.[28-30]

a   b   c   d
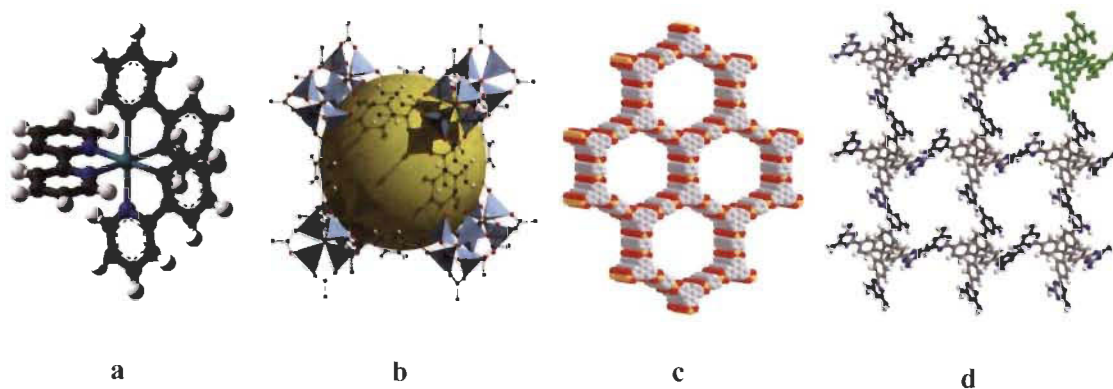
Figure 8. Materials known for their properties in energy conversion and energy storage. a) Molecular Complexes, (b) Metal-Organic Frameworks (MOFs), c) Covalent Organic Frameworks (COFs), and d) Hydrogen-bonded Organic Frameworks (HOFs).

a. Metal-Organic Frameworks (MOFs) for Energy Applications

Metal-organic frameworks (MOFs) also known as porous coordination polymers (PCPs), are an emerging class of crystalline porous materials, which are constructed by metal ion/ cluster centers coordinated with organic linkers. MOF based materials possess several advantages such as, crystalline porous structures, diverse and tunable chemical components, and high specific surface area, which offers attractive functions for catalysis. The high gas storage capacity of MOFs under ambient conditions has directed their rapid growth, offering a large number of new adsorbents for applications in fuel cells, vehicle gas tanks and stationary power facilities.[31-36] Now a days, MOFs with photo and electroactive ligands and metal ions are also being prepared and used for energy conversion and energy storage devices.[37] Moreover, the well-organized low-dimensional structures with controllable size and morphologies have opened new avenues for their applications and offers several advantages as far as post-synthetic modifications are concerned. The structure and properties of MOF-based materials are strongly dependent on the diverse combinations of metal ions/ cluster nodes and coordinated organic linkers. In the case of metal nodes, catalytically active metal ions can be selected to design MOFs. Due to their intriguing structure and properties, MOFs can also be used as supports and sacrificial precursors. Many active functional materials like metal nanoparticles,[38] metal oxides,[39] semiconductors,[40] and molecular complexes[41] can be immobilized on the surface of MOFs to create new advanced materials with unique characteristics and properties, providing new momentum for energy applications. Due to their tailorable properties, MOFs can be synthesized with specific surface area ranging from 1000 to over 6000 $m^2 g^{-1}$, which can be beneficial in the case of post-synthetic modifications. Series of MOF-supported catalysts and MOF derivatives (see Figure 9 below) have been designed and synthesized by post-synthetic modifications.[42]
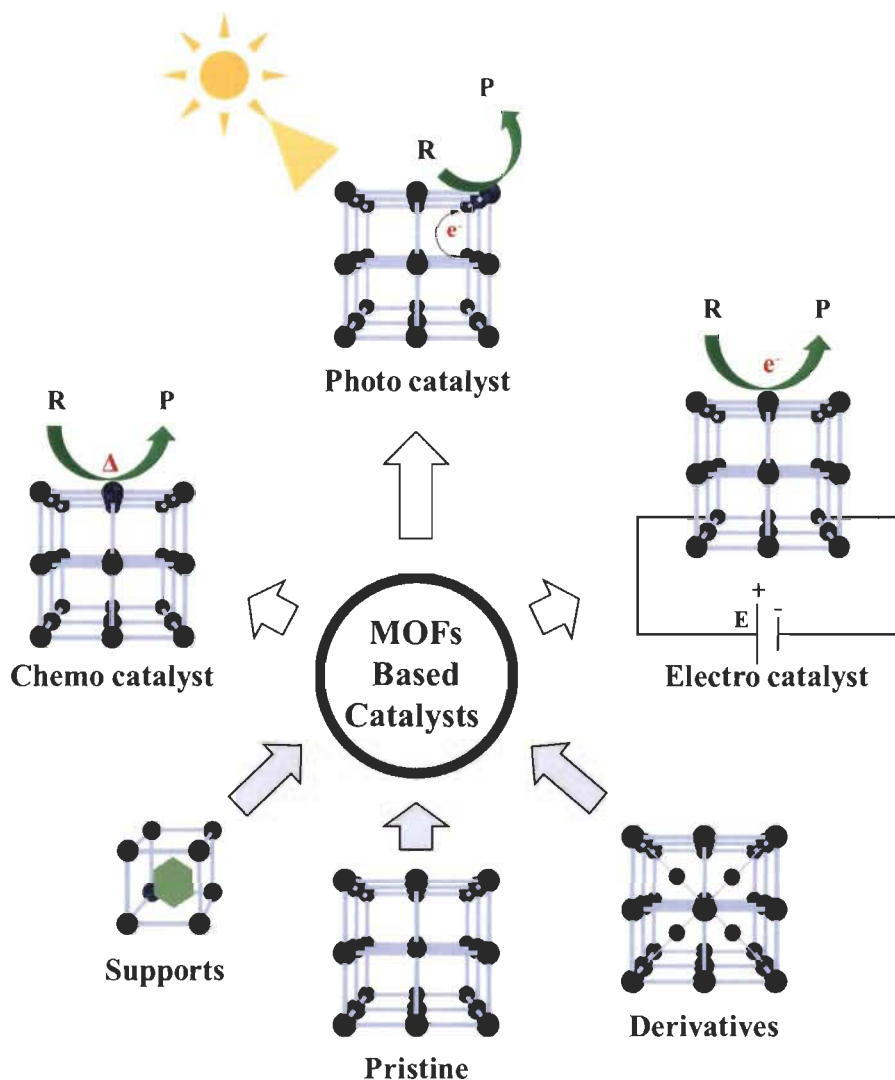
Figure 9. Flow chart of MOF-based catalysts for different type of catalytic reactions. Apart from their pristine forms, MOFs can also be used as precursor materials and supporting frameworks for chemocatalytic, photocatalytic and electrocatalytic reactions.

These MOF-based catalysts are currently being used in energy conversion reactions such as oxygen reduction reactions (ORR),[43] oxygen evolution reactions (OER),[44] metal-air/ O_2 batteries,[45] CO_2 reductions,[46] as well as hydrogen evolution reactions (HER).[42] When MOFs are used as supports or precursors, they inherit the porous structure of their pristine forms, however their surface areas and porosities reduce. This is the consequence of pore occupation or blocking

by guest molecules. The decrease in porosity strongly depends on the sizes and extent of dispersion of guest molecules. Nevertheless, this decrease in porosity does not necessarily diminish their catalytic performances. In the case of MOF derivatives, the decline of porosity results from the collapse of their crystal structures, which is caused by the decomposition of elements when subjected to high temperature treatments. The large surface areas and pore volumes of MOF-based catalysts ensure sufficient contact between the reactants and the surface of the catalyst, thus improving the catalytic performance as more active sites of the catalyst are being exposed for the reaction to take place.[47] Although MOF-based catalysts have gained enormous amount of interest, their performance in the field of artificial photosynthesis still remains underdeveloped. Catalyst leaching and uncontrollable agglomeration of nanoparticles are two main drawbacks of MOF-based catalysts.[8]

b. Covalent Organic Frameworks (COFs) for Energy Applications

Over the last three decades, numerous chemical architectures have been constructed by gathering different building units in a systematic manner. Specifically, these materials are fascinating because, they have a wide range of applications in materials science,[48] optoelectronics,[49] catalysis,[50] drug delivery,[51] energy conversion and energy storage.[52] However, contemporary scientists are facing challenges in re-establishing catalytic materials with greener methods, easily available feedstocks, efficient materials, and advanced assembly systems to achieve sustainable development. Persistent efforts are undertaken for designing nano porous materials ranging from conventional mesoporous zeolites to coordination polymers like metal-organic frameworks (MOFs). However, their chemistry of formation depends on kinetically controlled irreversible coupling reactions which often results in structural disorders and inseparable oligomers that prevent their catalytic applications. Therefore, the search for ordered, porous and crystalline organic materials has become a modern-day task for several researchers. Covalent organic frameworks are two-dimensional and three-dimensional organic materials with extended

structures in which the building blocks are linked by reversible covalent bonds. They represent an emerging class of crystalline porous materials that can be constructed by selecting appropriate building blocks and linkage motifs. They are one of the most important and dynamic members of porous organic materials providing an ideal system for constructing efficient catalysts. COFs are porous and crystalline materials made entirely from light elements like hydrogen, boron, carbon, nitrogen, and oxygen. They possess high surface areas and physicochemical stabilities, and with appropriate building blocks and layered stacking sequences, COFs have exhibited high charge carrier mobilities.[53, 54]

Even though the research in the field of COFs is still at its initial stages, the well-defined structure, easy modification of functional groups, high surface area with simple and diverse structural design has given COFs a very high potential in various applications such as, catalysis, gas storage and separation, optoelectronics and sensing[55]. Nevertheless, it is expected that the formation of COFs by linking organic building blocks is thermodynamically unfavorable. To obtain crystalline COFs, the bond formation must be reversible, and the rate of reaction should be such that it allows the defects to be self-corrected. Reversible covalent bond formation is considered to be the primary criterion to build crystalline COF materials.[57] COFs are also regarded as "organic zeolites" because, in contrast to MOFs, they are constructed from pure organic building blocks through reversible covalent bonds with predictable control over composition, topology and porosity. To date, the linkages involved in the formation of COFs consists of B-O (boroxine, boronate ester, spiroborate, and borosilicate), C=N (imine, hydrazone, and squaraine), C-N (β-ketoenamine, imide, and amide), etc.[48, 57] The organic skeletons of COFs make them simple for post-synthetic modifications and suitable for affixing functional groups. Contrary to MOFs, the densities of COFs are lower, and they show excellent stability in organic solvents, and even under changing acidic, alkaline, and redox conditions[58]. Moreover, COFs can withstand severe conditions and can conserve their ordered structure and crystallinity. This may be due to their metal-free skeleton

connected with strong covalent bonds instead of coordinate covalent bonds in MOFs. Furthermore, the combinations of existing weak interactions like hydrogen-bonding and π-π stacking further reinforces the skeleton, protecting it from solvation and hydrolysis. As compared to inorganic zeolites and porous silica materials, COFs possess higher porosity and tunable pore size which increases the tendency of diffusion of reactants as well as desorption of products enhancing their catalytic performances with high yield and selectivity.[59]

Metal nanoparticles supported on COFs have proven to be highly efficient catalysts in many chemical reactions.[60] Due to the excellent physicochemical properties of COFs, they provide countless features that are advantageous from the heterogeneous catalysis point of view. They serve as a host for several metal nanoparticles since their well-organized structure minimizes the agglomeration of immobilized nanoparticles. The considerable spatial distance allows the inclusion of numerous catalytic sites in the same COF, which bestows synergistic catalytic effects. They also have permeable channels that allow the substrates to easily access the catalytically active sites, allowing constricted chemical reactions to occur easily and efficiently. In addition, the catalysts can also be separated from the reaction mixture and reused (catalyst recycling). As a result, metal nanoparticles supported on COFs are of significant interest for applications in heterogeneous catalysis.[60] Several COF based catalysts has been developed for oxygen reduction reactions (ORR),[61] oxygen evolution reactions (OER),[62] hydrogen evolution reactions (HER),[63] and CO_2 reduction reactions (CRR)[64] in energy conversion and fuel generation (see Figure 10).
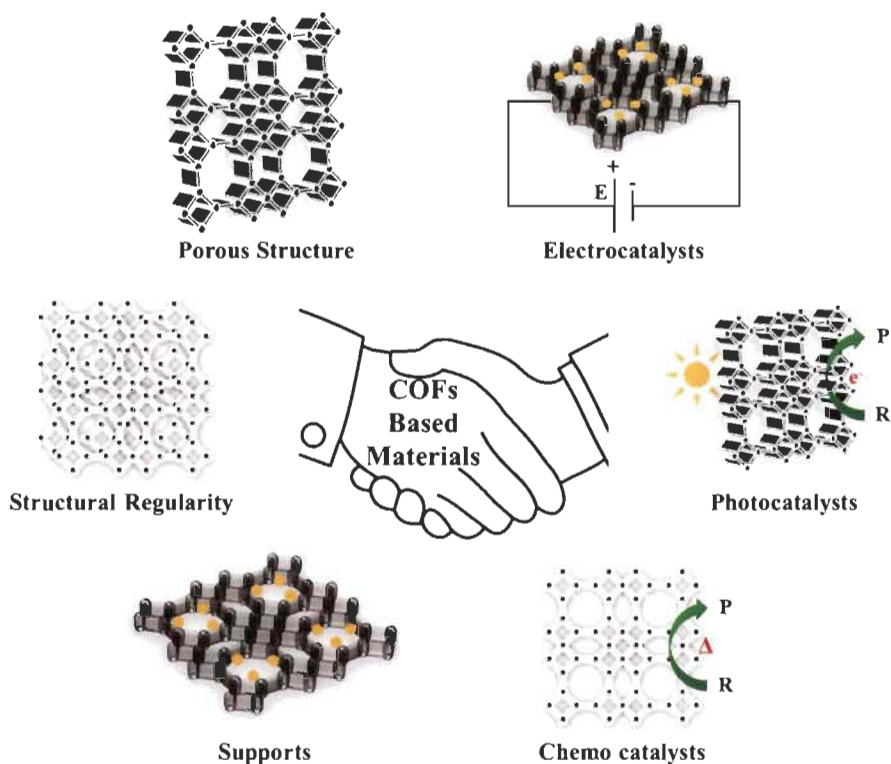
Figure 10. Flow chart of COF-based catalysts for different types of catalytic reactions. Other than their pristine forms, like MOFs, COFs can also be used as precursor materials and supporting frameworks for chemo catalytic, photo catalytic and electro catalytic reactions.

c. Hydrogen-Bonded Organic Frameworks (HOFs) for Energy Applications

Hydrogen-bonded organic frameworks are strong and flexible porous networks, constructed from pure organic building blocks mostly by hydrogen-bonding interactions. They are mainly built from aromatic scaffolds and hydrogen-bonding interacting sites, also called the backbone and sticky sites, respectively. Basically, HOFs are constructed by combining the host molecules (organic building blocks) with solvent guests in the solution via self-assembly. The organic building blocks are prepared in such a way that they possess the two most important requirements to build HOF materials *viz.* the backbone, which is usually an organic compound, and the sticky sites, which can be organic or inorganic substituents. Figures 11 and 12 below display various examples of

aromatic scaffolds and sticky sites, respectively, from which HOFs can be prepared. The structure and the properties of HOFs strongly depend on the type of organic building blocks and their self-assembly, from which various HOF molecules with diverse morphologies and pore structures can be obtained.[65]
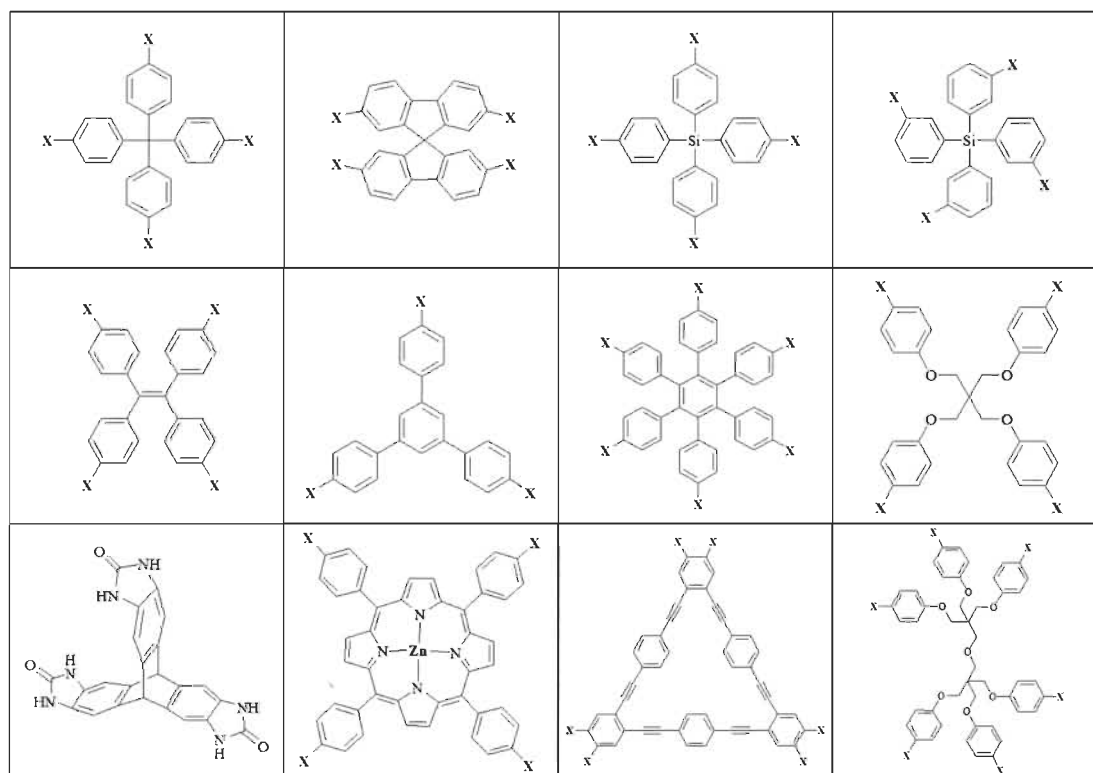
Where **X** = Hydrogen-bonding interacting sites or sticky sites

Figure 11. Types of aromatic scaffolds/ backbone constructed from pure organic building blocks.[65]

Hydroxyl or Amine Groups	Carboxylic Groups and Pyrazole Moieties	Amides and Urea groups	Macrocyclic Receptors

Peptides Groups	Pyridone's Moieties	DAT's Moieties
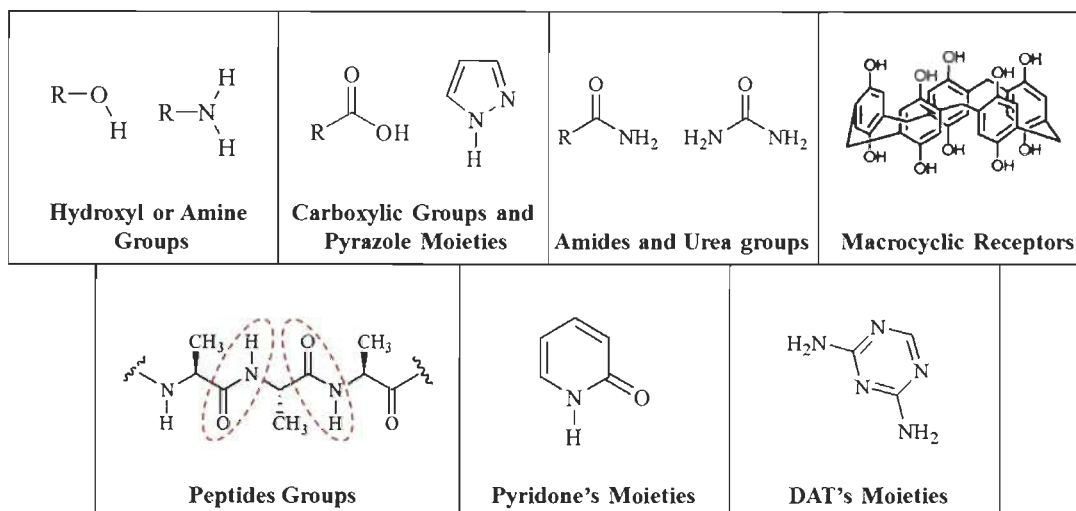
Where R = Scaffold's or Backbone of HOFs

Figure 12. Types of hydrogen-bond interacting sites/ sticky sites constructed from pure organic building blocks.[65]

In order to rationally design porous hydrogen-bonded organic frameworks, some systematic in-depth studies on the use of new hydrogen bonding motifs (sticky sites), backbones (aromatic scaffolds) and detailed crystallographic studies on framework robustness and flexibility are highly required. [66] Even though, HOFs materials were proposed as potential porous materials about two decades ago, their permanent porosities were not established until 2010.[67] This is mainly because the hydrogen bonds and other interactions in HOFs are weak, which makes them difficult to stabilize, therefore the structurally porous HOFs collapse once the solvent guest molecules are removed after thermal or vacuum activation treatment. Such a failure situation also happened in the early stages of development of porous MOFs, until a few MOFs with permanent porosity were discovered. HOFs are more fragile and difficult to stabilize because, as compared to MOFs and COFs, which are constructed from coordination and covalent bonding, HOFs are built from weak hydrogen-bonding interactions. It is hence not surprising that the research on HOFs lags behind as compared to MOFs and COFs, although the ideas to construct MOFs and HOFs were basically proposed during the same period i.e. around the early 1990s.[67] However, once the solvent guests

are removed, the supramolecular structure of HOFs may or may not collapse, depending upon how the self-assembly has taken place. If the solvent guests have limited influence on the stability of assembled supramolecular networks, the HOF will not collapse, while if the solvent guests have some influence, the HOF structure would collapse. Even though weak hydrogen bonds are responsible for the low stability of HOFs, as compared to strong covalent and coordination bonds, they are more flexible. In order to construct flexible HOFs, the organic molecules should also be somewhat flexible. With the combination of soft hydrogen bonding and flexible organic building blocks, it is possible to develop purely organic flexible HOFs. Flexible HOFs can have several modes of structural transformation in response to different types of external stimuli, including both physical and chemical stimuli. The greater flexibilities of HOFs as compared to MOFs make them superior candidates for applications in sensing, host-guest chemistry, gas separation and some other fields. Although, several HOFs have been reported in the literature from the last two decades, the examples of HOFs with permanent porosities are very scarce.[68]

In contrast to MOFs and COFs, hydrogen-bonded organic frameworks have several advantages, (i) they are self-assembled by weaker hydrogen-bonding interactions, (ii) they have predictable non-covalent directional interactions, (iii) they can be built from identical or different organic components, (iv) they are less expensive and easy to synthesize and characterize, (v) they can be easily recovered and purified, (vi) they are simple to crystallize and recrystallize a countless number of times, (vii) they have easy solution processability and, (viii) they have potentially high thermal stability. Due to all these advantages, HOFs are quite promising materials. In addition to gas storage and separation,[69] they also have applications in proton conduction,[70] molecular recognition[71] and optical applications.[72]

By identifying the permanent porosities of several HOFs around 2010, it has become a very hot topic in chemistry and materials science for mainly gas storage and separation applications. However, there are not many examples of HOF based catalysts neither in their pristine forms nor

after any post-synthetic modifications. However, nowadays studies are aiming for the preparation of highly porous carbons derived from HOFs. The porous carbons are prepared from the carbonization of HOFs. These porous carbons can be used as catalysts for hydrogen evolution reactions (HERs),[73] oxygen reduction reactions (ORRs)[74] and they also have applications in batteries[75] and super capacitors[76]. Figure 13 below is an example for the preparation of highly porous carbons synthesized after the self-assembly, and the isolation of supramolecular structure made from melamine and trimesic acid by the process of carbonization.[77]
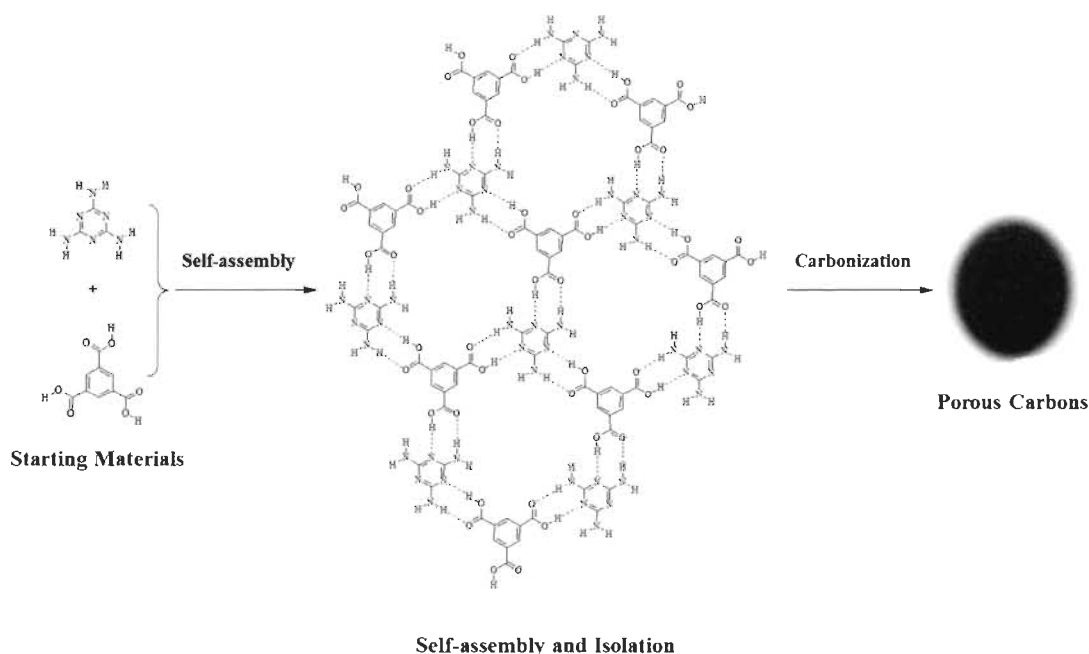
Figure 13. Carbonization of a HOF prepared from melamine and trimesic acid.[73]

3.2. Catalytic Materials for Hydrogen Production

Around 85 % of global energy needs are provided by the burning of fossil fuels. Such a large-scale utilization of fossil fuels has caused grave problems on human health, environment, and sustainability. Therefore, it is very crucial to develop alternative energy resources through clean and renewable paths, thereby ensuring environmental protection. Every day, Earth receives a great amount (in the range of terawatts) of solar radiation. Even if a small quantity of this abundant,

22

clean, and free energy can be converted and stored, the global energy demands can be easily met. In order to reduce our dependency on fossil fuels, the development of clean and sustainable energy sources utilizing solar radiation is highly needed.[78] Sun light triggered water splitting into hydrogen and oxygen, fuel cells for the conversion of fuels (H_2 and O_2) into electricity, and batteries for the storage of electricity, are technologies that are promising for current and future energy demands in portable energy carriers, engines and power plants. Due to their very high energy density and almost zero carbon emission, such energy conversion and storage technologies are presently under intensive research and development.[79] The core of these renewable energy technologies consists of four main chemical reactions: (i) oxygen reduction reactions (ORR), (ii) oxygen evolution reactions (OER), (iii) hydrogen evolution reactions (HER), and (iv) carbon dioxide reduction reactions (CRR). The efficiency of artificial photosynthesis devices is determined by these reactions. Since the photochemical and electrochemical reactions are slow, catalysts must be added to accelerate their reaction rates. Noble metals and metal oxides are the most widely used and reported catalysts for these processes. Platinum group metal catalysts are used in fuel cells and metal-air batteries to improve the electrochemical processes and metal oxides are used as catalysts and electrolytes for OER and HER.[80, 81] Nevertheless, these metal-based catalysts often suffer from high cost, poor durability and at times harmful environmental effects, which limits their applications.[82] Therefore, there is a necessity to develop and use materials that are earth-abundant, less expensive, stable and active in catalyzing ORR, OER, HER and CRR.

In nature, there are certain enzymes found in bacteria, algae, and archaea, termed as 'hydrogenases' (H_2ases), which catalyse the reversible oxidation of dihydrogen molecules and play a crucial role in microbial energy metabolism. Hydrogenase enzymes catalyze the reaction in both the directions, that is, they produce and consume hydrogen at the same time.

$$2H^+ + 2e^- \leftrightarrows H_2$$
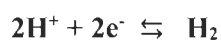
There are three types of hydrogenases, based on the metal content: mononuclear [Fe] and dinuclear [FeFe] and [NiFe]. As shown in Figure 14, hydrogenases have some common features in their structures. Each enzyme has an active site which is engulfed by the surrounding protein. The catalysis occurs at the active site of the H_2ases. The active site is also a metallocluster, and each metal is coordinated to carbon monoxide (CO) and cyanide (CN^-) ligands, apart from proteins. The H_2ases are very efficient catalysts for biological hydrogen production, one particular H_2ase produces hydrogen with a TOF frequency (TOFs) of 9000 s^{-1}. It is due to their outstanding catalytic activities; that the hydrogenases are of special interest for researchers to create biomimetic and bioinspired catalysts.[83, 84]

Dinuclear [FeFe], [NiFe]   **Mononuclear [Fe]**
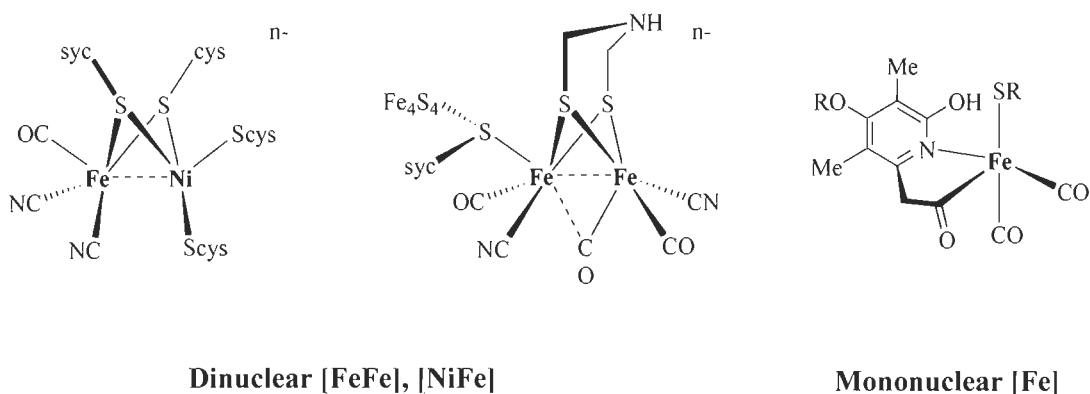
Figure 14. Three types of hydrogenases based on the active sites: dinuclear [FeFe], [NiFe] and mononuclear [Fe].[85]

One of the most important hydrogenase enzymes is the [NiFe] H_2ase enzyme, which contains a heterobimetallic active site that is very rare. Since the discovery of the protein structures of the H_2ases, many model molecular complexes have been synthesized that imitate the active sites of H_2ases. So far, of all the reported model H_2ases complexes, only a few of them have been found to be catalytically active. Therefore, scientifically it is very important to design and synthesize biomimetic and bioinspired catalysts that can imitate the active site of H_2ases for large scale

hydrogen production. And if the bioinspired catalysts are based on earth abundant materials, they will be cost effective, which will lead to the formation of sustainable energy technologies.[85]

a. Photocatalytic Hydrogen Evolution Reactions (HER)

To harvest the abundant and inexhaustible power of solar energy in the form of chemical bonds, the hydrogen evolution reaction driven by sunlight has proven to be a fascinating solution. A hydrogen evolution reaction is based on visible light induced activation of photosensitizer (PS) from which the electrons are transferred to the photocatalytic (PC) centre, with the help of a sacrificial electron donor (SED), to produce hydrogen. Cobaloxime complexes ($[Co^{III}(dmgH)_2(L)X]$ type, where L = ligand and X = counter ion) are the most studied and reported photocatalysts in the literature[86] while the most common photosensitizers are based on ruthenium complexes for example, $Ru(bpy)_3(PF_6)_2$.[87] The proton source can be any acid and usually tertiary amines are used as sacrificial electron donors.[88] The solvent is generally used depending on the solubility of all the reaction components. The figure 15 below displays a general reaction scheme for the hydrogen evolution reaction in presence of cobaloxime ($[Co^{III}(dmgH)_2(py)Cl]$) as a photo catalyst (PC), $Ru(bpy)_3(PF_6)_2$ as photosensitizer (PS), triethanolamine as the sacrificial electron donor (SED), aqueous HBF_4 as the proton source and DMF as a solvent, under blue LED light (λ = 452 nm).
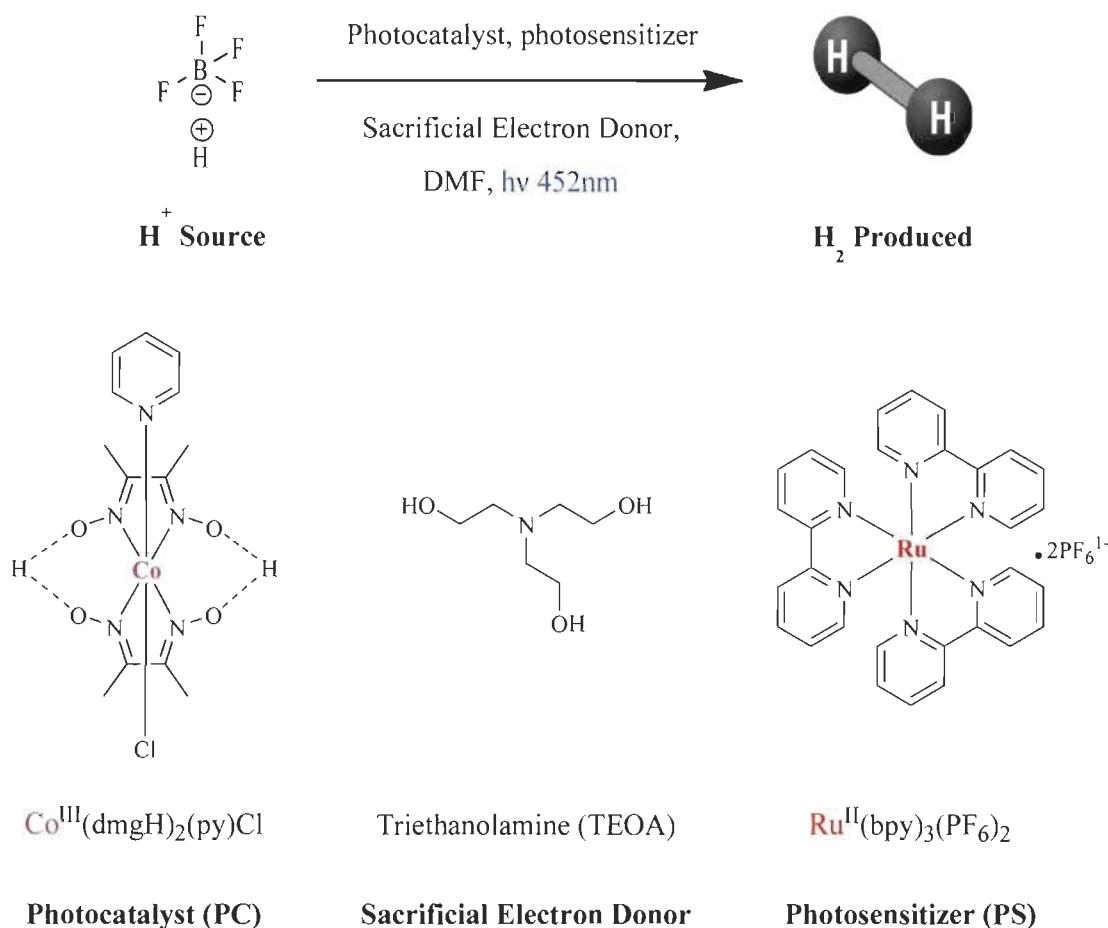
Figure 15. General reaction scheme for hydrogen evolution reaction (HER) in presence of standard reference [Co^{III}(dmgH)$_2$(py)Cl] photo catalyst (PC) with aqueous HBF$_4$ as the proton source, Ru(bpy)$_3$(PF$_6$)$_2$ as photosensitizer (PS), triethanolamine as the sacrificial electron donor (SED), and DMF as a solvent, under blue LED light (λ = 452 nm).

b. Mechanism of Hydrogen Evolution Reaction

The mechanism of hydrogen evolution reaction occurs by two main steps, (i) the activation of the molecular photocatalyst with the help of the photosensitizer driven by visible light, and (ii) catalytic hydrogen evolution, *via* electron transfer and the ability of the photocatalyst to undergo a change in its oxidation state.

Step I: Activation of photocatalyst *via* photosensitizer
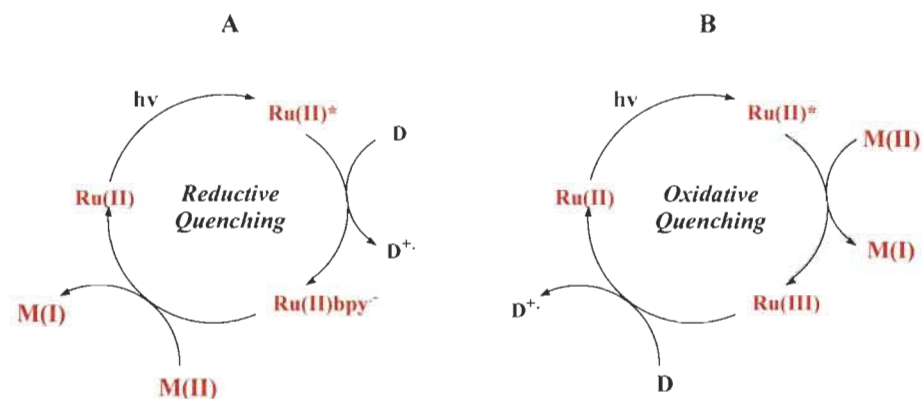
Figure 16. Photosensitizer based processes in light-driven hydrogen evolution reaction, reductive quenching (A), oxidative quenching (B).

Firstly, the activation of molecular photocatalyst occurs, which can take place by two pathways, (i) by reductive quenching, or (ii) by oxidative quenching as shown in Figure 16. The activation mainly occurs with the help of the photosensitizer (PS). Light from the visible region is used for activation where initially the photosensitizer (PS) undergoes excitation. In the process of reductive quenching (A), the excited PS* accepts an electron from the sacrificial electron donor (SED) and shares it with the photocatalyst. The oxidation state of Ru(II) remains the same during this process. In the case of the oxidative quenching process (B), the excited PS* undergoes oxidation to activate the photocatalyst and then abstracts an electron from the sacrificial electron donor. This path involves redox changes in the Ru(II) PS.

Step II: Catalytic hydrogen evolution
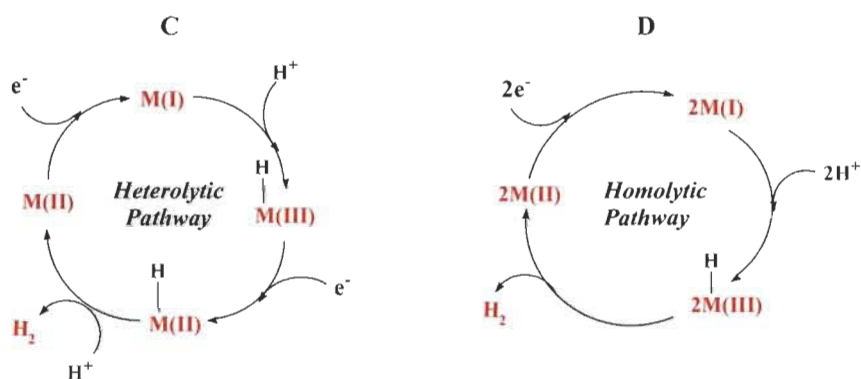
Figure 17. Heterolytic (C) and homolytic (D) mechanisms of hydrogen evolution, catalysed by molecular catalyst.

In step II, the hydrogen evolution can take place by two possible mechanisms: (i) heterolytic or (ii) homolytic mechanism as shown in Figure 17. In the heterolytic mechanism, hydrogen evolution occurs by the protonation of the metal hydride intermediate. In this process two electrons are transferred either alternatively or consecutively to the catalytic cycle, whereas in the homolytic pathway, the hydrogen evolution occurs by the collision of two metal hydride intermediates.[7]

The hydrogen evolution reaction occurs mostly by the oxidative quenching mechanism as for example, $[Ru(phen)_3]^{2+}$ (PS) shows an emission peak at 610 nm upon excitation at 450 nm. When the photocatalyst (PC) was slowly added into the $[Ru(phen)_3]^{2+}$ solution (CH$_3$CN/ H$_2$O; v/v = 4:1), its fluorescence intensity started decreasing and was directly proportional to the concentration of the added photo catalyst. However, when triethanolamine was added, there was no change in the fluorescence intensity. This indicates that the excited photosensitizers prefer to oxidize as compared to reduce (Figure 18).[89]

(a)   (b)
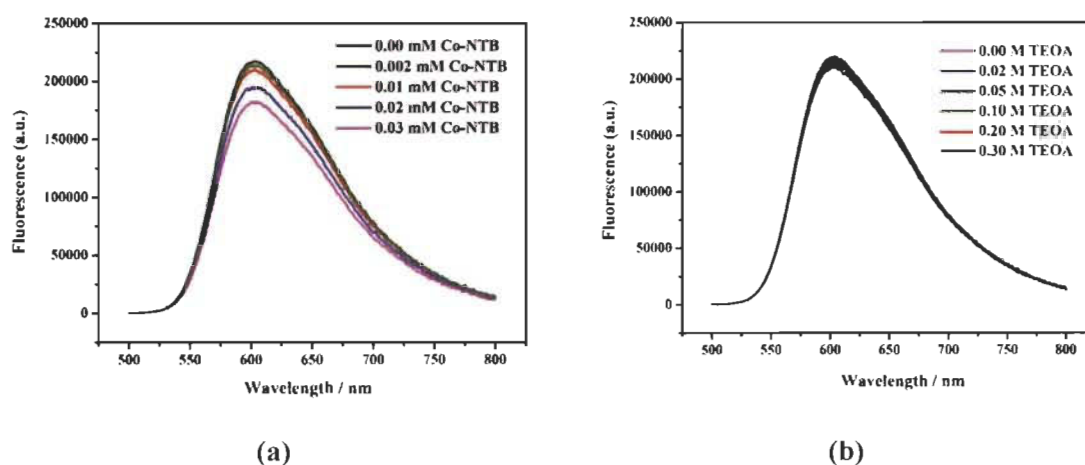
Figure 18. (a) Fluorescence spectra of 0.01 mM [Ru^{II}(phen)$_3$](PF$_6$)$_2$ in CH$_3$CN/ H$_2$O solution (*v/v* = 4:1) with the addition of 0, 0.002, 0.01, 0.02, and 0.03 mM molecular cobalt catalyst, (b) Fluorescence spectra of 0.01 mM [Ru^{II}(phen)$_3$](PF$_6$)$_2$ in CH$_3$CN/ H$_2$O solution (*v/v* = 4:1) with the addition of 0, 0.02, 0.05, 0.1, 0.2, and 0.3 M TEOA.

In the case of homogeneous catalysts, the HER can take place by both homolytic as well as heterolytic pathways. However, in the case of heterogeneous catalysts, it can occur only by heterolytic pathway, because the homolytic path involves the collision of the two metal hydride intermediates.[90]

c. Role of the Sacrificial Electron Donor (SED)

Usually, aliphatic tertiary amines are used as sacrificial electron donors (or sacrificial reductants) in the photocatalytic hydrogen evolution reactions. According to previous reports, each tertiary amine molecule undergoes two single-electron oxidations alternatively, followed by degradation (Figure 19, equations 1-4). In the first step, TEA undergoes oxidation to form a radical cation TEA$^{\cdot+}$ and gives out an electron (e$^-$). In step two, the proton from the α carbon atom of the radical cation (TEA$^{\cdot+}$) is rapidly deprotonated rendering a neutral carbon radical species (TEA$^{\cdot}$) on the α carbon atom with the release of a proton (H$^+$). This neutral carbon radical species is highly reducing and further undergoes a second oxidation to give an electron and form an iminium cation, in the step three. In step 4, the iminium cation undergoes hydrolysis to give diethyl amine (DEA), acetaldehyde and a proton (H$^+$). Each TEA molecule can donate two electrons and two protons during the course of the reaction. Since the oxidized TEA species is highly active, its rapid conversion avoids any side reactions with photosensitizers or photocatalyst species.

+ e^- (1)

+ H$^+$ (2)

+ e^- (3)
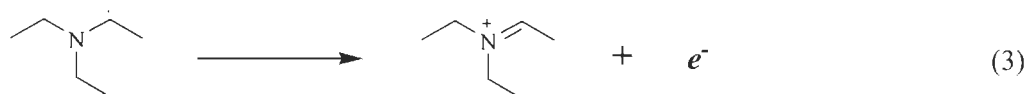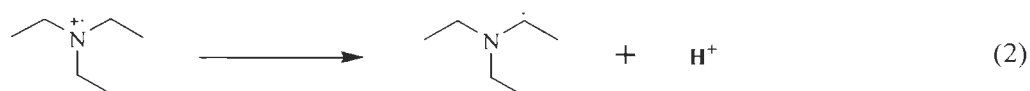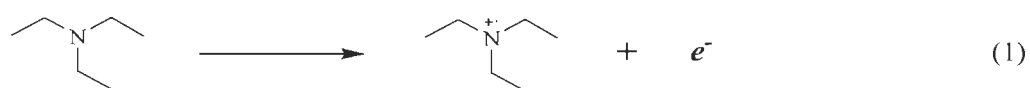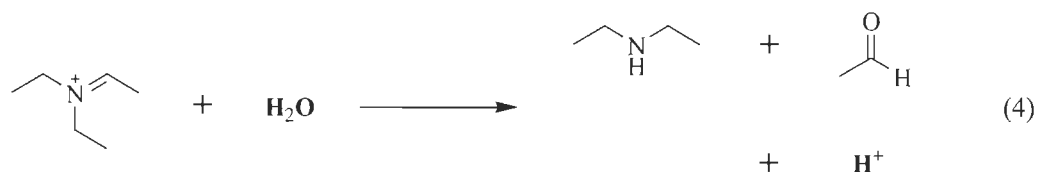
Figure 19. The role of tertiary amines as sacrificial electron donors in hydrogen evolution reactions.

However, the decomposition products of TEA may possibly affect the structures and reactivities of photosensitizers and photocatalysts. Nevertheless, according to literature reports, it does not affect the rate and activity of the reaction.[91]

3.3. Choice of Metal ions

Ruthenium and cobalt complexes are the most widely studied and reported complexes as photosensitizers and photocatalysts respectively.[87, 92] For effective electron transfer, the photosensitizers and the photocatalysts must be closer to each other. Direct contact between the photosensitizer and photocatalysts in the form of covalent and coordination bonds can be beneficial but these are more complicated and expensive to prepare.[93, 94] However, the largest focus of research in this area is the design and development of highly efficient and non-expensive molecular catalysts. In order to be cost effective, the molecular catalysts should be made from earth abundant metals. So far, the majority of catalysts based on Fe, Co, Ni and Cu complexes have been reported for the hydrogen evolution reactions, among which cobalt complexes are widely used due to their efficient electro and photocatalytic properties. In fact, cobaloxime is the utmost studied molecular catalyst. In the case of photosensitizers, ruthenium complexes are the most extensively studied and reported molecular complexes as photosensitizers due to the low cost and abundance of Ru as compared to other transition metals. Research on ligand-based modification of Ru-based photosensitizers is ongoing and is at a progressive stage. The goal of

ligand modification is mostly based on lowering the energies and stabilities of Ru-based photosensitizers.[95]

a. Based on Noble Metals

The first examples of molecular catalysts for photocatalytic hydrogen evolution reactions were based on Rh complexes with polypyridyl ligands. After this finding, numerous Rh-based molecular complexes were developed for photocatalytic hydrogen evolution.[96] In fact, the Bernhard group reported the most efficient Rh based photocatalyst *via* modification of polypyridyl ligands, producing H_2 with a catalytic turnover number (TON) of 5472 (Figure 20). [Rh(dtbbpy)$_3$](PF$_6$)$_3$ was used as a photocatalysts and [Ir(f-mppy)$_2$(dtbbpy)](PF$_6$) as photosensitizer in presence of 0.6 M TEA in 80 % THF-H$_2$O, λ = 460 nm for 22 h (where dtbbpy = 4,4'-Di-tert-butyl-2,2'-bipyridyl and f-mppy = 2-(4-Fluoro-phenyl)-5-methyl-pyridine). The concentrations of the photocatalyst and photosensitizer were kept identical.[91]

[Rh(dtbbpy)$_3$](PF$_6$)$_3$ [Ir(f-mppy)$_2$(dtbbpy)](PF$_6$)
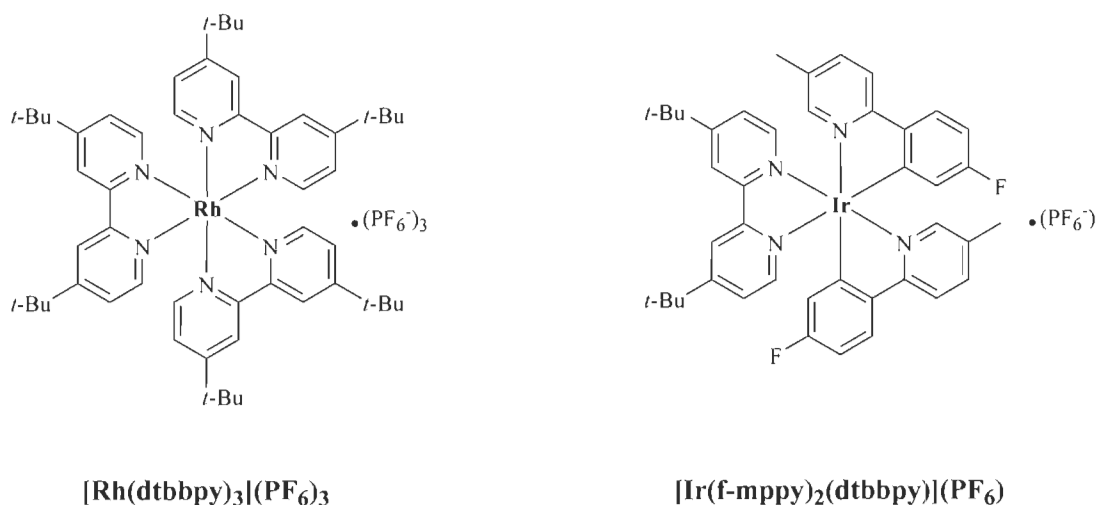
Figure 20. The Rh based photocatalyst and Iridium based photosensitizer used by Bernhard's group.[91]

There are also several other reports based on noble metal molecular complexes for hydrogen evolution reactions, especially on platinum and palladium based molecular complexes which were reported by Sakai *et al.*[80] (Figure 21) However, the high price, toxicity and insufficiency of the noble metals limits their commercial use as photocatalysts and photosensitizers.
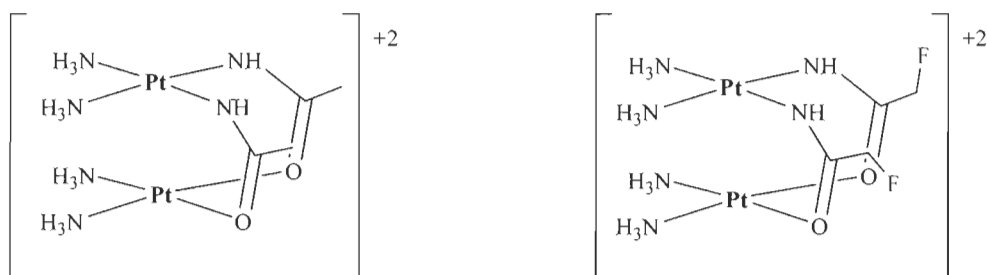
Figure 21. The $[(Pt^{II})_2(NH_3)_4(\mu\text{-amidato})_2]^{2+}$ type complexes reported by Sakai *et al.*[80]

b. Based on Non-Noble Metals

Due to their high activity and stability, many noble metal complexes made from Pt, Pd, Ir, Rh and Re metals ions were used as catalyst.[91, 97, 98] However, the rarity and expensiveness of these metals rendered them unsustainable. Therefore, the feasibility of hydrogen economy relies on the design of molecular complexes based on earth abundant elements. Since the activities of many biological systems to produce hydrogen depends on the first-row transition metals,[99] many researchers and scientists have focused their attention in the field of bio-inspired noble metal free, hydrogen evolution catalysts. From the last decade, large amounts of effort have been made on developing noble metal free catalysts for hydrogen evolution. Many structural and functional mimics of [FeFe] and [NiFe] hydrogenases have been developed to understand the mechanism of biological H_2 evolution and to prepare hydrogen artificially. For instance, complexes **a** and **b** shown in Figure 22, were reported by Rauchfuss *et al.* as [FeFe][100] and [NiFe][101] hydrogenase mimics respectively.
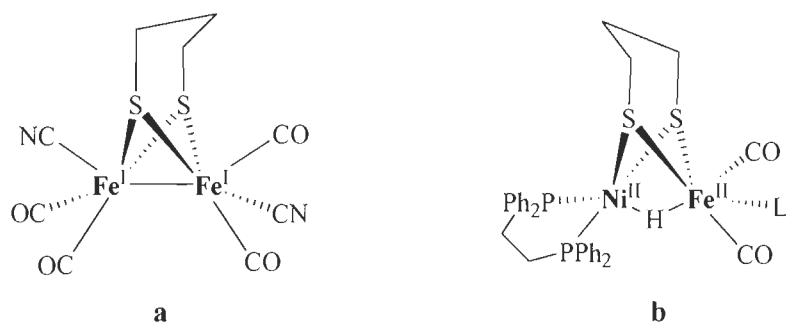
Figure 22. (a) [FeFe] and (b) [NiFe] hydrogenases mimics reported by Rauchfuss *et al.*[100, 101]

Until now, there are more than hundreds of reported synthetic mimics. As seen in the above figure, the structures of these complexes are analogous to the active sites of [FeFe] and [NiFe] hydrogenases, respectively. However, their low stability, large overpotential requirements and poor catalytic performances have limited their use.[102] To obtain essential and cost-effective hydrogen evolving catalysts, several researchers have synthesized different ligands for coordination with earth abundant transition metals such as Fe, Co, Ni, Cu and Mo etc.[103] Currently, the most active and stable molecular catalysts are based on Ni complexes, with diphosphine ligands, reported by DuBois and co-workers (Figure 23). In an acetonitrile solution with 1.2 M H_2O, Ni complex **c** produces H_2 with a TOF of 10^5 s^{-1} at -1.13 V which is very high overpotential.[104] Generally, in water electrolysis, the reduction occurs at -0.83 V. In contrast, the other Ni complex **d** doesn't require much higher overpotential but produces less amount of H_2 as compared to **c**. The dangling amines were proven to be very important for proton transfer in this case.[105]
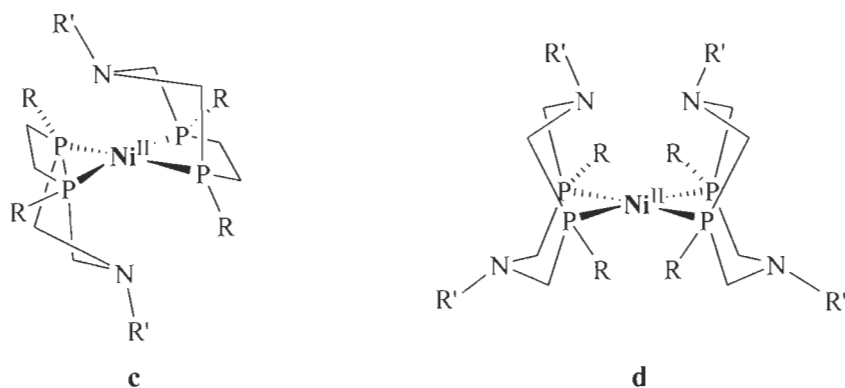
Figure 23. Ni (II) complexes with diphosphine ligands studied by DuBois and co-workers.[104, 105]

Cobaloxime and its derivatives are found to be one of the most studied photocatalysts in the area of hydrogen evolution. Their catalytic activities were first reported by Lehn[106] in 1983 and then by Espenson[107] in 1986. Later in 2005, the Peters[108] and Fontecave[109] groups at the same time started to study more about the structure, function and catalytic activities of cobaloximes. They also studied several other cobaloxime derived molecular complexes - one of the examples is given in figure 24 (complex **f**). By following these pioneering works and due to their high efficiency and low overpotential requirements, cobaloxime catalysts have become the most broadly studied catalysts over the last ten years.
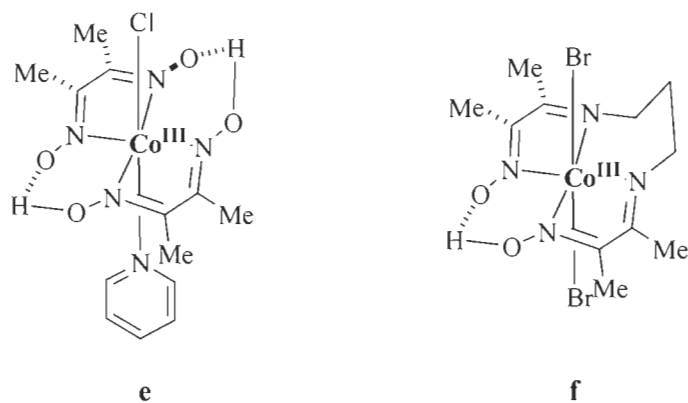
Figure 24. Cobaloxime complex **e** reported by Lehn and cobalt diamine-dioxime complex **f** reported by Fontecave group.[106, 109]

3.4. Choice of Ligands

To prepare highly active molecular catalysts, the choice of ligands plays a very important role in order to synthesize a stable complex. Besides, the ligands can be modified by (i) extending their aromatic systems and (ii) functionalization, so as to improve the properties of molecular catalysts. In the case of modification of ligands, designing extended aromatic systems are typically considered significant for example, the incorporation of [2,2';6',2";6",2"']-Quaterpyridine type ligands as compared to [2,2';6',2"]-Terpyridine and [2,2']-Bipyridine type ligands. Generally, macrocyclic ligands are more promising in stabilizing metal ions as compared to smaller ligands. According to literature reports, the ligands having greater denticities and smaller chelate rings (especially 5 membered) show higher stabilities and catalytic activities as compared to those having lower denticities. The stability of these complexes is also related to the light absorption and conversion efficiencies: the higher the stability, the higher will be the wavelength of absorption, the quantum yield, the excited state lifetime, and eventually the higher will be the catalytic activity. The stability of these complexes is due to the effect of extended π-conjugation which lowers the energy levels of the molecular orbitals.

In the case of the functionalization of ligands, there are several examples where the functionalization of ligands allows the fine tuning of photophysical properties of the complexes. Functionalization of ligands can be less expensive and may lead to the formation of stable and active molecular photocatalysts or photosensitizers. As for instance, the bisamide based ligand used by Schott *et al.* proved to be efficient in stabilizing the metal complex with a simultaneous improvement in the catalytic activity.[110]

a. Based on 2,2'-Bipyridine Ligands

2,2'-bipyridine has been widely used in coordination with metal ions ever since its discovery towards the end of nineteenth century. This is because, it can form stable molecular complexes with various metal ions mainly due to its metal chelating ability, redox stability, and easy

functionalization. Besides as compared to other ligands, 2,2'-bipyridine is neutral in nature, thus forming charged complexes with metal cations. It is due to this property that a large number of metal-bipyridine complexes have been synthesized and exploited. A majority of the bipyridine complexes of transition metals are electroactive, which means that the electrochemical reactions on both, the metal centre, and the ligand centre can be reversible depending upon the nature of the complex. This redox behaviour can be easily detected by performing cyclic voltammetry. Complexes of bipyridine and its derivatives have several applications in catalysis,[111] ion exchange,[112] materials separation[113] and purification[114]. Specific to hydrogen evolution reactions, Bernhard and co-workers reported, $[Co(bpy)_3]Cl_2$ complex (2.5 mM) which produced hydrogen with the turnover numbers of 100 in the presence of 0.05 mM $[Ru(bpy)_3](PF_6)_2$ as a photosensitizer (PS). [115]

b. Based on [2,2';6',2"]-Terpyridine Ligands

2,2':6',2''-Terpyridine ligands generally form more stable complexes than bipyridine ligands, because of their more efficient binding ability and stability due to their tridentate association. The [2,2';6',2"]-terpyridine ligand was synthesized around about 60 years ago. It is widely studied due to its excellent complexing ability with a wide range of transition metal ions. The great advancement in the design of terpyridine and its derivatives has led to an increase in their potential applications. Some intriguing properties pertaining to the coordination of terpyridine ligand and its derivatives include, (i) they mostly form octahedral complexes with bivalent metal ions, (ii) the three pyridine rings of each terpyridine ligand adopt a planar conformation after coordination, allowing perfect fusion between the metal ion and the ligand, (iii) in their octahedral complexes, the binding mode of terpyridine ligands is such that each terpyridine ligand is perpendicular to the other. Like bipyridine ligands, they also show good redox stability and photophysical properties which can also be tuned by functionalization. Due to these active properties, terpyridine metal complexes can catalyze several organic and inorganic transformations as for instance, addition[116]

36

and coupling reactions.[117, 118] However, pertaining to hydrogen evolution reactions, the standard terpyridine ligand based photocatalysts and photosensitizers are less active. The main reason behind this may be due to their low quantum yields and short excited state lifetimes. Nevertheless, the functionalization of terpyridine ligands has been known to improve its catalytic properties. For example, a photosensitizer made up of Ru (II) based on a new terpyridine ligand (4'-(4-bromophenyl)-4,4''':4'',4''''-dipyridinyl- 2,2':6',2''-terpyridine (Bipytpy)) reported by Mira et al. possessed high quantum yield and long-lived excited state lifetime as compared to other terpyridine complexes and was quite stable and active in producing hydrogen for 10 days with a TON$_{PS}$ of 764. The photocatalytic HER was performed by using 1 mM [Co^{III}(dmgH)$_2$(py)Cl] as a catalyst, 0.1 mM [Ru(Tolyltpy)(Bipytpy)](PF$_6$)$_2$ (Tolyltpy = 4'-tolyl-2,2':6',2'-terpyridine) as a photosensitizer (PS), dmgH$_2$ (6 mM) as an additional ligand, TEOA as a sacrificial donor (1 M) and HBF$_4$ as a proton source (0.1 M).[119]

c. Based on [2,2';6',2'';6'',2''']-Quaterpyridine Ligand

From bipyridine to terpyridine and from terpyridine to quaterpyridine, the denticities of ligands increases which in turn grants greater stabilities to the metal complexes even in their reduced states. This is mainly due to the increased chelate effect in quaterpyridine ligands consequently improving the efficiency of the catalytic system. In the case of octahedral complexes with tetradentate quaterpyridine ligands, the two coordination sites always remains vacant on the metal centre for catalysis to occur as compared to terpyridine where there are no vacant sites, while in the case of bipyridine complex, usually loss of a bipyridine ligand takes place before the catalytic activity.[120] The stability and activity of [Co(qpy)(OH$_2$)$_2$]$^{2+}$ complex was proven by Lau and co-workers when they compared its photocatalytic activity with [Co(bpy)$_3$]$^{2+}$ and [Co(bpy)$_2$(OH$_2$)$_2$]$^{2+}$. [Co(qpy)(OH$_2$)$_2$]$^{2+}$ produced H$_2$ with a TON$_{PS}$ of 530 (0.0159 moles of H$_2$) as compared to [Co(bpy)$_3$]$^{2+}$ and [Co(bpy)$_2$(OH$_2$)$_2$]$^{2+}$ which produced H$_2$ with TON$_{PS}$ of 237 (0.0071 moles of H$_2$) and 210 (0.0063 moles of H$_2$), respectively. Upon the addition of more amount of photosensitizer

(PS) (0.03 µmol) a photocatalytic activity of only $[Co(qpy)(OH_2)_2]^{2+}$ was restored, producing H_2 with a total TON$_{PS}$ of 860 after 60 hours whereas, the photocatalytic activity of $[Co(bpy)_3]^{2+}$ and $[Co(bpy)_2(OH_2)_2]^{2+}$ couldn't be restored thus indicating the simultaneous decomposition of the photosensitizer (PS) as well as the photocatalyst (PC). The enhanced catalytic activity of $[Co(qpy)(OH_2)_2]^{2+}$ may be attributed to the trans-orientation of the labile aqua ligands as compared to $[Co(bpy)_2(OH_2)_2]^{2+}$ in which the aqua ligands have a cis geometry.[121] (Figure 25)
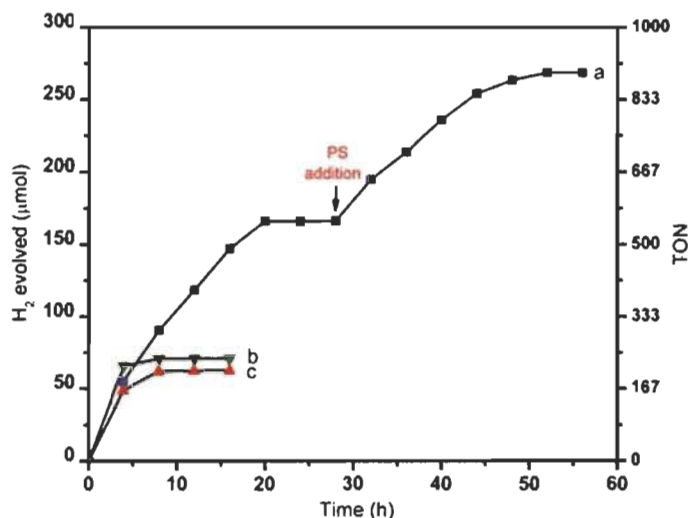
Figure 25. H_2 evolution vs. time plot by 0.6 mM of (a) $[Co(qpy)(OH_2)_2]^{2+}$, (b) $[Co(bpy)_3]^{2+}$ and (c) $[Co(bpy)_2(OH_2)_2]^{2+}$ in acetonitrile, TEOA (0.2 M), p-cyanoanilinium tetrafluoroborate (0.025 M) as a proton source, $\lambda > 390$ nm and $[Ir(ppy)_2(bpy)]PF_6$ (0.03 mM) as a photosensitizer (PS) which was added in the beginning as well as at the end to check the revival of the activity.[121]

In case of HER, the main reason behind the decomposition of bipyridine based complexes is the formation of dihydrobipyridine by the reduction of the bipyridine ligand.[122] In addition, the photosensitizer in most cases decomposes due to continuous irradiation by the LED light. For instance, the UV-Vis absorption spectra of $[Ru(phen)_3](PF_6)_2$ studied by Ouyang *et al.* in CH$_3$CN/ H$_2$O solution (v/v = 4:1) after irradiation for 0, 4 and 10 h by a LED light (λ = 450 nm, Irradiance = 100 mW.cm^{-2}) shows hypochromism with an increase in the irradiation time.[89] (Figure 26)

38
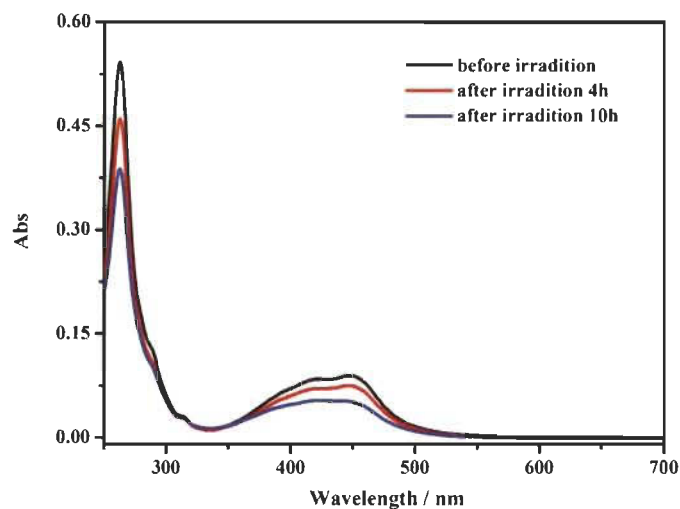
Figure 26. UV-Vis spectra of [Ru(phen)$_3$](PF$_6$)$_2$ studied by Ouyang *et al.* in CH$_3$CN/ H$_2$O solution (v/v = 4:1) after the irradiation for 0, 4 and 10 h by a LED light (λ = 450 nm, Irradiance = 100 mW.cm^{-2}).[89]

However, the photocatalyst may not decompose under the influence of light. One such example studied by Ouyang *et al.* clearly indicates that the photocatalyst remains stable even after irradiation for 10 hours as can be seen in the Figure 27 that displays no decrease in the absorbance.[89]
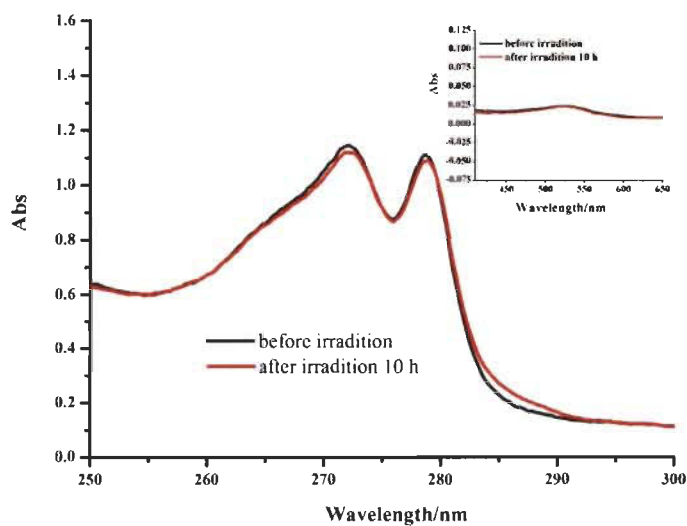
Figure 27. UV-Vis spectra of [Co(NTB)CH$_3$CN](ClO$_4$)$_2$ (NTB = tris(benzimidazolyl-2-methyl)amine) (5.5 × 10^{-5} M) reported by Ouyang *et al.*, in CH$_3$CN/ H$_2$O (v/v = 4:1) before irradiation and after irradiation for 10 h by a 450 nm LED light with an intensity of 100 mW. cm^{-2} at 25 °C.[89]

3.5. Chemocatalytic Hydrogen Evolution

Chemo catalytic HER can also be an option, where hydrogen can be produced by the catalytic decomposition of hydrogen precursors, such as ammonia borane, hydrazine monohydrate, and sodium borohydride.[123] More often, precious metals like platinum, iridium, palladium and ruthenium are used as catalysts for such reactions.[124] The applications of these catalysts have been limited due to their low stability and expensiveness. Consequently, many nonprecious metals catalysts, such as transition metal oxides, sulfides and nitrides have been synthesized and tested as an alternative option, however, they lack good performance as compared to the precious metals which limits their applications and at the same time encourages researchers to find new solutions.[125]

4. Ph. D Objectives

My Ph. D objectives are: (i) to design and synthesize new series of molecular complexes, (ii) to study the structure and properties of these molecular complexes, (iii) to create efficient molecular photocatalysts, and (iv) to modify the photocatalysts by modifying the structure of ligands. By employing the strategy of supramolecular chemistry and crystal engineering, 16 novel molecular complexes were synthesized and used as photocatalysts for hydrogen evolution reactions. We mainly focused on the coordination of first row transition metal ions such as Fe (II), Co (II), Ni (II), Cu (II) and Zn (II) owing to their abundance, low cost, and redox stabilities. The synthesis of ligands was also simple, efficient, and cost effective as compared to several other ligands. The synthetic steps used to prepare molecular complexes were also simple and less expensive. All the

molecular complexes were pure, crystalline, homogeneous and had single phases with good thermal stabilities. After analyzing and studying the structures and properties of synthesized molecular complexes, we tested their catalytic properties for visible light-driven hydrogen evolution reactions. To the best of our knowledge, these molecular complexes are the first examples of a fusion of coordination chemistry and molecular catalysts for hydrogen evolution reactions. Most of our molecular catalysts were stable and active towards visible light driven HER. The HER was performed by using 1 mM photocatalyst, 0.1 mM $[Ru(bpy)_3]^{2+}$ as photosensitizer (PS), 1 M triethanolamine as a sacrificial electron donor and 0.1 M fluoroboric acid (HBF_4) as a proton source in DMF as solvent.

4.1. Design and Development of Molecular Photocatalysts for H_2 Production

For the last fifteen years, the earth-abundant cobalt molecular complexes have proven to be efficient photocatalysts for hydrogen evolution reactions even though they have no pertinence to biological hydrogen production. In fact, over the last three decades, a large amount of research has been conducted in the preparation of efficient molecular catalysts. The design of molecular catalysts involves a proper blend of the following: (i) the ligand design, (ii) the synthesis and characterization of ligand, (iii) the coordination of the ligand with suitable metal ions, (iv) the electrochemical analysis, (v) electrocatalytic investigations, (vi) catalytic and photocatalytic testing, and (vii) mechanistic studies. During the last 10 years, cobalt complexes containing polydentate polypyridyl ligands are the most widely considered molecular catalysts and have received a great deal of attention.[86] A variety of polypyridine ligands and their complexes have been synthesized by building different types of pyridyl ligands and by modifying the ligands *via* functionalization. The structure-property relationship plays an important role in photocatalytic hydrogen production. This is a kind of optimization process which needs more time and efforts.[126, 127] For instance, the pentapyridyl cobalt complex $[Co^{II}(PY_5Me_2)(H_2O)_2]^{2+}$ produces more H_2 as compared to its tetrapyridyl analogue $[Co^{II}(PY_4Me_2H)(MeCN)(OTf)]^+$ under identical

photocatalytic conditions, possibly due to higher catalyst stability *via* chelate effect from higher denticity.[127] The impact of electron donating and electron withdrawing groups on photocatalysts for HER is unpredictable however, in the case of photosensitizers, they do have a strong influence. For example, bis(terpyridine) based photosensitizers were disregarded due to their low quantum yields and short excited state lifetimes. However, by developing a new bis(terpyridine) based photosensitizer by functionalization and with extended aromatization, Mira *et al.* were able to prepare a very active photosensitizer recently, which exhibited sustained activity for 10 days and produced hydrogen with a total turnover number of 764.[119] Elisa *et al.* prepared a series of functionalized heteroleptic Ru (II) tris(bipyridine) based photosensitizers (PS) which outperformed the typical $[Ru(bpy)_3]^{2+}$. However, depending on the reaction components and conditions, the activity lasted only for 2 hours.[128] Photosensitizers have a very strong influence on HER activity as they are more susceptible to degradation. For example, Khnayzer *et al.* reported the regeneration of photocatalytic hydrogen production caused by the addition of fresh photosensitizer at the end of the reaction. The reaction conditions were 2×10^{-5} M $[Co(bpyPY_2Me)(CH_3CN)(CF_3SO_3)](CF_3SO_3)$ (PC), 2×10^{-5} M $[Ru(bpy)_3]^{2+}$ (PS), and 0.3 M aqueous ascorbic acid/ascorbate⁻ solution (pH = 4) (Figure 28).[126]
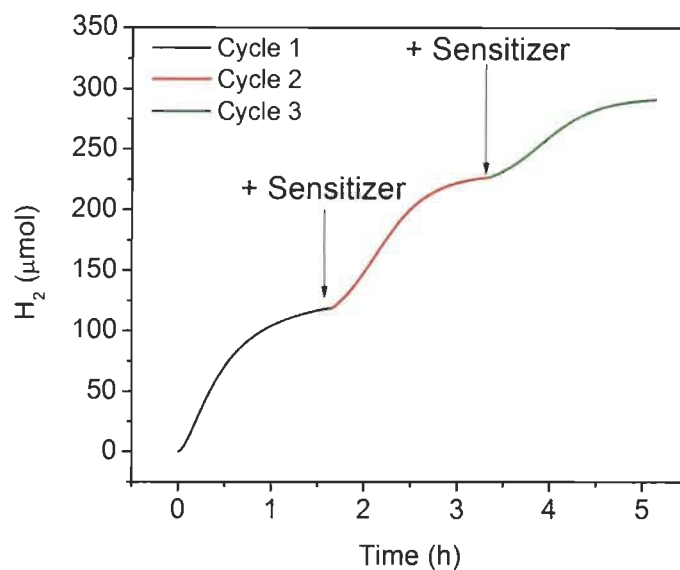
Figure 28. Regeneration of photocatalytic activity by the addition of PS after the end of the first cycle. Conditions: 2×10^{-5} M of photocatalyst, 2×10^{-5} M of photosensitizer, and 0.3 M aqueous ascorbic acid/ ascorbate⁻ solution (pH = 4).[126]

A careful synthesis of an active photosensitizer can make a huge difference in HER performance as the activity can be sustained for a longer period of time. Molecular photocatalyst is just one part of the multicomponent photocatalytic system. Photocatalytic systems can be optimised through numerous other modifications such as (i) by testing new photosensitizers, (ii) by screening different sacrificial electron donors (SEDs), (iii) by using different types of proton source, and (iv) by changing the solvent. As mentioned before, the regeneration of hydrogen production strongly depends on the PS and if the degradation of PSs is slow, the activities can be sustained for a longer period. It is also proved that the PS is the only component from which the activity can be renewed, while the activity cannot be renewed by other components. There are several blank experiments carried out in the literature to prove the evidence of the number of components needed. For instance, the photocatalytic reduction of CO_2 to CO was carried by Ouyang *et al.* by adding equal amount of (a) [Ru(phen)₃](PF₆)₂ (0.4 mM) (PS), and (b) TEOA (0.3 M) (SED), to the nearly completed catalytic reaction (Figure 29).[89]

(a)   **(b)**
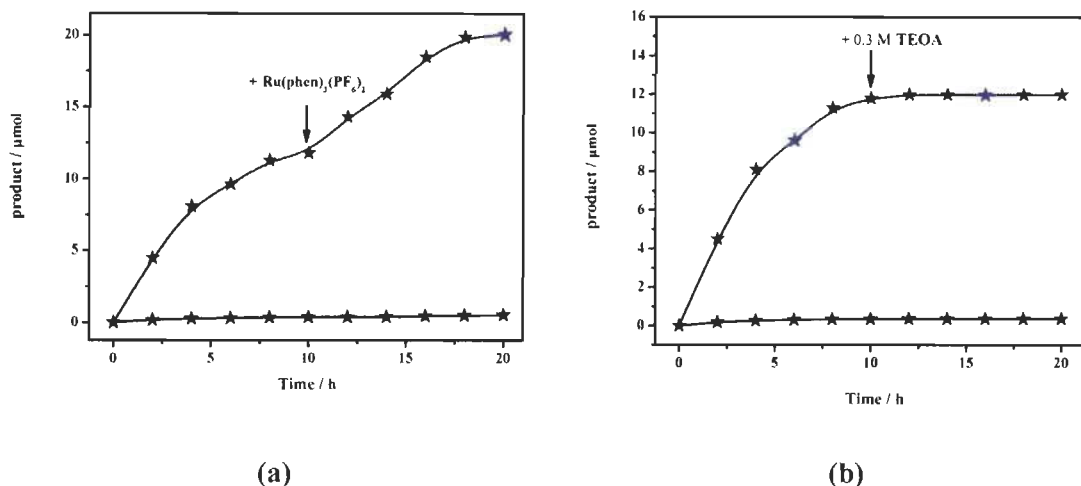
Figure 29. Consecutive photocatalytic reduction of CO_2 to CO (blue) by adding equal amount of (a) [Ru(phen)$_3$](PF$_6$)$_2$ (0.4 mM), and (b) TEOA (0.3 M) to the nearly completed catalytic system, the black curve indicates the production of H_2.[89]

The photocatalytic hydrogen evolution also takes place in the same fashion. The production of hydrogen increases with an increase in concentration of the photosensitizer and at the same time the activity can be regenerated by the addition of fresh photosensitizer once all the photosensitizer is degraded.[121, 129] In the case of the molecular photocatalysts, Brooker and coworkers tested 17 different cobalt complexes, from which 11 were dinuclear, three were tetranuclear and the rest of the three were mononuclear complexes for photocatalytic hydrogen evolution, in the presence of 0.1 mM [Ru(bpy)$_3$]$^{2+}$ as photosensitizer (PS), 1 M triethanolamine as a sacrificial electron donor and 0.1 M fluoroboric acid (HBF$_4$) as a proton source in DMF as a solvent. Among all the tested photocatalysts, a dinuclear cobalt complex with the molecular formula [Co^{II}$_2$($^{t\text{-}BuPh}$Trz$_{Me/Me}$)(μ-BF$_4$)](BF$_4$)$_3$ (where **Trz** = 1,2,4-triazole used as central bridging moiety, $^{t\text{-}BuPh}$**Trz**$_{Me/Me}$ = an example of bis-tetradentate ligands) proved to be the best photocatalyst producing H_2 with a TON$_{PS}$ of 150 moles of H_2 per mole of PS. Other dinuclear cobalt complexes such as [Co^{II}$_2$(^{Pyrr}**Trz**$_{Me/Me}$)(H$_2$O)$_2$](BF$_4$)$_3$,   [Co^{II}$_2$(Pym$_{Et/Me}$)(H$_2$O)$_4$](BF$_4$)$_4$ and [Co^{II}$_2$(Pym$_{Me/Me}$)(H$_2$O)$_2$](BF$_4$)$_4$ also displayed good results and produced H_2 with a TON$_{PS}$ of 140,

65 and 63 moles of H_2 per mole of PS, respectively (Figures 30, 31 and Table 1). In addition, the three tetranuclear cobalt complexes *viz.* $[Co^{II}_4(Pym_{Et/Me})_2F_4](BF_4)_4$, $[Co^{II}_2Co^{III}_2(Pym_{Me/Me})_2F_4](BF_4)_6$ and $[Co^{II}_2Co^{III}_2(Pym_{Et/Me})F_4](BF_4)_6$ also exhibited interesting results by producing H_2 with TON of 77, 82 and 76 moles of H_2 per mole of PS, respectively (Figure 32 and Table 1). Furthermore, the three mononuclear cobalt complexes $[Co^{II}(M_{Et})](BF_4)$, $[Co^{II}(^{Br}M_{Et})](BF_4)$ and $[Co^{II}(M_{pr})](BF_4)$ (where **M** ligands are three different tetradentate diimine macrocycles featuring a diphenylamine head unit) produced H_2 with TON of 130, 94 and 25 moles of H_2 per mole of PS, respectively (Figure 33 and Table 1). Note that under similar conditions, the most reported standard reference cobaloxime catalyst ($[Co^{III}(dmgH)_2(py)Cl]$) produces H_2 with a TON of 68. Modifications of photocatalysts have also been done by surface immobilisation techniques to prepare heterogeneous catalysts. However, the drawback of heterogeneous catalysts is that the HER is only restricted to the heterolytic pathway whereas HER can occur by both the homolytic and heterolytic mechanisms.[130]

$[Co^{II}_2(^{t\text{-}BuPh}Trz_{Me/Me})(\mu\text{-}BF_4)](BF_4)_3$ $[Co^{II}_2(^{pyrr}Trz_{Me/Me})(H_2O)_2](BF_4)_3$
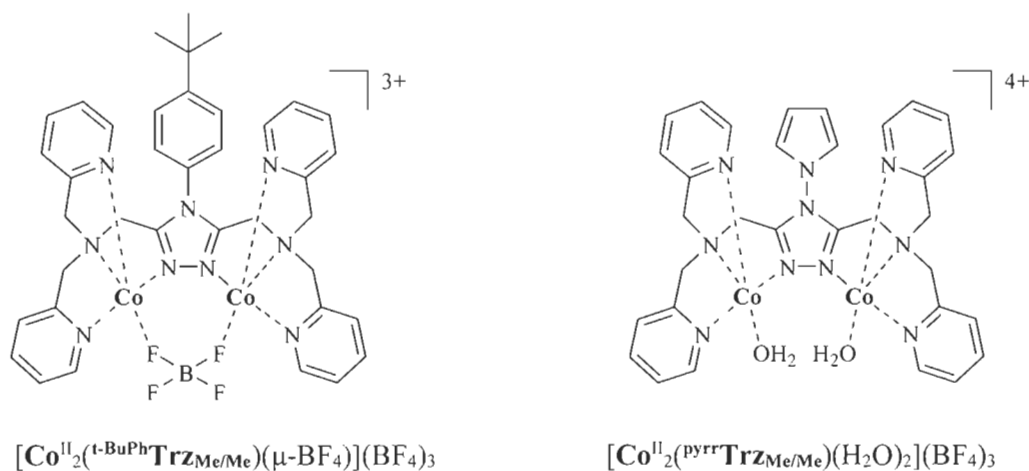
Figure 30. The two dicobalt (II) complexes of bis-tetradentate **Trz** (Trz = 1,2,4-triazole) ligands.

$[Co^{II}_2(Pym_{Et/Me})(H_2O)_4](BF_4)_4$

$[Co^{II}_2(Pym_{Me/Me})(H_2O)_2](BF_4)_4$
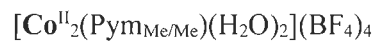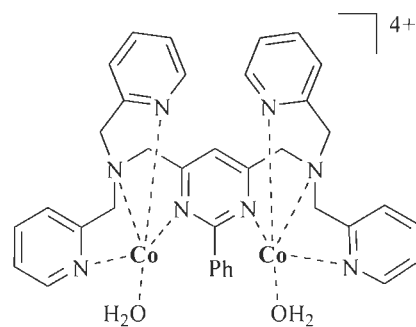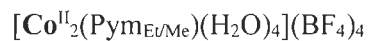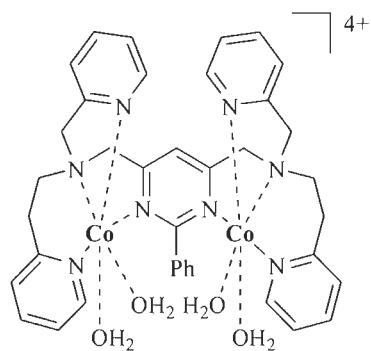
Figure 31. The two dicobalt (II) complexes of the bis-tetradentate pym ligands.

$[Co_4(Pym_{Et/Me})F_4](BF_4)_6$

$[Co_4(Pym_{Et/Me})F_4](BF_4)x$
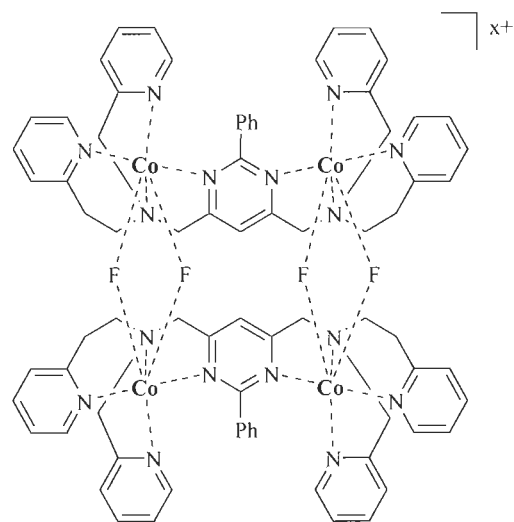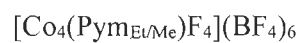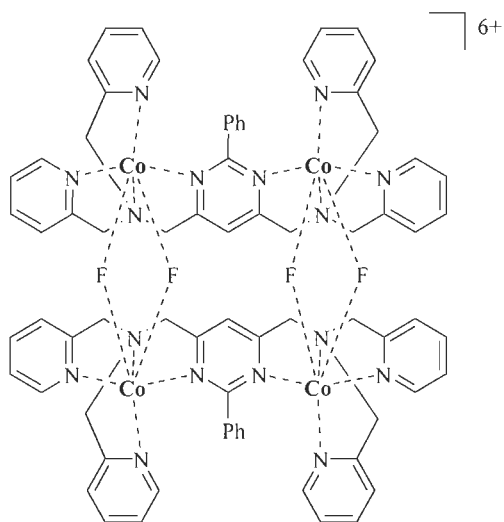
Figure 32. The tetra cobalt complexes of the bis-tetradentate pym ligands.

$[Co^{II}(M_{Et})](BF_4)$ $[Co^{II}(^{Br}M_{Et})](BF_4)$ $[Co^{II}(M_{pr})](BF_4)$
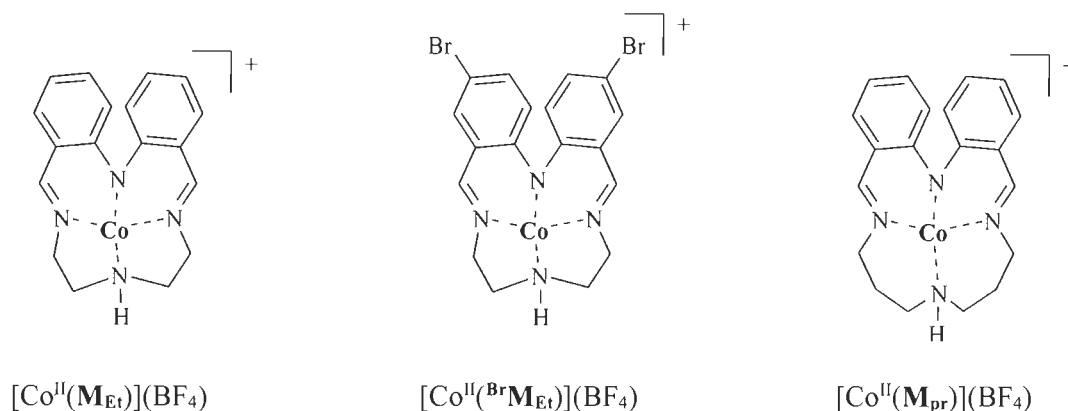
Figure 33. The monocobalt(II) complexes of the tetradentate Schiff base macrocyclic ligands.

Photocatalyst	c_{cat} (mM)	c_{PS} (mM)	TON_{PS}	Moles of H_2
$[Co^{II}_2(^{t-BuPh}Trz_{Me/Me})(\mu-BF_4)](BF_4)_3$	0.5	0.1	150	0.015
$[Co^{II}_2(^{pyrr}Trz_{Me/Me})(H_2O)_2](BF_4)_3$	0.5	0.1	140	0.014
$[Co^{II}_2(Pym_{Et/Me})(H_2O)_4](BF_4)_4$	0.5	0.1	65	0.0065
$[Co^{II}_2(Pym_{Me/Me})(H_2O)_2](BF_4)_4$	0.5	0.1	63	0.0063
$[Co^{II}_4(Pym_{Et/Me})_2F_4](BF_4)_4$	0.5	0.1	77	0.0077
$[Co^{II}_2Co^{III}_2(Pym_{Me/Me})_2F_4](BF_4)_6$	0.5	0.1	82	0.0082
$[Co^{II}_2Co^{III}_2(Pym_{Et/Me})F_4](BF_4)_6$	0.5	0.1	76	0.0076
$[Co^{II}(M_{Et})](BF_4)$	0.5	0.1	130	0.013
$[Co^{II}(^{Br}M_{Et})](BF_4)$	0.5	0.1	94	0.0094
$[Co^{II}(M_{pr})](BF_4)$	0.5	0.1	25	0.0025

Table 1. Photocatalytic hydrogen evolution by cobalt complexes screened by Hogue *et al.* Conditions: 0.1 mM $[Ru(bpy)_3]^{2+}$ (PS), 1 M triethanolamine (SED), 0.1 M fluoroboric acid (HBF_4) as a proton source in DMF as a solvent, under blue light LED ($\lambda = 452$ nm).

a. Metallotectons

In crystal engineering and material science, metallotectons are the units made up of both organic as well as inorganic components. These units are formed by the coordination of the molecular components. The molecular components are basically inorganic metal salts and organic ligands. The perspective of inorganic chemistry creates preferences for molecular components linked by coordination to diverse metals, whereas the perception of organic chemistry favours the exploitation of intra as well as inter molecular interactions by a phenomenon known as self-assembly, which in turn leads to the formation of supramolecular networks.[131] Tectoligands are the ligands used for the formation of metallotectonic units or metallotectons. These are a special type of designed, synthesized organic ligands which can strongly bind to several metals according to their standard patterns of coordination and can simultaneously engage in predictable intra as well as inter molecular interactions such as hydrogen-bonding.[132] Due to their noticeable advantages, the utilization of the strategies to engineer new materials using metallotectons has already started. Several metallotectons bearing tectoligands have been developed by the Wuest and Duong group.[133, 134] The metal complexes with these features are highly attractive as modules for the planned construction of molecules due to the ease of their synthesis which involves the straightforward mixing of tectoligands with suitable metal salts. The strategy of metallotectons is advantageous because: (i) the materials can be simply and easily prepared in pure and crystalline forms, thus making them easy to characterize, (ii) the materials can be prepared from less expensive raw materials, (iii) the materials can be obtained in very high yields, (iv) the structures can be predictable and (v) the materials are usually stable at high temperatures. Figure 34 below shows bipyridine (bpy) **1**, terpyridine (tpy) **2**, quaterpyridine (qpy) **3** and their functionalized derivatives which are labelled tectoligands **4-6**.
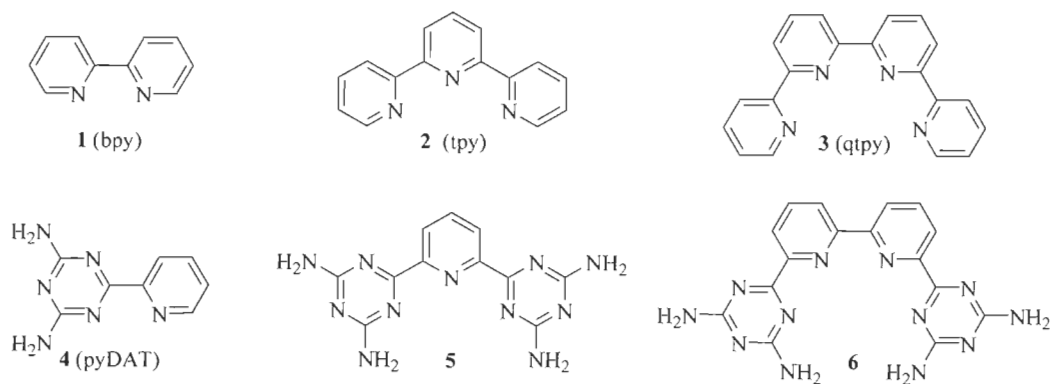
Figure 34. Molecular structure of 2,2'-bypyridine **1** (bpy), [2,2';6',2"]-terpyridine **2** (tpy) and [2,2';6',2";6",2'"]-quaterpyridine **3** (qpy) and their functionalized derivatives also called as tectoligands **4-6**.

b. Mimicking Bipyridine, Terpyridine and Quaterpyridine Ligands

Polypyridine ligands are considered as the most versatile chelating ligands. Their chemistry has become a dynamic field of research, as lots of metal complexes with polypyridine ligands have been synthesized and reported with rich electrochemical and photophysical properties. The polypyridine based complexes have applications mainly in photocatalysis, electrocatalysis, chemocatalysis, artificial photosynthesis and also in the biomedical field.[121, 135] Many researchers are focusing on synthesizing molecular complexes with ligands such as bpy **1**, tpy **2**, qpy **3** and their functionalized derivatives. These ligands possess diverse features such as (i) they have N-heterocyclic scaffolds, (ii) their coordination chemistry is predictable, (iii) they have better oxidation resistance and (iv) they have a low energy orbital for metal to ligand charge transfer transition. Even though these ligands bear interesting structural and physicochemical properties, their use has declined because of the synthetic difficulties associated with them which limits their possible applications. We have come up with an alternative synthetic approach which is less expensive and easy to carry out. It consists of replacing one of the various pyridine rings by a

diamino-1,3,5-triazinyl group (DAT) group. The DAT group has been employed to facilitate simple preparation of bpy, tpy and qpy type ligands **1-3**. Compounds **4-6** in Figure 34 were designed to remove the serious drawbacks pertinent to functionalization of bpy, tpy and qtpy synthesis. Compounds **4-6** are pyridyl and bipyridyl substituted in ortho with one or two DAT groups. These compounds retain their characteristic chelating ability and at the same time incorporate diamino-1,3,5-triazinyl (DAT) groups, which are known to participate in hydrogen-bonding according to the well-established DAT group motifs I-III (Figure 35).
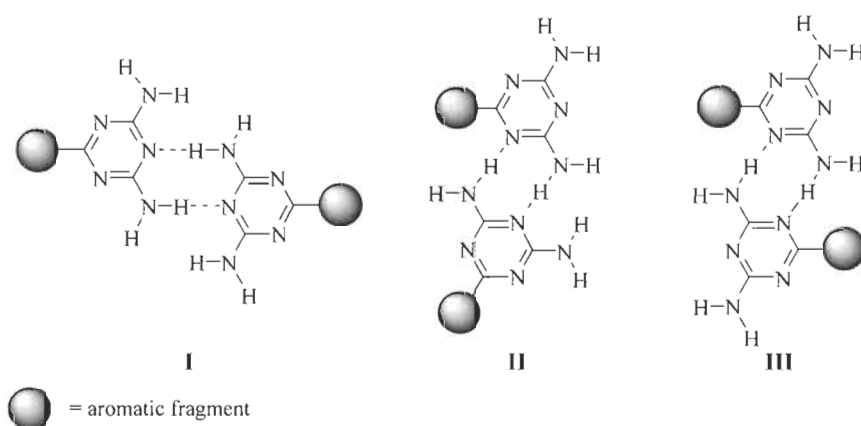
Figure 35. Three types of hydrogen bonds motifs of the DAT groups.

c. Importance of Diaminotriazine (DAT) Based Ligands

There are various advantages of introducing diaminotriazine systems in the organic ligands: (i) the synthesis of polypyridine mimics are comparatively less expensive and easy, (ii) the synthetic yields of the ligands and their complexes are generally very high, (iii) they serve as simple and efficient examples of functionalization of bpy, tpy and qpy ligands, (iv) the ligands can form chelates as well as form hydrogen bonds, (v) the nitrogen-rich ligands can donate their electron density to metal centers, thus making them electron rich, (vi) the ligands and their complexes can be easily crystallized which facilitates their characterization. In material science and crystal engineering, these molecules are termed as tectoligands because of their dual ability to coordinate

metal ions and at the same time, engage in predictable intermolecular interactions such as hydrogen-bonding according to reliable patterns. The self-assembly of tectoligands with metal ions forms metallotectons. Synthesis of metallotectons using ligands **4-6** has numerous advantages: (i) facile synthesis with high yield and purity, (ii) the coordination patterns are similar to **1-3**, (iii) consistent hydrogen-bonded networks with predetermined organizations are expected, (iv) the presence of the diamino-1,3,5-triazinyl (DAT) groups may lead to the modification of activities of the metal complexes for catalysis.

5. References

1. https://www.bp.com/content/dam/bp/business-sites/en/global/corporate/pdfs/energy-economics/statistical-review/bp-stats-review-2019-full-report.pdf

2. Armaroli, N.; Balzani, V., Solar electricity and solar fuels: status and perspectives in the context of the energy transition. *Chemistry–A European Journal* **2016,** *22* (1), 32-57.

3. Armaroli, N.; Balzani, V., The future of energy supply: challenges and opportunities. *Angewandte Chemie International Edition* **2007,** *46* (1-2), 52-66.

4. Balzani, V.; Credi, A.; Venturi, M., Photochemical conversion of solar energy. *ChemSusChem* **2008,** *1* (1-2), 26-58.

5. Vennestrøm, P.; Osmundsen, C. M.; Christensen, C.; Taarning, E., Beyond petrochemicals: the renewable chemicals industry. *Angewandte Chemie International Edition* **2011,** *50* (45), 10502-10509.

6. Balzani, V.; Armaroli, N., *Energy for a sustainable world: from the oil age to a sun-powered future*. John Wiley & Sons: 2010.

7. Artero, V.; Chavarot-Kerlidou, M.; Fontecave, M., Splitting water with cobalt. *Angewandte Chemie International Edition* **2011,** *50* (32), 7238-7266.

8. Zhang, B.; Sun, L., Artificial photosynthesis: opportunities and challenges of molecular catalysts. *Chemical Society Reviews* **2019,** *48* (7), 2216-2264.

9. Atmospheric concentrations of CO_2 measured at Mauna Loa Observatory, https://www.esrl.noaa.gov/gmd/ccgg/trends/mlo.html

10. Le, T. H.; Somerville, R.; Cubash, U.; Ding, Y.; Mauritzen, C.; Mokssit, A.; Peterson, T.; Prather, M., Historical overview of climate change science. **2007**.

11. Dau, H.; Fujita, E.; Sun, L., Artificial photosynthesis: Beyond mimicking nature. *ChemSusChem* **2017,** *10* (BNL-114802-2017-JA).

12. Armaroli, N.; Balzani, V., The hydrogen issue. *ChemSusChem* **2011,** *4* (1), 21-36.

13. Ellabban, O.; Abu-Rub, H.; Blaabjerg, F., Renewable energy resources: Current status, future prospects and their enabling technology. *Renewable and Sustainable Energy Reviews* **2014,** *39*, 748-764.

14. Ahmed, S.; Jaber, A.; Dixon, R., Renewables 2010 Global Status Report: Renewable Energy Policy Network for the 21st Century. REN.

15. McEvoy, J. P.; Brudvig, G. W., Water-splitting chemistry of photosystem II. *Chemical reviews* **2006,** *106* (11), 4455-4483.

16. https://www.livescience.com/51720-photosynthesis.html

17. LIDDELL, H. G.; SCOTT, R., A Greek-English Lexicon. Henry Stuart Jones, rev. Oxford: Clarendon Press. Perseus Digital Library Project. Gregory R. Crane ...: 2005.

18. Amunts, A.; Drory, O.; Nelson, N., The structure of a plant photosystem I supercomplex at 3.4 Å resolution. *Nature* **2007,** *447* (7140), 58-63.

19. Umena, Y.; Kawakami, K.; Shen, J.-R.; Kamiya, N., Crystal structure of oxygen-evolving photosystem II at a resolution of 1.9 Å. *Nature* **2011,** *473* (7345), 55-60.

20. Verne, Jules (April 1874). "The Mysterious Island". *Scribner's Monthly*. Vol. 7 no. 6. pp. 722–734.

21. Balzani, V.; Moggi, L.; Manfrin, M.; Bolletta, F.; Gleria, M., Solar energy conversion by water photodissociation: Transition metal complexes can provide low-energy cyclic systems for catalytic photodissociation of water. *Science* **1975,** *189* (4206), 852-856.

22. Dawson, J., Prospects for hydrogen as an energy resource. *Nature* **1974,** *249* (5459), 724-726.

23. Robertson, I. M.; Sofronis, P.; Nagao, A.; Martin, M.; Wang, S.; Gross, D.; Nygren, K., Hydrogen embrittlement understood. *Metallurgical and Materials Transactions B* **2015,** *46* (3), 1085-1103.

24. Rand, D.; Dell, R., Hydrogen energy challenges and prospects the royal society of chemistry. *Thomas Graham House, Science Park, Milton Road, Cambridge CB4 0WF, UK ISBN* **2008,** 978-0.

25. Züttel, A.; Borgschulte, A.; Schlapbach, L., Hydrogen as a future energy carrier. 2008.

26. Olah, G. A.; Goeppert, A.; Prakash, G. S., *Beyond oil and gas: the methanol economy.* John Wiley & Sons: 2018.

27. Kean, S., Eco-alchemy in Alberta. American Association for the Advancement of Science: 2009.

28. Andreiadis, E. S.; Chavarot-Kerlidou, M.; Fontecave, M.; Artero, V., Artificial Photosynthesis: From Molecular Catalysts for Light-driven Water Splitting to Photoelectrochemical Cells. *Photochemistry and photobiology* **2011,** *87* (5), 946-964.

29. Wang, S.; Wang, Q.; Shao, P.; Han, Y.; Gao, X.; Ma, L.; Yuan, S.; Ma, X.; Zhou, J.; Feng, X., Exfoliation of covalent organic frameworks into few-layer redox-active nanosheets as cathode materials for lithium-ion batteries. *Journal of the American Chemical Society* **2017,** *139* (12), 4258-4261.

30. Zhou, H.-C.; Kitagawa, S., Metal-organic frameworks (MOFs). *Chemical Society Reviews* **2014,** *43* (16), 5415.

31. Schoedel, A.; Ji, Z.; Yaghi, O. M., The role of metal–organic frameworks in a carbon-neutral energy cycle. *Nature Energy* **2016,** *1* (4), 1-13.

32. Rosi, N. L.; Eckert, J.; Eddaoudi, M.; Vodak, D. T.; Kim, J.; O'Keeffe, M.; Yaghi, O. M., Hydrogen storage in microporous metal-organic frameworks. *Science* **2003,** *300* (5622), 1127-1129.

33. Furukawa, H.; Ko, N.; Go, Y. B.; Aratani, N.; Choi, S. B.; Choi, E.; Yazaydin, A. Ö.; Snurr, R. Q.; O'Keeffe, M.; Kim, J., Ultrahigh porosity in metal-organic frameworks. *Science* **2010,** *329* (5990), 424-428.

34. Lin, J. M.; He, C. T.; Liu, Y.; Liao, P. Q.; Zhou, D. D.; Zhang, J. P.; Chen, X. M., A metal–organic framework with a pore size/shape suitable for strong binding and close packing of methane. *Angewandte Chemie* **2016,** *128* (15), 4752-4756.

35. Li, B.; Wen, H.-M.; Wang, H.; Wu, H.; Tyagi, M.; Yildirim, T.; Zhou, W.; Chen, B., A porous metal–organic framework with dynamic pyrimidine groups exhibiting record high methane storage working capacity. *Journal of the American Chemical Society* **2014,** *136* (17), 6207-6210.

36. Mason, J. A.; Oktawiec, J.; Taylor, M. K.; Hudson, M. R.; Rodriguez, J.; Bachman, J. E.; Gonzalez, M. I.; Cervellino, A.; Guagliardi, A.; Brown, C. M., Methane storage in flexible metal–organic frameworks with intrinsic thermal management. *Nature* **2015,** *527* (7578), 357-361.

37. Dhakshinamoorthy, A.; Asiri, A. M.; Garcia, H., Metal–organic framework (MOF) compounds: photocatalysts for redox reactions and solar fuel production. *Angewandte Chemie International Edition* **2016,** *55* (18), 5414-5445.

38. Wang, C.; DeKrafft, K. E.; Lin, W., Pt nanoparticles@ photoactive metal–organic frameworks: efficient hydrogen evolution via synergistic photoexcitation and electron injection. *Journal of the American Chemical Society* **2012,** *134* (17), 7211-7214.

39. Nohra, B.; El Moll, H.; Rodriguez Albelo, L. M.; Mialane, P.; Marrot, J.; Mellot-Draznieks, C.; O'Keeffe, M.; Ngo Biboum, R.; Lemaire, J.; Keita, B., Polyoxometalate-based metal organic frameworks (POMOFs): structural trends, energetics, and high electrocatalytic efficiency for hydrogen evolution reaction. *Journal of the American Chemical Society* **2011,** *133* (34), 13363-13374.

40. Zhan, W.; Sun, L.; Han, X., Recent progress on engineering highly efficient porous semiconductor photocatalysts derived from metal–organic frameworks. *Nano-Micro Letters* **2019,** *11* (1), 1.

41. Dong, R.; Zheng, Z.; Tranca, D. C.; Zhang, J.; Chandrasekhar, N.; Liu, S.; Zhuang, X.; Seifert, G.; Feng, X., Immobilizing molecular metal dithiolene–diamine complexes on 2D metal–organic frameworks for electrocatalytic H2 production. *Chemistry–A European Journal* **2017,** *23* (10), 2255-2260.

42. Zhu, B.; Zou, R.; Xu, Q., Metal–organic framework based catalysts for hydrogen evolution. *Advanced Energy Materials* **2018,** *8* (24), 1801193.

43. Yang, K.; Jiang, P.; Chen, J.; Chen, Q., Nanoporous PtFe Nanoparticles Supported on N-Doped Porous Carbon Sheets Derived from Metal–Organic Frameworks as Highly Efficient and Durable Oxygen Reduction Reaction Catalysts. *ACS applied materials & interfaces* **2017,** *9* (37), 32106-32113.

44. Lu, X.-F.; Liao, P.-Q.; Wang, J.-W.; Wu, J.-X.; Chen, X.-W.; He, C.-T.; Zhang, J.-P.; Li, G.-R.; Chen, X.-M., An alkaline-stable, metal hydroxide mimicking metal–organic framework for efficient electrocatalytic oxygen evolution. *Journal of the American Chemical Society* **2016,** *138* (27), 8336-8339.

45. Liu, Y.; Jiang, H.; Hao, J.; Liu, Y.; Shen, H.; Li, W.; Li, J., Metal–Organic Framework-Derived Reduced Graphene Oxide-Supported $ZnO/ZnCo_2O_4/C$ Hollow Nanocages as Cathode Catalysts for Aluminum–O_2 Batteries. *ACS applied materials & interfaces* **2017,** *9* (37), 31841-31852.

46. Chambers, M. B.; Wang, X.; Elgrishi, N.; Hendon, C. H.; Walsh, A.; Bonnefoy, J.; Canivet, J.; Quadrelli, E. A.; Farrusseng, D.; Mellot-Draznieks, C., Photocatalytic Carbon Dioxide Reduction with Rhodium-based Catalysts in Solution and Heterogenized within Metal–Organic Frameworks. *ChemSusChem* **2015,** *8* (4), 603-608.

47. Yan, L.; Cao, L.; Dai, P.; Gu, X.; Liu, D.; Li, L.; Wang, Y.; Zhao, X., Metal-organic frameworks derived nanotube of nickel–cobalt bimetal phosphides as highly efficient electrocatalysts for overall water splitting. *Advanced Functional Materials* **2017,** *27* (40), 1703455.

48. Feng, X.; Ding, X.; Jiang, D., Covalent organic frameworks. *Chemical Society Reviews* **2012,** *41* (18), 6010-6022.

49. Mandal, A. K.; Mahmood, J.; Baek, J. B., Two-Dimensional Covalent Organic Frameworks for Optoelectronics and Energy Storage. *ChemNanoMat* **2017,** *3* (6), 373-391.

50. Yan, S.; Guan, X.; Li, H.; Li, D.; Xue, M.; Yan, Y.; Valtchev, V.; Qiu, S.; Fang, Q., Three-dimensional Salphen-based Covalent–Organic Frameworks as Catalytic Antioxidants. *Journal of the American Chemical Society* **2019,** *141* (7), 2920-2924.

51. Fang, Q.; Wang, J.; Gu, S.; Kaspar, R. B.; Zhuang, Z.; Zheng, J.; Guo, H.; Qiu, S.; Yan, Y., 3D porous crystalline polyimide covalent organic frameworks for drug delivery. *Journal of the American chemical society* **2015,** *137* (26), 8352-8355.

52. Heidary, N.; Harris, T. G.; Ly, K. H.; Kornienko, N., Artificial photosynthesis with metal and covalent organic frameworks (MOFs and COFs): challenges and prospects in fuel-forming electrocatalysis. *Physiologia plantarum* **2019,** *166* (1), 460-471.

53. Diercks, C. S.; Yaghi, O. M., The atom, the molecule, and the covalent organic framework. *Science* **2017,** *355* (6328).

54. Garcia, J. C.; Justo, J.; Machado, W.; Assali, L., Functionalized adamantane: Building blocks for nanostructure self-assembly. *Physical Review B* **2009,** *80* (12), 125421.

55. Liu, X.; Huang, D.; Lai, C.; Zeng, G.; Qin, L.; Wang, H.; Yi, H.; Li, B.; Liu, S.; Zhang, M., Recent advances in covalent organic frameworks (COFs) as a smart sensing material. *Chemical Society Reviews* **2019,** *48* (20), 5266-5302.

56. Rowan, S. J.; Cantrill, S. J.; Cousins, G. R.; Sanders, J. K.; Stoddart, J. F., Dynamic covalent chemistry. *Angewandte Chemie International Edition* **2002,** *41* (6), 898-952.

57. Ding, S.-Y.; Wang, W., Covalent organic frameworks (COFs): from design to applications. *Chemical Society Reviews* **2013,** *42* (2), 548-568.

58. Khattak, A. M.; Ghazi, Z. A.; Liang, B.; Khan, N. A.; Iqbal, A.; Li, L.; Tang, Z., A redox-active 2D covalent organic framework with pyridine moieties capable of faradaic energy storage. *Journal of Materials Chemistry A* **2016,** *4* (42), 16312-16317.

59. Segura, J. L.; Mancheño, M. J.; Zamora, F., Covalent organic frameworks based on Schiff-base chemistry: synthesis, properties and potential applications. *Chemical Society Reviews* **2016,** *45* (20), 5635-5671.

60. Sharma, R. K.; Yadav, P.; Yadav, M.; Gupta, R.; Rana, P.; Srivastava, A.; Zbořil, R.; Varma, R. S.; Antonietti, M.; Gawande, M. B., Recent development of covalent organic frameworks (COFs): synthesis and catalytic (organic-electro-photo) applications. *Materials Horizons* **2020,** *7* (2), 411-454.

61. Ma, W.; Yu, P.; Ohsaka, T.; Mao, L., An efficient electrocatalyst for oxygen reduction reaction derived from a Co-porphyrin-based covalent organic framework. *Electrochemistry Communications* **2015,** *52*, 53-57.

62. Chen, J.; Tao, X.; Li, C.; Ma, Y.; Tao, L.; Zheng, D.; Zhu, J.; Li, H.; Li, R.; Yang, Q., Synthesis of bipyridine-based covalent organic frameworks for visible-light-driven photocatalytic water oxidation. *Applied Catalysis B: Environmental* **2020,** *262*, 118271.

63. Stegbauer, L.; Schwinghammer, K.; Lotsch, B. V., A hydrazone-based covalent organic framework for photocatalytic hydrogen production. *Chemical Science* **2014,** *5* (7), 2789-2793.

64. Fu, Y.; Zhu, X.; Huang, L.; Zhang, X.; Zhang, F.; Zhu, W., Azine-based covalent organic frameworks as metal-free visible light photocatalysts for CO_2 reduction with H_2O. *Applied Catalysis B: Environmental* **2018,** *239*, 46-51.

65. Han, Y.-F.; Yuan, Y.-X.; Wang, H.-B., Porous hydrogen-bonded organic frameworks. *Molecules* **2017,** *22* (2), 266.

66. Wang, H.; Li, B.; Wu, H.; Hu, T.-L.; Yao, Z.; Zhou, W.; Xiang, S.; Chen, B., A flexible microporous hydrogen-bonded organic framework for gas sorption and separation. *Journal of the American Chemical Society* **2015,** *137* (31), 9963-9970.

67. Huang, Q.; Li, W.; Mao, Z.; Qu, L.; Li, Y.; Zhang, H.; Yu, T.; Yang, Z.; Zhao, J.; Zhang, Y., An exceptionally flexible hydrogen-bonded organic framework with large-scale void

regulation and adaptive guest accommodation abilities. *Nature communications* **2019,** *10* (1), 1-8.

68. Hisaki, I.; Suzuki, Y.; Gomez, E.; Cohen, B.; Tohnai, N.; Douhal, A., Docking Strategy To Construct Thermostable, Single-Crystalline, Hydrogen-Bonded Organic Framework with High Surface Area. *Angewandte Chemie* **2018,** *130* (39), 12832-12837.

69. He, Y.; Xiang, S.; Chen, B., A microporous hydrogen-bonded organic framework for highly selective C_2H_2/C_2H_4 separation at ambient temperature. *Journal of the American Chemical Society* **2011,** *133* (37), 14570-14573.

70. Karmakar, A.; Illathvalappil, R.; Anothumakkool, B.; Sen, A.; Samanta, P.; Desai, A. V.; Kurungot, S.; Ghosh, S. K., Hydrogen-Bonded Organic Frameworks (HOFs): A New Class of Porous Crystalline Proton-Conducting Materials. *Angewandte Chemie International Edition* **2016,** *55* (36), 10667-10671.

71. Li, P.; He, Y.; Guang, J.; Weng, L.; Zhao, J. C.-G.; Xiang, S.; Chen, B., A homochiral microporous hydrogen-bonded organic framework for highly enantioselective separation of secondary alcohols. *Journal of the American Chemical Society* **2014,** *136* (2), 547-549.

72. Wang, H.; Bao, Z.; Wu, H.; Lin, R.-B.; Zhou, W.; Hu, T.-L.; Li, B.; Zhao, J. C.-G.; Chen, B., Two solvent-induced porous hydrogen-bonded organic frameworks: solvent effects on structures and functionalities. *Chemical Communications* **2017,** *53* (81), 11150-11153.

73. Tang, Y.; Yuan, M.; Jiang, B.; Xiao, Y.; Fu, Y.; Chen, S.; Deng, Z.; Pan, Q.; Tian, C.; Fu, H., Inorganic acid-derived hydrogen-bonded organic frameworks to form nitrogen-rich carbon nitrides for photocatalytic hydrogen evolution. *Journal of Materials Chemistry A* **2017,** *5* (41), 21979-21985.

74. Liu, J.; Li, L.; Niu, W.; Wang, N.; Zhao, D.; Zeng, S.; Chen, S., A Hydrogen-Bonded Organic-Framework-Derived Mesoporous N-Doped Carbon for Efficient Electroreduction of Oxygen. *ChemElectroChem* **2016**, *3* (7), 1116-1123.

75. Han, X.; Sun, L.; Wang, F.; Sun, D., MOF-derived honeycomb-like N-doped carbon structures assembled from mesoporous nanosheets with superior performance in lithium-ion batteries. *Journal of Materials Chemistry A* **2018**, *6* (39), 18891-18897.

76. Wei, J.; Zhou, D.; Sun, Z.; Deng, Y.; Xia, Y.; Zhao, D., A controllable synthesis of rich nitrogen-doped ordered mesoporous carbon for CO_2 capture and supercapacitors. *Advanced Functional Materials* **2013**, *23* (18), 2322-2328.

77. Yang, Y.; Gu, L.; Guo, S.; Shao, S.; Li, Z.; Sun, Y.; Hao, S., N-Doped Mesoporous Carbons: From Synthesis to Applications as Metal-Free Reduction Catalysts and Energy Storage Materials. *Frontiers in chemistry* **2019**, *7*.

78. Lewis, N. S.; Nocera, D. G., Powering the planet: Chemical challenges in solar energy utilization. *Proceedings of the National Academy of Sciences* **2006**, *103* (43), 15729-15735.

79. Zhang, T.; Lin, W., Metal–organic frameworks for artificial photosynthesis and photocatalysis. *Chemical Society Reviews* **2014**, *43* (16), 5982-5993.

80. Sakai, K.; Ozawa, H., Homogeneous catalysis of platinum (II) complexes in photochemical hydrogen production from water. *Coordination Chemistry Reviews* **2007**, *251* (21-24), 2753-2766.

81. Lee, Y.; Suntivich, J.; May, K. J.; Perry, E. E.; Shao-Horn, Y., Synthesis and activities of rutile IrO_2 and RuO_2 nanoparticles for oxygen evolution in acid and alkaline solutions. *The journal of physical chemistry letters* **2012**, *3* (3), 399-404.

82. Su, D. S.; Zhang, J.; Frank, B.; Thomas, A.; Wang, X.; Paraknowitsch, J.; Schlögl, R., Metal-free heterogeneous catalysis for sustainable chemistry. *ChemSusChem: Chemistry & Sustainability Energy & Materials* **2010,** *3* (2), 169-180.

83. Heinekey, D. M., Hydrogenase enzymes: recent structural studies and active site models. *Journal of Organometallic Chemistry* **2009,** *694* (17), 2671-2680.

84. Mulder, D. W.; Shepard, E. M.; Meuser, J. E.; Joshi, N.; King, P. W.; Posewitz, M. C.; Broderick, J. B.; Peters, J. W., Insights into [FeFe]-hydrogenase structure, mechanism, and maturation. *Structure* **2011,** *19* (8), 1038-1052.

85. Kaur-Ghumaan, S.; Stein, M., [NiFe] hydrogenases: how close do structural and functional mimics approach the active site? *Dalton Transactions* **2014,** *43* (25), 9392-9405.

86. Dempsey, J. L.; Brunschwig, B. S.; Winkler, J. R.; Gray, H. B., Hydrogen evolution catalyzed by cobaloximes. Accounts of chemical research 2009, 42 (12), 1995-2004.

87. Pal, A. K.; Hanan, G. S., Design, synthesis and excited-state properties of mononuclear Ru (II) complexes of tridentate heterocyclic ligands. *Chemical Society Reviews* **2014,** *43* (17), 6184-6197.

88. Cohen, S. G.; Parola, A.; Parsons Jr, G. H., Photoreduction by amines. *Chemical Reviews* **1973,** *73* (2), 141-161.

89. Ouyang, T.; Hou, C.; Wang, J.-W.; Liu, W.-J.; Zhong, D.-C.; Ke, Z.-F.; Lu, T.-B., A highly selective and robust Co (II)-based homogeneous catalyst for reduction of CO_2 to CO in CH_3CN/H_2O solution driven by visible light. *Inorganic Chemistry* **2017,** *56* (13), 7307-7311.

90. Willkomm, J.; Muresan, N. M.; Reisner, E., Enhancing H_2 evolution performance of an immobilised cobalt catalyst by rational ligand design. *Chemical Science* **2015,** *6* (5), 2727-2736.

91. Cline, E. D.; Adamson, S. E.; Bernhard, S., Homogeneous catalytic system for photoinduced hydrogen production utilizing iridium and rhodium complexes. *Inorganic chemistry* **2008,** *47* (22), 10378-10388.

92. Queyriaux, N.; Jane, R. T.; Massin, J.; Artero, V.; Chavarot-Kerlidou, M., Recent developments in hydrogen evolving molecular cobalt (II)–polypyridyl catalysts. Coordination chemistry reviews 2015, 304, 3-19.

93. Lentz, C. d.; Schott, O.; Auvray, T.; Hanan, G.; Elias, B., Photocatalytic hydrogen production using a red-absorbing Ir (III)–Co (III) dyad. *Inorganic Chemistry* **2017,** *56* (18), 10875-10881.

94. Jacques, A.; Schott, O.; Robeyns, K.; Hanan, G. S.; Elias, B., Hydrogen Photoevolution from a Green-Absorbing Iridium (III)–Cobalt (III) Dyad. *European Journal of Inorganic Chemistry* **2016,** *2016* (12), 1779-1783.

95. Rousset, E.; Chartrand, D.; Ciofini, I.; Marvaud, V.; Hanan, G., Red-light-driven photocatalytic hydrogen evolution using a ruthenium quaterpyridine complex. *Chemical Communications* **2015,** *51* (45), 9261-9264.

96. Kirch, M.; Lehn, J. M.; Sauvage, J. P., Hydrogen generation by visible light irradiation of aqueous solutions of metal complexes. An approach to the photochemical conversion and storage of solar energy. *Helvetica Chimica Acta* **1979,** *62* (4), 1345-1384.

97. Rau, S.; Schäfer, B.; Gleich, D.; Anders, E.; Rudolph, M.; Friedrich, M.; Görls, H.; Henry, W.; Vos, J. G., A supramolecular photocatalyst for the production of hydrogen and the selective hydrogenation of tolane. *Angewandte Chemie International Edition* **2006,** *45* (37), 6215-6218.

98. Zarkadoulas, A.; Koutsouri, E.; Kefalidi, C.; Mitsopoulou, C. A., Rhenium complexes in homogeneous hydrogen evolution. *Coordination Chemistry Reviews* **2015,** *304*, 55-72.

99. Lubitz, W.; Ogata, H.; Rüdiger, O.; Reijerse, E., Hydrogenases. *Chemical reviews* **2014,** *114* (8), 4081-4148.

100. Gloaguen, F.; Lawrence, J. D.; Rauchfuss, T. B., Biomimetic hydrogen evolution catalyzed by an iron carbonyl thiolate. *Journal of the American Chemical Society* **2001,** *123* (38), 9476-9477.

101. Barton, B. E.; Whaley, C. M.; Rauchfuss, T. B.; Gray, D. L., Nickel— iron dithiolato hydrides relevant to the [NiFe]-hydrogenase active site. *Journal of the American Chemical Society* **2009,** *131* (20), 6942-6943.

102. Schilter, D.; Camara, J. M.; Huynh, M. T.; Hammes-Schiffer, S.; Rauchfuss, T. B., Hydrogenase enzymes and their synthetic models: the role of metal hydrides. *Chemical reviews* **2016,** *116* (15), 8693-8749.

103. Thoi, V. S.; Sun, Y.; Long, J. R.; Chang, C. J., Complexes of earth-abundant metals for catalytic electrochemical hydrogen generation under aqueous conditions. *Chemical Society Reviews* **2013,** *42* (6), 2388-2400.

104. Helm, M. L.; Stewart, M. P.; Bullock, R. M.; DuBois, M. R.; DuBois, D. L., A synthetic nickel electrocatalyst with a turnover frequency above 100,000 s^{-1} for H_2 production. *Science* **2011,** *333* (6044), 863-866.

105. Kilgore, U. J.; Roberts, J. A.; Pool, D. H.; Appel, A. M.; Stewart, M. P.; DuBois, M. R.; Dougherty, W. G.; Kassel, W. S.; Bullock, R. M.; DuBois, D. L., [Ni (PPh$_2$NC$_6$H$_4$X$_2$)$_2$]$^{2+}$ complexes as electrocatalysts for H_2 production: effect of substituents, acids, and water on catalytic rates. *Journal of the American Chemical Society* **2011,** *133* (15), 5861-5872.

106.   Hawecker, J.; Lehn, J.; Ziessel, R., Efficient homogeneous photochemical hydrogen generation and water reduction mediated by cobaloxime or macrocyclic cobalt complexes. *Nouv. J. Chim* **1983,** *7*, 271-277.

107.   Connolly, P.; Espenson, J. H., Cobalt-catalyzed evolution of molecular hydrogen. *Inorganic Chemistry* **1986,** *25* (16), 2684-2688.

108.   Hu, X.; Cossairt, B. M.; Brunschwig, B. S.; Lewis, N. S.; Peters, J. C., Electrocatalytic hydrogen evolution by cobalt difluoroboryl-diglyoximate complexes. *Chemical communications* **2005,** (37), 4723-4725.

109.   Razavet, M.; Artero, V.; Fontecave, M., Proton electroreduction catalyzed by cobaloximes: Functional models for hydrogenases. *Inorganic chemistry* **2005,** *44* (13), 4786-4795.

110.   Schott, O.; Pal, A. K.; Chartrand, D.; Hanan, G. S., A Bisamide Ruthenium Polypyridyl Complex as a Robust and Efficient Photosensitizer for Hydrogen Production. *ChemSusChem* **2017,** *10* (22), 4436-4441.

111.   Wu, G. G.; Wong, Y.; Poirier, M., Novel 2, 2-Bipyridine Ligand for Palladium-Catalyzed Regioselective Carbonylation. Organic Letters 1999, 1 (5), 745-747.

112.   Kavallieratos, K.; Rosenberg, J. M.; Bryan, J. C., Pb (II) Coordination and Synergistic Ion-Exchange Extraction by Combinations of Sulfonamide Chelates and 2, 2'-Bipyridine. Inorganic chemistry 2005, 44 (8), 2573-2575.

113.   Girnt, D.; Roesky, P. W.; Geist, A.; Ruff, C. M.; Panak, P. J.; Denecke, M. A., 6-(3, 5-dimethyl-1 H-pyrazol-1-yl)-2, 2'-bipyridine as ligand for actinide (III)/lanthanide (III) separation. Inorganic chemistry 2010, 49 (20), 9627-9635.

114.   Fletcher, N. C.; Nieuwenhuyzen, M.; Rainey, S., The isolation and purification of tris-2, 2'-bipyridine complexes of ruthenium (II) containing unsymmetrical ligands. Journal of the Chemical Society, Dalton Transactions 2001, (18), 2641-2648.

115.   Goldsmith, J. I.; Hudson, W. R.; Lowry, M. S.; Anderson, T. H.; Bernhard, S., Discovery and high-throughput screening of heteroleptic iridium complexes for photoinduced hydrogen production. *Journal of the American Chemical Society* **2005,** *127* (20), 7502-7510.

116.   Winter, A.; Newkome, G. R.; Schubert, U. S., Catalytic applications of terpyridines and their transition metal complexes. *ChemCatChem* **2011,** *3* (9), 1384-1406.

117.   Budnikova, Y. H.; Vicic, D. A.; Klein, A., Exploring mechanisms in Ni terpyridine catalyzed C–C cross-coupling reactions—a review. *Inorganics* **2018,** *6* (1), 18.

118.   Wei, C.; He, Y.; Shi, X.; Song, Z., Terpyridine-metal complexes: Applications in catalysis and supramolecular chemistry. *Coordination chemistry reviews* **2019,** *385*, 1-19.

119.   Rupp, M.; Auvray, T.; Rousset, E.; Mercier, G. M.; Marvaud, V.; Kurth, D. G.; Hanan, G. S., Photocatalytic Hydrogen Evolution Driven by a Heteroleptic Ruthenium (II) Bis (terpyridine) Complex. *Inorganic chemistry* **2019,** *58* (14), 9127-9134.

120.   Schwarz, H. A.; Creutz, C.; Sutin, N., Homogeneous catalysis of the photoreduction of water by visible light. 4. Cobalt (I) polypyridine complexes. Redox and substitutional kinetics and thermodynamics in the aqueous 2, 2'-bipyridine and 4, 4'-dimethyl-2, 2'-bipyridine series studied by the pulse-radiolysis technique. *Inorganic Chemistry* **1985,** *24* (3), 433-439.

121.   Leung, C.-F.; Ng, S.-M.; Ko, C.-C.; Man, W.-L.; Wu, J.; Chen, L.; Lau, T.-C., A cobalt (II) quaterpyridine complex as a visible light-driven catalyst for both water oxidation and reduction. Energy & Environmental Science 2012, 5 (7), 7903-7907.

122.   Krishnan, C.; Sutin, N., Homogeneous catalysis of the photoreduction of water by visible light. 2. Mediation by a tris (2, 2'-bipyridine) ruthenium (II)-cobalt (II) bipyridine system. *Journal of the American Chemical Society* **1981,** *103* (8), 2141-2142.

123.   Sakintuna, B.; Lamari-Darkrim, F.; Hirscher, M., Metal hydride materials for solid hydrogen storage: a review. *International journal of hydrogen energy* **2007,** *32* (9), 1121-1140.

124.   Holladay, J. D.; Hu, J.; King, D. L.; Wang, Y., An overview of hydrogen production technologies. *Catalysis today* **2009,** *139* (4), 244-260.

125.   Zou, X.; Zhang, Y., Noble metal-free hydrogen evolution catalysts for water splitting. *Chemical Society Reviews* **2015,** *44* (15), 5148-5180.

126.   Khnayzer, R.; Thoi, V.; Nippe, M.; King, A.; Jurss, J.; El Roz, K.; Long, J.; Chang, C.; Castellano, F., Towards a comprehensive understanding of visible-light photogeneration of hydrogen from water using cobalt (II) polypyridyl catalysts. *Energy & Environmental Science* **2014,** *7* (4), 1477-1488.

127.   Lo, W. K.; Castillo, C. E.; Gueret, R.; Fortage, J. r. m.; Rebarz, M.; Sliwa, M.; Thomas, F.; McAdam, C. J.; Jameson, G. B.; McMorran, D. A., Synthesis, characterization, and photocatalytic H_2-evolving activity of a family of [Co (N4Py)(X)] n+ complexes in aqueous solution. *Inorganic chemistry* **2016,** *55* (9), 4564-4581.

128.   Deponti, E.; Natali, M., Photocatalytic hydrogen evolution with ruthenium polypyridine sensitizers: unveiling the key factors to improve efficiencies. *Dalton Transactions* **2016,** *45* (22), 9136-9147.

129.   Yuan, Y.-J.; Tu, J.-R.; Lu, H.-W.; Yu, Z.-T.; Fan, X.-X.; Zou, Z.-G., Neutral nickel (II) phthalocyanine as a stable catalyst for visible-light-driven hydrogen evolution from water. *Dalton Transactions* **2016,** *45* (4), 1359-1363.

130.   Hogue, R. W.; Schott, O.; Hanan, G. S.; Brooker, S., A smorgasbord of 17 cobalt complexes active for photocatalytic hydrogen evolution. *Chemistry–A European Journal* **2018,** *24* (39), 9820-9832.

131.   Duong, A.; Maris, T.; Wuest, J. D., Using Pyridinyl-Substituted Diaminotriazines to Bind Pd (II) and Create Metallotectons for Engineering Hydrogen-Bonded Crystals. *Inorganic chemistry* **2011,** *50* (12), 5605-5618.

132.   Duong, A.; Métivaud, V.; Maris, T.; Wuest, J. D., Surrogates of 2, 2'-Bipyridine Designed to Chelate Ag (I) and Create Metallotectons for Engineering Hydrogen-Bonded Crystals. *Crystal growth & design* **2011,** *11* (5), 2026-2034.

133.   Telfer, S. G.; Wuest, J. D., Metallotectons: using enantiopure tris (dipyrrinato) cobalt (III) complexes to build chiral molecular materials. *Chemical communications* **2007,** (30), 3166-3168.

134.   Pal, A. K.; Duong, A.; Wuest, J. D.; Hanan, G. S., Long-lived, red-emitting excited state of a Ru (II) complex of a diaminotriazine ligand. Polyhedron 2016, 108, 100-103.

135.   Ma, D. L.; He, H. Z.; Leung, K. H.; Chan, D. S. H.; Leung, C. H., Bioactive luminescent transition-metal complexes for biomedical applications. *Angewandte Chemie International Edition* **2013,** *52* (30), 7666-7682

Chapter 2

Programmed Molecular Construction: Driving the Self-Assembly by Coordination and Hydrogen Bonds Using 6-(Pyridin-2-yl)-1,3,5-triazine-2,4-diamine Ligand with $M(NO_3)_2$ Salts

2.1. Introduction

Crystal engineering is a common approach to prepare well-defined structures with suitable topologies and an ability to engage in multiple predictable interactions with neighbors producing reliable patterns. Innovation in this field has led to a hybrid approach that combines both inorganic and organic chemistry to produce ordered materials. The resulting assembly gives rise to crystalline materials with predictable organizations. 2,2'-bipyridine (2,2'-bipy) due to its good chelating ability forms an integral part of the numerous versatile supramolecular architectures. The properties of 2,2'-bipy have been further enhanced by the facile incorporation of diaminotriazine (DAT) groups into the organic fragments to synthesize tectoligands. These tectoligands apart from easy synthesis have the ability to bind to the metal ions with same ligating mode as 2,2'-bipy forming metallotectons and to undergo self-assembly by multiple hydrogen bonds with reliable patterns. The perspective of making metallotectons is to use the combination of both coordination and hydrogen-bonded motifs to create supramolecular networks. The supramolecular networks formed by the self-assembly of metallotectons are highly ordered, crystalline and the structures are predictable. Ordered materials with predetermined properties are known to solve a wide range of applications related to the fields of energy and nanotechnology. Using metallotectonic approach we have thus synthesized a wide range of ordered materials with closely related structures. These 2D and 3D crystalline transition metal complexes are potentially valuable for applications in catalysis, photovoltaics, fuel cells, energy conversion and storage.

2.2. Article 1

Programmed Molecular Construction: Driving the Self-Assembly by Coordination and Hydrogen Bonds Using 6-(Pyridin-2-yl)-1,3,5-triazine-2,4-diamine Ligand with $M(NO_3)_2$ Salts

Sanil Rajak, Midhun Mohan, Alexandre A. Tremblay, Thierry Maris, Silvano Leal do Santos, Everaldo Carlos Venancio, Sydney Ferreira Santos, and Adam Duong*

2.3. Author's Contribution

Sanil Rajak: Investigation, conceptualization, methodology, synthesis and characterization, interpretation of results, redaction of the draft of manuscript.

Dr. Midhun Mohan: Chemistry software assistance.

Alexandre A. Tremblay: Laboratory assistance.

Dr. Thierry Maris: Crystallographic data analysis.

Silvano Leal do Santos: Thermo gravimetric analysis and differential scanning calorimetry studies (TGA-DSC).

Prof. Everaldo Carlos Venancio: TGA-DSC supervision.

Prof. Sydney Ferreira Santos: TGA-DSC supervision and interpretation.

Prof. Adam Duong: Supervision, finding financial supports, project administration, conceptualization, interpretation of results, writing- review and editing.

1. Abstract

A new series of hydrogen-bonded metallotecton networks **6-9** of the general formula [M(**2**)$_2$(NO$_3$)$_2$] were obtained from the reaction of 6-pyridin-2-yl-[1,3,5]-triazine-2,4-diamine **2** with transition-metal ions [M: Co(II), Ni(II), Cu(II), and Zn(II)]. Their supramolecular networks and associated properties were characterized by single-crystal and powder X-ray diffraction, IR, solid-state UV-vis spectroscopy, and thermogravimetric analysis associated with differential scanning calorimetry. On the basis of standard patterns of coordination involving 2,2'-bipyridine and simple derivatives, compound **2** binds transition-metal ions with predictable constitution and the diaminotriazinyl (DAT) groups serve orthogonally to ensure the intermetallotecton interactions by hydrogen bonding according to well-established motifs I–III. As expected, compound **2** formed octahedral 2:1 metallotectons with M(NO$_3$)$_2$, and further self-assembled by hydrogen bonding of the DAT groups to produce pure, crystalline, homogeneous, and thermally stable materials. In these structures, nitrate counterions also play an important role in the cohesion of intermetallotectons to form two-dimensional and three-dimensional networks. These results illustrated the effectiveness of the synthetic approach to create a wide range of novel ordered materials with controllable architectures and tunable properties achieved by varying the central metal ion. Crystal morphologies of **6-9** were also investigated by scanning electron microscopy and calculation using Bravais-Friedel-Donnay-Harker method from their single-crystal structure.

2. Introduction

Enhancements and innovations in the fields of chemistry, physics, and engineering have provided a better understanding of the structure-property relationships in several classes of materials. As a result, considerable effort has been made to develop strategies to precisely control the chemical composition and the structure to tailor properties of novel materials. Among others, ordered materials have attracted much attention due to their importance in numerous technological fields such as catalysis, photovoltaics, batteries, nanotechnology, and so forth.[1-3] A common approach to prepare well-defined structures is based on the concept of crystal engineering in which molecular components with suitable topologies and ability to engage in multiple predictable interactions with neighbors produce reliable patterns.[4,5] Even though reliable methods have been used to create ordered materials, it should be noted that the synthesis of the molecular components is usually not trivial. Thus, a hybrid approach, combining both inorganic and organic chemistry, is exploited to produce ordered materials driven by the self-assembly of organic units linked by coordination to metal ions and other directional forces.[6-10] This approach has numerous advantages: (i) it allows to prepare molecular crystals with high yields; (ii) the self-assemblies are predictable; (iii) ordered materials with various properties owing to the presence of transition metal ions are developed; and (iv) the supramolecular networks and properties can be easily tuned by varying the metal center.

In coordination chemistry, ligand like 2,2'-bipyridine (**1** = 2,2'-bipy) has been widely used due to its chelating ability (in self-assembly with metal ions) to form predictable coordination complexes.[11-17] Many functional materials with 2,2'-bipy and related ligands have been developed and applied to material separation/purification, catalysis, and ions exchange.[18-23]

However, these materials are comparatively difficult to prepare because their syntheses are laborious. In addition, crystal structures with 2,2'-bipy complexes are not predictable due to lack of functional groups to direct the self-assembly.

Of special interest are diaminotriazinyl-substituted pyridine, pyrazine, and pyrimidine **2-4**, a family of compounds that can engage in predictable intermolecular interactions such as hydrogen bonds and can simultaneously bind metal ions according to reliable patterns (Chart 1).[24-31] Because of this dual ability, they were called tectoligands.[31] In crystal engineering, the self-assembly of tectoligands with metal ions produces metallotectons.[32,33]
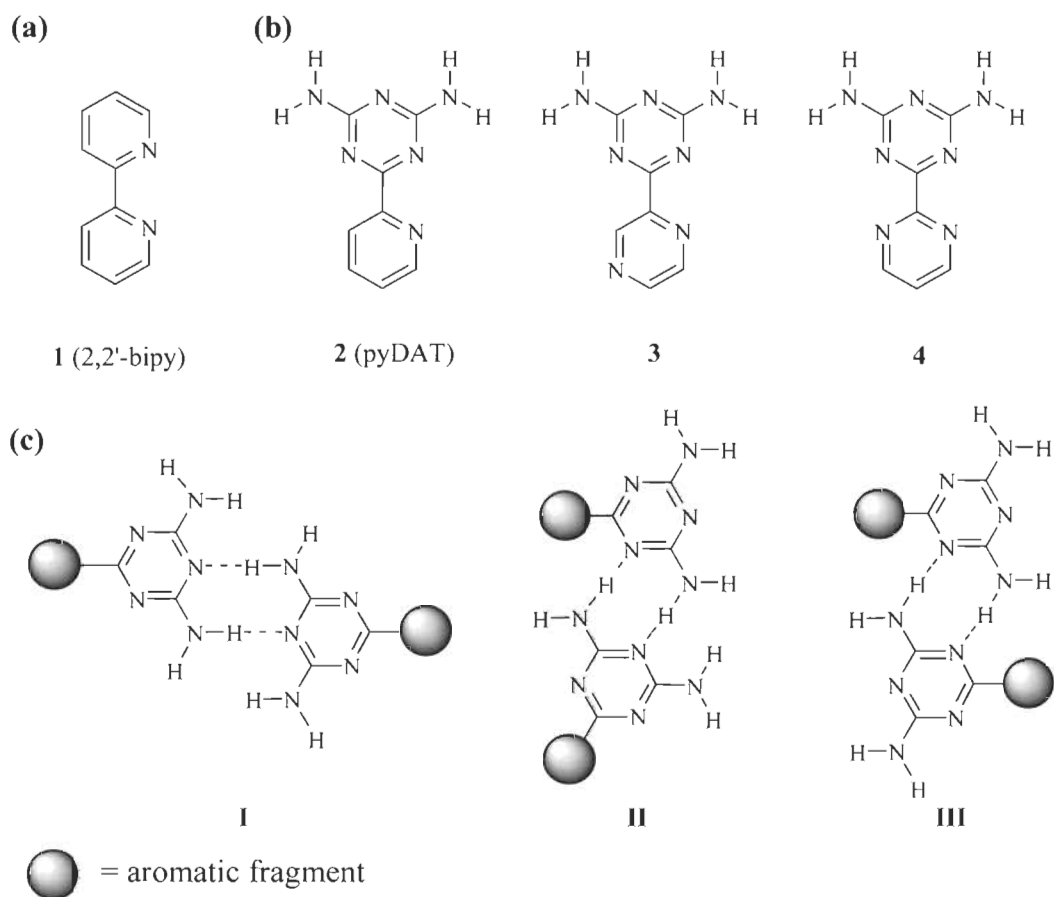
Chart 1. Representation of the Molecular Structures of (a) 2,2'-Bipyridine **1**, (b) Tectoligands **2-4**, and (c) Cyclic Hydrogen Bonding Motifs **I-III** of Diamino-1,3,5-triazinyl Group (DAT)

Here, we report the synthesis and the solid-state characterizations of a new series of crystalline materials **6-9** obtained under mild reaction conditions by the assembly of **2** with Co(II), Ni(II), Cu(II), and Zn(II) ions (Scheme 2b). By focusing on a single tectoligand with a predictable behavior, bound with various transition metal ions, we designed our study to produce wide range

of ordered materials with closely related structures to reveal the principles of the molecular construction based on the metallotectonic approach.

(a)

(b)

6. M = Co(II)
7. M = Ni(II)
8. M = Cu(II)
9. M = Zn(II)
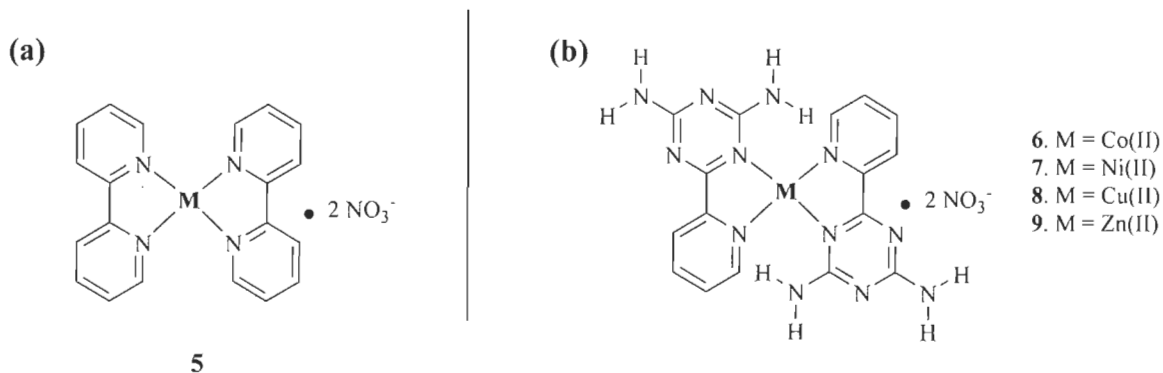
Chart 2. Representation of the Molecular Structures of (a) Complexes Without Hydrogen-Bonding Sticky Site and (b) Metallotectons **6-9**

3. Results and Discussions

3.1. Syntheses and Characterization. To evaluate the potential of the hybrid approach to form various molecular crystals, we have chosen to study the behavior of **2** to bind transition-metal ions (Co(II), Ni(II), Cu(II), and Zn(II)) that have d^7 to d^{10} electronic configurations. Compound **2** is basically an organic compound consisting of a diamino-1,3,5-triazinyl group (DAT) and a pyridine, which are known as the building blocks of many inorganic materials and biological molecules.[34-43] In this work, we focused on $M(NO_3)_2$ salts because nitrate ions can engage in multiple hydrogen bonding, which can strengthen the supramolecular networks. 6-(Pyridin-2-yl)-1,3,5- triazine-2,4-diamine **2** was prepared by reported methods.[44] The reaction of **2** and metal(II) nitrate in methanol produces metallotectons **6-9**, which were crystallized by slow diffusion in MeOH/Et$_2$O in good yields. As a result, structures of **6-9** reflect intra- and intermetallotecton interactions and multiple strong hydrogen bonds characteristic of DAT groups.

3.2. Three-Dimensional Molecular and Supramolecular Structure.

3.2.1. Crystal Structures of 6 and 7.

Crystals of **6** grown from MeOH/Et$_2$O are pink. They belong to the orthorhombic space group Fdd2. Views of the structure are shown in Figure 1. Other crystallographic data are summarized in Table 1. The structure of **6**, with 2:1 pyDAT-to-Co ratio, is Co(pyDAT)$_2$(NO$_3$)$_2$. The cobalt atom coordinated with two pyDAT and two nitrate ions form a cis-conformation (Figure 1a). The metallotecton **6** has a strongly distorted octahedral geometry. This coordination geometry is reinforced by intramolecular hydrogen bonds N−H···O involving oxygen atoms of the nitrate and adjacent NH$_2$ group (2.917(4) Å). The average distance of Co-N and Co-ONO$_2$ in the metallotecton is normal (2.131(4) and 2.146(3) Å, respectively).[45] The Co atom and one pair of coordinated N atoms of the triazine rings of different pyDAT ligands form almost a straight line, with a N$_2$-Co-N$_2$^{i} angle of 167.4(2)°. In contrast, the other coordinated pair of N atoms of the pyridine rings is not linear, with a N$_1$-Co-N$_1$^{i} angle of 109.0(2)°. The pyridine and DAT rings in both ligands are tilted around the C-C bond by 12.6°. The average plane of bound ligands forms an angle of 57.9°. As expected, the DAT groups in metallotecton **6** are placed in trans-orientation. In the structure, each DAT group is linked by two N−H···N hydrogen bonds of type **IV** (Scheme 3, distance N−H···N = 3.104(5) Å), giving rise to a three-dimensional network (Figure 1b).

IV
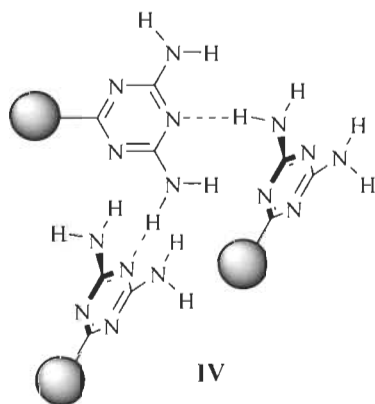
Chart 3. Representation of the Molecular Structures of a Polymeric Hydrogen Bonding Motifs IV of Diamino-1,3,5- triazinyl Group (DAT)

Additional $N-H\cdots O$ hydrogen bonds involving nitrates and free NH_2 groups reinforced the supramolecular network. Details of the hydrogen bonds and their angles are provided in Table S1.

The reaction of **2** with nickel(II) nitrate 2:1 ratio in methanol subsequently crystallized from MeOH/Et$_2$O produced cyan crystals of **7**. The crystal structure determined by single-crystal X-ray diffraction is isostructural to **6**. Views of the structure of **7** are shown in Figure S3. Other crystallographic data are given in Table 1. The structural formula of metallotecton **7** consists of Ni(pyDAT)$_2$(NO$_3$)$_2$. The nickel atom is coordinated with pyDAT and nitrates similarly to **6** (Ni-N and Ni-ONO$_2$ average distances are 2.092(5) and 2.125(5) Å, respectively). In the structure of **7**, the $N_2-Ni-N_2^i$ angle is 170.5(3)°, which is slightly different from that of **6**. Selected hydrogen bonds and their angles are provided in Table S2.

a

b
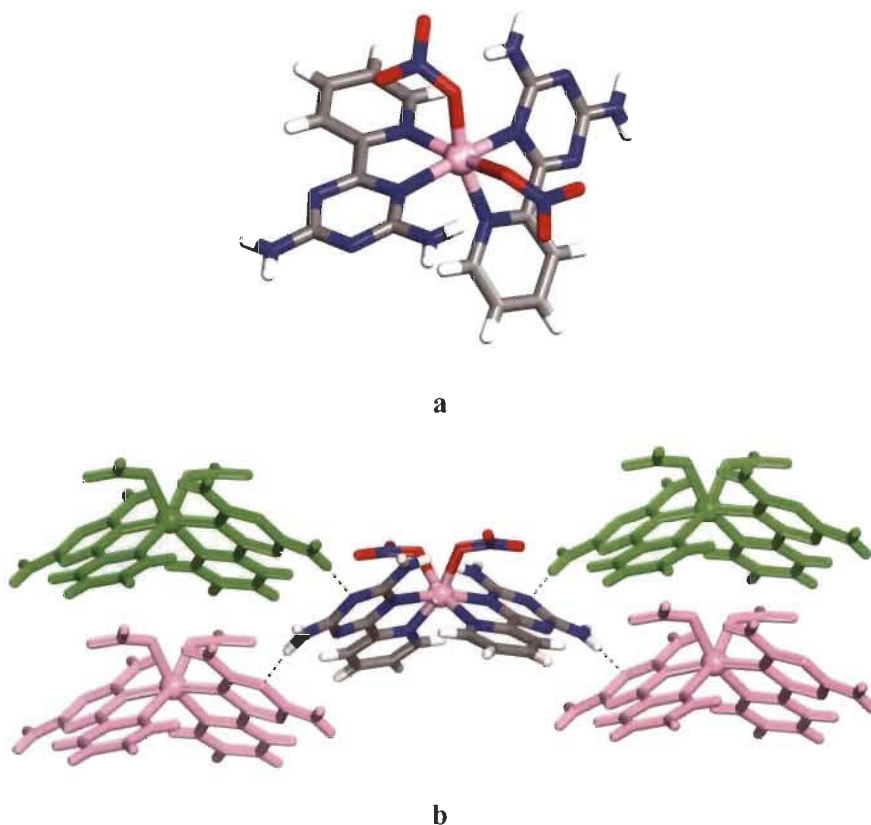
Figure 1. Views of the crystal structure of **6** grown from MeOH/Et$_2$O. Hydrogen bonds are represented by dashed lines. Unless stated otherwise, carbon atoms are shown in gray, hydrogen atoms in white, oxygen atoms in red, nitrogen atoms in blue, and cobalt atoms in pink. (a) Structure of the metallotecton **6** and (b) alternating of enantiomeric metallotectons of **6** joined by N−H···N hydrogen bonds of DAT groups according to motif **IV** to produce the three-dimensional network. For clarity, few metallotectons are marked in green and pink.

3.2.2. Table 1. Crystallographic Data for 6-9

	6	7	8	9
Formula	Co(C$_8$H$_8$N$_6$)$_2$(NO$_3$)$_2$	Ni(C$_8$H$_8$N$_6$)$_2$(NO$_3$)$_2$	Cu(C$_8$H$_8$N$_6$)$_2$(NO$_3$)$_2$	Zn(C$_8$H$_8$N$_6$)$_2$(NO$_3$)$_2$
Mr	559.36	559.14	563.97	565.80
crystal system	Orthorhombic	Orthorhombic	Monoclinic	Monoclinic
Radiation	GaKα	GaKα	GaKα	CuKα
λ (Å))	1.34139	1.34139	1.34139	1.54178
F(000)	2280	2288	1148	1152
space group	*Fdd*2	*Fdd*2	*P*2$_1$/*c*	*C*2/*c*
a (Å)	39.7939(16)	39.702(2)	15.2840(11)	9.0912(1)
b (Å)	8.9352(4)	8.8392(4)	9.0360(7)	11.4484(2)
c (Å)	11.7989(5)	11.9162(6)	16.0867(11)	19.9334(3)
α (deg)	90	90	90	90
β (deg)	90	90	105.075(3)	94.019(1)
γ (deg)	90	90	90	90
V (Å^3)	4195.3(3)	4181.9(4)	2145.2(3)	2069.56(5)
Z	8	8	4	4
ρ_{calcd} (g cm^{-3})	1.771	1.776	1.746	1.816
T (K)	120	120	110	100
μ (mm^{-1})	4.911	5.483	5.940	2.316
measured reflns	21847	20085	36457	20812
independent reflns	2325	2253	4913	2028
Rint	0.0652	0.0798	*N/A*	0.0229

observed reflns	2180	2070	4504	1966
$I > 2\sigma(I)$				
$R_1, I > 2\sigma(I)$	0.0426	0.0560	0.0672	0.0251
R_1, all data	0.0467	0.0615	0.0758	0.0258
$\omega R_2, I > 2\sigma(I)$	0.0976	0.1430	0.1716	0.0695
ωR_2, all data	0.0999	0.1470	0.1834	0.0690
GoF	1.071	1.078	1.086	1.067

3.2.3. Crystal Structure of 8.

The blue crystals of **8** grown from MeOH/Et$_2$O proved to belong to the monoclinic space group P2$_1$/c and have the composition Cu(pyDAT)$_2$(NO$_3$)$_2$. Figure 2 shows the views of the structure. Other crystallographic data are summarized in Table 1. The metallotecton **8** with a 2:1 pyDAT-to-Cu ratio consists of [(pyDAT)$_2$Cu]$^{2+}$ cation and two nitrate anions in trans-fashion (Figure 2a). The cationic [(pyDAT)$_2$Cu]$^{2+}$ is flattened, and the average plane of bound ligands forms an angle of 39.8°. The copper (II) atom is coordinated to two pyDAT and two nitrate ions. The copper coordination polyhedron can be described as a strongly distorted octahedron. This coordination geometry is reinforced by intramolecular N−H···O hydrogen bonds involving oxygen atoms and NH$_2$ groups. In the metallotecton **8**, the average Cu−N bonds length is 2.005(1) Å. The two nitrates are coordinated in an apical position with Cu−O nonequal bond lengths of 2.457(3) and 2.845(4) Å. These values are within the 2.4-2.9 Å range and consistent with an axial elongation caused by a Jahn-Teller distortion of the octahedral geometry of Cu(II).[46,47] The observed structure consists of enantiomeric metallotectons of **8**, which are linked alternatively into chains joined via characteristic N−H···N hydrogen bonds of DAT groups according to the motif **I** (Figure 2b). The average N−H···N distances in hydrogen-bonded pairs of DAT groups (3.073(6) Å) have normal values.[48] The chains are held together by π-stacking of DAT groups and pyridyl rings to form sheets (average distance 3.988 Å). The sheets are reinforced by additional N−H···O hydrogen bonds involving oxygen atoms of nitrate and NH$_2$ groups that are simultaneously engaged in

hydrogen bonding according to motif **I**. Packing of the sheets directly by multiple N—H···O

hydrogen bonds involving nitrate and free NH_2 groups produce the three-dimensional structure

(Figure 2c). Selected hydrogen bonds and their angles are given in Table S3.

a

b

c
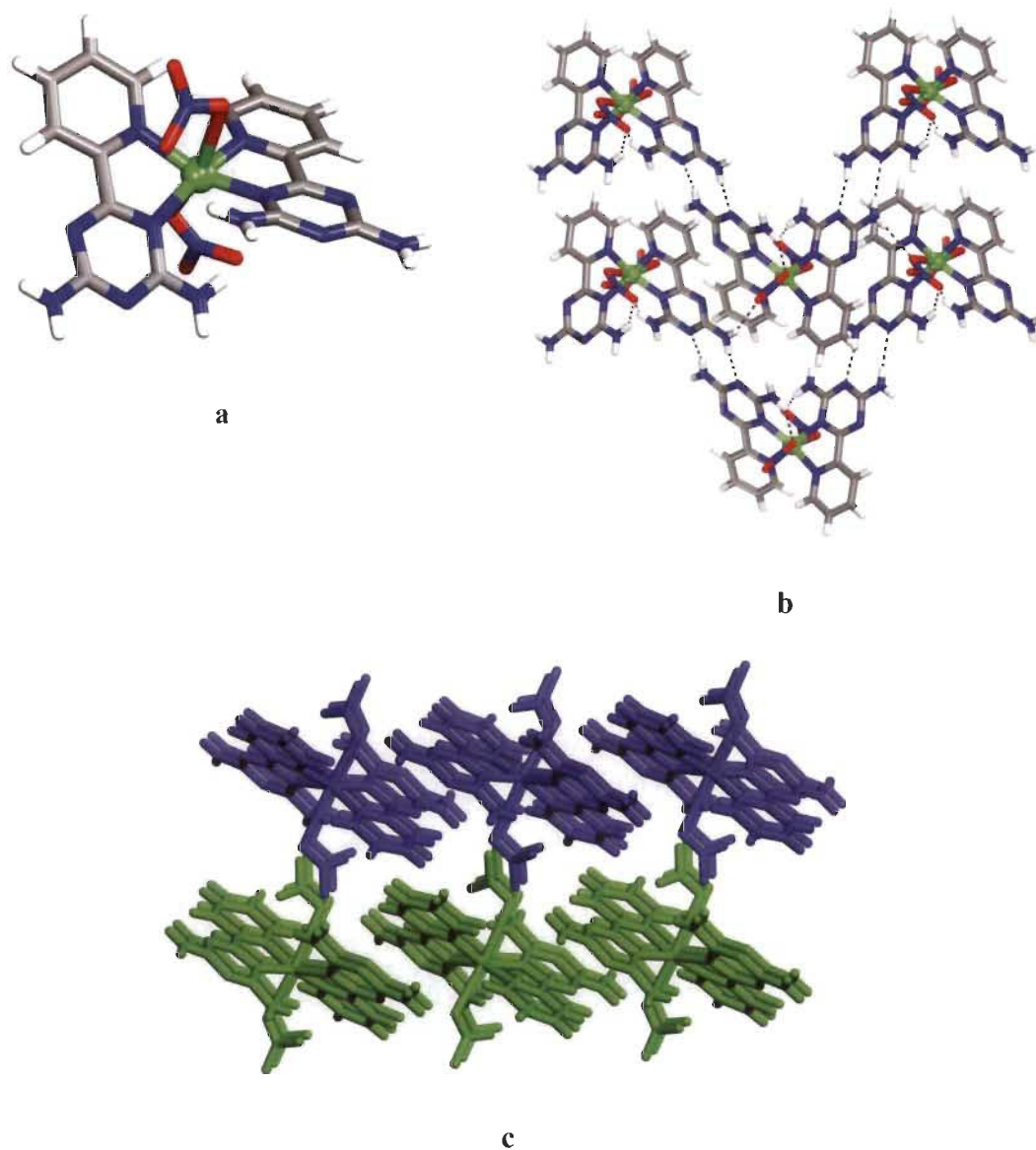
Figure 2. Views of crystal structure of **8** grown from $MeOH/Et_2O$. Hydrogen bonds are

represented by dashed lines. Unless stated otherwise, carbon atoms are shown in gray, hydrogen

atoms in white, oxygen atoms in red, nitrogen atoms in blue, and copper atoms in green. (a)

Structure of the metallotecton **8**. (b) Alternating zigzag chains of $Cu(pyDAT)_2(NO_3)_2$ and its

enantiomer joined together by hydrogen bonding of DAT groups according to the motif **I**,

strengthened by hydrogen bonding involving bridging nitrates. (b) View showing sheets packed together to form the three-dimensional structure. For clarity, layers are marked in green and blue.

3.2.4. Crystal Structure of 9.

The reaction of zinc nitrate with **2** in a ratio of 1:2 produced **9** in high yield. Colorless crystals of **9** grown from MeOH/Et$_2$O proved to belong to the monoclinic space group C2/c and have the composition Zn(pyDAT)$_2$(NO$_3$)$_2$. Views of the structure are shown in Figure 3, and additional crystallographic data are given in Table 1. The observed structure incorporates enantiomer of metallotectons. The coordination around the zinc atom in **9** is identical to that in metallotectons **6** and **7** (Figure 3a). The average plane of bound ligands in cationic [(pyDAT)$_2$Zn]$^{2+}$ forms an angle of 57.3° and the two DAT groups are in trans orientation. The zinc atom can be considered as having a distorted octahedral geometry. Within each ligand, the triazine and pyridine rings are almost coplanar, and the average planes form angles of 12.9 and 17.6°. The nitrogen atoms of two different DATs are axially coordinated with an almost linear N$_2$–Zn–N$_2^i$ angle of 168.3°. The pyridine rings are in an equatorial position with the N$_1$–Zn–N$_1^i$ angle of 114.3°. The distances Zn–N in the metallotecton **9** are normal (average distance 2.160 Å).[49] The average distance of the Zn–O bond is 2.181(1) Å. This suggests that nitrates are strongly coordinated to the metal ion. Details of the hydrogen bonds and their angles are summarized in Table S4. In the structure of **9**, the trans-orientation of the DAT groups allows pairing of metallotectons by the formation of four hydrogen bonds according to motif **I** (average N–H···N distance = 3.019(2) Å) to form chains. With the assistance of hydrogen bonds involving nitrate and free NH$_2$ groups (average distance N–H···O = 2.945(5) Å), the chains are held together to form sheets (Figure 3b). These sheets pack via π-stacking to produce the observed three-dimensional structure (Figure 3c).

It should be noted that although metallotectons in (**6** and **7**) and **9** have identical coordination geometry and topology, the supramolecular networks resulting from the same crystallization condition (MeOH/Et$_2$O) provide different association motifs of DAT groups. Comparison of the

structures of **9** and $[Zn(\mathbf{2})_2(N_3)_2]$ reported from the literature[50] shows similar association motifs of DAT groups. However, the replacement of azide ions by nitrate ions generates different cohesion of adjacent sheets, which play an important role in the self-assembly.

Together, crystal structures of **6-9** and $[Zn(\mathbf{2})_2(N_3)_2]$ indicate that the molecular organization is dependent not only on the topology of metallotectons but also on the integration of subtle details, which collectively direct the supramolecular association.

a

b

c
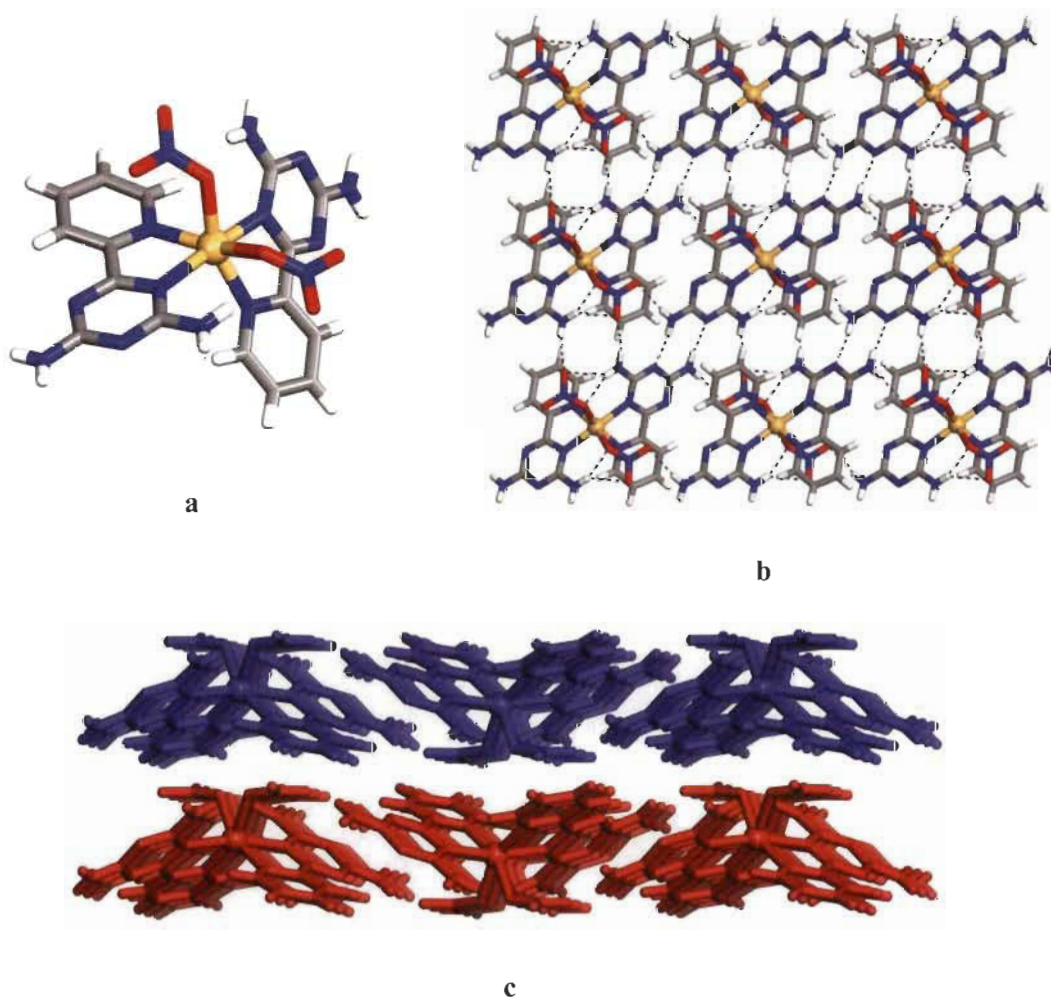
Figure 3. Views of the crystal structure of **9** grown from MeOH/Et₂O. Hydrogen bonds are represented by dashed lines. Unless stated otherwise, carbon atoms are shown in gray, hydrogen atoms in white, oxygen atoms in red, nitrogen atoms in blue, and zinc atoms in orange. (a) Structure of the metallotecton **9**. (b) Racemic pairs of metallotecton held together by four N−H···N

hydrogen bonds of type **I** and multiple hydrogen bonds involving bridging nitrates to form the two-dimensional (2D) sheet. (c) View showing sheets packed together to form the three-dimensional structure. For clarity, layers are marked in red and blue.

3.3. Crystallinity, Purity, and Homogeneity of Bulk Materials of 6-9.

The evaluation of homogeneity and phase purity is an important aspect in material science. Indeed, in the crystallization process, the crystal growth of a sample might result in a blend of several crystalline phases, thereafter, producing a sample with heterogeneous properties. Therefore, we first verified the homogeneity and purity of **6-9** by elemental analysis (EA) (see the Experimental Section). The compositions found by EA for each sample have the general chemical formula $M(C_8H_8N_6)_2(NO_3)_2$ (M = Co^{II}, Ni^{II}, Cu^{II}, or Zn^{II}), which are consistent with the single-crystal X-ray diffraction data. Since we cannot confirm the phase purity by EA, the bulk products of the as-grown crystals of **6-9** were evaluated by powder X-ray diffraction (PXRD). Generally, due to the fragility of crystals outside of the solvents of crystallization, the analysis by PXRD is difficult. In our case, all crystals were stable outside the mother liquors. The PXRD measurements in transmission mode for **6-9** confirmed the phase purity of products. Indeed, all peaks of measured PXRD (in black) match well with the simulated (in red) patterns (Figure 4). This result demonstrates the absence of secondary phases for all samples. The phase purity of **6-9** was reinforced by scanning electron microscopy (SEM), which confirms the absence of contaminations by an amorphous phase that cannot be observed in PXRD (see Figure S8). Together, the XRD, PXRD, EA, and SEM demonstrate that each bulk sample of **6-9** can be prepared in a single-phase, pure, and crystalline forms.
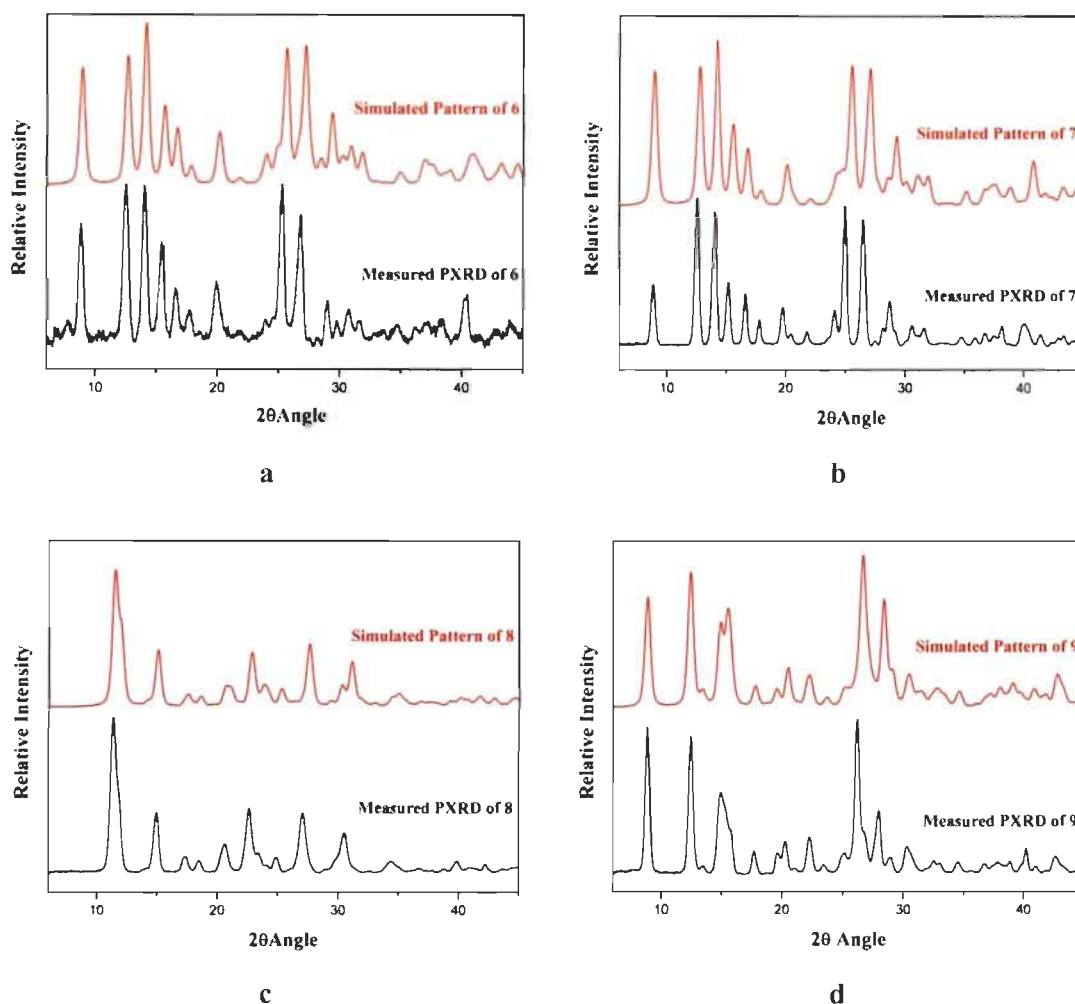
Figure 4. PXRD of **6-9**. Comparison of the measured powder X-ray diffraction (in black) with simulated patterns (in red) calculated from single crystal structures. (a-d) **6-9**, respectively.

3.4. Thermal and Photophysical Properties.

Thermal behaviors of **6-9** were determined using a combination of thermogravimetric analysis and differential scanning calorimetry (TGA-DSC) measured simultaneously. TGA and DSC curves of these compounds are shown in Figure 5. All samples were studied from 35 to 800 °C, with a heating rate of 10 °C/min under air atmosphere. DSC curves of **6** and **7** showed a sharp exothermic peak at about 337 and 350 °C, respectively (Figure 5a, b, red curves). These are followed by exothermic peaks between 410 and 485 °C. DSC curve measured for **8** displayed three small

84

recognizable exothermic peaks between 300 and 400 °C, followed by an intense broad exothermic peak (Figure 5c, red curve). The DSC curve of **9** showed a sharp exothermic peak at 345 °C, followed by broad exothermic peaks (Figure 5d). Compounds **6** and **7** have virtually the same TG thermal decomposition curves (Figure 5a, b, black curves). Their DSC curves show sharp exothermic peaks, which are associated to a pronounced loss of mass of ~44%. In the second decomposition step, a loss of mass of the same magnitude is again observed to give the final residues. TG curve of **8** displayed three distinguishable decomposition steps in the 300-517 °C temperature range, with mass losses of 13 % for the first two and 49.4 % for the last one (Figure 5c, black curve). Compound **9** decomposed in three steps between 345 and 592 °C (Figure 5d, black curve). The first two decomposition steps occurred at 345-532 °C, with a net loss of mass of ~34 % each. The third decomposition step between 532 and 592 °C showed ~25 % loss of mass. A summary of temperature ranges, mass losses (%) found and calculated, and proposed assignment of decomposition of **6-9** determined by TGA are listed in Table S5.

a   b

85
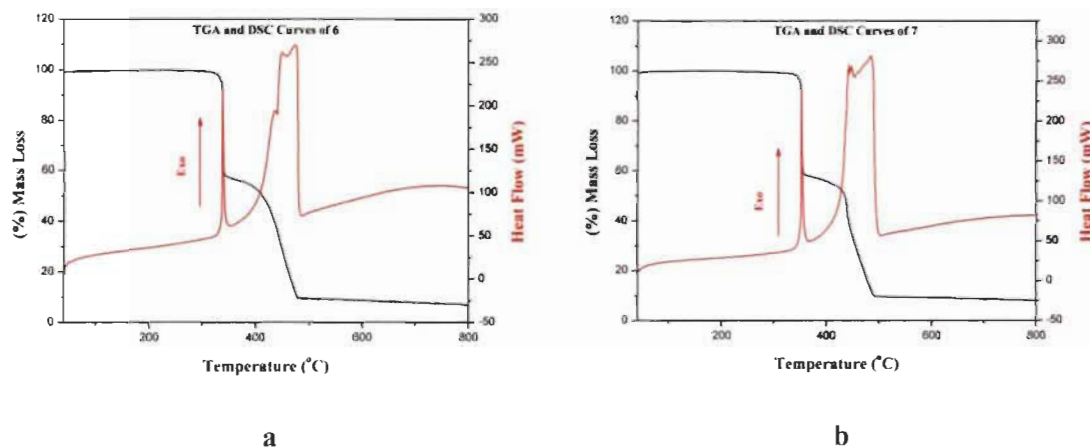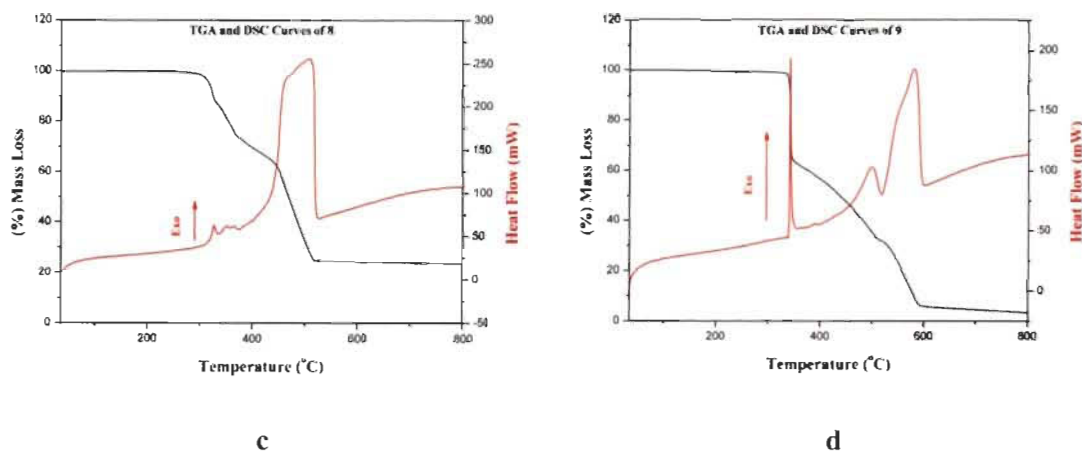
Figure 5. Thermogravimetric analysis (TGA, black) and differential scanning calorimetry (DSC, red) curves of 6–9. (a–d) 6–9, respectively.

Solid-state UV-vis spectra of **2** and **6-9** were measured at room temperature (Figure 6). The primary objective of the investigation in solid state is to correlate the absorption bands with the crystallographic data. Indeed, in liquid state, the geometry of the transition-metal complex and the oxidation state of the metal ion could be different from the single-crystal structure, which could vary the electronic transitions.

In solid state, the UV-vis spectrum of the free ligand **2** showed a strong absorption band at 320 nm, which is attributed to the n-π* and π-π* electron transitions typical of aromatic compounds. As excepted for **9**, d-d transitions centered on the metal ion are observed for **6-8**. Because the electronic configuration of Zn(II) is d^{10}, all electrons in the d orbitals are paired; therefore, d-d transitions do not occur for **9**. However, in the UV region of the spectrum of **9**, two absorption bands are observed at 321 and 331 nm. These bands can be attributed to the electronic transitions centered to the ligand. Compounds **6-8** have electronic configurations of d^7, d^8, and d^9 for Co(II), Ni(II), and Cu(II) ions, respectively. Their d orbitals are not fully occupied, which allows d-d transitions to occur.[51] In solid state, the absorption bands in the visible region of Co(pyDAT)$_2$(NO$_3$)$_2$ in **6** are situated at 560 and 478 nm, which may be assigned to $v_1[^4T_{1g}(F) \rightarrow {}^4T_{2g}(F)]$ and $v_2[^4T_{1g}(F) \rightarrow {}^4T_{1g}(P)]$ transitions, respectively, in an idealized O_h symmetry. Those of

86

Ni(pyDAT)$_2$(NO$_3$)$_2$ in **7** are at 788 and 615 nm, which could be attributed to $v_1[^3A_{2g}(F) \rightarrow {}^3T_{2g}(F)]$

and $v_2[^3A_{2g}(F) \rightarrow {}^3T_{1g}(F)]$ transitions, respectively, again in an O_h symmetry. That of

Cu(pyDAT)$_2$(NO$_3$)$_2$ in **8** is at 734 nm, which may correspond to $v_1[^2E_g(D) \rightarrow {}^2T_{2g}(D)]$ transition,

also in an O_h symmetry. All these absorption bands are consistent with the spin-allowed d-d

transitions with an octahedral environment around the metal ions. In the UV region, the absorption

bands at (327 and 360 nm), (328, 347, and 380 nm), and (325 and 372 nm) for **6-8**, respectively,

are indicative of charge-transfer transitions occurring due to the coordination of the ligands to

metal ions. Comparing the solid-state UV-vis spectrum of **2** with those of **6-9**, we notice that when

the same ligand is coordinated to different metal ions with oxidation state +II, the electronic

absorption spectra of the metallotectons varied significantly due to the coordination geometry and

the different extranuclear electron distribution of the metal ions.

Liquid UV-vis spectra of **2** and **6-9** in dimethyl sulfoxide solutions were measured at room

temperature at concentration 8.8 x 10^{-6} M (Figure S9). All spectra display similar electronic

transition in the UV region. However, the positions and the intensities of the two absorption bands

varies depending on the metal ions. In the visible region, none of the typical d-d electron transitions

are observed for **6-9**.
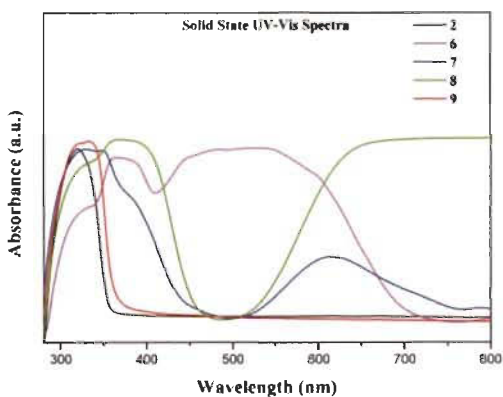
Figure 6. Solid state UV-vis spectra of **2** and **6-9**.

IR spectra were measured for samples **2** and **6-9** (Figure S10). The peak positions for each spectrum are listed in Table S6 along with their proposed assignments.

As the pyDAT molecule is coordinated to metal ions, the vibration frequencies, intensities, and shapes of the N–H, C–N, C=C, C–C, and C–H bonds could change in the infrared absorption spectra of **6-9**. Three factors, such as steric effect, field effect, and ring strain, can contribute to the spatial effect.

In the 2000-600 cm^{-1} region, several metal-sensitive bands are observed. The absorption bands between 680 and 700 cm^{-1} of **6-9** are sensitive to different metal ions. The main difference between compounds **2** and **6-9** is a strong wide band appearing near 1270-1295 cm^{-1}. This is assigned to the NO_3^- stretching vibration. In the 3500-2800 cm^{-1} region, the infrared spectra of **2** and **6-9** show typical broad bands characteristics of symmetric and asymmetric N–H stretching of the NH_2 groups. Positions and intensities of these bands in **6-9** are different from that of pyDAT, indicating different hydrogen bonding motifs of the DAT groups. The infrared spectra of **6** and **7** are almost identical. This is due to their similar crystal structures. Within the deformation region between 2000 and 600 cm^{-1}, the infrared spectrum of **9** is almost the same as those of **6** and **7**. However, in the stretch region, the absorption bands of NH_2 groups are different from those of **6** and 7. These observations can be explained by the similar spatial configuration but the different intermolecular hydrogen bonding motifs of the DAT groups of **6** and **9** (**7** and **9**, respectively). These results concur with their crystal structures. The IR spectrum of **8** shows the characteristic vibrational bands of pyDAT and nitrate counterions. The absorption bands are different from those of **6**, **7**, and **9**. This result is in good agreement with the crystallographic data.

Crystal morphology is an importance aspect for both research and industries applications as physical properties of many crystals are implicitly dependent on their shapes.[52,53] Thus, an attempt was made to understand the crystal growth of compounds **6-9**. Microscopy observation of the crystal morphologies of **6-9** was carried out by scanning electronic microscopy (SEM) (Figure

S11a-d). The calculated crystal morphology of **6-9** was obtained from the Bravais-Friedel-Donnay-Harker (BFDH) calculation method[54] using their crystal structures (Figure S11e−h). All the theoretical calculations were performed using Materials Studio 4.0.[55] Morphologies based on BFDH calculations were compared with the experimental data obtained from solution growth, showing a good correlation. Combining the calculated morphology and the crystal structure, assignment of the surface chemistry was proposed for the largest facets of crystals of **6-9** (Figure S11i−l). In the case of (**6**, **7**), and **9**, the facets (400) and (002), respectively, expose the -NH$_2$ of DAT groups on the surface at the molecular level. For crystal of **8**, the surface of facet (100) is composed of nitrate groups pointing outside. These results indicate that hydrogen bond interactions play a critical role in the crystal morphology of **6-9**.

4. Conclusions

This work demonstrates how a large range of ordered materials can be prepared using the metallotectonic approach that exploits the use of coordination bonds to metal ions as a primary directing force assisted by other strong intermolecular interactions such as hydrogen bonds. An obvious advantage of building crystalline materials from metallotectons is that they allow (i) to decrease the number of synthetic steps and (ii) to quickly obtain molecular topologies and properties not otherwise available in pure organic chemistry.

We have successfully prepared a series of crystalline materials by coordination of **2** with Co(II), Ni(II), Cu(II), and Zn(II). All compounds **6-9** were obtained in high yields as single-phase materials, as determined by XRD, PXRD, EA, and SEM. Single crystal X-ray diffraction investigations of the synthesized compounds revealed that the supramolecular networks are mainly directed by coordination and hydrogen bonds as well as by van der Waals forces. Their physical properties were characterized by UV-vis, IR, TGA, and DSC. The solid-state UV-vis absorption spectroscopy spectra of **6-9** concord with their d-d transitions. All samples exhibit high

stability under thermal conditions, as determined by TGA. The IR spectra of **6** and **7** are nearly identical, which is in agreement with the crystallographic data.

The external morphologies and crystal facets of **6-9** were measured by SEM and predicted by theoretical calculations using the BFDH method. Comparisons of experimental and calculated morphologies were in agreement, supporting the effectiveness of the BFDH method. Furthermore, the surface chemistry of crystals of **6-9** was proposed using a combination data including SEM measurement, morphology prediction, and XRD.

Our study demonstrates that properties of ordered materials can be tuned using the metallotectonic approach. The results show that the investigated approach allowed creating materials with different properties while preserving identical supramolecular architectures as exemplified with compounds **6** and **7**.

5. Experimental section

5.1. General Notes and Procedures for the Synthesis of 6-9.

6-(Pyridin-2-yl)-1,3,5-triazine-2,4-diamine **2** was synthesized by known reported methods.[44] Their complexes with Co, Ni, Cu, and Zn, respectively, were prepared by the experimental procedure described below. Other chemicals were commercially available and purchased and used without any additional purification. Solid of **2** (2.0 equiv) was added in small portions at 25 °C to the stirred solutions of $M(NO_3)_2 \cdot xH_2O$ (1 equiv) in MeOH (25 mL). The mixtures were refluxed for 12 h and the resulting homogeneous solutions were cooled to room temperature and subject to crystallization by slow diffusion with diethyl ether.

5.1.1. Compound 6.

The reaction of **2** (0.05 g, 0.2656 mmol) with $Co(NO_3)_2.6H_2O$ (0.039 g, 0.1328 mmol) according to the general procedure yielded 90 % of pink crystals of **6** with the composition of $Co(2)_2 \cdot (NO_3)_2$. FTIR (ATR): 3436.52, 3306.53, 3214.29, 3149.30, 1645.50, 1610.88, 1588.36, 1563.40, 1538.40, 1506.64, 1487.93, 1464.66, 1449.55, 1435.91, 1395.07, 1291.03, 1259.03, 1194.19, 1146.45, 1054.25, 1020.08, 989.15, 911.93, 823.05, 787.32, 748.70, 686.35 cm^{-1}. HRMS (ESI) calcd for $[C_{16}H_{16}N_{12}CoNO_3]^+$ m/z 497.0825, found 497.0831. Anal. calcd for $C_{16}H_{16}CoN_{14}O_6$: C, 34.36; H, 2.88; N, 35.06. Found: C, 34.38; H, 2.75; N, 34.78.

5.1.2. Compound 7.

The reaction of **2** (0.05 g, 0.2656 mmol) with $Ni(NO_3)_2.6H_2O$ (0.039 g, 0.1328 mmol) according to the general procedure yielded 93 % of cyan crystals of **7** with the composition of $Ni(2)_2 \cdot (NO_3)_2$. FTIR (ATR): 3437.74, 3303.23, 3215.47, 3149.30, 1646.40, 1611.10, 1589.57, 1565.29, 1538.93, 1510.46, 1489.22, 1466.07, 1436.80, 1396.94, 1291.06, 1261.01, 1197.18, 1148.01, 1054.44, 1021.71, 991.07, 822.95, 786.86, 750.28, 687.91 cm^{-1}. HRMS (ESI) calcd for $[C_{16}H_{16}N_{12}NiNO_3]^+$ m/z 496.0847, found 496.0856. Anal. calcd for $C_{16}H_{16}N_{14}NiO_6$: C, 34.37; H, 2.88; N, 35.07. Found: C, 34.63; H, 2.84; N, 34.62.

5.1.3. Compound 8.

The reaction of **2** (0.05g, 0.2656 mmol) with $Cu(NO_3)_2.2.5H_2O$ (0.031 g, 0.1328 mmol) according to the general procedure yielded 90 % blue crystals **8** with the composition of $Cu(2)_2 \cdot (NO_3)_2$. FTIR (ATR): 3461.75, 3321.61, 3205.23, 3164.44, 3061.00, 1612.35, 1589.04, 1567.94, 1519.67, 1488.64, 1447.38, 1393.23, 1315.35, 1271.13, 1057.87, 1040.90, 1016.51, 820.00, 789.50, 755.58, 719.14 cm^{-1}. HRMS (ESI) calcd for $[C_{16}H_{16}N_{12}CuNO_3]^+$ m/z 501.08951, found 501.0800. Anal. calcd for $C_{16}H_{16}CuN_{14}O_6$: C, 34.08; H, 2.86; N, 34.77. Found: C, 34.34; H, 2.85; N 34.77.

5.1.4. Compound 9.

The reaction of **2** (0.05 g, 0.2656 mmol) with $Zn(NO_3)_2 \cdot 6H_2O$ (0.039 g, 0.1328 mmol) according to the general procedure yielded 99 % colorless crystals **9** with the composition of $Zn(\mathbf{2})_2 \cdot (NO_3)_2$. FTIR (ATR): 3443.23, 3371.81, 3312.99, 3211.12, 3171.54, 3113.98, 1672.16, 1644.16, 1610.99, 1587.80, 1558.28, 1516.19, 1489.62, 1470.80, 1446.24, 1428.34, 1395.70, 1292.37, 1265.96, 1194.79, 1144.84, 1095.17, 1064.21, 1021.02, 993.41, 911.39, 824.24, 787.76, 748.94, 681.16 cm⁻¹. HRMS (ESI) calcd for $[C_{16}H_{16}N_{12}ZnNO_3]^+$ m/z 502.0785, found 502.0796. Anal. calcd for $C_{16}H_{16}N_{14}O_6Zn$: C, 33.97; H, 2.85; N, 34.66. Found: C, 33.93; H, 2.87; N, 34.39.

5.2. Instrumentation.

Crystallographic data were collected using a Bruker Venture Metaljet diffractometer with Ga Kα radiation and a Bruker APEX2 diffractometer equipped with a Cu Kα radiation from a microfocus source. The structures were solved by direct methods using SHELXT,[56] and nonhydrogen atoms were refined anisotropically with least-squares minimization.[57] Hydrogen atoms were treated by first locating them from different Fourier maps, recalculating their positions using standard values for distances and angles, and then refining them as riding atoms. Microcrystalline powders were analyzed in transmission-mode geometry using a Bruker D8-Discover instrument (θ-θ geometry) equipped with a XYZ platform and a HI-STAR gas detector. X-rays were generated using a conventional sealed-tube source with a copper anode producing Cu Kα radiation ($\lambda = 1.54178$ Å). The samples were gently ground and then mounted on a flat Kapton sample holder. The data collection involved acquisition of two different sections with increasing angular position, giving two different 2D frames. These frames were integrated and combined to produce the final one-dimensional powder X-ray diffraction pattern. Calculated powder X-ray diffraction patterns were generated from the structural data in the corresponding CIF resulting from single crystal analyses. The calculation was performed using MERCURY[58] software of the Cambridge Crystallographic

Data Center. A unique value of the full width at half maximum for the diffraction peaks was adjusted to get a better match between the resolution of the experimental and the calculated patterns. The determination of the total carbon, hydrogen, nitrogen, and sulfur (C, H, N, and S) contents in the compounds was performed using an EA 1108 Fisons CHNS Element analyzer by quantitative "dynamic flash combustion" method. The solid-state UV-vis spectra were recorded on a Cary 5000 spectrometer. The crystals are gently ground and placed on quartz holders. The ATR-FTIR spectra were collected with a Nicolet iS 10 Smart FT-IR Spectrometer within 600-4000 cm^{-1}. The thermogravimetric analysis and differential scanning calorimetry were performed simultaneously using a simultaneous thermal analysis (STA) System Setaram, model Labsys Evo STA. The samples were loaded in Al_2O_3 pans and isochronically heated from 35 to 800 °C with a heating rate of 10 °C/min. The scanning electron microscopy was performed using a Hitachi SU1510 microscope.

6. Associated Content

6.1. Supporting Information.

The Supporting Information is available free of charge on the ACS Publications website at DOI: 10.1021/acsomega.8b03517. Diffraction patterns, photographs of the samples, scanning electron microscopy images, liquid UV-vis, and IR spectra (PDF).

CCDC 1566407-1566410; crystallographic details (including thermal atomic displacement ellipsoid plots) (CIF) (CIF) (CIF) (CIF).

6.2. Author information

Corresponding Author

*E-mail: adam.duong@uqtr.ca.

ORCID id

Thierry Maris: 0000-0001-9731-4046

Adam Duong: 0000-0002-4927-3603

Present Address

Fellow of the Canadian Queen Elizabeth II Diamond Jubilee Scholarships (S.R. and M.M.).

Notes

The authors declare no competing financial interest.

7. References

(1) Serrano, D. P.; Coronado, J. M.; Víctor, A.; Pizarro, P.; Botas, J. Á. Advances in the design of ordered mesoporous materials for low-carbon catalytic hydrogen production. *J. Mater. Chem. A* **2013**, *1*, 12016-12027.

(2) Lee, D. Y.; Shinde, D. V.; Yoon, S. J.; Cho, K. N.; Lee, W.; Shrestha, N. K.; Han, S.-H. Cu-Based Metal-Organic Frameworks for Photovoltaic Application. *J. Phys. Chem. C* **2014**, *118*, 16328-16334.

(3) Hausbrand, R.; Cherkashinin, G.; Ehrenberg, H.; Gröting, M.; Albe, K.; Hess, C.; Jaegermann, W. Fundamental degradation mechanisms of layered oxide Li-ion battery cathode materials: Methodology, insights and novel approaches. *Mater. Sci. Eng., B* **2015**, *192*, 3-25.

(4) Han, Y.-F.; Yuan, Y.-X; Wang, H.-B. Porous Hydrogen-Bonded Organic Frameworks. *Molecules* **2017**, *22*, 266.

(5) Brunet, P.; Simard, M.; Wuest, J. D. Molecular Tectonics. Porous Hydrogen-Bonded Networks with Unprecedented Structural Integrity. *J. Am. Chem. Soc.* **1997**, *119*, 2737-2738.

(6) El Garah, M.; Marets, N.; Mauro, M.; Aliprandi, A.; Bonacchi, S.; De Cola, L.; Ciesielski, A.; Bulach, V.; Hosseini, M. W.; Samori, P. Nanopatterning of Surfaces with Monometallic and Heterobimetallic 1D Coordination Polymers: A Molecular Tectonics Approach at the Solid/Liquid Interface. *J. Am. Chem. Soc.* **2015**, *137*, 8450-8459.

(7) Rigby, N.; Jacobs, T.; Reddy, J. P.; Hardie, M. J. Metal Complexes of 2,2'-Bipyridine-4,4'-diamine as Metallo-Tectons for Hydrogen Bonded Networks. *Cryst. Growth Des.* **2012**, *12*, 1871-1881.

(8) Stefanou, V.; Matiadis, D.; Tsironis, D.; Igglessi-Markopoulou, O.; McKee, V.; Markopoulos, J. Synthesis and single crystal X-ray diffraction studies of coumarin-based Zn(II) and Mn(II) complexes, involving supramolecular interactions. *Polyhedron* **2018**, *141*, 289-295.

(9) Wang, X.; Gao, C.-Q.; Gao, Z.-Y.; Wu, B.-L.; Niu, Y.-Y. Synthesis, crystallographic and spectral studies of homochiral cobalt(II) and nickel(II) complexes of a new terpyridylaminoacid ligand. *J. Mol. Struct.* **2018**, *1157*, 355-363.

(10) Chen, P.; Du, L.; Zhou, J.; Qiao, Y.; Li, B.; Zhao, Q. Four complexes with triazine derivative and terephthalate: synthesis, structures, and luminescent, magnetic properties. *Chin. J. Inorg. Chem.* **2014**, *30*, 1038-1044.

(11) Williams, B. N.; Huang, W.; Miller, K. L.; Diaconescu, P. L. Group 3 Metal Complexes of Radical-Anionic 2,2'-Bipyridyl Ligands. *Inorg. Chem.* **2010**, *49*, 11493-11498.

(12) Irwin, M.; Jenkins, R. K.; Denning, M. S.; Kramer, T.; Grandjean, ̈F.; Long, G. J.; Herchel, R.; McGrady, J. E.; Goicoechea, J. M. Experimental and Computational Study of the Structural and Electronic Properties of $Fe^{II}(2,2'\text{-bipyridine})(mes)_2$ and $[Fe^{II}(2,2'\text{-bipyridine})(mes)_2]^{\cdot}$, a Complex Containing a 2,2'-Bipyridyl Radical Anion. *Inorg. Chem.* **2010**, *49*, 6160-6171.

(13) Larsen, R. W.; Wojtas, L. Photoinduced inter-cavity electron transfer between Ru(II)tris(2,2'-bipyridne) and Co(II)tris(2,2'-bipyridine) Co-encapsulated within a Zn(II)-trimesic acid metal organic framework. *J. Mater. Chem. A* **2013**, *1*, 14133-14139.

(14) Petkova, E. G.; Lampeka, R. D.; Gorichko, M. V.; Palamarchuk, G.; Dyakonenko, V. V.; Zubatyuk, R. I.; Shishkin, O. V. Copper(II), Nickel(II), Cobalt(II), and Chromium(III) Complexes Based on 6,6'- Bis{[methyl(oxido)imino]methyl}-2,2'-bipyridine. *Z. Naturforsch., B* **2008**, *63*, 841-847.

(15) Bellusci, A.; Crispini, A.; Pucci, D.; Szerb, E. I.; Ghedini, M. Structural Variations in Bipyridine Silver(I) Complexes: Role of the Substituents and Counterions. *Cryst. Growth Des.* **2008**, *8*, 3114-3122.

(16) La Porte, N. T.; Martinez, J. F.; Hedström, S.; Rudshteyn, B.; Phelan, B. T.; Mauck, C. M.; Young, R. M.; Batista, V. S.; Wasielewski, M. R. Photoinduced electron transfer from rylenediimide radical anions and dianions to $Re(bpy)(CO)_3$ using red and near-infrared light. *Chem. Sci.* **2017**, *8*, 3821-3831.

(17) Clark, M. L.; Grice, K. A.; Moore, C. E.; Rheingold, A. L.; Kubiak, C. P. Electrocatalytic CO_2 reduction by M(bpy-R)(CO)$_4$ (M = Mo, W; R = H, tBu) complexes. Electrochemical, spectroscopic, and computational studies and comparison with group 7 catalysts. *Chem. Sci.* **2014**, *5*, 1894-1900.

(18) Wu, G. G.; Wong, Y.; Poirier, M. Novel 2,2′-Bipyridine Ligand for Palladium-Catalyzed Regioselective Carbonylation. *Org. Lett.* **1999**, *1*, 745-747.

(19) Kawahara, R.; Fujita, K.-I.; Yamaguchi, R. Dehydrogenative Oxidation of Alcohols in Aqueous Media Using Water-Soluble and Reusable Cp*Ir Catalysts Bearing a Functional Bipyridine Ligand. *J. Am. Chem. Soc.* **2012**, *134*, 3643-3646.

(20) Bindra, G. S.; Schulz, M.; Paul, A.; Soman, S.; Groarke, R.; Inglis, J.; Pryce, M. T.; Browne, W. R.; Rau, S.; Maclean, B. J.; Vos, J. G. The effect of peripheral bipyridine ligands on the photocatalytic hydrogen production activity of Ru/Pd catalysts. *Dalton Trans.* **2011**, *40*, 10812-10814.

(21) Kavallieratos, K.; Rosenberg, J. M.; Bryan, J. C. Pb(II) Coordination and Synergistic Ion-Exchange Extraction by Combinations of Sulfonamide Chelates and 2,2′-Bipyridine. *Inorg. Chem.* **2005**, *44*, 2573-2575.

(22) Malkov, A. V.; Pernazza, D.; Bell, M.; Bella, M.; Massa, A.; Teply, F.; Meghani, P.; Kocovsky, P. Synthesis of New Chiral 2,2′-Bipyridine Ligands and Their Application in Copper-Catalyzed Asymmetric Allylic Oxidation and Cyclopropanation. *J. Org. Chem.* **2003**, *68*, 4727-4742.

(23) Kaes, C.; Katz, A.; Hosseini, M. W. Bipyridine: The Most Widely Used Ligand. A Review of Molecules Comprising at Least Two 2,2′- Bipyridine Units. *Chem. Rev.* **2000**, *100*, 3553-3590.

(24) Duong, A.; Maris, T.; Wuest, J. D. Using Pyridinyl-Substituted Diaminotriazines to Bind Pd(II) and Create Metallotectons for Engineering Hydrogen-Bonded Crystals. *Inorg. Chem.* **2011**, *50*, 5605-5618.

(25) Wu, J.; Jung, J.; Zhang, P.; Zhang, H.; Tang, J.; Le Guennic, B. Cis-trans isomerism modulates the magnetic relaxation of dysprosium single-molecule magnets. *Chem. Sci.* **2016**, *7*, 3632-3639.

(26) Duan, R.-R.; Ou, Z.-B.; Wang, W.; Chen, S.; Zhou, X.-H. Synthesis, crystal structures, photoluminescence properties and DNA binding of triazine-nickel(II) complexes for DNA detection. *Spectrochim. Acta, Part A* **2015**, *151*, 64-71.

(27) Duan, R.-R.; Wang, L.; Huo, W.-Q.; Chen, S.; Zhou, X.-H. Synthesis, characterization, and DNA binding of two copper (II) complexes as DNA fluorescent probes. *J. Coord. Chem.* **2014**, *67*, 2765-2782.

(28) Li, J.-Y.; Xie, M.-J.; Jiang, J.; Chang, Q.-W.; Ye, Q.-S.; Liu, W.-P.; Chen, J.-L.; Ning, P. Synthesis and Crystal Structure of Two Polydimensional Molecular Architectures from Cobalt(II), Copper(II) Complexes of 2,4-Diamino-6-pyridyl-1,3,5-triazine. *Asian J. Chem.* **2014**, *26*, 419.

(29) Busto, N.; Valladolid, J.; Aliende, C.; Jalon, F. A.; Manzano, B. R.; Rodríguez, A. M.; Gaspar, J. F.; Martins, C.; Biver, T.; Espino, G.; Leal, J. M. Preparation of Organometallic Ruthenium-Arene-Diaminotriazine Complexes as Binding Agents to DNA. *Chem. - Asian J.* **2012**, *7*, 788-801.

(30) Zhao, Q. H.; Fan, A. L.; Li, L. N.; Xie, M. Diazidobis[2,4-diamino-6-(2-pyridyl)-1,3,5-triazine-κ2 N1,N6]zinc(II). *Acta Crystallogr., Sect. E: Struct. Rep. Online* **2009**, *65*, m622.

(31) Maly, K. E.; Gagnon, E.; Maris, T.; Wuest, J. D. Engineering Hydrogen-Bonded Molecular Crystals Built from Derivatives of Hexaphenylbenzene and Related Compounds. *J. Am. Chem. Soc.* **2007**, *129*, 4306-4322.

(32) Duong, A.; Metivaud, V.; Maris, T.; Wuest, J. D. Surrogates of 2,2'-Bipyridine Designed to Chelate Ag(I) and Create Metallotectons for Engineering Hydrogen-Bonded Crystals. *Cryst. Growth Des.* **2011**, *11*, 2026-2034.

(33) Telfer, S. G.; Wuest, J. D. Metallotectons: Comparison of Molecular Networks Built from Racemic and Enantiomerically Pure Tris(dipyrrinato)cobalt(III) Complexes. *Cryst. Growth Des.* **2009**, *9*, 1923-1931.

(34) Li, K.; Tong, G. S.; Wan, Q.; Cheng, G.; Tong, W.-Y.; Ang, W.-H.; Kwong, W.-L.; Che, C.-M. Highly phosphorescent platinum (II) emitters: photophysics, materials and biological applications. *Chem. Sci.* **2016**, *7*, 1653-1673.

(35) Leung, C.-H.; Lin, S.; Zhong, H.-J.; Ma, D.-L. Metal complexes as potential modulators of inflammatory and autoimmune responses. *Chem. Sci.* **2015**, *6*, 871-884.

(36) Singla, P.; Luxami, V.; Paul, K. Triazine as a promising scaffold for its versatile biological behavior. *Eur. J. Med. Chem.* **2015**, *102*, 39-57.

(37) Corbo, R.; Georgiou, D. C.; Wilson, D. J.; Dutton, J. L. Reactions of [PhI(pyridine)$_2$]$^{2+}$ with Model Pd and Pt II/IV Redox Couples. *Inorg. Chem.* **2014**, *53*, 1690-1698.

(38) Fernandez-Moreira, V.; Marzo, I.; Gimeno, M. C. Luminescent Re(I) and Re(I)/Au(I) complexes as cooperative partners in cell imaging and cancer therapy. *Chem. Sci.* **2014**, *5*, 4434-4446.

(39) Ji, S.; Wu, W.; Wu, W.; Song, P.; Han, K.; Wang, Z.; Liu, S.; Guo, H.; Zhao, J. Tuning the luminescence lifetimes of ruthenium(II) polypyridine complexes and its application in luminescent oxygen sensing. *J. Mater. Chem.* **2010**, *20*, 1953-1963.

(40) Mooibroek, T. J.; Gamez, P. The s-triazine ring, a remarkable unit to generate supramolecular interactions. *Inorg. Chim. Acta* **2007**, *360*, 381-404.

(41) Gamez, P.; Reedijk, J. 1,3,5-Triazine-Based Synthons in Supramolecular Chemistry. *Eur. J. Inorg. Chem.* **2006**, *2006*, 29-42.

(42) Alcock, N. W.; Bartlett, P. N.; Eastwick-Field, V. M.; Pike, G. A.; Pringle, P. G. Reinvestigation of the nickel phosphine catalysed electrochemical synthesis of poly(2,5-pyridine). X-Ray crystal structures of [$Ni_2Br_2(\mu$-5-BrC$_5$H$_3$N-C^2, N)$_2$(PPh$_3$)$_2$] and [PtBr(5-BrC$_5$H$_3$N-C^2)(PPh$_3$)$_2$]. *J. Mater. Chem.* **1991**, *1*, 569-576.

(43) Cushman, M.; Nagarathnam, D.; Gopal, D.; Geahlen, R. L. Synthesis and evaluation of new protein-tyrosine kinase inhibitors. Part 1. pyridine-containing stilbenes and amides. *Bioorg. Med. Chem. Lett.* **1991**, *1*, 211-214.

(44) Case, F. H.; Koft, E. The Synthesis of Certain Substituted 1,3,5- Triazines Containing the Ferroin Group. *J. Am. Chem. Soc.* **1959**, *81*, 905-906.

(45) Zheng, Y.-Q.; Lin, J.-L. Crystal structure of bis(2,2'-bipyridineN,N')nitratocobalt(II) nitrate pentahydrate, [Co(2,2'-bpy)$_2$(NO$_3$)]-NO$_3$. 5H$_2$O. *Z. Kristallogr. New Cryst. Struct.* **2002**, *217*, 331-332.

(46) Murphy, B.; Aljabri, M.; Ahmed, A. M.; Murphy, G.; Hathaway, B. J.; Light, M. E.; Geilbrich, T.; Hursthouse, M. B. Structural systematics of the [Cu(chelate)3][Y]2 series. An interesting crystallographic structural insight involving vibronic coupling and the Jahn-Teller effect (JTE). The syntheses and low temperature crystal structures of tris(2,2'-bipyridyl)copper(II)

tetraphenylborate and tris(2,2'-bipyridyl)zinc(II) tetraphenylborate. *Dalton Trans.* **2006**, **2**, 357-367.

(47) Meyer, A.; Schnakenburg, G.; Glaum, R.; Schiemann, O. Bis(terpyridine))copper(II) Tetraphenylborate: A Complex Example for the Jahn-Teller Effect. *Inorg. Chem.* **2015**, *54*, 8456-8464.

(48) Nakai, H. The Crystal Structure of Bis(2,2'-bipyridine)-nitratocopper(II) Nitrate Monohydrate [Cu(NO₃)(bpy)₂]NO₃.H₂O. *Bull. Chem. Soc. Jpn.* **1980**, *53*, 1321-1326.

(49) Zhou, L. Crystal structure of bis(2,2'-bipyridine-N,N')-(nitrato-O)zinc(II) nitrate monohydrate, [Zn(C₁₀H₈N₂)(NO₃)][NO₃]. H₂O. *Z. Kristallogr. New Cryst. Struct.* **2011**, *226*, 27-28.

(50) Zhao, Q.-H.; Fan, A.-L.; Li, L.-N.; Xie, M.-J. The Crystal Structure of Bis(2,2'-bipyridine)nitratocopper(II) Nitrate Monohydrate [Cu(NO₃)(bpy)₂]NO₃·H₂O. *Acta Crystallogr., Sect. E: Struct. Rep. Online* **2009**, *65*, m622.

(51) Woolley, R. Ligand-field analysis of transition-metal complexes. *Int. Rev. Phys. Chem.* **1987**, *6*, 93-141.

(52) Rohl, A. L. Computer prediction of crystal morphology. *Curr. Opin. Solid State Mater. Sci.* **2003**, *7*, 21-26.

(53) Long, C. X.; Zhang, L. J.; Qian, Y. Preparation and Crystal Modification of Ibuprofen-Loaded Solid Lipid Microparticles. *Chin. J. Chem. Eng.* **2006**, *14*, 518-525.

(54) Berkovitch-Yellin, Z. Toward an ab initio derivation of crystal morphology. *J. Am. Chem. Soc.* **1985**, *107*, 8239-8253.

(55) *Materials Studio 4.0;* Accelrys Software Inc.: San Diego, CA, 2005.

(56) Sheldrick, G. M. *SHELXT*-Integrated space-group and crystal-structure determination. *Acta Crystallogr., Sect. A: Found. Adv.* **2015**, *71*, 3-8.

(57) Sheldrick, G. M. Crystal structure refinement with S*HELXL. Acta Crystallogr., Sect. C: Struct. Chem.* **2015**, *71*, 3-8.

(58) Macrae, C. F.; Bruno, I. J.; Chisholm, J. A.; Edgington, P. R.; McCabe, P.; Pidcock, E.; Rodriguez-Monge, L.; Taylor, R.; van de Streek, J.; Wood, P. A. Mercury CSD 2.0 - new features for the visualization and investigation of crystal structures. *J. Appl. Crystallogr.* **2008**, *41*, 466-470.

2.4. Conclusions

Our work illustrates the synthesis of ordered materials using the strategy of metallotectons, that employs the utilization of coordination bonds to metal ions as a main conducting force along with strong intermolecular interactions such as hydrogen bonds. The advantage of building crystalline materials by the strategy of metallotectons is that (i) it allows us to prepare supra molecules with less number of synthetic steps, (ii) the raw materials used for the synthesis of these molecules are comparatively less expensive as compared to other molecules, (iii) the yield of the products is usually very high and (iv) it allows us to obtain molecules with topologies and properties that are not available in pure organic chemistry. We have successfully prepared a sequence of crystalline materials by coordination of **2** with Co(II), Ni(II), Cu(II), and Zn(II). All compounds **6-9** are easy to obtain, in very high yields and as single-phase materials as determined by SC-XRD, PXRD, EA, and SEM. The crystal structure of **6** was isostructural with the crystal structure of **7**. All samples exhibit high stability up to ~ 300 °C, as determined by TGA. This project demonstrates the tuning of properties of materials and the synthesis of diverse supramolecular networks by employing metallotectonic approach.

2.5. Supporting Information

Contents		Page

1. X-ray Crystallographic data

Figure S1. Thermal atomic displacement ellipsoid plot of the structure of **6** grown from MeOH/Et₂O. The ellipsoids of non-hydrogen atoms are drawn at 50% probability level, and hydrogen atoms are represented by a sphere of arbitrary size.
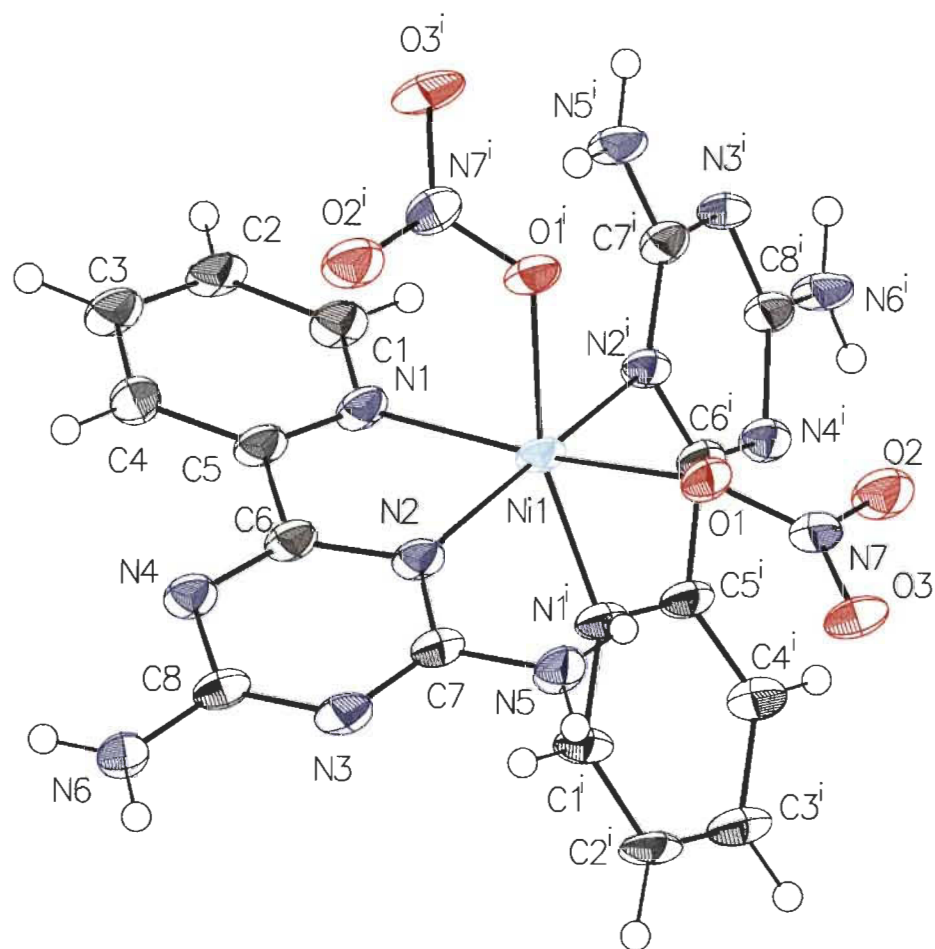
Figure S2. Thermal atomic displacement ellipsoid plot of the structure of **7** grown from MeOH/Et$_2$O. The ellipsoids of non-hydrogen atoms are drawn at 50% probability level, and hydrogen atoms are represented by a sphere of arbitrary size.
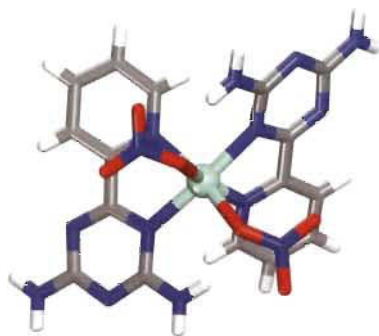
a
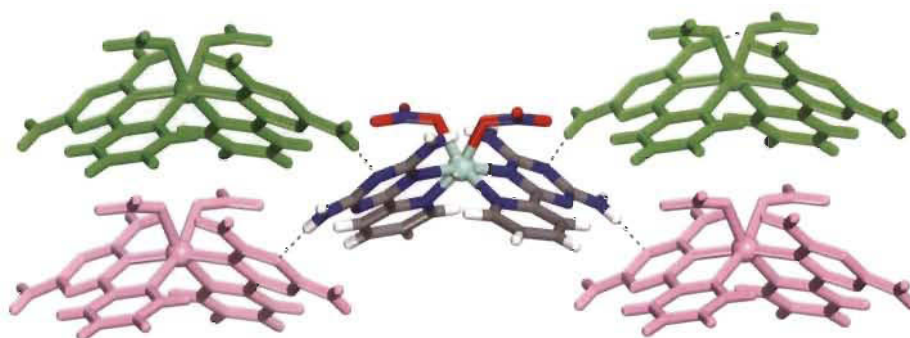
b

Figure S3. Views of the crystal structure of **7** grown from MeOH/Et$_2$O. Hydrogen bonds are represented by dashed lines. Unless stated otherwise, carbon atoms are shown in grey, hydrogen atoms in white, oxygen atoms in red, nitrogen atoms in blue and nickel atoms in cyan. (a) Structure of the metallotecton **7** and (b) Alternating of enantiomeric metallotectons of 6 joined by N-H...N hydrogen bonds of DAT groups according to motif **IV** to produce the three-dimensional network. For clarity few metallotectons are marked in green and pink.
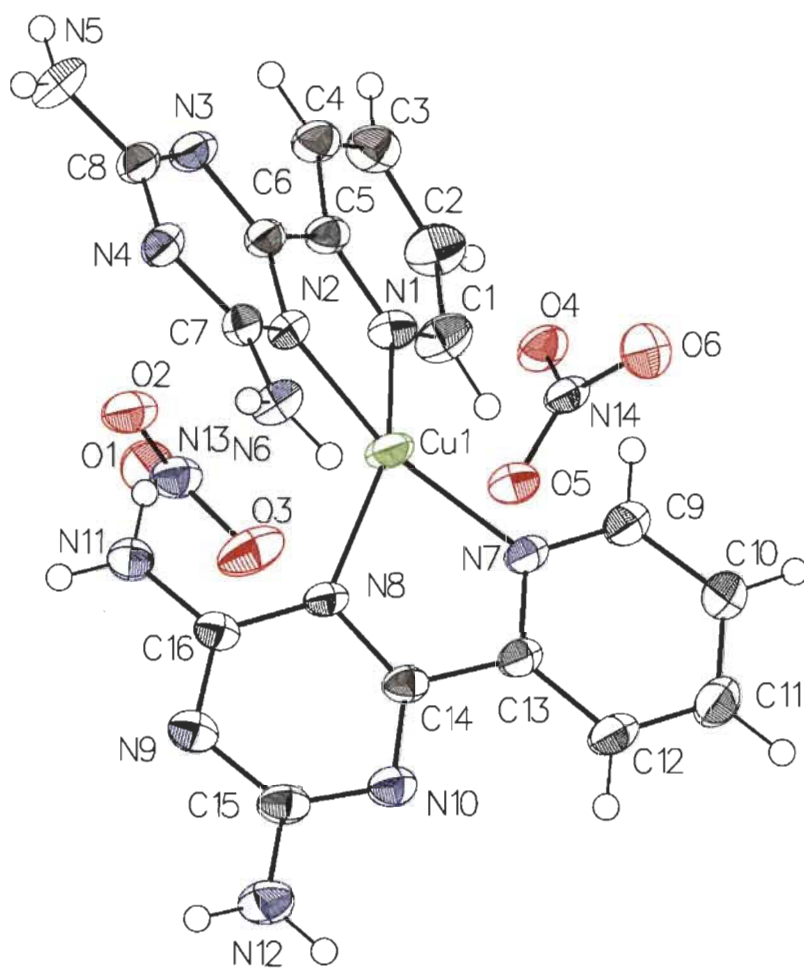
Figure S4. Thermal atomic displacement ellipsoid plot of the structure of **8** grown from Et₂O/MeOH. The ellipsoids of non-hydrogen atoms are drawn at 50% probability level, and hydrogen atoms are represented by a sphere of arbitrary size.
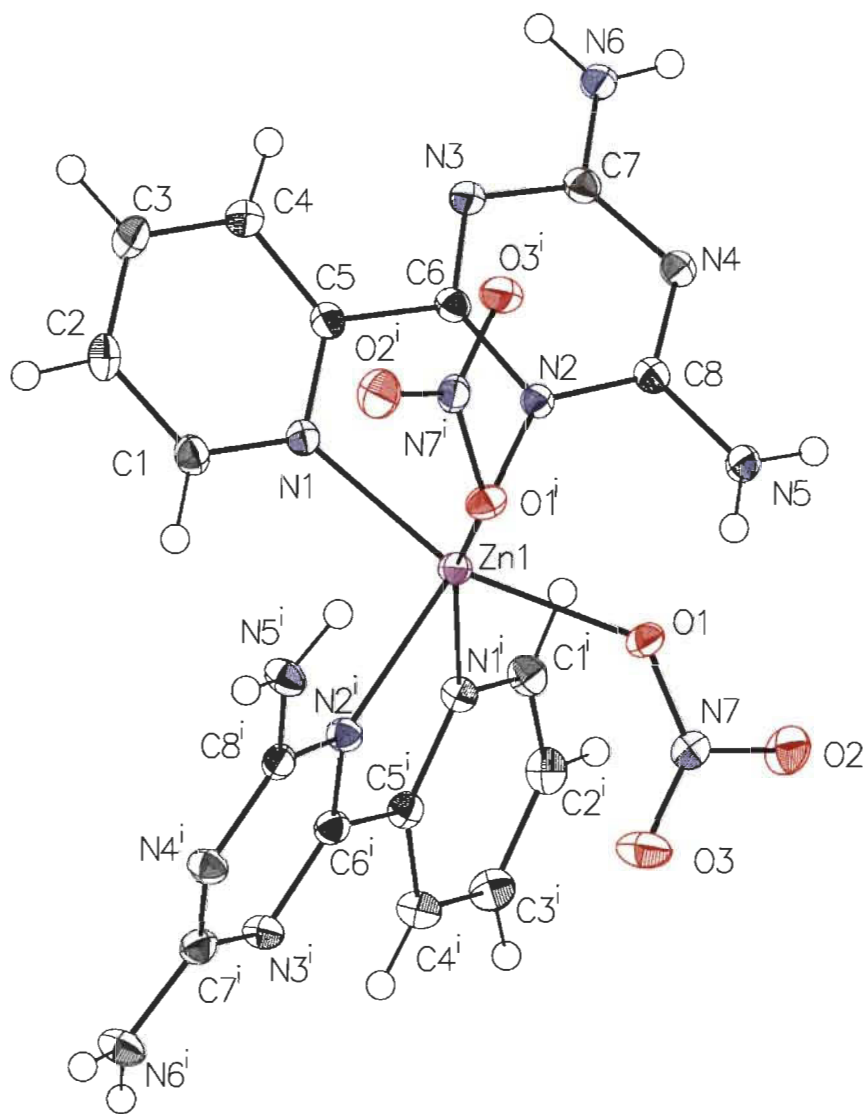
Figure S5. Thermal atomic displacement ellipsoid plot of the structure of **9** grown from MeOH. The ellipsoids of non-hydrogen atoms are drawn at 50% probability level, and hydrogen atoms are represented by a sphere of arbitrary size.

Table S1. Hydrogen-bond geometry (Å, °) in structure of **6**

$D—H \cdots A$	$D—H$	$H \cdots A$	$D \cdots A$	$D—H \cdots A$
N5—H5$A \cdots$O2^{i}	0.88	2.12	2.992 (5)	174
N5—H5$B \cdots$O1	0.88	2.09	2.917 (4)	156
N5—H5$B \cdots$O2	0.88	2.43	3.204 (5)	147
N5—H5$B \cdots$N7	0.88	2.59	3.469 (5)	173
N6—H6$A \cdots$O3^{ii}	0.88	2.31	3.068 (5)	144
N6—H6$B \cdots$N3^{iii}	0.88	2.25	3.104 (5)	164
C2—H2$\cdots$O1^{iv}	0.95	2.45	3.281 (5)	146

Symmetry codes: (i) $-x+3/2, -y+5/2, z$; (ii) $x-1/4, -y+9/4, z-1/4$; (iii) $-x+5/4, y-1/4, z-1/4$;

(iv) $-x+3/2, -y+1, z-1/2$.

Table S2. Hydrogen-bond geometry (Å, °) in structure of **7**

$D—H \cdots A$	$D—H$	$H \cdots A$	$D \cdots A$	$D—H \cdots A$
N5—H5$A \cdots$O3^{i}	0.88	2.12	2.996 (7)	173
N5—H5$B \cdots$O1	0.88	2.04	2.866 (7)	155
N5—H5$B \cdots$O3	0.88	2.45	3.238 (7)	149
N5—H5$B \cdots$N7	0.88	2.58	3.459 (7)	173
N6—H6$A \cdots$O2^{ii}	0.88	2.32	3.071 (7)	143
N6—H6$B \cdots$N3^{iii}	0.88	2.26	3.113 (7)	165
C1—H1$\cdots$N2^{iv}	0.95	2.65	3.210 (8)	118
C2—H2$\cdots$O1^{v}	0.95	2.46	3.300 (8)	148

Symmetry codes: (i) $-x+1, -y+2, z$; (ii) $x+1/4, -y+7/4, z-1/4$; (iii) $-x+5/4, y-1/4, z-1/4$;

(iv) $-x+1, -y+1, z$; (v) $-x+1, -y+1/2, z-1/2$.

Table S3. Hydrogen-bond geometry (Å, °) in structure of **8**

$D—H \cdots A$	$D—H$	$H \cdots A$	$D \cdots A$	$D—H \cdots A$
N5—H5$A \cdots$N9^{i}	0.88	2.12	2.987 (6)	167
N5—H5$B \cdots$O1^{ii}	0.88	2.22	2.914 (5)	136

N6—H6A···O6^{iii}	0.88	2.05	2.913 (5)	167
N6—H6B···N8	0.88	2.62	3.238 (5)	128
N6—H6B···O5	0.88	2.14	2.889 (5)	142
N11—H11A···O1^{iv}	0.88	2.03	2.872 (5)	160
N11—H11A···N13^{iv}	0.88	2.68	3.355 (5)	134
N11—H11B···N2	0.88	2.53	3.184 (5)	131
N11—H11B···O2	0.88	2.16	2.899 (5)	142
N12—H12A···N4^{v}	0.88	2.28	3.159 (5)	172
N12—H12B···O4^{vi}	0.88	2.30	3.032 (5)	141
N12—H12B···O6^{vii}	0.88	2.43	2.988 (5)	122
C1—H1···O1^{viii}	0.95	2.42	3.079 (6)	126

Symmetry codes: (i) $x, -y+5/2, z-1/2$; (ii) $-x+1, y+1/2, -z+1/2$; (iii) $-x+2, -y+2, -z+1$; (iv) $-x+1, -y+2, -z+1$; (v) $x, -y+5/2, z+1/2$; (vi) $x, -y+3/2, z+1/2$; (vii) $-x+2, y+1/2, -z+3/2$; (viii) $-x+1, -y+1, -z+1$.

Table S4. Hydrogen-bond geometry (Å, °) in structure of **9**

D—H···A	D—H	H···A	D···A	D—H···A
N6—H6A···O3^{i}	0.84 (2)	2.18 (2)	2.9817 (19)	159 (2)
C2—H2···O1^{ii}	0.96 (2)	2.49 (2)	3.3270 (19)	145.3 (16)
N6—H6B···N4^{iii}	0.85 (2)	2.17 (2)	3.019 (2)	172 (2)
N5—H5A···O1	0.86 (2)	2.10 (2)	2.9066 (18)	156.0 (19)
N5—H5A···O2	0.86 (2)	2.42 (2)	3.1687 (18)	145.4 (18)
N5—H5A···N7	0.86 (2)	2.61 (2)	3.4591 (19)	166.9 (18)
N5—H5B···O2^{iv}	0.84 (2)	2.17 (2)	2.9837 (18)	163.1 (19)

Symmetry codes: (i) $x, -y+1, z-1/2$; (ii) $-x+3/2, y+1/2, -z+3/2$; (iii) $-x, -y+1, -z+1$; (iv) $-x, y, -z+3/2$
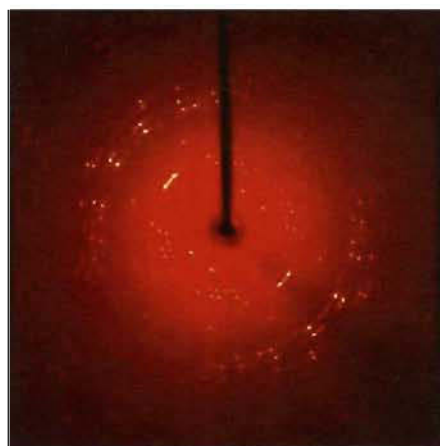
a
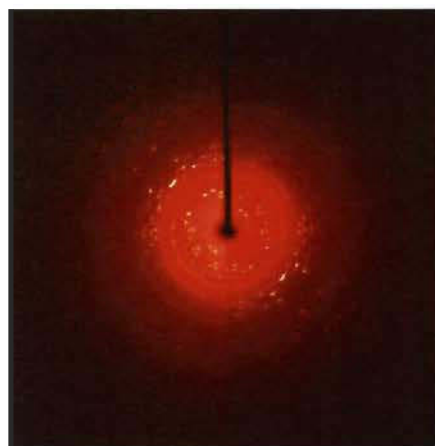
b

c
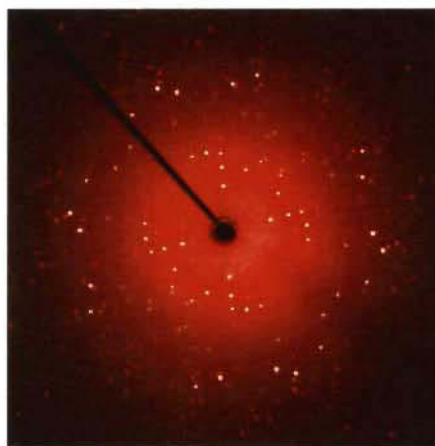
d

Figure S6. a)-d) Diffraction patterns (recorded with a 360° phi rotation) of single-crystals of **6-9** respectively

2. Crystal colors

| 6 | 7 | 8 | 9 |
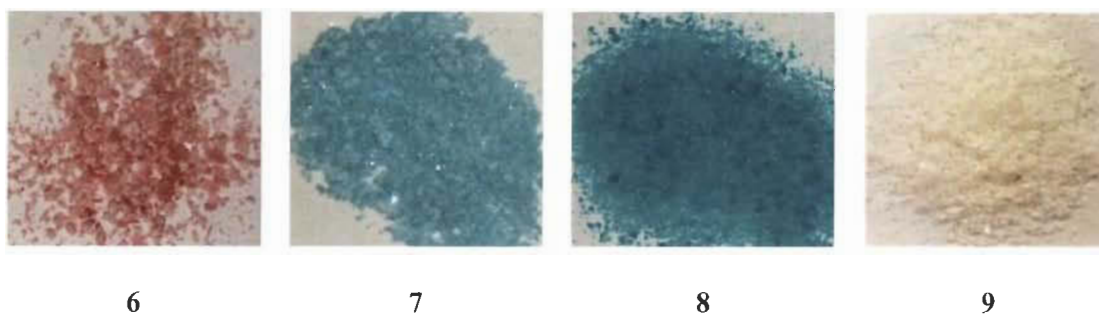
Figure S7. Photographs of bulk crystals showing the colours of **6-9**.

3. Crystal morphologies

a

b

c

d
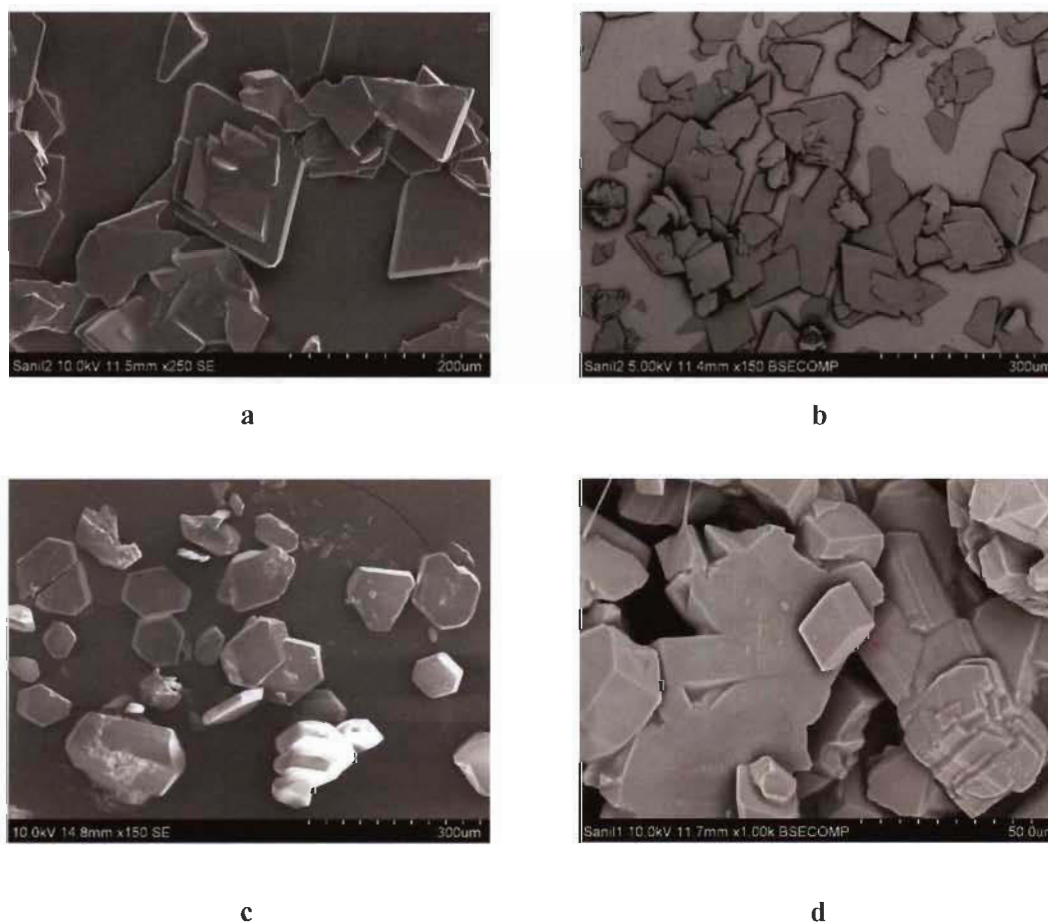
Figure S8. a)-d) SEM images of crystals of **6-9** respectively.

4. Thermal analysis

Table S5. Summary of temperature ranges, percentage mass losses during the decomposition of **6-9** determined by TGA

Sample	Step	Temperature range/°C	DSC	%/Mass loss found (calc.)	Assignment[a]
6	I	337-416	exo	44.4 (44.7)	NO_3^- + pyDAT
	II	416-480	-	44.3 (44.7)	NO_3^- + pyDAT
	residue		-	10.3 (10.6)	-
7	I	350-430	exo	44.3 (44.7)	NO_3^- + pyDAT
	II	430-482	-	44.7 (44.7)	NO_3^- + pyDAT
	residue		-	9.7 (10.6)	-
8	I	300-346	exo	12.7 (11.0)	NO_3^-
	II	346-449	-	13.1 (11.0)	NO_3^-
	III	449-517	-	49.4 (-)	-
	residue		-	24.8 (-)	-
9	I	345-453	exo	34.3 (33.3)	pyDAT
	II	453-532	-	33.8 (33.3)	pyDAT
	III	532-592	-	25.4 (22.0)	2 x NO_3^-
	residue		-	7.4 (11.4)	-

[a] PyDAT: tectoligand **2**; NO_3^-: nitrate

5. Liquid UV-Vis spectroscopy
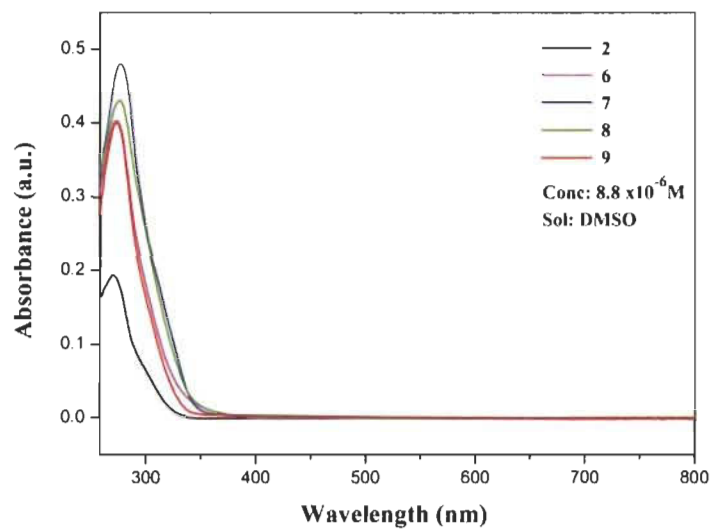
Figure S9. Liquid UV-Vis spectra of **2** and **6-9**

6. Infrared spectroscopy
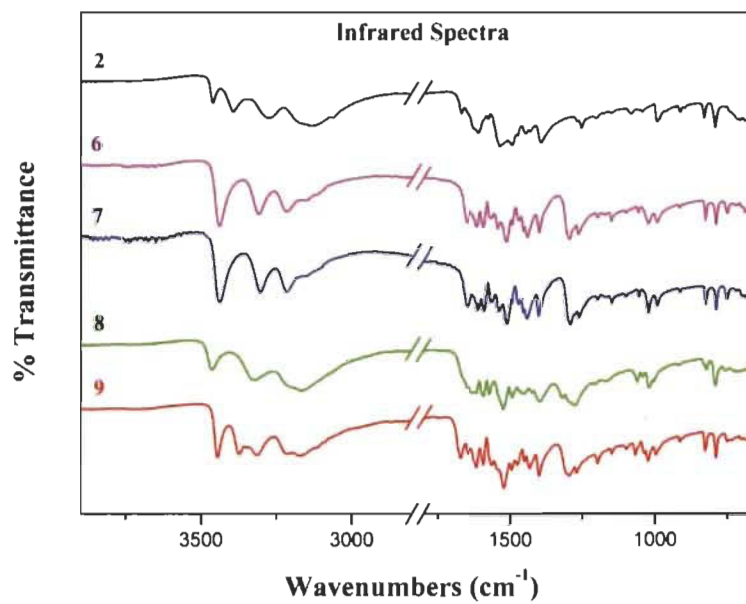
Figure S10. Infrared spectra of **2** and **6-9**

Table S6. IR data and assignments of tectoligand **2** and **6-9**[a]

2	6	7	8	9	Assignment
					$\tilde{\nu}$/cm^{-1}
			667vw		
			676vw		
686m	686w	687w		681w	
		697w	699w	699w	Ring breathing, δ(NH$_2$)
705w			708w		
	716vw	718vw	719w	714w	
				732w	
	748w	750w	755w	748w	
792s	787m	786m	789s	787s	Ring out-of-plane def., γ(C-H)
830m	823m	822m	820s	824s	Ring out-of-plane def.
913w	911w	913w	914w	911w	
993m	989m	991m	1000w	993m	Ring breathing, ρ(NH$_2$)
1043w	1020m	1021m	1016m	1021m	Ring def.
	1054w	1054w	1040w	1033w	
1082w	1097w	1099w	1057m	1064m	δ(C-H), δ(N-H)
1153w	1146w	1148w		1144w	
	1168w	1167w	1163w		
1203w	1194w	1197w	1201w	1194m	δ(C-H)
1253m	1259s	1261s	1315m	1265s	ν(C-N)
	1291s	1291s	1271s	1292s	ν(NO$_3^-$)
1393s	1395s	1396s	1393s	1395s	δ(C-H)
	1435s	1436s	1418w	1428m	
1446w	1449w	1450w	1447w	1446w	ν(C-N), δ(NH$_2$)
	1464w	1466w	1462w	1470w	
1494s	1487w	1489m	1488m	1489w	Ring breathing, ν(C-N), δ(C-H),
	1506s	1510w	1519s	1516s	δ(C-N)

1576s	1538w	1538w		1537w	
	1563w	1565w	1567m	1558w	Ring breathing, ν(C-C), ν(C-N)
	1588m	1589m	1589m	1587s	
1612m	1610m	1611m	1612m		
1668w	1645m	1646m	1625m	1644w	δ(NH$_2$)
	1651m	1651m	1651w	1672m	
3063vw			3067vw	3111w	ν(C-H)
3131s	3146w	3146w	3164s	3172s	
3274m	3214m	3215m	3213w	3209s	ν(N-H)
3394m	3306m	3303m	3321m	3312s	
3461m	3436s	3437s	3461m	3444s	

[a]Abbreviation used for the type of vibration mode. def.: deformation; δ: bending vibration; ν: stretching vibration; ρ: rocking vibration.

7. Crystal Morphology prediction using BFDH method

a

b

e

f

i
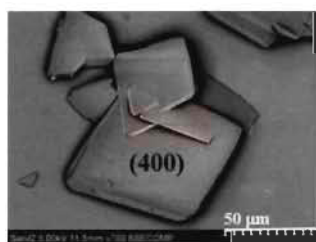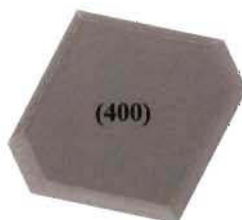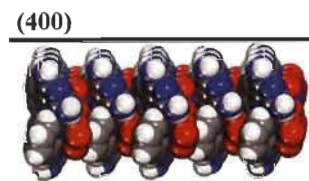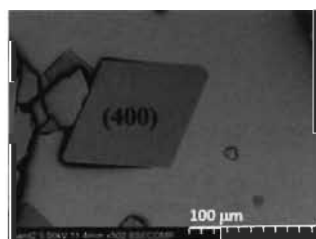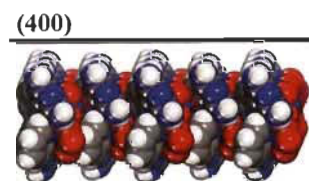
j
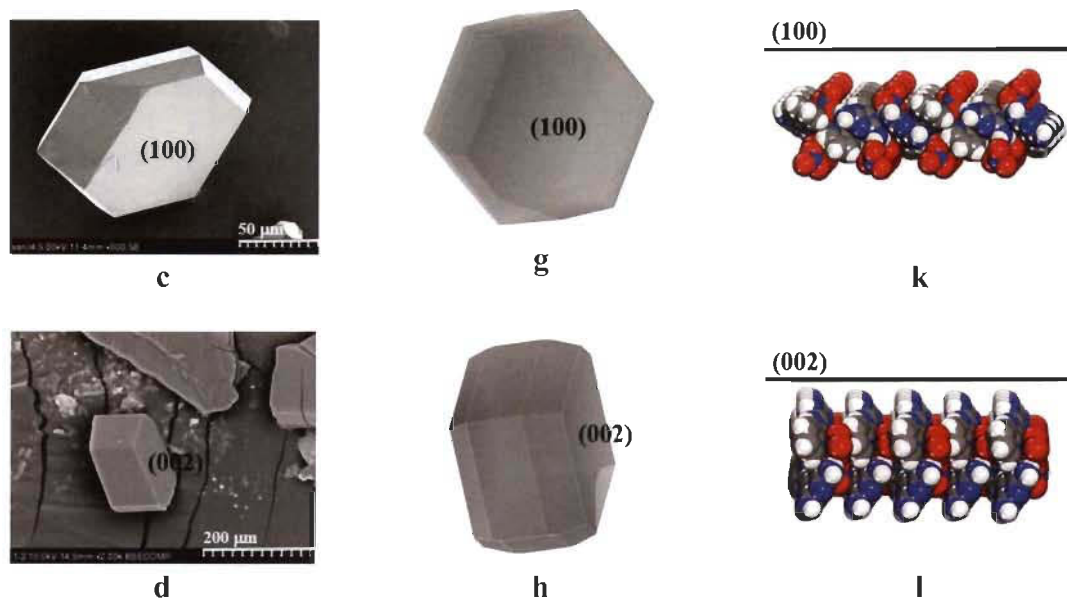
Figure S11. Experimental and calculated morphology of **6-9**. (a)-(d) SEM of **6-9** respectively, (e)-(h) predicted crystal morphology from BFDH model of **6-9** respectively and (i)-(l) Side view of the molecular arrangements of facets with Miller index (400), (100) and (002) for **6-9** respectively.The solid line represents the crystal face.

Chapter 3

Synthesis, Crystal Structure, Characterization of Pyrazine Diaminotriazine based Complexes and their Systematic Comparative Study with Pyridyl Diaminotriazine based Complexes for Light-Driven Hydrogen Production

3.1. Introduction

Taking inspiration from natural photosynthesis, solar energy can be stored in high-density chemical bonds of hydrogen molecules. A sunlight-triggered hydrogen evolution reaction (HER) is an interesting alternative to produce pure hydrogen and has emerged as an important solution to subdue the ongoing depletion of fossil fuels and to control environmental pollution. Currently, the major concern associated with this application is, the preparation of novel and efficient catalysts to convert the abundant and inexhaustible solar energy into chemical energy. Although various MOFs, COFs and HOFs have been utilized as photocatalysts towards HER as discussed in the introduction, only a few of them are effective in terms of the cost associated to the synthetic procedure. Metal-organic complexes with incorporated DAT groups have an ability to undergo hydrogen bonding *via* self-assembly. The metallotecton approach has been used as before with a different tectoligand *viz.* pyrazine DAT to produce a series of transition metal complexes. The effect of change of tectoligand on the photocatalytic efficiency of the synthesized complexes towards HER has been carried out.

3.2. Article 2

Synthesis, Crystal Structure, Characterization of Pyrazine Diaminotriazine based Complexes and their Systematic Comparative Study with Pyridyl Diaminotriazine based Complexes for Light-Driven Hydrogen Production

Sanil Rajak, Olivier Schott, Prabhjyot Kaur, Thierry Maris, Garry S. Hanan, Adam Duong*

3.3. Author's Contribution

Sanil Rajak: Investigation, conceptualization, methodology, synthesis and characterization, photo catalytic testing, electrochemical analysis, interpretation of results and writing of the article.

Olivier Schott: Mentoring, conceptualization, methodology, interpretation of results.

Dr. Prabhjyot Kaur: Writing- review and editing.

Dr. Thierry Maris: Crystallographic data analysis.

Prof. Garry S. Hanan: Co-supervision, conceptualization, methodology.

Prof. Adam Duong: Supervision, finding financial supports, project administration, conceptualization, interpretation of results, writing- review and editing.

1. Abstract

The present world has a dire need to increase its energy input in order to meet with the demands of growing population. Combining the most abundant renewable energy source such as sunlight with a clean fuel having the capacity to store and carry renewable energy viz. hydrogen is a promising alternative to control the detrimental effects of fossil fuels on our environment. A sunlight-triggered hydrogen evolution reaction (HER) would be an interesting approach for the production of pure hydrogen. Working towards this direction, we have synthesized complexes **8-10** by the reaction of 6-(pyrazin-2-yl)-1,3,5-triazine-2,4-diamine (PzDAT), with Co(II), Ni(II) and Cu(II) respectively. As indicated by single-crystal X-ray diffraction, the molecular organization of all the complexes is mainly dictated by the coordination modes of the ligands and the hydrogen bonds involving the DAT groups with reliable patterns. In conjunction with the synthesis and characterization, we investigated and compared the catalytic activities for HER of **8-10** with **5-7** (complexes of pyridine DAT (PyDAT) with Co(II), Ni(II) and Cu(II)) that we have reported previously. In the presence of triethanolamine (TEOA) as the sacrificial electron donor, $Ru^{(II)}(bpy)_3(PF_6)_2$ as the photosensitizer (PS) and aqueous HBF_4 as the proton source under blue light, the highest turnover number amongst **5-10** is observed for PyDAT copper complex **7** with TON of 72 mol of hydrogen per mole of PS. This value is higher compared to some Cu complexes reported in literature.

2. Introduction

The ever-increasing human population demands equally increasing energy resources. Until now fossil fuels have been the world's primary energy resource. However, their growing utility has caused a detrimental effect on our environment [1-3]. In order to achieve a balance with our environment, the dependency on fossil fuels needs to be reduced. This can be done by increasing our dependency on renewable and environmentally friendly energy resources and finding a possible substitute for fossil fuels [4-7]. Among the diverse renewable energy resources, sunlight is the predominant one which has the potential to fulfil all our energy demands. Hydrogen is a possible future alternative to fossil fuels as it is a clean fuel that can be used in near future to store renewable energy. Hence, sunlight and hydrogen are two clean and pollution free energy source and carrier, respectively, which can be combined to meet the present-day energy crisis and other environmental issues [8-10]. Taking inspiration from natural photosynthesis, solar energy can be stored in high-density chemical bonds of hydrogen molecules. A sunlight-triggered hydrogen evolution reaction (HER) would be an interesting alternative to produce pure hydrogen.

Currently, one of the key challenges for HER is the development of efficient catalysts. Many of the studies reported so far have used platinum group metal viz. Pt [11], Rh [12], Ir [13, 14] based complexes as catalysts and PSs for hydrogen evolution. However, photocatalysts based on first row transition metals are also being increasingly explored because of their low cost and good electrochemical stability. Although previously, researchers have used these low-cost metals viz. Co, Ni, Cu, Zn [15-19] as PSs and catalysts for H_2 production, there is an ever increasing need to synthesize more efficient and better improved catalytic systems for HER [20-23].

Considering the potential of transition metal complexes as catalysts for hydrogen production, we synthesized and studied the photocatalytic activity of complexes **5-10** which comprise of Co(II), Ni(II) and Cu(II) transition metals (denoted by M) in M(2,2'-bipy)$_2$(NO$_3$)$_2$ framework functionalized with a diaminotriazinyl (DAT) and a pyrazinyl group by replacing one or two

pyridyl rings (Chart 1). DAT-substituted pyridine and pyrazine complexes are called as tectoligands (2 and 3) and their self-assembly with metal ions forms metallotectons [24,25]. The main advantages associated with the synthesis of coordination complexes using tectoligands are facile synthetic route and predictable intermolecular hydrogen bonding interactions along with simultaneous binding with metal ions to produce reliable patterns (Chart 2) [24,26-31].

1 (2,2'-bipy)   2 (pyDAT)   3 (pzDAT)

4

5. M = Co(II)
6. M = Ni(II)
7. M = Cu(II)

8. M = Co(II)
9. M = Ni(II)
10. M = Cu(II)
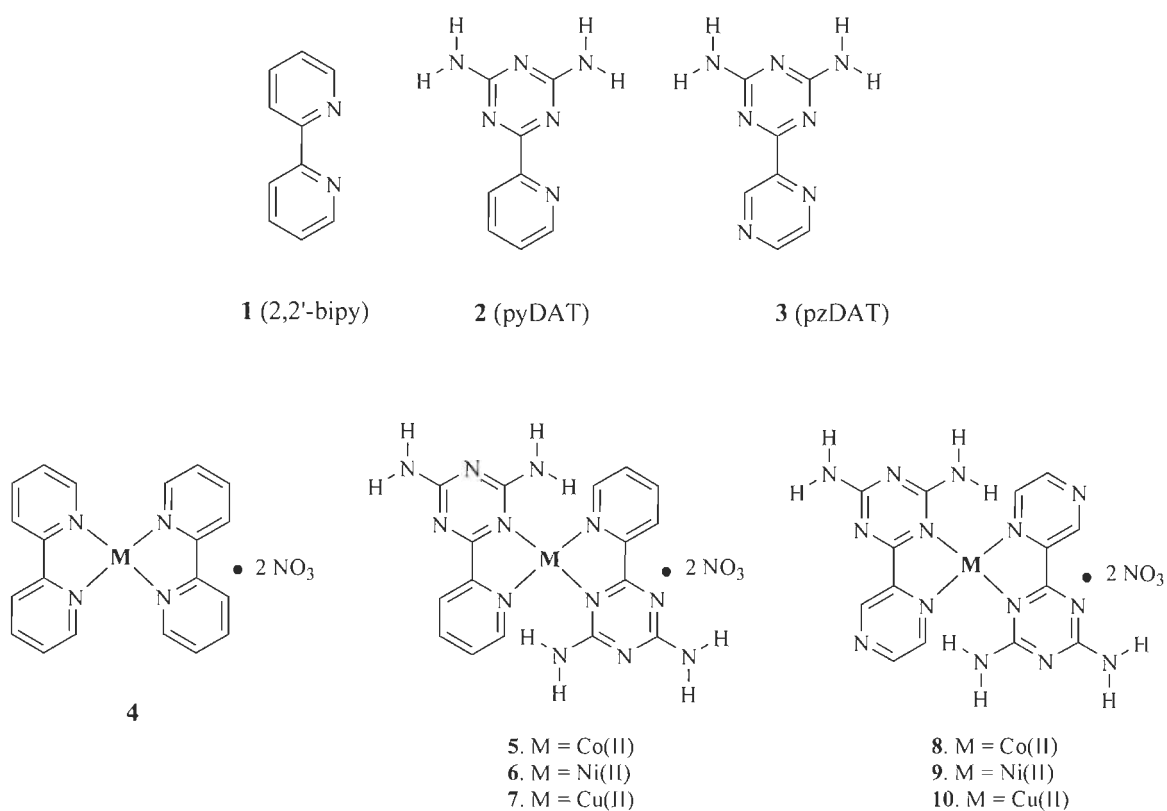
Chart 1. Molecular structure of ligands 1-3 and complexes 4-10.

The investigation to prepare functionalized catalysts is an important task in order to modify their properties. Herein, we focus our work on the design, synthesis and characterization of DAT functionalized complexes 8-10 which are easy to obtain. As part of our ongoing research in the area of energy application, we studied and compared the catalytic activities of 5-10 for HER

125

[32,33]. In this work, along with the design and characterization of PzDAT complexes, a systematic comparative photocatalytic study of six complexes comprised of DAT groups (three PzDAT and three PyDAT) towards hydrogen evolution reaction has been presented.

3. Experimental section

3.1. General notes and procedures for the synthesis of complexes 8-10

6-Pyridin-2-yl-[1,3,5]-triazine-2,4-diamine ligand **2**, 6-pyrazin-2-yl-[1,3,5]-triazine-2,4-diamine ligand **3** and complexes **5-7** were synthesized by reported methods [34-36]. Complexes **8-10** were prepared by the experimental procedure described below. Other chemicals were commercially available, purchased and used without any additional purification. A solid sample of ligand **3** (2.0 equiv) was added in small portions at 25 °C to the stirred solutions of $M(NO_3)_2$. xH_2O (1 equiv) in MeOH (25 mL). The mixtures were refluxed for 12 h and the resulting homogeneous solutions were cooled to room temperature and subjected to crystallization by slow diffusion with diethyl ether.

3.1.1. Compound 8.

The reaction of ligand **3** (0.05 g, 0.2644 mmol) with $Co(NO_3)_2$. $6H_2O$ (0.038 g, 0.1322 mmol) according to the general procedure yielded 87 % of pink crystals of complex **8** with the composition $Co(3)_2(NO_3)_2$. FTIR (ATR): 3450.61, 3392.94, 3318.76, 3224.71, 3170.05, 1672.10, 1653.75, 1641.17, 1598.87, 1576.29, 1540.28, 1503.21, 1484.83, 1451.17, 1429.80, 1372.96, 1289.24, 1271.33, 1196.52, 1175.07, 1160.91, 1066.92, 1038.76, 1013.13, 989.38, 954.49, 910.94, 847.18, 824.22, 808.43, 770.55, 737.13, 697.28 cm^{-1}. HRMS (ESI) for $[C_{14}H_{14}N_{15}O_3Co]^+$ m/e 499.0732, found 499.0731. Anal. calcd for $C_{14}H_{14}CoN_{16}O_6$: C, 29.96; H, 2.51; N, 39.93. Found: C, 30.05; H, 2.25; N, 39.40.

3.1.2. Compound 9.

The reaction of ligand **3** (0.05 g, 0.2644 mmol) with $Ni(NO_3)_2.6H_2O$ (0.038 g, 0.1322 mmol) according to the general procedure yielded 90 % of cyan crystals of complex **9** with the composition $[Ni(3)_2(MeOH)(NO_3)].NO_3$. FTIR (ATR): 3427.54, 3383.71, 3330.85, 3158.68, 1662.55, 1622.82, 1602.10, 1574.52, 1515.64, 1486.09, 1459.67, 1378.07, 1277.62, 1212.06, 1175.03, 1166.50, 1043.71, 1014.14, 995.70, 914.10, 850.20, 807.10, 771.26, 731.53 cm^{-1}. HRMS (ESI) for $[C_{14}H_{14}N_{15}O_3Ni]^+$ m/e calcd 498.0765, found 498.052. Anal. calcd for $C_{15}H_{18}N_{16}NiO_7$: C, 30.38; H, 3.06; N, 37.79. Found: C, 29.82; H, 2.67; N, 38.12.

3.1.3. Compound 10.

The reaction of ligand **3** (0.05 g, 0.2644 mmol) with $Cu(NO_3)_2.2.5H_2O$ (0.030 g, 0.1322 mmol) according to the general procedure yielded 92 % green crystals of complex **10** with the composition $Cu(3)_2(NO_3)_2$. FTIR (ATR): 3481.68, 3403.44, 3321.96, 3221.84, 3150.14, 1653.76, 1617.58, 1580.80, 1559.45, 1507.24, 1486.40, 1462.61, 1429.85, 1375.55, 1295.82, 1279.38, 1205.88, 1178.18, 1157.85, 1064.20, 1041.40, 994.75, 954.68, 944.62, 911.26, 871.13, 830.49, 818.92, 804.82, 714.27 cm^{-1}. HRMS (ESI) for $[C_{14}H_{14}N_{15}O_3Cu]^+$ m/e calcd for 503.0800, found 503.0684. Anal. calcd for $C_{14}H_{14}CuN_{14}O_6$: C, 29.71; H, 2.49; N, 39.60. Found: C, 29.98; H, 2.50; N 39.41.

3.2. Instrumentation

Crystallographic data were collected using a Bruker Venture Metaljet diffractometer with Ga Kα radiation. The structures were solved by intrinsic phasing using SHELXT [37], and non-hydrogen atoms were refined anisotropically with least-squares minimization [37]. Hydrogen atoms were treated by first locating them from different Fourier maps, recalculating their positions using standard values for distances and angles, and then refining them as riding atoms. Microcrystalline powders were analyzed in transmission mode geometry using a Bruker D8-Discover instrument (θ-θ geometry) equipped with a XYZ platform and a HI-STAR gas detector. X-rays were

generated using a conventional sealed-tube source with a copper anode producing Cu Kα radiation (λ = 1.54178 Å). The samples were gently ground and then mounted on a flat Kapton sample holder. The data collection involved acquisition of two different sections with increasing angular position, giving two different 2D frames. These frames were integrated and combined to produce the final one-dimensional powder X-ray diffraction pattern. Calculated powder X-ray diffraction patterns were generated from the structural data in the corresponding CIF resulting from single crystal analyses. The calculation was performed using MERCURY [38] software of the Cambridge Crystallographic Data Center. A unique value of the full width at half maximum for the diffraction peaks was adjusted to get a better match between the resolution of the experimental and the calculated patterns. The determination of the total carbon, hydrogen, nitrogen and sulfur (C, H, N, and S) contents in the compounds was performed by using EA 1108 Fisons CHNS Element analyser by quantitative "dynamic flash combustion" method. The UV-Vis spectra were recorded on a Cary 5000 spectrometer. The ATR-FTIR spectra were collected with a Nicolet iS 10 Smart FT-IR Spectrometer within 600-4000 cm^{-1}. The thermogravimetric analysis was performed using Mettler Toledo TGA Instrument at 10 °C/min, under N_2 gas.

3.3. Electrochemical measurements

Electrochemical measurements were performed with a BAS SP-50 potentiostat, in pure dimethylformamide purged with nitrogen at room temperature. Glassy carbon electrode was used as a working electrode, the counter electrode was a Pt wire and silver wire was the pseudo-reference electrode. The reference of electrochemical potential was set using 1 mM ferrocene as an internal standard and the values of potentials are reported vs SCE [39]. The concentrations of samples were 1 mM. Tetrabutylammonium hexafluorophosphate (TBAP) (0.1 M) was used as supporting electrolyte. Cyclic voltammograms were obtained at a scan rate of 100 mV/s and current amplitude of 100 mA.

3.4. Photocatalytic experiments

A PerkinElmer Clarus-480 gas chromatograph (GC) was used to measure hydrogen evolution for our complexes. The assembly of this chromatograph consists of a thermal conductivity detector, a 7-inch HayeSep N 60/80 pre-column, a 9-inch molecular sieve 13*45/60 column, a 2 mL injection loop and argon gas as carrier and eluent. DMF was the solvent of choice for our experiments. Three separate solutions of 1) sacrificial donor and proton source, 2) photosensitizer $[Ru(bpy)_3]$ $(PF_6)_2$ and 3) catalyst were prepared in order to obtain 5 mL of sample solutions in standard 20 mL headspace vials. In DMF, the resulting molar concentration of photocatalytic components were: 1 M for triethanolamine (TEOA), 0.1 M for HBF_4 (proton source), 0.56 M for water, 0.1 mM for the photosensitizer $[Ru(bpy)_3](PF_6)_2$ and 1 mM catalysts (pH apparent = 8, 9). (Aqueous HBF_4 solution acts as the proton source and TEOA as the sacrificial electron donor). This was followed by placing the vials on a panel of blue LED 10 W center at 445 nm in a thermostatic bath set at 20 °C which was sealed with a rubber septum and two stainless-steel tubes pierced in it. Argon was carried in the first tube at a flow rate of 10 mL.min^{-1} (flow rate adjusted with a manual flow controller (Porter, 1000) and referenced with a digital flowmeter (Perkin Elmer Flow Mark)). The second stainless steel tube carried the flow to the GC sample loop passing through a 2 mL overflow protection vial and an 8-port stream select valve (VICCI). Timed injections were done by a microprocessor (Arduino Uno) coupled with a custom PC interface. Corresponding to a specific argon flow, H_2 production rate was calibrated. For calibration of H_2 production rate at a specific argon flow, a syringe pump (New Era Pump) equipped with a gas-tight syringe (SGE) and a 26s-gauge needle (Hamilton) was used to bubble different rates of pure hydrogen gas into the sample, to a minimum of 0.5 μL/minute. For calibration testing, stock cylinders of known concentration of H_2 in argon replaced the argon flow (inserted at the pre-bubbler, to keep the same vapor matrix). The measured results independent of flow rate (under

same pressure) can be easily converted into the rate of hydrogen using Eq. (1). The errors associated to the TON and TOF are estimated to be 10 % [40].

Equation 1

Rate of production of H_2 (μL min^{-1}) = [H_2 standard] (ppm) x Ar flow rate (L min^{-1})

4. Results and discussion

In comparison to a pyridine ring, the DAT group present in our synthesized compounds consists of a triazinyl ring and two -NH_2 groups. Located in ortho position of a coordination site, the DAT group can participate by binding with metal ions to produce functionalized transition metal complexes. As the catalytic properties can be severely altered depending upon the metal ion used and the functional groups attached to the catalysts, we examined the effect of DAT group for HER. We have previously reported the synthesis and the characterization of compounds $M(PyDAT)_2(NO_3)_2$ **5-7** obtained by coordination of 6-(pyridin-2-yl)-1,3,5-triazine-2,4-diamine (PyDAT) with earth-abundant metal ions (M = Co(II), Ni(II) and Cu(II)).[34] These complexes can be prepared easily in high yield and purity (Chart 1). Herein, we discuss the synthesis and the structural study of three novel complexes **8-10** obtained by the reaction of 6-(pyrazin-2-yl)-1,3,5-triazine-2,4-diamine (PzDAT) with Co^{II}, Ni^{II} and Cu^{II}. Moreover, we have studied the physicochemical properties of complexes **5-10** by thermogravimetric analysis (TGA), UV-Vis, infrared and cyclic voltammetry (CV). In this work, we also investigated the catalytic activities of **5-10** for HER.

4.1. Structural analysis and characterization of complexes 8-10

Based on the coordination of 2,2'-bipy and related bidentate ligands, we expect ligand **3** to yield well established coordination motifs with transition metal ions and to further associate in solid-

state by hydrogen bonding of DAT groups (Chart 2) to generate crystalline molecular materials. Complexes **8-10** were obtained by mixing ligand **3** (2 equiv) with $M(NO_3)_2.x(H_2O)$ (1 equiv) in methanol and purified by crystallization. Analyses by electrospray ionization mass spectrometry (ESI-MS) measurements confirm the presence of the metal ions in the complexes with the masses and isotope distribution patterns corresponding to that of $[M(pzDAT)_2(NO_3)]^+$ for complexes **8-10**. The infrared spectra of **8-10** (Fig. S3) indicate the presence of the ligand **3** with typical broad bands characteristic of symmetric and asymmetric N-H stretching of the NH_2 group between 3500 and 3200 cm^{-1}. The band appearing between 1300 and 1200 cm^{-1} that is not observed in the IR spectrum of the free ligand is assigned to NO_3^- group (Table S1). The compositions confirmed by elemental analysis (EA) for the samples are $M(pzDAT)_2(NO_3)_2$ for complexes **8** and **10** and $M(pzDAT)_2(MeOH)(NO_3)_2$ for complex **9** (see experimental section). Except for **8**, we have studied the molecular organization in solid state by single-crystal X-ray diffraction (SCXRD).
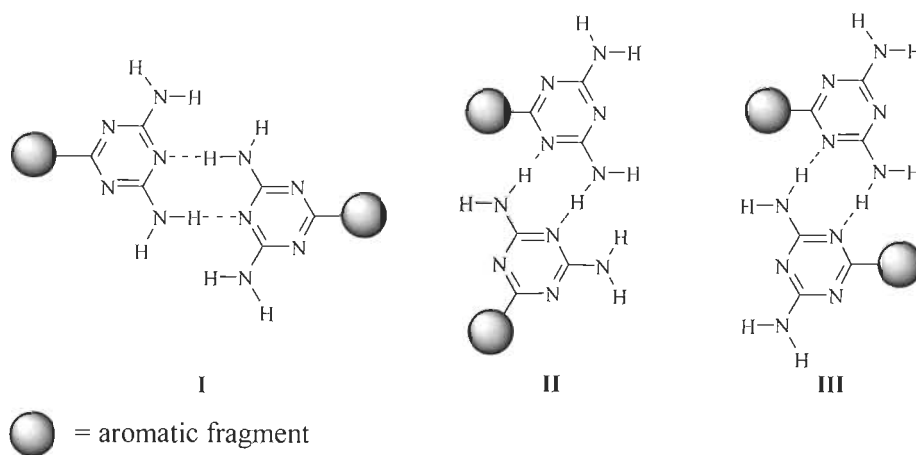
Chart 2. Cyclic hydrogen bonding motifs **I-III** of diamino-1,3,5-triazinyl group (DAT).

4.1.1. Structure of 6-(pyridin-2-yl)-1,3,5-triazine-2,4-diamine 2 with M(NO₃)₂.6(H₂O) (Complexes 5-7, M = Co(II), Ni(II) or Cu(II))

In the previous work, we have reported the single-crystal structures of compounds **5-7** [34]. In order to facilitate a comparison of these known structures with new ones we summarized succinctly their supramolecular organization. Molecular structures of **5-7** are shown in Fig. 1. The chemical compositions of **5-7**, with 2:1 pyDAT-to-M ratio, are $M(PyDAT)_2(NO_3)_2$ (M = Co(II), Ni(II) or Cu(II)). Isostructural crystal structures were determined for **5** and **6** by single-crystal X-ray diffraction. A strongly distorted octahedral coordination geometry was observed for complexes **5-7**. The observed structures of **5-7** consist of enantiomeric metallotectons that are linked alternatively *via* N−H···N hydrogen bonds of DAT groups to produce the three-dimensional supramolecular networks.

a   b
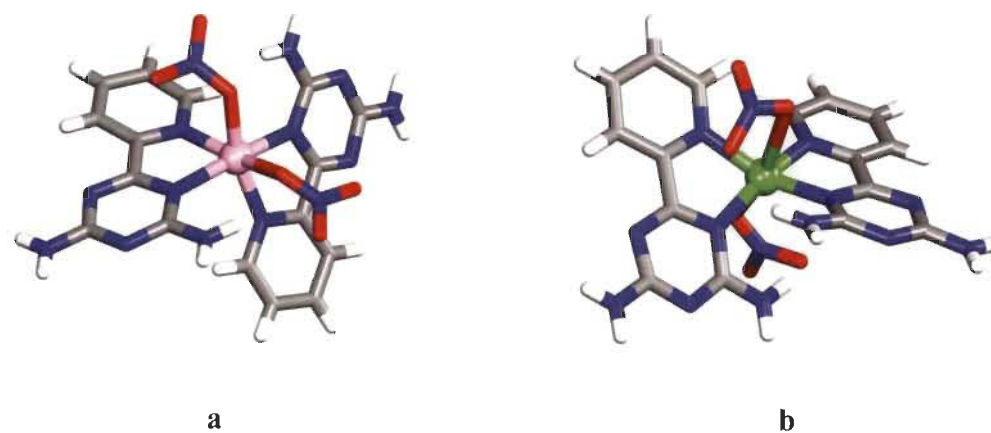
Fig. 1. Molecular structures of (a) **5** and **6** and (b) **7**. Unless stated otherwise, carbon atoms are shown in grey, hydrogen atoms in white, oxygen atoms in red, nitrogen atoms in blue, cobalt or nickel atoms in pink and copper atoms in green.

4.1.2. Structure of 6-(pyrazin-2-yl)-1,3,5-triazine-2,4-diamine 3 with Ni(NO₃)₂.6(H₂O) (Complex 9)

Ligand 3 chelates with Ni(II) in the ratio 2:1 to form a cationic complex 9. Crystals of this complex are grown in MeOH/Et₂O and belong to the triclinic space group $P\bar{1}$. Perspective views of the crystal structure are shown in Fig. 2 and other crystallographic data is provided in Table 1. As expected, the pyrazinyl-substituted diaminotriazine ligand 3 reacts with Ni(II) to form a mononuclear complex, which then engages in multiple hydrogen bonding directed in part by the DAT groups resulting in [Ni(PzDAT)₂(NO₃)(MeOH)].(NO₃) structure for complex 9 (Fig. S1). Ni(II) displays a distorted octahedral coordination geometry with the two DAT groups in trans conformation, and the nitrato and methanol in cis conformation. The Ni atom and one pair of coordinated N atoms from different DAT groups gives a N–Ni–N angle of 169.3(2)°. The other coordinated pair of N atoms of pyridine rings has N–Ni–N angle of 96.6(1)°. The pyrazinyl and DAT rings of one of the ligand is nearly coplanar and the other is distorted at an angle of 14.1(1)°. As anticipated, DAT groups engage in intermolecular N–H···N hydrogen bonding according to type I (Chart 2) (average distance = 3.058 Å) to produce tapes of alternating complexes (Δ and λ) (Fig. 2a). These tapes are further connected to form the three-dimensional structure by multiple hydrogen bonds involving bridging of nitrate and N–H···O_methanol (Fig. 2b). Selected hydrogen bonds and angles are given in Table S2. It is worth noticing that intramolecular N–H···O hydrogen bonds involving the free hydrogen atom from -NH₂ group and oxygen atom from methanol reinforce the geometry of coordination of the complex. Moreover, the observed structure reflects intra- and inter-complex interactions which are strongly directed by the multiple hydrogen bonds involving DAT groups and nitrate counterions. However, unpredictably, a methanol molecule is coordinated to the nickel atom during the crystallization process.

| | a | b |
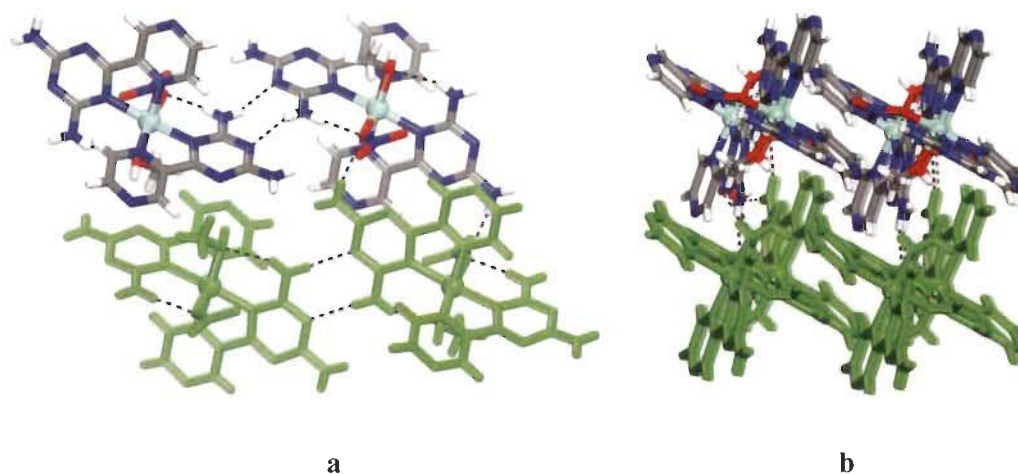
Fig. 2. Views of the crystal structure of the bis[6-(pyrazin-2-yl)-1,3,5-triazine-2,4-diamine](methanolato)(nitrato-O)Nickel(II) nitrate **9** grown from MeOH/Et$_2$O. Hydrogen bonds are represented by broken lines. Unless stated otherwise, carbon atoms are shown in grey, hydrogen atoms in white, oxygen atoms in red, nitrogen atoms in blue and nickel atoms in cyan. (a) Alternating arrangement of complex **9** and its enantiomer joined together by hydrogen bonding of DAT groups according to motif **I** and by free N—H···O$_{nitrate.}$ to generate chains (b) Chains are maintained together by hydrogen bonding involving bridging nitrates to form the three-dimensional structure. For clarity a chain is marked in green.

4.1.3. Table 1

Crystallographic data for **9** and **10**.

	9	10
Formula	[(Ni(C$_7$H$_7$N$_7$)$_2$(MeOH)(NO$_3$)](NO$_3$)	Cu(C$_7$H$_7$N$_7$)$_2$(NO$_3$)$_2$
Mr	593.16	565.95
Crystal size/mm^3	0.15 × 0.14 × 0.1	0.17 × 0.11 × 0.06
Crystal system	Triclinic	Triclinic
radiation	GaKα	GaKα
λ (Å)	1.34139	1.34139
F(000)	608.0	574.0
Space group	P$\bar{1}$	P$\bar{1}$
a (Å)	7.9534(3)	8.3550(4)

b (Å)	10.3562(4)	10.4080(5)
c (Å)	14.6063(6)	12.2948(5)
α (deg)	100.637(2)	93.120(2)
β (deg)	104.771(2)	96.497(2)
γ (deg)	97.685(2)	97.972(2)
V (Å^3)	1122.45(8)	1049.33(8)
Z	2	2
ρ_{calc}g/cm^3	1.755	1.791
T (K)	100	100
μ (mm^{-1})	5.175	6.058
Measured reflns	26335	36360
independent reflns	5040	3582
R_{int}	0.0691	0.0681
observed reflns $I > 2\sigma$ (I)	4308	3410
R_1, $I > 2\sigma$ (I)	0.0478	0.0623
R_1, all data	0.0594	0.0642
ωR_2, $I > 2\sigma$ (I)	0.1144	0.1645
ωR_2, all data	0.1243	0.1677
GoF	1.038	1.097

4.1.4. Structure of 6-(pyrazin-2-yl)-1,3,5-triazine-2,4-diamine 3 with Cu(NO$_3$)$_2$.2.5(H$_2$O) (Complex 10)

In complex **9**, nitrate plays a structural role by serving as a counterion and by forming multiple hydrogen bonds to stack the tapes together. Moreover, we have seen that methanol molecule is not only playing as a solvent of crystallization but also as a ligand. To probe the importance of these effects, we prepared the 2:1 complex of ligand **3** with Cu(NO$_3$)$_2$.(H$_2$O) under the same conditions. Crystals of **10** were grown from MeOH/Et$_2$O and proved to belong to the triclinic space group $P\bar{1}$. Views of the crystal structure are shown in Fig. 3, and other crystallographic data are summarized in Table 1. The chemical composition of complex **10**, with 2:1 PzDAT-to-Cu ratio, is [Cu(PzDAT)$_2$(NO$_3$)](NO$_3$) (Fig. S2). In the structure, DAT groups of ligand **3** are positioned in trans conformation as expected and the nitrato is in an equatorial position creating a typical Cu(II)

135

coordination geometry that can be described as a distorted bipyramid. The other nitrate ion is present outside the coordination sphere. The Cu atom and two coordinated N atoms from different DAT groups are almost linear with N–Cu–N angle of 177.5(2)°. The other coordinated pair of N atoms forms N–Cu–N angle of 128.7(6)°. The pyrazinyl and DAT rings of both ligands are nearly coplanar with an average torsional angle of 2.76°. As anticipated, complex **10** self-assembles to form tapes via hydrogen bonding of DAT groups according to the modified version of standard motif **I** (average distance N–H···N = 3.109 Å) (Fig. 3a). The overall molecular organization involves N–H···O hydrogen bonding involving bridging of nitrato ligands and nitrate counterions and π-π stacking (3.835 Å) of pyrazinyl and DAT rings to generate the three-dimensional structure (Fig. 3b). Details of the hydrogen bonds and their angles are provided in Table S3. Again, the results confirm that complex **10** can be obtained with predictable number of ligands **3** as well as a single well-defined constitution. The DAT groups and the counterions play a key role in directing molecular association by engaging in multiple hydrogen bonds. However, the topology of complexes can not be easily predicted owing to the diverse coordination geometries associated with Cu(II). As can be seen, in the structure of complex **10**, methanol molecules used in the crystallization are not involved in coordination with the Cu(II).

a   b
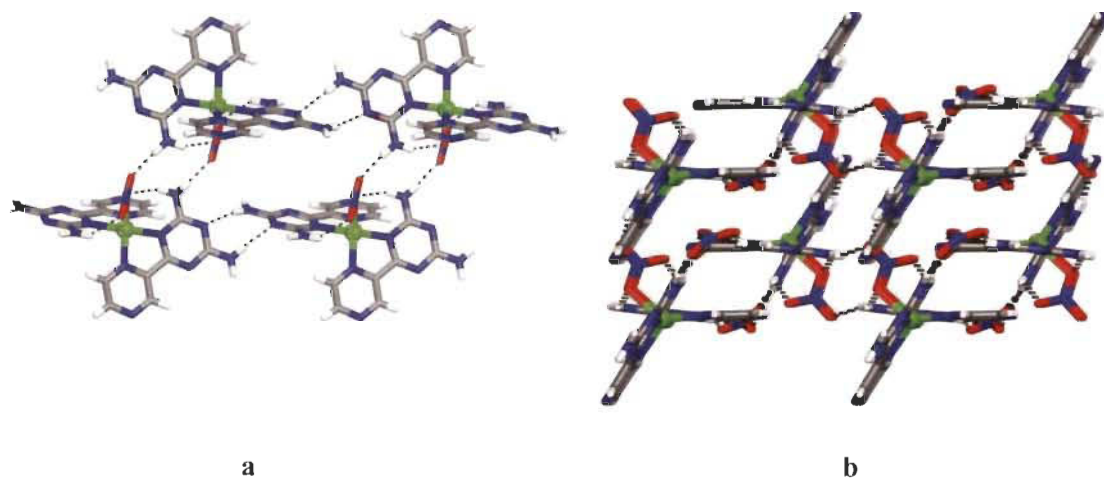
Fig. 3. Views of the crystal structure of the bis[6-(pyrazin-2-yl)-1,3,5-triazine-2,4-diamine](nitrato-O)Copper(II) nitrate **10** grown from MeOH/Et₂O. Hydrogen bonds are represented by broken lines. (a) Alternating arrangement of complex **10** and its enantiomer joined together by hydrogen bonding of DAT groups according to the modified version of motif **I** to generate tapes. Tapes are maintained together by hydrogen bonding involving bridging nitrate counterion and nitrato ligand to form the 3D networks. Furthermore, π-stacking reinforce the structure. (b) View showing stacking of tapes to form the three-dimensional structure. Carbon atoms are shown in grey, hydrogen atoms in white, oxygen atoms in red, nitrogen atoms in blue and copper atoms in green.

Comparing the structures of compounds **5-7** and **8-10**, we note that their structures are similar to each other and the association of these complexes is mainly dictated by the self-assembly via hydrogen bonds of the DAT groups with typical association motifs. In the conditions of preparation of complexes **8-10**, the other nitrogen atom of the pyrazinyl ring in the DAT group does not participate in coordination to metal ions. Within the six crystal structures analyzed by SCXRD, methanol molecules are observed only in the crystal structure of complex **9**. In this case, methanol not only acts as a solvent of crystallization but also as a ligand which participates in the first nickel coordinating sphere.

The phase purity of complexes **9** and **10** were evaluated by powder X-ray diffraction (PXRD) which confirmed the absence of secondary phase. Fig. S4 shows the comparison of the measured PXRD (in black) and the simulated patterns (in red) obtained from the SCXRD. As can be seen the two patterns are matching well which confirms the phase purity of the bulk samples **9** and **10**. Together, the SCXRD and PXRD demonstrate that samples **9** and **10** can be prepared in a single phase.

Thermal behaviours of complexes **8-10** were studied by thermogravimetric analysis (TGA). The TG curves of these compounds are shown in Fig. S5. Compounds **8-10** show similar

decomposition curves with two main weight loss steps in the range of ~32-39% at 300-306 °C and 36-46 % at 305-795 °C which are attributed to the de-coordination of the nitrates and ligands to produce the final residue. In the case of complex **9**, an additional step is observed in the range 45-107 °C with net mass loss of ~3 % that is assigned to the loss of methanol.

4.2. UV-visible spectroscopy

For successful utilization of the synthesized complexes as photocatalysts in HER, they must show absorption in the visible region of the spectrum and must be able to accept an electron from the excited photosensitizer. To better understand the electronic properties of compounds **2-10**, we measured their UV-Vis spectra and cyclic voltammetry (CV). UV-Vis spectra of these compounds were measured at room temperature in DMF solutions at concentration 8.8×10^{-6} M (Fig. 4). The UV-Vis spectra in DMF solution of the free ligands **2** and **3** displayed two absorption bands between 200 and 350 nm which can be attributed to the π- π^* electronic transitions of aromatic rings. In the case of complexes **5-10**, the presence of transition metal ions produced significant variation in the intensities of the absorption bands in the UV region of the spectra but only a slight shift towards lower energy as compared to the absorption bands of free ligands. This red shift is well supported by literature [41]. The transitions in the visible region (400-900 nm) are attributed to weak d-d transitions. Selected data (maximum absorption wavelengths, λ_{max}, molar absorption coefficients, ε) are summarized in Table 2. As d-d transitions are weak, we also recorded the UV-Vis of **5-10** at room temperature in DMF solutions at concentration 8.8×10^{-3} M to be able to see clearly the absorption bands (see inset Fig. 4).

4.2.1. Table 2

UV-Vis spectroscopy data of **2** and **3** and **5-10** in DMF solution.

Parameters	DMF			
	Conc = 8.8 x 10⁻⁶		Conc = 8 x 10⁻³	
	From 250 to 900 nm		From 350 to 900 nm	
Sample	λ_{max} (nm)	ε (mol⁻¹ dm³ cm⁻¹)	λ_{max} (nm)	ε (mol⁻¹ dm³ cm⁻¹)
2	268	1.21×10^4		
	288(sh)	6.17×10^3		
3	274	2.49×10^4		
	320(sh)	4.19×10^3		
5	273	3.21×10^4	404	60
	310(sh)	1.35×10^4	444	49
	350(sh)	4.97×10^3		
6	275	2.90×10^4	492	6
	311(sh)	1.09×10^4	685	2
			882	10
7	275	2.17×10^4	658	19
	304(sh)	8.59×10^3		
	275	4.09×10^4	405	26
8	302(sh)	1.95×10^4	553	3
	393(sh)	2.36×10^3		

9	279	4.39×10^4	514	4
	314(sh)	1.87×10^4	701	' 1
10	275	4.24×10^4	412	4
	308	1.50×10^4	663	5

sh: shoulder
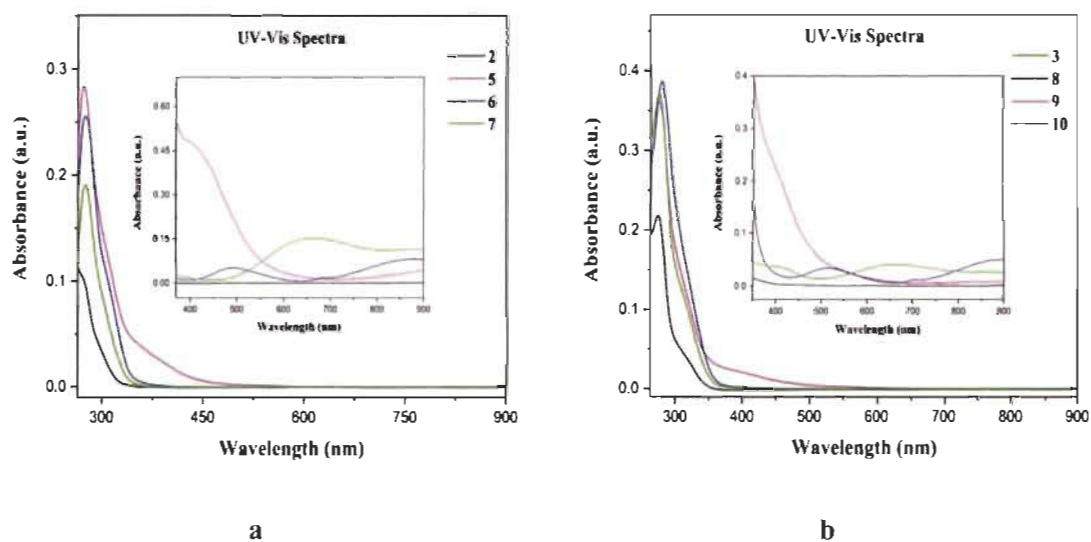
Fig. 4. UV-Vis spectra of **2-3** and **5-10** in DMF solution at room temperature at a concentration of 8.8×10^{-6} M. Inset is shown the visible region (450-800 nm) at a concentration 8×10^{-3} M (a) **2** and **5-7** and (b) **3** and **8-10**.

4.3. Cyclic Voltammetric Studies

The electrochemical behavior of ligands **2** and **3** and complexes **5-10** were measured using CV in DMF solutions at a concentration of 1 mM for ligands and complexes with 1 M TBA-PF$_6$ (tetrabutylammonium hexafluorophosphate) as supporting electrolyte at a scan rate 100 mV/s (Fig. 5). A summary of the wave peaks of these compounds are provided in Table 3. Cyclic voltammograms of the complexes exhibit oxidation and reduction peaks, which are attributed to the different redox states of the metal ions and reduction of the ligands.

Cyclic voltammograms (CV) of ligands **2** and **3** show two reversible redox waves at -2.22 and -2 V, and -2.31 and -1.72 V versus the Saturated Calomel Electrode (SCE), respectively. These redox signals can be assigned as the two consecutive one electron redox reaction of ligands. The CV of complex **5** shows three sequential redox waves at -2, -1.34 and at -1.15 V out of which, the first and the third redox waves are reversible. The first redox signal can be assigned to be ligand and the third signal can be of a $Co^{I/II}$ couple. In the CV of **8**, there are four reversible redox waves occurring at -1.89, -1.71, -1.54 and -0.93 V, from which the second wave is indistinguishable due to overlapping of waves. The first and the second redox signal can be assigned as ligand based and the third and fourth signal are for $Co^{I/0}$ and $Co^{II/I}$ couple respectively. [42] The CV of complexes **6** and **9** with nickel (II) metal ion shows two quasi-reversible redox waves at -1.30 and -1.05 V, and -1.54 and -0.88 V versus SCE, respectively. These redox signals can be assigned to a first ligand reduction and a $Ni^{I/II}$ couple, respectively. In case of the complexes **7** and **10** with copper (II) metal ion, only the ligand based redox waves at -1.96 and -1.19 V respectively, appears to be quasi reversible but its not completely distinct due to overlapping of the waves. Whereas in case of the metal ion, no quasi reversible redox waves were observed. However, Cu (II) metal ions gets reduced at 0.0063 and 0.089 V for **7** and **10** respectively, it further undergoes oxidation at 0.32 and 0.42 V respectively, Vs SCE. This might be due to the dimerization of copper complexes. [43] These values have been found comparable to those of 2,2'-bipyridine complexes reported in literature (Table S4) [42,44,45]. The possibility of multiple redox states for our complexes indicates their ability to be employed as redox catalysts especially for HER.

4.3.1. Table 3

Redox data of the ligands **2** and **3** and the complexes **5-10** in DMF solution.

Compound	Eox$_{1/2}$ [V]	Ered1$_{1/2}$ [V]	Ered2$_{1/2}$ [V]	Ered3$_{1/2}$ [V]	Ered4$_{1/2}$ [V]
2		-2	-2.22		
3		-1.72(74)	-2.31(38)		
5		-1.15(18)	-1.34(02)		
6		-1.05(20)	-1.30(32)	-1.74(56)	-1.99(68)
7	0.13(24)	-1.04(20)	-1.55(52)		
8		-0.93(96)	-1.54(04)	-1.71(99)	-1.89(02)
9		-0.88(91)	-1.54(39)	-1.90(61)	
10	0.09(95)	-0.57(27)	-0.85(80)		

a

b

c

d
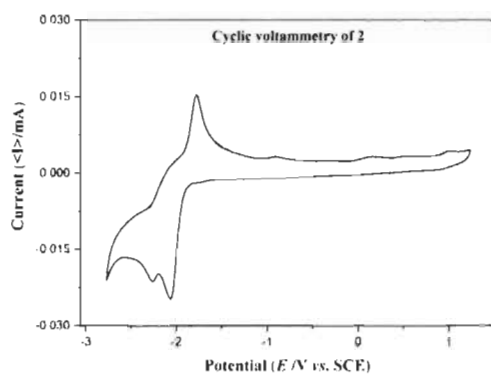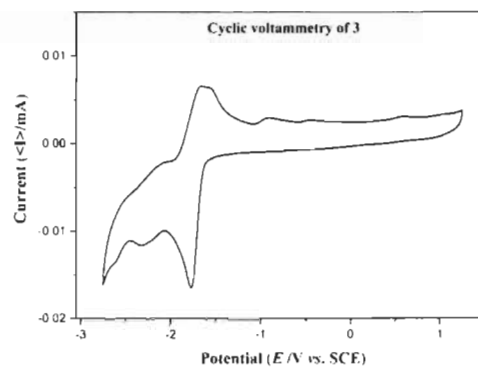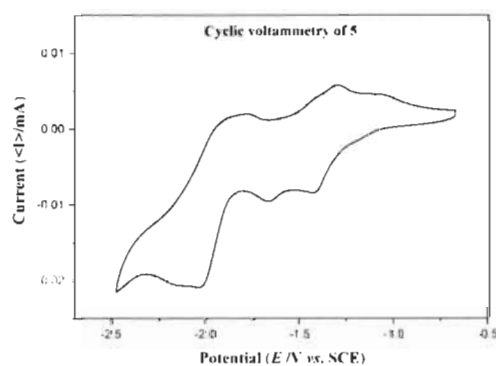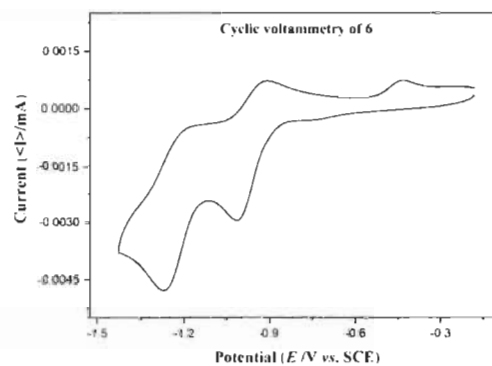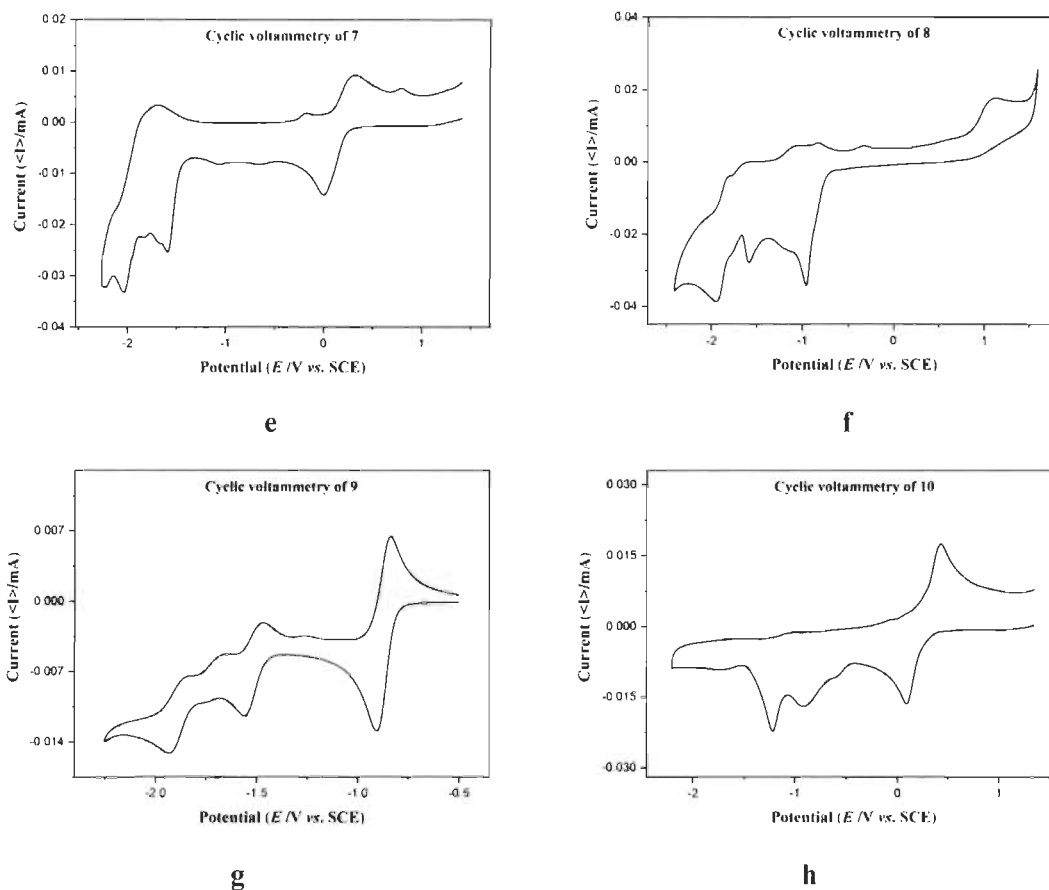
Fig. 5. Cyclic voltammetry of 1 mM (a-b) **2-3** and (c-h) **5-10** respectively in DMF vs SCE.

4.4. Catalytic hydrogen evolution

In order to study the effect of substituent and metal ion on the suitability of complexes **5-10** as photocatalysts for hydrogen production, we examined their photocatalytic properties. The hydrogen production displayed by 1 mM of each complex **5-10** in DMF using 1 M triethanolamine (TEOA) as the sacrificial electron donor, 0.1 mM $Ru^{(II)}(bpy)_3(PF_6)_2$ as the photosensitizer (PS) and aqueous 0.1 M HBF_4 as the proton source at an apparent pH between 8 and 9 was recorded (Fig. 6). The experiment was conducted for 15 h (after which no further change in photocatalytic activity is observed) and the hydrogen production rate, TON and TOF have been reported in millimoles per hour (mmol/h), moles of hydrogen per mole of PS and mmol of hydrogen per mole of PS per minute [32,46], respectively, for each compound (Table 4).

143

In the visible region, under blue irradiation (445 nm) the production of H_2 starts after turning on the light. This irradiation wavelength is sufficient to excite the photosensitizer $[Ru^{II}(bpy)_3](PF_6)_2$. The proposed mechanism for the process is shown in Fig. S7 [47,48]. Benjamin Probst and group studied the effect of pH on the photocatalytic production of hydrogen, under different pH conditions using reference catalyst $[Co(dmgH)_2]$. It was observed that although acetic acid was the main proton source, photocatalysis also occurred without acetic acid, at a very slow rate, due to the residual protons coming from water present in the system and the decomposition of TEOA. Similarly, we can deduce that in the current photocatalysis experiment, HBF_4 is the major source of proton while water and TEOA are acting as a subsidiary proton source [49]. Control experiments were conducted in the presence of PS/TEOA alone with and without light and no H_2 production was recorded which was consistent with the previous results [50]. We also conducted blank experiments with $Co(NO_3)_2.6H_2O$, $Ni(NO_3)_2.6H_2O$, $Cu(NO_3)_2.2.5H_2O$, **2** (PyDAT) and **3** (PzDAT) which displayed TON's of 9.96, 18.54, 0.58, 5.25 and 0.12 mol_{H2} mol_{PS}^{-1} respectively (Fig. S9, S10). Amongst the synthesized complexes, Cu complex **7** and Co complex **8** display TON's of 72 and 37 mol_{H2} mol_{PS}^{-1}. However, the remaining complexes don't prove to be efficient photocatalysts towards HER.

The replacement from the PyDAT (complex **5**) to PzDAT (complex **8**) significantly modifies the capacity of Co(II) complexes in the production of H_2 with TONs that almost increase to three times. However, for copper complexes **7** and **10**, PyDAT based Cu (II) complex **7** has TON almost thirty-five times higher, than its PzDAT analogue complexes **10**. Since, different combinations of metals and ligands result in different TONs and TOFs, we can suggest that the combined effect of the metal ion and the ligand leads to the overall hydrogen production. Hence, the variation of substituent/ligand and the metal ion affects the hydrogen production rate in photocatalytic experiments. The maximum TON and hydrogen production rate of 72 mol_{H2}. mol_{PS}^{-1} and 0.48 mmol of H_2 per hour, respectively, observed for complex **7**, is moderately higher than the TON

and the H_2 production rate of the literature standard cobaloxime catalyst, which has 68 and 0.45 mmol/h values, respectively (Fig. 6).

Amid all the tested complexes, Cu and py-DAT proved to be the most effective combination as a photocatalyst to produce hydrogen. This can be due to the inherent nature of Cu metal which displays diverse valence states, well-defined coordination chemistry and special d-d spin-allowed transitions [51,52]. However, Cu complex **10** with PzDAT doesn't display good H_2 production. This indicates that for H_2 production along with the metal, the organic part of the complex also plays a major role and the combined effect of the two leads to the final TON and TOF values. The values obtained for hydrogen production are better than some of the previously reported copper based photocatalysts. For instance, Wu and coworkers synthesized $\{[Cu^ICu^{II}_2\text{-}(DCTP)_2]NO_3 \cdot 1.5DMF\}_n$ 3D framework where DCTP = 4'-(3,5-dicar-boxyphenyl)-4,2':6',4''-terpyridine and observed its photocatalytic activity in UV-visible light in the presence of methanol as sacrificial agent and H_2PtCl_6 as cocatalyst. 0.032 mmol/g/h was the observed hydrogen production rate [53]. Song and group synthesized $C_{42}H_{46}CuN_6O_{21}S_4$ compound, the hydrogen production rate of 0.006 mmol/h was observed in visible light using TEOA as sacrificial agent [54]. The same group later synthesized $C_{21}H_{21}CuN_3O_{10}S_2$ metal organic framework and observed a hydrogen production rate of 0.073 mmol/h using TEOA as sacrificial electron donor and platinum as co-catalyst in visible light [55]. Majee and coworkers synthesized $[Cu(DQPD)]_2$ photocatalyst (where DQPD = deprotonated N2,N6-di(quinolin-8-yl)pyridine-2,6-dicarboxamide) that produced 427 µmol H_2/h/µmol PS, using a PS (fluorescein) concentration of 2 mM and TEA as a sacrificial electron donor [56].

145

4.4.1. Table 4

Turnover number and maximal turnover frequency for complexes **5-10**.

Compound	Molecular Formula	H₂ production (mmol/hour)	TON$_{max}$	TOF$_{max}$ (min^{-1})
std.*	[Co(dmgH)₂(py)Cl]	0.45	68	1892
5	Co(pyDAT)₂(NO₃)₂	0.11	16	307
6	Ni(pyDAT)₂(NO₃)₂	0.14	21	793
7	Cu(pyDAT)₂(NO₃)₂	0.48	72	314
8	Co(pzDAT)₂(NO₃)₂	0.25	37	841
9	Ni(pzDAT)₂(MeOH)(NO₃)₂	0.06	9.1	215
10	Cu(pzDAT)₂(NO₃)₂	0.01	2.1	90

*std. stands for standard in literature *viz.* cobaloxime; TON is reported in moles of hydrogen per mole of PS and TOF in mmol of hydrogen per mole of PS per minute.
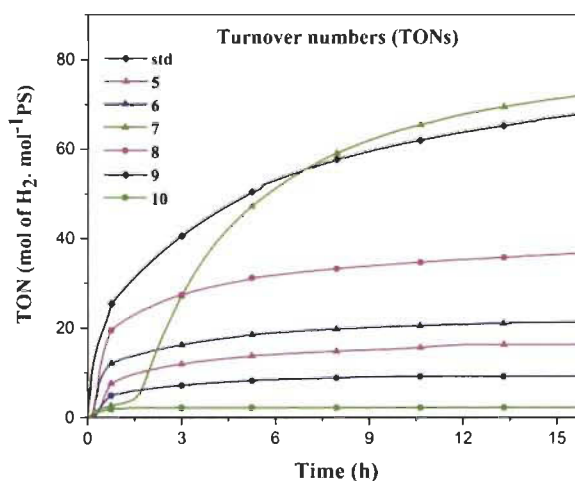
Fig. 6. Turn-over number with respect to PS for hydrogen evolution reaction of complexes **5-10** and literature standard (std: [Co(dmgH)₂(py)Cl]).

5. Conclusions

A series of functionalized transition metal ion complexes **8-10**, M(PzDAT)$_2$(NO$_3$)$_2$, with molecular structures that resemble M(bpy)$_2$(NO$_3$)$_2$ was easily prepared by a facile procedure. The solid-state structures of complexes **8-10** reveals that all cation complexes have 2:1 ligand to metal ion ratio. In the solid-state the molecular organization of the complexes is mainly dictated by the coordination modes of the ligands and the hydrogen bonds involving the DAT groups with reliable patterns. An analysis of the thermal stability and electronic properties of complexes **8-10** synthesized herein and pyridine DAT based complexes **5-7**, (PyDAT)(NO$_3$)$_2$ previously synthesized indicates the complexes to be stable up to ~300 °C and their ability to be employed as redox catalysts for HER respectively. An investigation on the effect of substituent and metal ion on the catalytic activity of complexes **5-10** for hydrogen evolution reaction designates copper complex **7** to be the best displaying the highest TON *viz.* 72 mol of hydrogen per mole of PS suggesting Cu and Py-DAT to be the best amongst the synthesized combinations of ligands and metal ions. This value observed for complex **7** (0.48 mmol/h) is higher compared to some previously reported Cu based catalysts (0.032 mmol/g/h, 0.006 mmol/h, 0.073 mmol/h, 427 µmol H$_2$/h/µmol PS) [53-56].

6. Declaration of Competing Interest

The authors declare that they have no known competing financial interests or personal relationships that could have appeared to influence the work reported in this paper.

8. Appendix A. Supplementary data

CCDC 1918901-1918902 contains the supplementary crystallographic data for this paper. These data can be obtained free of charge via http://www.ccdc.cam.ac.uk/conts/retrieving.html, or from the Cambridge Crystallographic Data Centre, 12 Union Road, Cambridge CB2 1EZ, UK; fax: (+44) 1223-336-033; or e-mail: deposit@ccdc.cam.ac.uk. Supplementary data to this article can be found online at https://doi.org/10.1016/j.poly.2020.114412.

9. References

[1] N.S. Lewis, D.G. Nocera, Proc. Natl. Acad. Sci. 103 (2006) 15729.

[2] M. Wang, L. Chen, L. Sun, Energy Environ. Sci. 5 (2012) 6763.

[3] M. Serra, J. Albero, H. García, ChemPhysChem 16 (2015) 1842.

[4] J.A. Turner, Science 305 (2004) 972.

[5] J. Barber, Chem. Soc. Rev. 38 (2009) 185.

[6] T.R. Cook, D.K. Dogutan, S.Y. Reece, Y. Surendranath, T.S. Teets, D.G. Nocera, Chem. Rev. 110 (2010) 6474.

[7] Y. Sun, J.P. Bigi, N.A. Piro, M.L. Tang, J.R. Long, C.J. Chang, J. Am. Chem. Soc. 133 (2011) 9212.

[8] H.B. Gray, Nat. Chem. 1 (2009) 112.

[9] J.R. McKone, S.C. Marinescu, B.S. Brunschwig, J.R. Winkler, H.B. Gray, Chem. Sci. 5 (2014) 865.

[10] A.J. Esswein, D.G. Nocera, Chem. Rev. 107 (2007) 4022.

[11] M.G. Pfeffer, T. Kowacs, M. Wächtler, J. Guthmuller, B. Dietzek, J.G. Vos, S. Rau, Angew. Chem. 54 (2015) 6627.

[12] J. Xie, C. Li, Q. Zhou, W. Wang, Y. Hou, B. Zhang, X. Wang, Inorg. Chem. 51 (2012) 6376.

[13] C.L. Pitman, A.J. Miller, ACS Catal. 4 (2014) 2727.

[14] P.N. Curtin, L.L. Tinker, C.M. Burgess, E.D. Cline, S. Bernhard, Inorg. Chem. 48 (2009) 10498.

[15] A. Fihri, V. Artero, M. Razavet, C. Baffert, W. Leibl, M. Fontecave, Angew. Chem. 47 (2008) 564.

[16] T.M. McCormick, B.D. Calitree, A. Orchard, N.D. Kraut, F.V. Bright, M.R. Detty, R. Eisenberg, J. Am. Chem. Soc. 132 (2010) 15480.

[17] M. Nippe, R.S. Khnayzer, J.A. Panetier, D.Z. Zee, B.S. Olaiya, M. Head-Gordon, C.J. Chang, F.N. Castellano, J.R. Long, Chem. Sci. 4 (2013) 3934.

[18] M.P. McLaughlin, T.M. McCormick, R. Eisenberg, P.L. Holland, ChemComm 47 (2011) 7989.

[19] M.A. Gross, A. Reynal, J.R. Durrant, E. Reisner, J. Am. Chem. Soc. 136 (2013) 356.

[20] E. Rousset, I. Ciofini, V.R. Marvaud, G.S. Hanan, Inorg. Chem. 56 (2017) 9515.

[21] A. Jacques, O. Schott, K. Robeyns, G.S. Hanan, B. Elias, Eur. J. Inorg. Chem. 2016 (2016) 1779.

[22] E. Rousset, D. Chartrand, I. Ciofini, V. Marvaud, G.S. Hanan, ChemComm 51 (2015) 9261.

[23] O. Schott, A.K. Pal, D. Chartrand, G.S. Hanan, ChemSusChem 10 (2017) 4436.

[24] A. Duong, A.V. Métivaud, T. Maris, J.D. Wuest, Cryst. Growth Des. 11 (2011) 2026.

[25] S.G. Telfer, J.D. Wuest, Cryst. Growth Des. 9 (2009) 1923.

[26] A. Duong, T. Maris, J.D. Wuest, Inorg. Chem. 50 (2011) 5605.

[27] A.K. Pal, A. Duong, J.D. Wuest, G.S. Hanan, Polyhedron 108 (2016) 100.

[28] A. Duong, S. Rajak, A.A. Tremblay, T. Maris, J.D. Wuest, Cryst. Growth Des. 19 (2019) 1299.

[29] J. Wu, J. Jung, P. Zhang, H. Zhang, J. Tang, B. Le Guennic, Chem. Sci. 7 (2016) 3632.

[30] R.-R. Duan, L. Wang, W.-Q. Huo, S. Chen, X.-H. Zhou, J. Coord. Chem. 67 (2014) 2765.

[31] K.E. Maly, E. Gagnon, T. Maris, J.D. Wuest, J. Am. Chem. Soc. 129 (2007) 4306.

[32] S. Rajak, O. Schott, P. Kaur, T. Maris, G.S. Hanan, A. Duong, RSC Adv. 9 (2019) 28153.

[33] S. Rajak, O. Schott, P. Kaur, T. Maris, G. S. Hanan, A. Duong, Int. J. Hydrog. Energy. https://doi.org/10.1016/j.ijhydene.2019.11.141.

[34] S. Rajak, M. Mohan, A.A. Tremblay, T. Maris, S. Leal do Santos, E.C. Venancio, S. Ferreira Santos, A. Duong, ACS Omega 4 (2019) 2708.

[35] F.H. Case, E. Koft, J. Am. Chem. Soc. 81 (1959) 905.

[36] C.-W. Chan, D.M.P. Mingos, A.J. White, D.J. Williams, Polyhedron 15 (1996) 1753.

[37] G.M. Sheldrick, Acta Cryst. A 71 (2015) 3.

[38] C.F. Macrae, I.J. Bruno, J.A. Chisholm, P.R. Edgington, P. McCabe, E. Pidcock, L. Rodriguez-Monge, R. Taylor, J.V.D. Streek, P.A. Wood, J. Appl. Crystallogr. 41 (2008) 466.

[39] N.G. Connelly, W.E. Geiger, Chem. Rev. 96 (1996) 877.

[40] C.D. Lentz, O. Schott, T. Auvray, G.S. Hanan, B. Elias, Inorg. Chem. 56 (2017) 10875.

[41] F. Gärtner, D. Cozzula, S. Losse, A. Boddien, G. Anilkumar, H. Junge, T. Schulz, N. Marquet, A. Spannenberg, S. Gladiali, Chem.: Eur. J. 17 (2011) 6998.

[42] S.-P. Luo, L.-Z. Tang, S.-Z. Zhan, Inorg. Chem. Commun. 86 (2017) 276.

[43] Z. Guo, F. Yu, Y. Yang, C.F. Leung, S.M. Ng, C.C. Ko, C. Cometto, T.C. Lau, M. Robert, ChemSusChem 10 (2017) 4009.

[44] B.J. Henne, D.E. Bartak, Inorg. Chem. 23 (1984) 369.

[45] H.-J. Park, J.-H. Kwon, T.-S. Cho, J.M. Kim, H.H. In, C. Kim, S. Kim, J. Kim, S.K. Kim, J. Inorg. Biochem. 127 (2013) 46.

[46] T. Auvray, R. Sahoo, D. Deschênes, G.S. Hanan, Dalton Trans. 48 (2019) 15136.

[47] V. Artero, M. Chavarot-Kerlidou, M. Fontecave, Angew. Chem. 50 (2011) 7238.

[48] N. Queyriaux, R.T. Jane, J. Massin, V. Artero, M. Chavarot-Kerlidou, Coord. Chem. Rev. 304–305 (2015) 3.

[49] B. Probst, C. Kolano, P. Hamm, R. Alberto, Inorg. Chem. 48 (2009) 1836.

[50] R.W. Hogue, O. Schott, G.S. Hanan, S. Brooker, Chem. Eur. J. 24 (2018) 9820.

[51] H.T. Lei, H.Y. Fang, Y.Z. Han, W.Z. Lai, X.F. Fu, R. Cao, ACS Catal. 5 (2015) 5145.

[52] L. Li, S. Zhu, R. Hao, Jia-Jun Wang, En-Cui Yang, Xiao-Jun Zhao, Dalton Trans. 47 (2018) 12726.

[53] Z.L. Wu, C.H. Wang, B. Zhao, J. Dong, F. Lu, W.H. Wang, W.C. Wang, G.J. Wu, J.Z. Cui, P. Cheng, Angew. Chem. Int. Ed. 55 (2016) 4938.

[54] T. Song, L. Zhang, P.Y. Zhang, J. Zeng, T.T. Wang, A. Ali, H.P. Zeng, J. Mater. Chem. A 5 (2017) 6013.

[55] T. Song, P.Y. Zhang, J. Zeng, T.T. Wang, A. Ali, H.P. Zeng, Int. J. Hydrogen Energy 42 (2017) 26605.

[56] K. Majee, J. Patel, B. Das, S.K. Padhi, Dalton Trans. 46 (2017) 14869.

3.4. Conclusions

We have developed an efficient and non-expensive method to synthesize molecular catalysts for hydrogen evolution reaction (HER). 6-(pyrazin-2-yl)-1,3,5-triazine-2,4-diamine ligand **3** forms octahedral complexes with Co (II), Ni (II) and Cu (II) nitrates. The synthetic strategy used is highly efficient in terms of crystallinity, purity, homogeneity, thermal stability and structural predictability. In the solid-state the molecular organization of the complexes **8-10** is mainly dictated by the coordination modes of the ligands and the hydrogen bonds involving the DAT groups with reliable patterns. All the complexes **5-10** are active photocatalysts which has been proved by their electronic properties determined by cyclic voltammetry prior to their hydrogen evolution reaction experiment. They are thermally stable up to ~ 300 °C and demonstrate good catalytic properties for the production of H_2. To the best of our knowledge, this is the first example of HER carried out by DAT-based complexes. The investigation on the effect of changing the substituent and the metal ion on the hydrogen evolution reaction for complexes **5-10** indicates the copper complex **7** to be the best combination of tectoligand and metal ion with a turnover number (TON) of 72 moles of H_2 per mole of PS. The hydrogen production rate observed for complex **7** (0.48 mmol/h) is higher compared to some previously reported Cu based catalysts.

3.5. Supporting Information

Fig. S1. Thermal atomic displacement ellipsoid plot of the structure of **9**. The ellipsoids of non-hydrogen atoms are drawn at 50% probability level, and hydrogen atoms are represented by a sphere of arbitrary size.

Fig. S2. Thermal atomic displacement ellipsoid plot of the structure of **10** grown from MeOH/Et₂O. The ellipsoids of non-hydrogen atoms are drawn at 50% probability level, and hydrogen atoms are represented by a sphere of arbitrary size.

Fig. S3. Infrared spectra of **3** and **8-10**

Table S1. IR data and assignments of **3** and **8-10**

$\tilde{v}$/cm^{-1}				Assignment
3	**8**	**9**	**10**	
734w	696w	732w	714w	Ring breathing, $\delta(NH_2)$
	737w			
765w	771w	771w		Ring out-of-plane def.
813m	808s	807s	804m	Ring out-of-plane def. (DAT ring)
858w	823w	850w	830w	
911w	910w	914w	911w	Ring out-of-plane def.
982w	989m	996w	995w	
	1013w	1014m		Ring breathing, $\delta(NH_2)$
1023w	1037s	1044m	1041m	
1044w			1065w	δ(C-H), δ(N-H)
1076w				

156

1151w	1161s	1167m	1158w	δ(C-H), δ(N-H), Ring breathing
1167w	1174s		1178w	
1208w	1197w	1212w	1206w	δ(C-H), δ(N-H)
1263w				δ(C-H), δ(N-H)
1290w				
	1272s	1278s	1281s	$\nu(NO_3^-)$
	1290s		1296s	
1376s	1371m	1378s	1375s	Ring breathing, δ(C-H), ν(C-C)
				Pyrazine-DAT bond
1417m	1430m	1460s	1431m	δ(C-H), ν(C-C) Pyrazine-DAT
1445m	1450s		1462w	bond
1473m	1485m	1486m	1487s	Ring breathing, δ(C-H), δ(N-H)
1516s	1508s	1516s	1508s	
1536s	1540m	1575s		
1590w	1575m	1602m	1581m	ν(C-NH₂), δ(C-H), ν(C-N), ν(C=N)
1622m	1598s	1623m	1621s	
1662w	1641w	1662w	1655w	
	1671m			
3139s	3173m	3159s	3154s	ν(C-H)
3318s	3225s	3331s	3221s	
	3318s	3383m	3321s	ν(N-H)
3431m	3392s	3431m	3403m	ν(N-H)
	3451s		3482w	

Abbreviation used for the type of vibration mode. def.: deformation; δ: bending vibration; ν: stretching vibration.

Table S2. Hydrogen-bond geometry (Å, °) in structure of **9**

D—H···A	D—H	H···A	D···A	D—H···A
N4—H4A···O5	0.82 (4)	2.52 (4)	3.036 (4)	122 (3)
N4—H4A···O7	0.82 (4)	2.21 (4)	2.985 (4)	156 (3)
N11—H11A···O1	0.85 (4)	1.91 (4)	2.735 (4)	163 (3)
N5—H5A···O5ⁱ	0.86 (4)	2.15 (4)	2.983 (4)	163 (3)
N4—H4B···N2ⁱ	0.90 (4)	2.21 (4)	3.105 (3)	174 (3)
C1—H1···O3ⁱⁱ	0.95 (3)	2.56 (3)	3.148 (4)	121 (2)
C1—H1···O6ⁱⁱⁱ	0.95 (3)	2.51 (3)	3.091 (4)	120 (2)
C1—H1···N8	0.95 (3)	2.59 (3)	3.160 (4)	119 (2)
C15—H15A···O4ⁱᵛ	0.98 (4)	2.59 (4)	3.303 (4)	130 (3)
C15—H15A···N8	0.98 (4)	2.66 (4)	3.206 (4)	116 (3)

	0.81 (4)	2.22 (4)	2.999 (3)	161 (4)
N5—H5B···O1^{v}	0.81 (4)	2.22 (4)	2.999 (3)	161 (4)
N5—H5B···O3^{v}	0.81 (4)	2.61 (4)	3.291 (4)	142 (3)
N5—H5B···N15^{v}	0.81 (4)	2.67 (4)	3.429 (4)	155 (3)
C9—H9···N2^{vi}	0.94 (5)	2.62 (5)	3.423 (4)	144 (4)
C3—H3···O2^{v}	0.89 (4)	2.40 (4)	3.246 (4)	160 (3)
N11—H11B···N9^{vii}	0.80 (5)	2.24 (5)	3.011 (4)	163 (5)
N12—H12B···O4^{viii}	0.81 (4)	2.50 (4)	3.275 (4)	161 (4)
N12—H12B···O6^{viii}	0.81 (4)	2.57 (4)	3.037 (4)	118 (3)
O7—H7···O4	0.83 (5)	1.88 (5)	2.704 (3)	169 (4)
O7—H7···O5	0.83 (5)	2.46 (5)	3.006 (3)	124 (4)
O7—H7···N16	0.83 (5)	2.53 (5)	3.287 (3)	151 (4)

Symmetry codes: (i) $-x$, $-y+1$, $-z+1$; (ii) $x+1$, y, z; (iii) x, $y-1$, z; (iv) $-x+1$, $-y+1$, $-z+2$;

(v) $-x$, $-y$, $-z+1$; (vi) $-x+1$, $-y+1$, $-z+1$; (vii) $-x+1$, $-y$, $-z+2$; (viii) $-x+2$, $-y+1$, $-z+2$.

Table S3. Hydrogen-bond geometry (Å, °) in structure of **10**

D—H···A	D—H	H···A	D···A	D—H···A
C1—H1···N13	0.95	2.60	3.239 (6)	125
C1—H1···O5^{i}	0.95	2.28	3.120 (6)	148
C2—H2···O6^{i}	0.95	2.37	3.145 (6)	138
C3—H3···O2^{ii}	0.95	2.47	3.261 (6)	141
N6—H6A···O3^{iii}	0.88	2.10	2.942 (6)	161
N6—H6B···O1	0.88	2.14	2.885 (5)	142
N7—H7A···N11^{iv}	0.88	2.16	3.043 (5)	177
N7—H7B···O4	0.88	2.03	2.892 (5)	167
N7—H7B···O5	0.88	2.50	2.948 (5)	112
N7—H7B···N16	0.88	2.47	3.190 (6)	139
C9—H9···N9^{v}	0.95	2.57	3.223 (6)	126
C10—H10···O1^{vi}	0.95	2.65	3.294 (6)	126
N13—H13A···O4^{ii}	0.88	2.36	2.940 (5)	123
N13—H13A···O6^{ii}	0.88	2.01	2.883 (5)	173
N13—H13A···N16^{ii}	0.88	2.44	3.228 (6)	149
N13—H13B···O2	0.88	2.19	2.921 (5)	140
N14—H14A···N4^{i}	0.88	2.31	3.176 (5)	167
N14—H14B···O3^{vii}	0.88	2.27	2.969 (6)	136

Symmetry codes : (i) $x-1$, $y-1$, z; (ii) $-x+1$, $-y+1$, $-z+1$; (iii) $-x+1$, $-y+1$, $-z$; (iv) $x+1$, $y+1$, z;

(v) $-x+2$, $-y$, $-z$; (vi) $-x+1$, $-y$, $-z$; (vii) x, $y-1$, z.
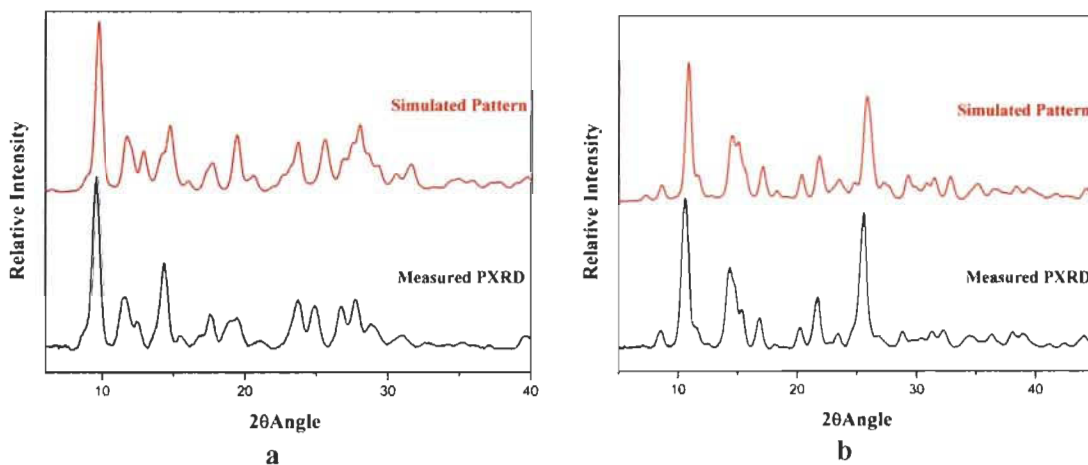
Fig. S4. PXRD patterns of complexes (a) **9** and (b) **10**.

Thermal analysis

a

b

c
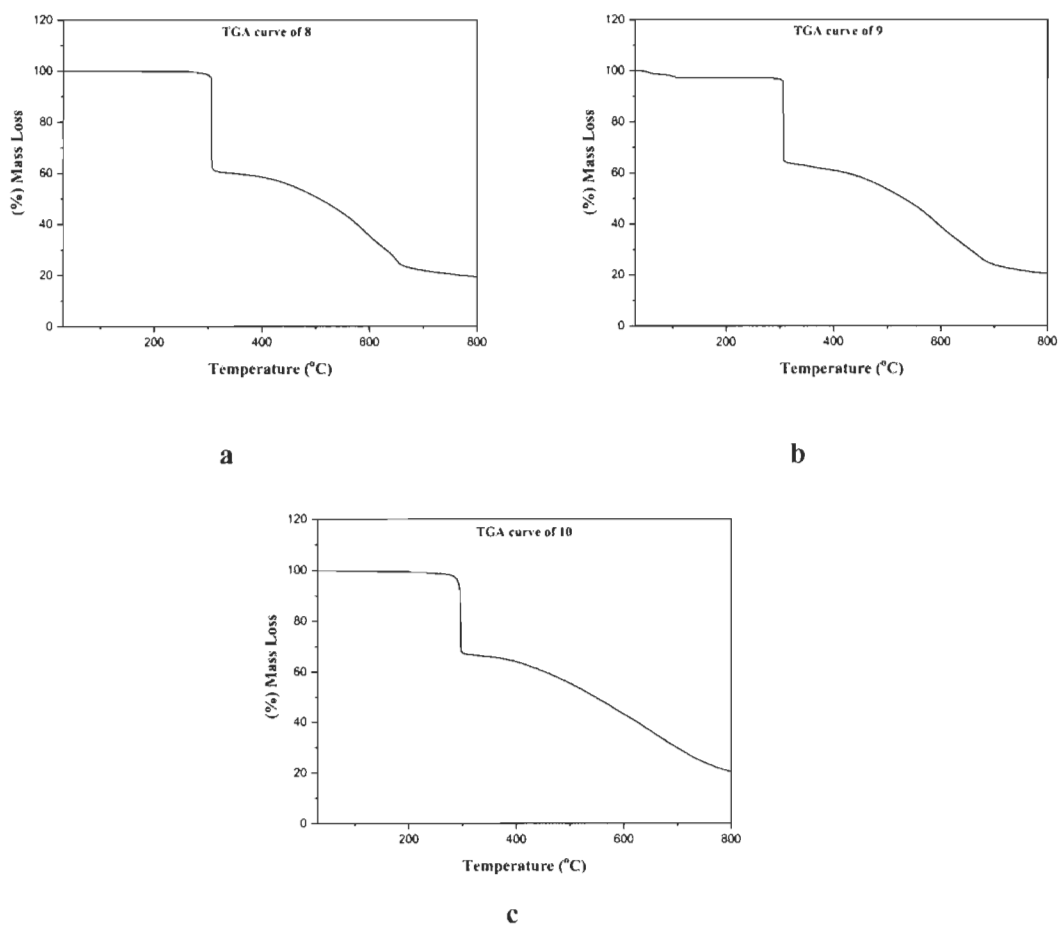
Fig. S5. Thermogravimetric analysis (TGA) curves of **8-10**

Cyclic Voltammetry

Table S4. Cyclic voltammetry data of 2,2'-bipyridine complexes reported in literature

Compound	Conditions	Ered1$_{1/2}$ [V]	Ered2$_{1/2}$ [V]	Ered3$_{1/2}$ [V]	Ered4$_{1/2}$ [V]
Co(bpy)$_2$(NO$_3$)$_2$[1]	MeCN	-1.20	-1.78		
Ni(bpy)$_2$(NO$_3$)$_2$	---	---	---	---	---
Cu(bpy)$_2$(NO$_3$)$_2$[2]	H$_2$O	-0.175			

bpy = 2,2'-bipyridine
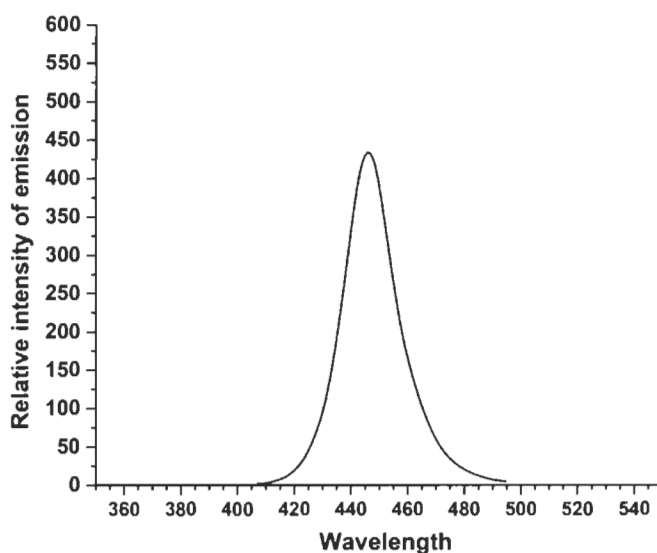
Fig. S6. Emission spectrum of blue LED.

Table S5: Emission maxima and amplitude of LED light.

Light source[a]	Blue
$\lambda_{max,em}$ (nm)	445
$\Delta\lambda$ (nm)	90
Photon flux in $\mu mol_{photons} \cdot min^{-1} \cdot cm^{-2}$ [b]	20

160

a blue LED 445 nm.

b an analog power-meter PM100A (THORLABS) associated with a compact photodiode power head with silicon detector S120C is used to evaluate the photon flux for the LEDs. Photo-diode detector is placed at the same distance from the LED surface than the bottom of illuminated vial.

Fig. S7. General mechanism for HER using Metal (M) - complexes as photocatalysts. [3,4]
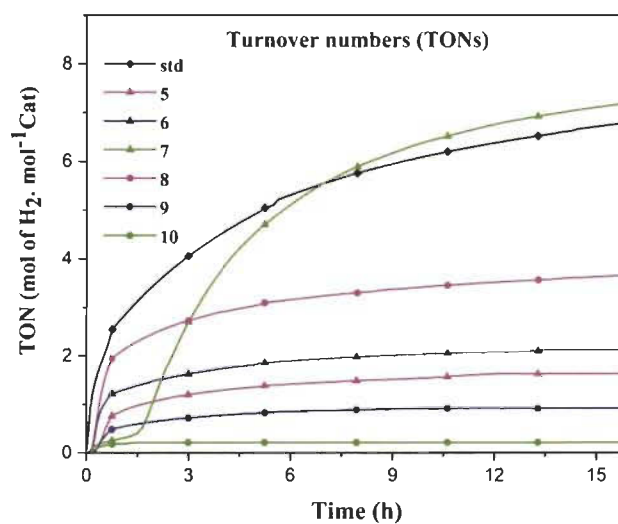
Fig. S8. Turn-over number with respect to Catalyst (TON_Cat) for hydrogen evolution reaction of standard reference (std: [Co(dmgH)₂(py)Cl]) and complexes 5-10.
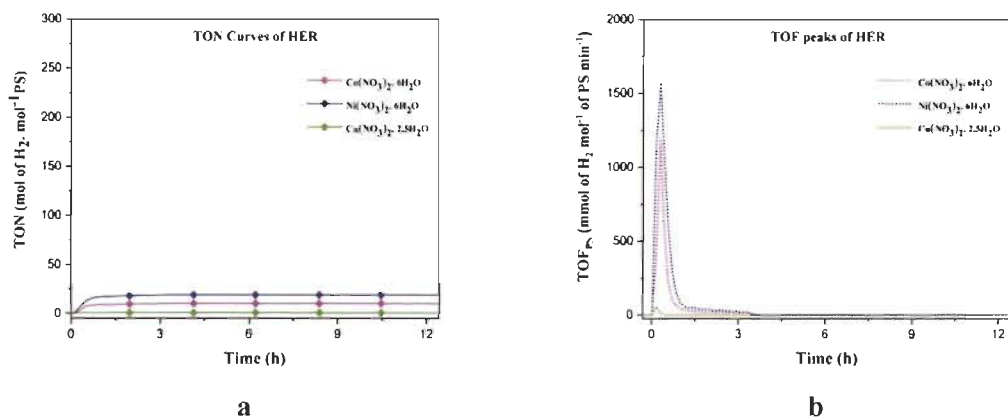
Fig. S9. Hydrogen evolution reaction of $Co(NO_3)_2 \cdot 6H_2O$, $Ni(NO_3)_2 \cdot 6H_2O$ and $Cu(NO_3)_2 \cdot 2.5H_2O$ (1 mM each) under blue light. (a) TON's and (b) TOF's.
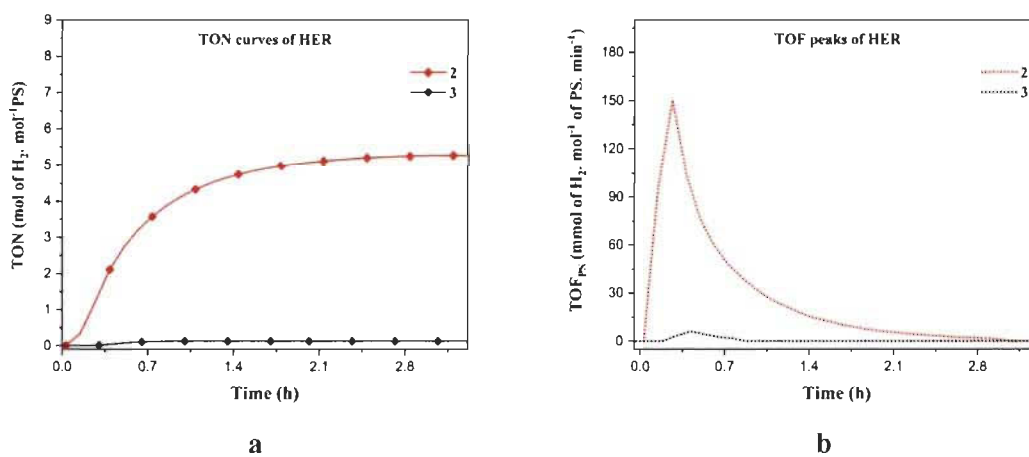
Fig. S10 Hydrogen evolution reaction of **2** (pyDAT) and **3** (pzDAT) (1 mM each) under blue light. (a) TON's and (b) TOF's.

References

[1] S-P. Luo, L-Z. Tang, S-Z. Zhan, *Inorg. Chem. Commun.* **2017,** 86, 276-280.

[2] H-J. Park, J-H. Kwon, T-S. Cho, J. M. Kim, H. H. In, C. Kim, S. Kim, J. Kim, S. K. Kim, *J. Inorg. Biochem.* **2013,** 127, 46–52.

[3] V. Artero, M. Chavarot-Kerlidou, M. Fontecave, *Angew. Chem.* **2011**, *50*, 7238-7266.

[4] N. Queyriaux, R. T. Jane, J. Massin, V. Artero, M. Chavarot-Kerlidou, *Coord. Chem. Rev.* **2015**, *304-305*, 3-19

Chapter 4

Mimicking 2, 2':6', 2":6", 2'''-Quaterpyridine Complexes for the Light-Driven Hydrogen Evolution Reaction: Synthesis, Structural, Thermal and Physicochemical Characterizations

4.1. Introduction

As discussed in introduction, numerous complexes of bipyridine (bpy), terpyridine (tpy) and quaterpyridine (qtpy) with transition metals have been reported in literature to form diverse metallosupramolecular structures. The major problem related to them is the lengthy synthetic procedures especially those associated with qtpy, which has limited its applications. Scientists are always working to find a synthetic route that requires minimal experimental steps (input) and maximum yield (output). An easy alternative approach for the synthesis of qtpy complexes is necessary for their better and higher utility in the synthesis of metal organic complexes. Additionally, incorporation of DAT based organic fragments into these complexes leads to a greater advantage in terms of their application in various energy related areas varying from catalysis to fuel cells. The use of these synthesized complexes as catalysts for light driven HER provides a huge scope to the present world facing depletion of fossil fuels.

4.2. Article 3

Mimicking 2, 2':6', 2":6", 2'''-Quaterpyridine Complexes for the Light-Driven Hydrogen Evolution Reaction: Synthesis, Structural, Thermal and Physicochemical Characterizations

Sanil Rajak, Olivier Schott, Prabhjyot Kaur, Thierry Maris, Garry S. Hanan and Adam Duong*

4.3. Author's Contribution

Sanil Rajak: Investigation, conceptualization, methodology, synthesis and characterization, photo catalytic testing, electrochemical analysis, interpretation of results and writing of the article.

Olivier Schott: Mentoring, conceptualization, methodology.

Dr. Prabhjyot Kaur: Writing- review and editing.

Dr. Thierry Maris: Crystallographic data analysis.

Prof. Garry S. Hanan: Co-supervision, conceptualization, methodology.

Prof. Adam Duong: Supervision, finding funding supports, project administration, conceptualization, interpretation of results, writing- review and editing.

1. Abstract

The synthetic difficulties associated with quaterpyridine (qtpy) complexes have limited their use in the formation of various metallosupramolecular architectures in spite of their diverse structural and physicochemical properties. Providing a new facile synthetic route to the synthesis of functionalised qtpy mimics, we herein report the synthesis of three novel -NH$_2$ functionalized qtpy-like complexes **12-14** with the general formula M(C$_{16}$H$_{14}$N$_{12}$)(NO$_3$)$_2$ (M = Co(II), Ni(II) and Cu(II)) in high yield and purity. Characterization of these complexes has been done by single crystal X-ray diffraction (SCXRD), thermogravimetric analysis, UV-Vis, infrared, mass spectrometry and cyclic voltammetry. As indicated by SCXRD, in all the synthesized complexes, the metal ions show a strongly distorted octahedral coordination geometry and typical hydrogen bonding networks involving DAT groups. In addition, complexes **12-14** have been analyzed as potential photocatalysts for hydrogen evolution reaction (HER) displaying good turnover numbers (TONs). Hydrogen produced from these photocatalysts can serve as the possible alternative for fossil fuels. To the best of our knowledge, this is the only study showcasing -NH$_2$ functionalized qtpy-like complexes of Co(II), Ni(II) and Cu(II) and employing them as photocatalysts for HER. Thus, a single proposed strategy solves two purposes-one related to synthesis while second is related to our environment.

2. Introduction

Complexes based on coordination of both unsubstituted and functionalized bipyridine (bpy), terpyridine (tpy) and quaterpyridine (qtpy) with transition metals have been widely studied in particular for the formation of various metallosupramolecular architectures.[1-8] There is very extensive literature concerning polypyridine ligands and their complexes, but a relatively few investigations have been done on functionalized systems, particularly on qtpy. Many interests were focused on qtpy, a tetradentate ligand that can form metal complexes of different geometries. qtpy presents diverse features such as (i) N-heterocyclic scaffolds, (ii) predictable coordination chemistry, (iii) better oxidation resistance as compared to bi-and terpyridine and (iv) a low energy orbital for metal-to-ligand charge transfer transition in the visible region. Although evaluation of their structural and physicochemical properties drew considerable attention, their use has rapidly declined because of the synthetic difficulties which limit the prospects of their application.

Therefore, an alternative synthetic approach that consists of replacing one or several pyridine rings by a diamino-1,3,5-triazinyl group (DAT) has been employed to facilitate easy preparation of bpy, tpy and qtpy-type ligands **1-3**.[9] Compounds **4-6** were designed to eliminate the most serious drawbacks concerning functionalization of bpy, tpy and qtpy synthesis (Chart 1a). These compounds are pyridyl and bipyridyl substituted in ortho with one or two DAT groups. In crystal engineering these molecules are known as tectoligands because of their dual ability to bind metal ions and simultaneously engage in predictable intermolecular interactions such as hydrogen bonds according to reliable patterns (Chart 1b).[5,10,11] In supramolecular chemistry, the self-assembly of tectoligands with metal ions forms metallotectons.[12-18] Creation of metallosupramolecules[19,20] using **4-6** has several advantages: (i) the synthesis is easy and the yield is high, (ii) the coordination chemistry is similar to **1-3**, (iii) in solid-state, reliable hydrogen bond networks with predefined structures are expected, (iv) the presence of amino groups and triazinyl rings may lead to fine tuning of activities of the metal complexes for catalysis.
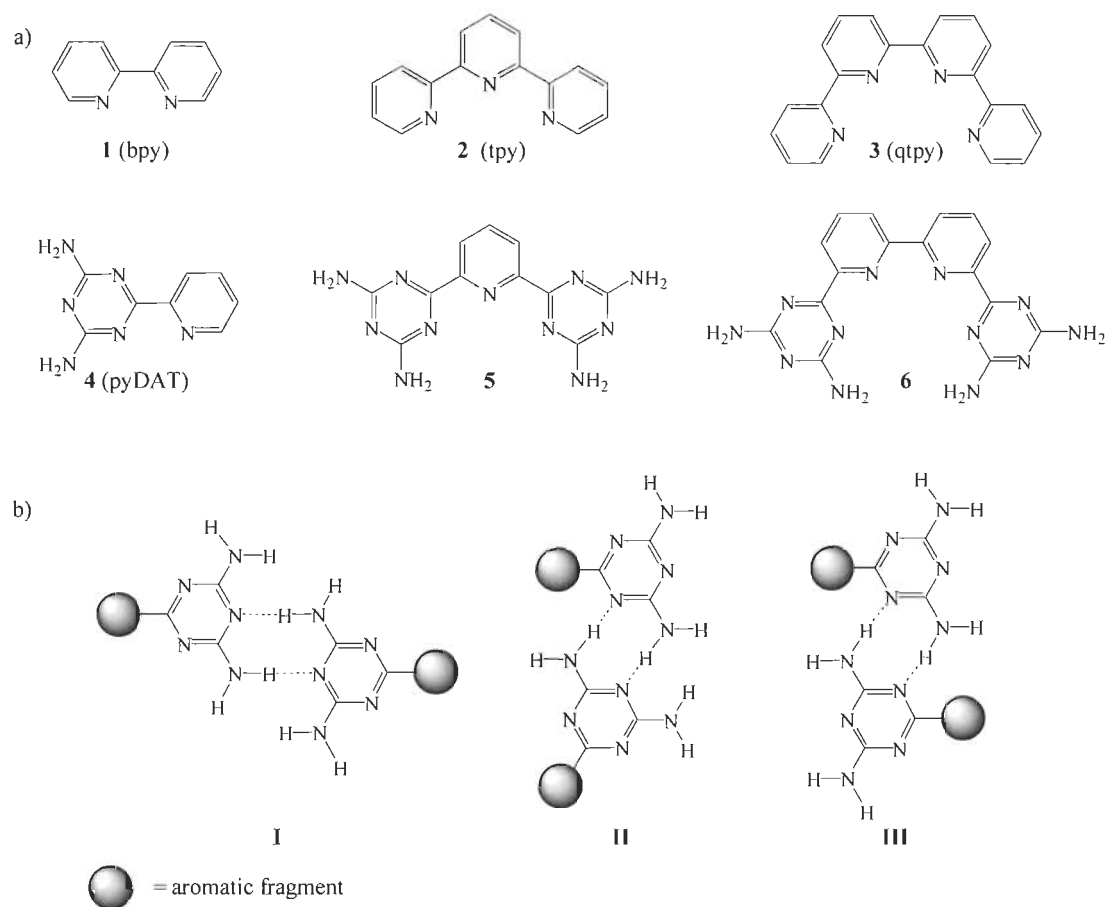
Chart 1. Molecular structures of (a) compounds **1-6** and (b) the hydrogen bonds motifs of DAT groups.

To the best of our knowledge, coordination chemistry of **6** has never been investigated. Compound **6** is expected to function as a tetradentate ligand chelating ions to form helical metallotectons **12-14** (Chart 2). The range of applications of complexes of **6** may include molecular machines, supramolecular functional devices, catalysts for both organic and inorganic reactions, biomedical like DNA binding, medicinal chemistry, nonlinear optical materials and so forth.[21-27]

In this present study, our interests focus on the coordination chemistry of **6** to form complexes **12-14** and their self-assembly by hydrogen bonds via the DAT groups. This work is an attempt to provide a remedy for the lack of straightforward and efficient synthetic pathways to prepare

functionalized 2,2':6',2":6",2"'-quaterpyridine (qtpy) complexes by minimizing the steps involved in their synthesis and obtain these complexes in high yield and purity without the need for any further purification. We have chosen first row transition metals to form complexes with **6** because of their low cost compared to platinum group metals. Another aspect of the present work is to provide a possible future alternative for fossil fuels in the form of a clean fuel-hydrogen which can be generated by a renewable energy source-sunlight so as to protect our environment from greenhouse effect and global warming and to meet the ever increasing energy requirements.[28-31] With the depletion of fossil fuels, considerable efforts have been made by chemists to convert solar energy into storable chemical forms. Currently, molecular hydrogen (H_2) is one of the most promising sustainable energy supplies to replace conventional gasoline and diesel fuel because its combustion produces high energy density and non-toxic emissions. However, hydrogen is not readily available in the atmosphere. It is mainly produced by electrolysis and steam reforming which are not economically viable and environmentally polluting, respectively. The search for efficient and cost-effective methods to produce H_2 is therefore one of the most challenging tasks for the next few decades. A sunlight-triggered hydrogen evolution reaction (HER) would be an interesting solution. Although, catalysts for HER have been the subject of several reviews, considerable efforts are needed to provide an effective method to convert solar energy into hydrogen.[32-37] Since complexes **12-14** are similar to qtpy complexes which are known to show diverse catalytic activities, they should be of particular utility in major contemporary fields such as solar energy conversion. In addition, the amino groups present in DAT group can further enhance the photocatalytic activity of complexes.[38,39] Therefore, we have also tested **12-14** for hydrogen evolution reaction (HER).
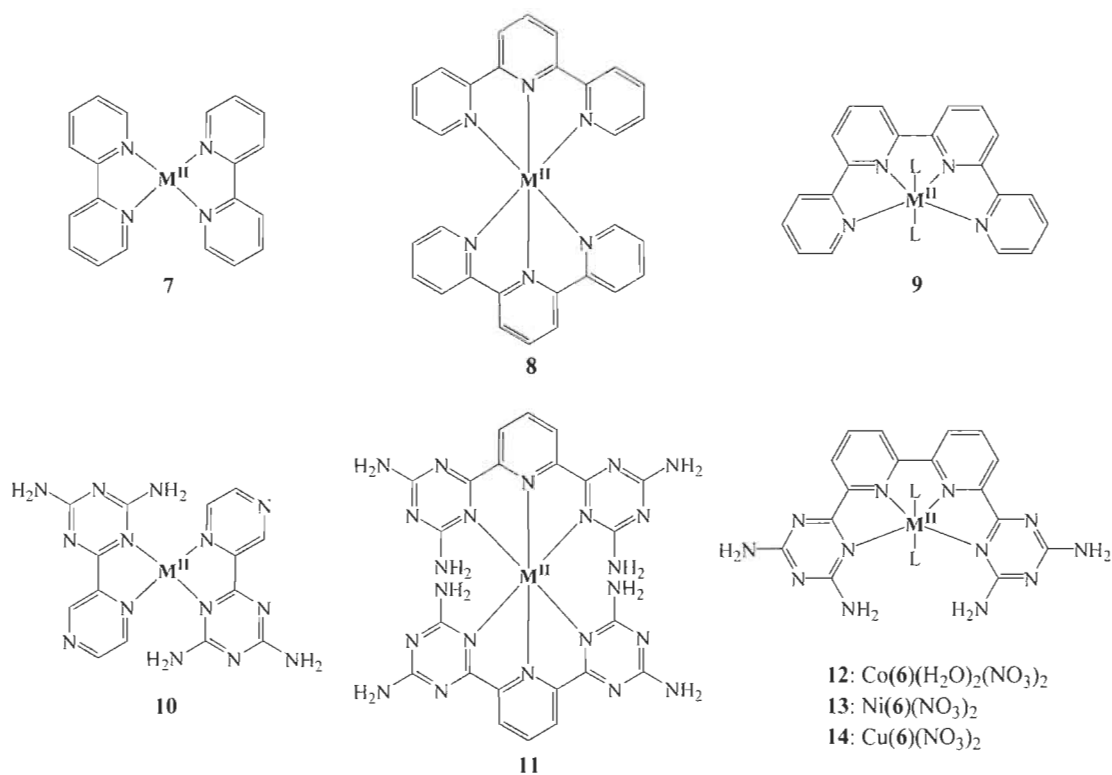
Chart 2. Molecular structures of complexes **7-14**.

3. Results and discussion

3.1. Syntheses and characterizations

6,6'-(2,2'-Bipyridine-6,6'-diyl)bis(1,3,5-triazine-2,4-diamine) **6** was obtained by reported method.[40] Complexes **12-14** were prepared by mixing the ligand (1 equiv.) with $M(NO_3)_2.xH_2O$ (1 equiv.) in MeOH. The precipitated solids were dissolved in DMSO and crystallized by slow diffusion with diethyl ether or ethyl acetate. Electrospray mass spectrometry of **12-14** gave peaks at m/z = 495.06, m/z = 216.04 and m/z = 218.54 which were assigned to species $[Co(6)(NO_3)]^+$, $[Ni(6)]^{2+}$ and $[Cu(6)]^{2+}$, respectively. The infrared spectra of these products showed the presence of NO_3^- group observed at 1313, 1313, 1323 cm^{-1} for complexes **12**, **13** and **14**, respectively (Fig. S5). The existence of ligand **6** was confirmed with -NH$_2$ bands in the range 3150-3500 cm^{-1}. The band positions for each spectrum are summarized in Table S4 along with their proposed

assignments. The compositions found by elemental analysis (EA) for each sample gives the general chemical formula $M(C_{16}H_{14}N_{12})(NO_3)_2$ (M = Co(II), Ni(II) and Cu(II)) which is consistent with the expected structures (see Experimental section).

3.2. Crystal structures of 12–14

In accordance with the previous investigation on qtpy ligands and their complexation by transition metal ions which demonstrate that 2,2':6',2":6",2'''-quaterpyridine tend to form mainly mononuclear complexes with metal ions favouring square planar or octahedral coordination geometry; the crystal structures of our complexes determined by SCXRD also showed that the ligand adopts a planar conformation with all N-donor sites oriented internally and the geometry of the resultant complexes were found to be distorted octahedral. However, these features can be modified upon the particular substitution pattern added to the oligopyridine core. The coordination of ligand **6** with cobalt(II), nickel(II) and copper(II) metal ions are expected to produce six-coordinate metal complexes in which the ligand has to twist out of planarity owing to steric interaction of the NH_2 of DAT groups. In all structures that we reported here, the metal ions show a strongly distorted octahedral coordination geometry and typical hydrogen bonding networks involving DAT groups (Chart 1b).

Crystals of **12** grown from DMSO/EtOAc were found to belong to the monoclinic space group *C2/c*. Views of the structure are shown in Fig. 1, and other crystallographic data are provided in Table 1. The central cobalt atom adopts the common coordination geometry for six-coordinated Co(II) with 2,2':6',2":6",2'''-quaterpyridine ligand type (Fig. 1a). The equatorial sites are occupied by the four inter nitrogen atoms of compound **6**. The two central Co-N_{py} bonds are slightly shorter than the two outer Co-N_{DAT} bonds. This is due to the constrained effect of the qtpy ligand type. Two water molecules are in axial positions to complete the coordination sphere to form the cationic complex $[Co(6)(H_2O)_2]^{2+}$. The distance Co-N and Co-O within the complex (2.173 °A for Co-N_{DAT}, 2.085 °A for Co-N_{py} and 2.124 °A for Co-O) have normal values in

comparison with reported structure of $[Co(qtpy)(H_2O)](NO_3)_2$.[41] The helicity of the ligand **6** in the complex is due to the steric interaction between the two NH_2 of DAT groups (Fig. 1a). In the crystal, both chiralities are observed and they are joined alternately into chains by characteristic hydrogen bonding of type **I** between DAT groups (average $N-H\cdots N$ distance = 3.059 °A), strengthened by additional $N-H\cdots O$ hydrogen bonds involving bridging of nitrate (Fig. 1b). With the assistance of hydrogen bonds involving bridging of DMSO and π-π stacking of heteroaromatic rings, the cationic chains pack to form layers, and the layers stack to produce the observed three-dimensional structure (Fig. 1c). Details of the hydrogen bonds and their angles are summarized in Table S1.
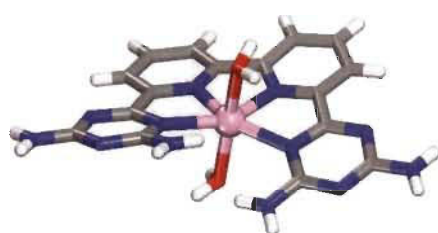
a
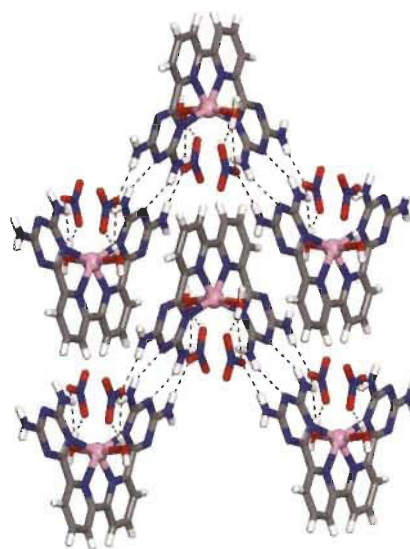
b
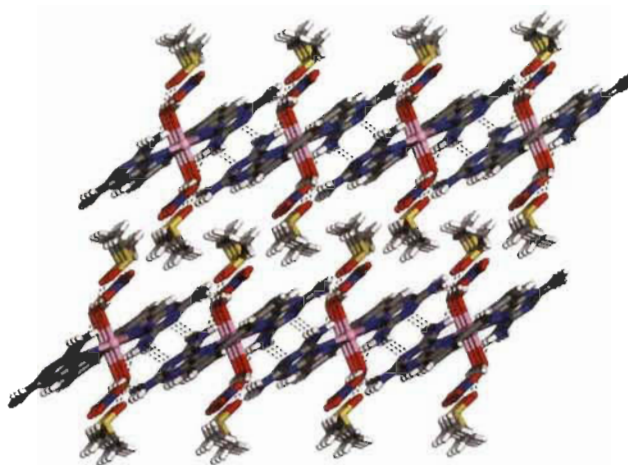
c

Fig. **1** Crystal structure of 6,6'-(2,2'-Bipyridine-6,6'-diyl)bis(1,3,5-triazine-2,4-diamine)(diaqua)cobalt(II) nitrate **12** grown from DMSO/EtOAc. (a) Perspective view of one cation of **12**, $[Co(6)(H_2O)_2]^{2+}$. (b) Alternating arrangement of complex **12** and its enantiomer to form chains mainly by hydrogen bonds involving DAT groups. Chains are then joined by π- π stacking of heteroaromatic rings. (c) Alternating packing of layers of complexes and layers of DMSO. Hydrogen bonds are represented by dashed lines. Unless stated otherwise, carbon atoms are shown in gray, hydrogen atoms in white, oxygen atoms in red, nitrogen atoms in blue and cobalt atoms in pink.

3.2.1. Table 1 Crystallographic data for complexes **12-14**[a]

	12	13	14
Crystallization condition	DMSO/EtOAc	DMSO/EtOAc	DMSO/THF
Empirical formula	$C_{10}H_{15}CoN_7O_5S$	$C_{32}H_{32}N_{28}Ni_2O_{14}$ + solvent	$C_{18}H_{18}CuN_{14}O_7$ + solvent
Formula weight	374.81	1150.27*	606.0*
Crystal system	monoclinic	triclinic	monoclinic
Radiation	GaKα	GaKα	GaKα
Temperature (K)	150	150	150

λ (Å))	1.34139	1.34139	1.34139
F(000)	1548.0	588*	1236*
Space group	$C2/c$	$P\bar{1}$	$P2_1/n$
Z	8	1	4
a (Å)	24.2963(6)	9.6118(5)	10.1245(3)
b (Å)	10.0731(3)	11.7609(6)	15.8382(4)
c (Å)	13.8796(4)	14.1181(8)	21.6268(6)
α (deg)	90	95.139(3)	90
β (deg)	111.1060(10)	91.020(3)	102.018(1)
γ (deg)	90	113.356(2)	90
V (Å³)	3169.00(15)	1456.81(14)	3391.93(16)
Crystal size/mm³	0.12 × 0.07 × 0.06	0.15 × 0.06 × 0.06	0.17 × 0.12 × 0.1
ρ_{calcd} (g/cm³)	1.571	1.311*	1.187*
μ (mm⁻¹)	4.163	3.961*	3.772*
Reflections collected	24490	21341	49606
Independent reflections	3634	6685	7797
R_{int}	0.0536	0.0583	0.0453
Observed reflections	3113	5349	7080
2θ range for data collection/°	6.79 to 121.48	5.46 to 121.67	6.06 to 121.65
Data/restraints/parameters	3634/0/217	6685/0/345	7797/4/393
R_1 [I > 2σ (I)]	0.0426	0.0554	0.0677
wR_2 [I >2σ (I)]	0.1057	0.1483	0.2067
R_1 (all data)	0.0531	0.0689	0.0721
wR_2 (all data)	0.1122	0.1569	0.2110
Goodness-of-fit on F^2	1.026	1.045	1.105
Largest diff. peak/hole / e Å⁻³	0.60/-0.48	0.562/-0.514	0.933/-0.583

[a] Disordered solvent molecules that were treated by a mask/squeeze procedure are not included in the calculation.

To further assess the potential of **6** to form various complexes with transition metals, we examined the product of the reaction of this ligand with $Ni(NO_3)_2.6H_2O$. Crystals of **13** grown from DMSO/EtOAc were found to have the composition $[Ni(6)(NO_3)(H_2O)].(NO_3).4DMSO$ and belonged to the triclinic space group $P\bar{1}$. Views of the structure are presented in Fig. 2, and other crystallographic data are provided in Table 1. In the structure, ligand **6**, a nitrate and a water molecule bind the metal ion to form a cationic complex $[Ni(6)(NO_3)(H_2O)]^+$ (Fig. 2a). The coordination geometry of the nickel can be considered as a distorted octahedral. The distance Ni-N and Ni-O within the complex (average distances = 2.166 °A for $Ni-N_{DAT}$, 2.021 °A for $Ni-N_{py}$, 2.083 °A for $Ni-O_{water}$ and 2.071 °A for $Ni-O_{nitrate}$) are consistent with those reported for quaterpyridine nickel complexes.[42] A direct comparison between the two structures with that of $[Co(6)(H_2O)_2]^{2+}$ and $[Ni(6)(NO_3)(H_2O)]^+$ reveals that the helicity is less marked in nickel complex **13**. As with **12**, the crystal structure of **13** is a racemate. The complex of **13** and its enantiomers are joined by hydrogen bonds of DAT groups according to motif I (average distance N–H···N = 2.462 °A) and by bridging of nitrate (N–H···O = 2.177 °A) to form zigzag chains. The chains are linked by hydrogen bonds involving oxygen atom from water molecule and the free hydrogen atom of -NH_2 group, and by the bridging of NO_3^- to produce layers (Fig. 2b). The final structure consists of alternating layers of complexes and molecules of DMSO (Fig. 2c). It is noteworthy that the geometry of coordination of the metal ion is reinforced by the intramolecular hydrogen bonds involving nitrato ligand and one of the -NH_2 groups. Selected hydrogen bonds and their angles are given in Table S2.

a

b

c
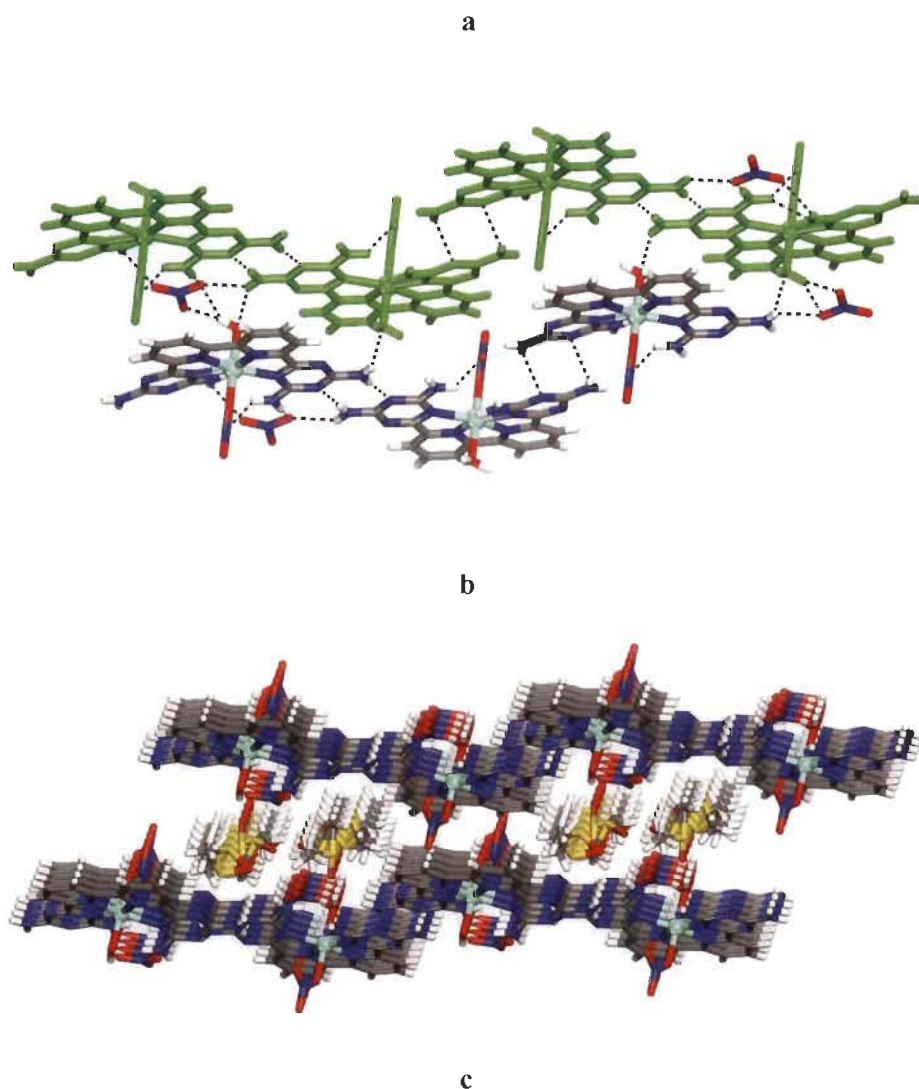
Fig. 2 Views of crystal structure of the 6,6'-(2,2'-Bipyridine-6,6'-diyl)bis(1,3,5-triazine-2,4-diamine)(aqua)(nitrato-O)nickel(II) **13** grown from DMSO/THF. (a) Perspective view of a cation of **13**, $[Ni(6)(NO_3)(H_2O)]^+$. (b) Alternating arrangement of complex **13** and its enantiomer held together by hydrogen bonds via DAT groups according to motif **I** and by bridging involving nitrate counter ion. For clarity one chain is marked in green. (c) View of alternating layers of complexes and disordered DMSO. Hydrogen bonds are represented by dashed lines. Unless stated otherwise, carbon atoms are shown in gray, hydrogen atoms in white, oxygen atoms in red, nitrogen atoms in blue and nickel atoms in cyan.

Unsurprisingly, the structure of Cu[II] complex **14** closely resembles that of **12** and **13**. Views of the structure are shown in Fig. 3, and other crystallographic data are given in Table 1. The coordination geometry of the copper atom can be described as a distorted octahedral with the four N inter atoms in equatorial and the two nitrates in axial positions. The average distances Cu-N_{py} and Cu-N_{DAT} are 1.962 °A and 2.065 °A, respectively (Fig. 3a). These values are consistent with those reported for quaterpyridine copper complexes.[41] The measured distances of the two Cu-O bonds (2.569 °A and 2.283 °A) suggest a Jahn-Teller effect.[43,44] In **14**, the N_{DAT}-Cu-N_{DAT} void angle of 125.3(4)° is somewhat less than the related value of 135.8(9)° in **12** and 129.4(1)° in **13**. In the structure of **14**, each DAT group is linked by two N–H···N hydrogen bonds of type **II** (average distance N–H···N = 3.075 °A) to form chains. Chains are then joined together via hydrogen bonds involving bridging of nitrato ligands to produce layers (Fig. 3b). Alternating packing of layers of complexes and DMSO generates the three-dimensional structure (Fig. 3c). Details of the hydrogen bonds and their angles are provided in Table S3.

a

b
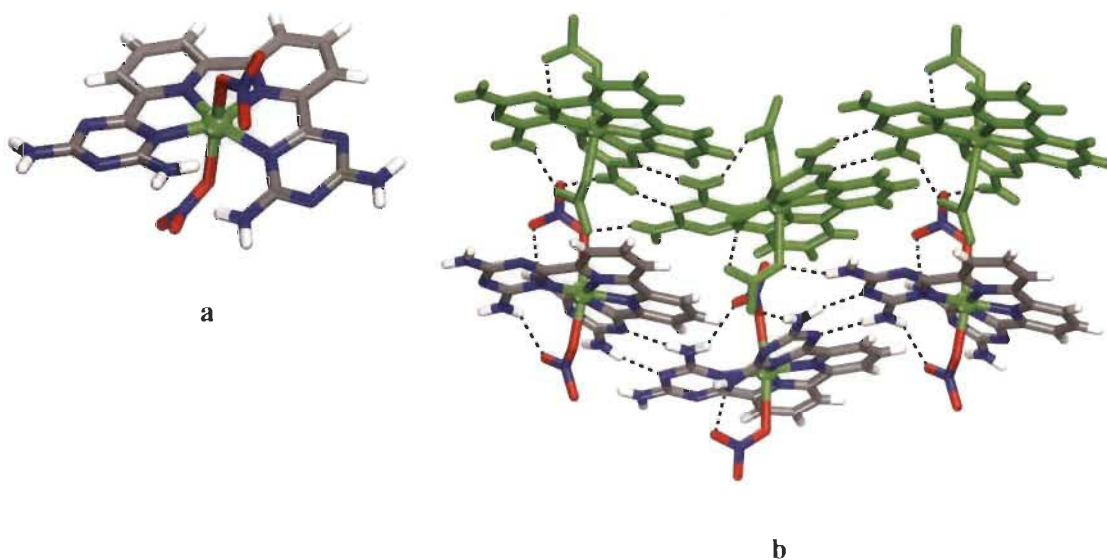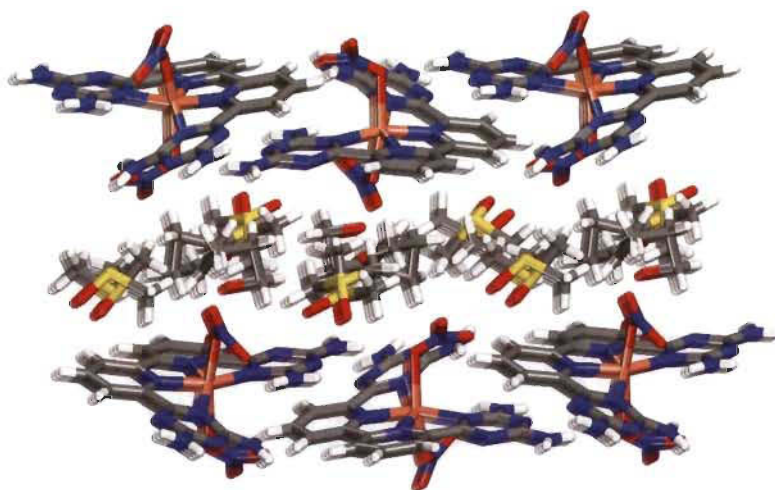
c

Fig. 3 Crystal structure of 6,6'-(2,2'-Bipyridine-6,6'-diyl)bis(1,3,5-triazine-2,4-diamine)(nitrato-O)copper(II) **14** grown from DMSO/THF. (a) Perspective view of **14**, Cu(**6**)(NO$_3$)$_2$. (b) Alternating arrangement of complex **14** and its enantiomer, which are held together by hydrogen bonds via DAT groups according to motif **II** and by bridging involving nitrato ligand and the free hydrogen of -NH$_2$ group. For clarity one chain is marked in green. (c) View of alternating layers of complexes and disordered DMSO. Hydrogen bonds are represented by dashed lines. Unless stated otherwise, carbon atoms are shown in gray, hydrogen atoms in white, oxygen atoms in red, nitrogen atoms in blue and copper atoms in green.

3.3. Thermal analysis of 6 and 12-14

Thermogravimetric analysis (TGA) were recorded on compounds **6** and **12-14** (Fig. S4). The samples were heated from ca. 25 to 800 °C at a rate of 10 °C min^{-1} under nitrogen atmosphere. The TG curve of the free ligand **6** present three steps (Fig. S4a). The first variation of mass at 117 °C is attributed to the loss of water molecules that are hydrogen bonded with the DAT groups. Decomposition of **6** starts at 434 °C. Compound **12** displays three steps mass losses (Fig. S4b). The first slight inflection at 100 °C with a mass loss of ~5 % is indicative of the loss of approximately two water molecules. The second and third steps in the range 307-367 °C and 367-

662 °C present mass losses of ~28 % and ~25 %, respectively. TG curves of **13** and **14** show similar patterns with the first decomposition that starts at ~270 °C (Fig. S4c and d).

3.4. Catalytic properties

3.4.1. Electronic characterization.

UV-Vis absorption spectra of **6** and **12-14** were performed at room temperature in DMF solution at concentration 8.8 x 10^{-6} M and at 8 x 10^{-3} M (Fig. 4). The electronic absorption spectrum of the free ligand **6** shows an intense absorption band at 292 nm accompanied with a small shoulder at 325 nm which is attributed to *n-π** and *π-π** transitions. The UV-Vis absorption spectra of **12** and **13** are similar. There are two intense intraligand transitions and a weak inflection between 350-500 nm that can be attributed to the *d-d* transitions.[45] In the case of **14**, one large band at around 275 nm is observed in the UV region and is assigned to intraligand transitions. Also, a broad band at 450 nm can be assigned to MLCT (Metal Ligand Charge Transfer) electronic transition.[46,47] Selected data (wavelengths (λ_{max}), molar absorptivity (ε)) are summarized in Table 2.
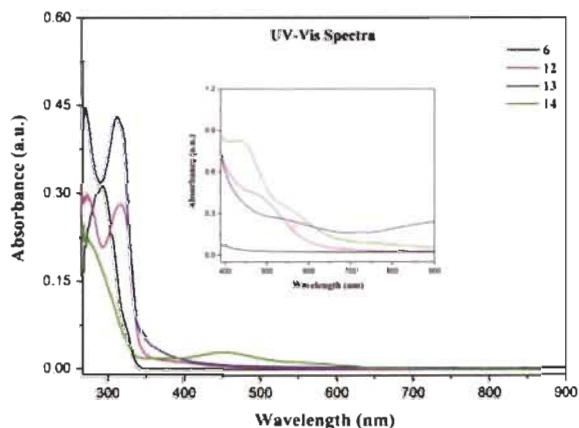
Fig. 4 UV-Vis spectra of **6** and **12-14** in DMF solution at room temperature at a concentration of 8.8 x 10^{-6} M. Inset shows the visible region (390-900 nm) at a concentration 8 x 10^{-3} M.

3.4.2. Table 2 Liquid state UV-Vis data of **6** and **12-14**[a]

Parameters / Sample	In DMF solution			
	Conc = 8.8 x 10^{-6} M From 267 to 900nm		Conc = 8 x 10^{-3} M From 390 to 900nm	
	λ_{max} (nm)	ε (mol^{-1} dm^3 cm^{-1})	λ_{max} (nm)	ε (mol^{-1} dm^3 cm^{-1})
6	292	3.56 x 10^4		
	325	8.44 x 10^3		
12	275	3.32 x 10^4	470	5.62 x 10^2
	318	3.19 x 10^4		
	400	1.45 x 10^3		
13	270	5.28 x 10^4	546	3.2 x 10^2
	311	4.92 x 10^4	722	2.06 x 10^2
	319	4.61 x 10^4		
14	275	2.52 x 10^4	435	1.03 x 10^3
	371	2.21 x 10^3	559	4.08 x 10^2
	455	3.64 x 10^3		
	555	1.38 x 10^3		

[a] λ: wavelength (nm); A: absorbance and ε: molar absorptivity's (mol^{-1} dm^3 cm^{-1}).

Electrochemical measurements of the free ligand **6** and complexes **12-14** were performed in anhydrous and degassed DMF solutions at concentration of compound 1 mmol dm^{-3} with 0.1 M TBA-PF$_6$ (tetrabutylammonium hexafluorophosphate) as a supporting electrolyte at a scan rate of 100 mV s^{-1}. Cyclic voltammograms (CV) of **6** did not show any reversible redox waves in the range -2.9 to -1.1 V (Fig. 5a). CV of complexes **12** and **13** shows clearly quasi reversible redox peaks at -1.18 V and -0.90 V and -1.08 V and -0.78 V, respectively which are attributed to the diverse redox states of the cobalt and nickel metal ions (Fig. 5b and c). These values are comparable with those of quaterpyridine complexes reported in literature (Table S5).[48,49] In the CV of complex **14**, there are multiple irreversible cathodic peaks in the negative range that correspond to the ligand reduction processes in **14** (Fig. 5d). The first redox event assimilated as the reduction of Cu(II) to Cu(I) occurs at 0.04 V, while the redox event occurring at 0.64 V is due to the oxidation of Cu(I) to Cu(II). The irreversible character of both linked events separated by 600 mV are presumably representative of rearrangement of coordination sphere or dimerization.[50] Table 3 summarizes the redox data of **6** and **12-14**.

a

b

c   d
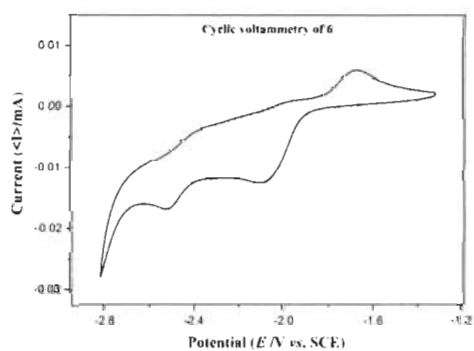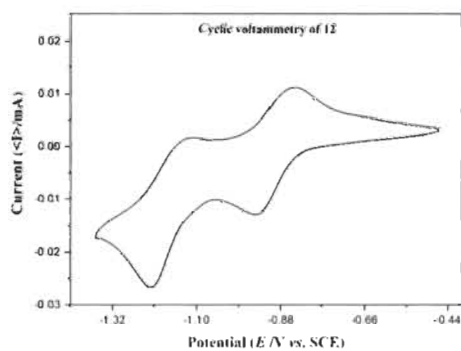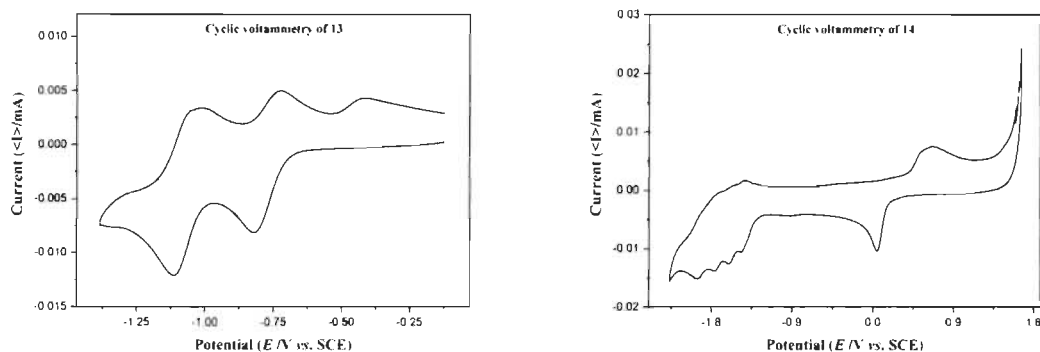
Fig. 5. Cyclic voltammograms of ligand **6** and complexes **12-14**.

3.4.3. Table 3 Cyclic voltammetry data of **6** and **12-14** in DMF solution

Compound	Eox1 |V|	Eox2 |V|	Ered1$_{1/2}$ |V|	Ered2$_{1/2}$ |V|	Ered3$_{1/2}$ |V|	Ered4$_{1/2}$ |V|	Ered5$_{1/2}$ |V|
6			-1.98(33)	-2.47(82)			
12			-0.90(15)	-1.18(09)	-1.47(02)	-1.78(22)	-2.19(49)
13			-0.78(43)	-1.08(29)	-1.63(45)	-1.94(48)	-2.25(50)
14	0.04(52) nr	0.67(00) nr	-1.43(85) nr	-1.56(74)	-1.73(79)	-1.90(84)	

nr: non-reversible

3.4.4. Hydrogen evolution reaction

The molecular structures of complexes **12-14** determined by single-crystal X-ray diffraction confirm that they are similar to mononuclear qtpy complexes. Previously, qtpy complexes have been used as photo/electro catalysts for CO_2 reduction.[48,50,51] As cobalt, nickel and copper complexes of 2,2':6',2':6''.2'''-quaterpyridine are known to be active catalysts for many chemical conversions, we have investigated the catalytic properties of complexes **12-14** for HER. To the best of our knowledge, there have been only two reports so far wherein non-functionalized qtpy complexes have been used for photocatalytic hydrogen production. In 2012, Leung and co-researchers synthesized $[Co^{II}(qtpy)(H_2O)_2]^{2+}$ complex which acted as an efficient photocatalyst

for hydrogen generation from $[Ir^{III}(dF(CF_3)ppy)_2(dtbbpy)]^+$/TEOA ($dF(CF_3)ppy$ = anion of 2-(2,4-difluorophenyl)-5-trifluoromethylpyridine, dtbbpy = 4,4'-di-*tert*-butyl-2,2'- bipyridine, TEOA = triethanolamine) in aqueous acetonitrile giving a maximum TON of 1730 at a 420 nm wavelength.[52] Recently, Hanan *et al.* synthesized $[Ru(qpy)_3]^{2+}$ (qpy = 4,4':2',2'':4'',4'''-quaterpyridine) complex and found it to be a suitable photosensitizer for hydrogen evolution in red light from triethanolamine (TEOA), HBF_4 (48 % in water) and $[Co(dmgH)_2]^{2+}$ catalyst exhibiting a TON of 375 far greater than the TON of 30 of the most studied photosensitizer $[Ru(bpy)_3]^{2+}$.[53] To the best of our knowledge, this is the first report wherein functionalised qtpy complexes have been used as potential photocatalysts for HER.

We performed HER under blue light (452 nm) in DMF solution containing the catalysts **12-14**, triethanolamine (TEOA) as the sacrificial electron donor, $Ru(bpy)_3(PF_6)_2$ as the photosensitizer (PS) and aqueous HBF_4 as the proton source. The experiment was conducted for 18 hours. The hydrogen production rate, turnover number (TON) and turnover frequency (TOF) have been reported in millimoles of hydrogen per hour, moles of hydrogen per mole of PS and mmol of hydrogen per mole of PS per minute respectively (Table 4). Under blue irradiation, the production of H_2 starts almost instantaneously after turning the light on (Fig. 6). Control experiments were conducted in the presence of PS/TEOA alone with and without light and no H_2 production was recorded which was consistent with the previous results.[54] For all our complexes, the maximum hydrogen production was reached after $\sim$ 3 h and stayed constant for up to 18 h. The maximum turnover numbers (TON's) are 56, 174 and 47 $mol_{H_2}\ mol_{PS}^{-1}$ for **12-14**, respectively (Fig. 6a). The turnover frequencies (TOF's) reached 1741 and 1782 $mmol_{H_2}\ mol_{PS}^{-1}.min^{-1}$ for **12** and **13**, respectively. In the case of complex **14**, the TOF's are 430 and 137 $mmol_{H_2}\ mol_{PS}^{-1}.min^{-1}$ (Fig. 6b). Complex **13** displayed superior HER properties because, the first reduction potential of **13** ($E_{1/2}^{red}$ = -0.78 V) is 120 mV less negative as compared to **12** ($E_{1/2}^{red}$ = -0.90 V) and since for **14**, no reversible event was observed, this indicates that the excited Ru(II) complex can more readily

185

transfer electrons to **13** as compared to **12** and **14**. To confirm the photocatalytic activity of our complexes, blank experiments were carried out with $Co(NO_3)_2.6H_2O$, $Ni(NO_3)_2.6H_2O$ and $Cu(NO_3)_2.2.5H_2O$ which displayed TON's of 9.96, 18.54 and 0.58 mol_{H_2} mol_{PS}^{-1} respectively, clearly indicating that the salt alone cannot act as a photocatalyst (Fig. S8). In accordance with the results obtained by Probst *et al.* in 2009 who studied the effect of pH on the photocatalytic HER using the reference catalyst $[Co(dmgH)_2]$, we deduce that in our photocatalytic experiments, HBF_4 is the major proton source, while water and TEOA acts as a subsidiary proton source.[55] The mechanism of hydrogen evolution reaction can occur by the process of oxidative quenching of the excited Ru(II)* complex proceeded by hydrogen production via heterolytic pathway, which is proposed in the ESI.[56]

a   b
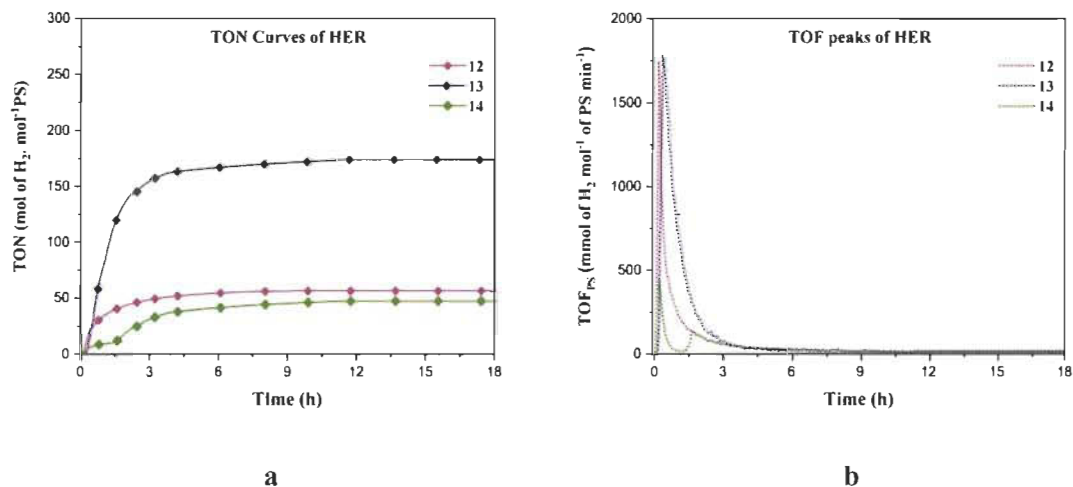
Fig. 6 Hydrogen evolution reaction of 1 mM of **12-14** in blue light. (a) TON's and (b) TOF's.

3.4.5. Table 4 Turnover number and turnover frequency maximal for complexes **12-14**[a]

Compound	Molecular Formula	H_2 production (mmol/hour)	TON_{max}	TOF_{max} (min^{-1})
12	$Co(6)(NO_3)_2$	0.31	56	1741
13	$Ni(6)(NO_3)_2$	0.96	174	1782
14	$Cu(6)(NO_3)_2$	0.26	47	430, 137

[a] TON is reported in moles of hydrogen per mole of PS and TOF in mmol of hydrogen per mole of PS per minute.

4. Conclusion

In this work, the synthesis and characterisation of $-NH_2$ functionalized qtpy-like complexes of Co(II), Ni(II) and Cu(II) is undertaken and they are employed as photocatalysts for HER. Three novel $-NH_2$ functionalized qtpy complexes **12-14** with the general formula $M(C_{16}H_{14}N_{12})(NO_3)_2$ (M = CoII, NiII or CuII) have been successfully synthesized *via* an easy synthetic procedure giving high yield and purity. In all complexes, the metal ions show a strongly distorted octahedral coordination geometry and typical hydrogen bonding networks involving DAT groups. In addition, we investigated the photocatalytic activity of complexes **12-14** in DMF solution for HER under blue light (452 nm) using triethanolamine (TEOA) as the sacrificial electron donor, $Ru(bpy)_3(PF_6)_2$ as the photosensitizer (PS) and aqueous HBF_4 as the proton source. Turnover numbers of 56, 174 and 47 moles of H_2 per mole of PS were observed for complexes **12-14**, respectively. Thus, the present work serves a dual purpose of easy synthesis of functionalized qtpy complexes **12-14** and their use as photocatalysts for HER.

5. Experimental section

5.1. General notes and procedures for the synthesis of complexes 12-14

6,6'-(2,2'-bipyridine-6,6'-diyl)bis(1,3,5-triazine-2,4-diamine) **6** was synthesized according to the reported method.[40] Their complexes with Co(II), Ni(II) and Cu(II), respectively, were prepared by the experimental procedure described below. Other chemicals were commercially available and were purchased and used without any additional purification. Solid of **6** (1.0 equiv, 0.05g, 0.1335mmol) was added in small portions at 25 °C to stirred solutions of Co(NO$_3$)$_2$. 6H$_2$O, Ni(NO$_3$)$_2$. 6H$_2$O and Cu(NO$_3$)$_2$. 2.5H$_2$O (1 equiv), respectively, in MeOH (25 mL). The mixtures were refluxed for 12 h and the resulting coloured precipitates were cooled to room temperature, filtered, dried and subjected to crystallization by slow diffusion using dimethyl sulfoxide as a solubilizing agent.

5.1.1. Synthesis of [6,6'-(2,2'-bipyridine-6,6'-diyl)bis(1,3,5-triazine-2,4-diamine)](nitrato-O)cobalt(II).

Complex **12** was synthesized and crystallized in 74 % yield by the slow diffusion of EtOAc over DMSO solution. FTIR (ATR): 3436, 3338, 3219, 3165, 3099, 3084, 1661, 1617, 1591, 1567, 1525, 1482, 1454, 1423, 1390, 1313, 1276, 1203, 1165, 1077, 1045, 1029, 991, 955, 832, 800, 758, 742, 705, 681, 648, 625, 572 cm^{-1}. HRMS (ESI) calcd for [C$_{16}$H$_{14}$CoN$_{12}$NO$_3$]$^+$ m/e 495.06690, found 495.06600. Anal. Calcd for C$_{16}$H$_{14}$CoN$_{14}$O$_6$: C, 34.48; H, 2.53; N, 35.19. Found: C, 34.71; H, 2.46; N, 34.78.

5.1.2. Synthesis of [6,6'-(2,2'-bipyridine-6,6'-diyl)bis(1,3,5-triazine-2,4-diamine)](nitrato-O)nickel(II).

Complex **13** was synthesized and crystallized in 71% yield by the slow diffusion of EtOAc over DMSO solution. FTIR (ATR): 3458, 3381, 3340, 3230, 3185, 3100, 3083, 1668, 1658, 1616, 1586,

1568, 1523, 1481, 1470, 1418, 1389, 1329, 1313, 1284, 1201, 1179, 1164, 1136, 1071, 1044, 1032, 987, 955, 927, 917, 831, 816, 800, 758, 745, 729, 705, 697, 688, 654, 623, 579 cm^{-1}. HRMS (ESI) calcd for $[C_{16}H_{14}NiN_{12}]^{2+}$ m/e 216.0403, found 216.0405. Anal. Calcd for $C_{16}H_{14}N_{14}NiO_6$: C, 34.50; H, 2.53; N, 35.20. Found: C, 34.72; H, 2.50; N, 34.76.

5.1.3. Synthesis of [6,6'-(2,2'-bipyridine-6,6'-diyl)bis(1,3,5-triazine-2,4-diamine)](nitrato-O)copper(II).

Complex **14** was synthesized and crystallized in 79% yield by the slow diffusion of THF over DMSO solution. FTIR (ATR): 3420, 3360, 3316, 3214, 3154, 3085, 3064, 1655, 1629, 1601, 1590, 1574, 1534, 1522, 1513, 1480, 1470, 1417, 1371, 1323, 1288, 1270, 1201, 1163, 1134, 1083, 1074, 1058, 1040, 981, 951, 912, 827, 799, 765, 749, 720, 700, 660 cm^{-1}. HRMS (ESI) calcd for $[C_{16}H_{14}CuN_{12}]^{2+}$ m/e 218.5430, found 218.5378. Anal. Calcd for $C_{16}H_{14}N_{14}CuO_6$: C, 34.20; H, 2.51; N, 34.90. Found: C, 34.28; H, 3.07; N, 33.68.

5.2. Characterization studies of compounds 6 and 12-14

Crystallographic data were collected using a Bruker Venture Metaljet diffractometer with Ga Kα radiation. The structures were solved by direct methods using Olex2, and non-hydrogen atoms were refined anisotropically with Least Squares minimization.[57,58] Hydrogen atoms were treated by first locating them from difference Fourier maps, recalculating their positions using standard values for distances and angles, and then refining them as riding atoms. Microcrystalline powders were analyzed in transmission-mode geometry using a Bruker D8-Discover instrument (θ-θ geometry) equipped with an XYZ platform and a HI-STAR gas detector. X-rays were generated using a conventional sealed-tube source with a copper anode producing Cu Kα radiation (λ = 1.54178 Å). The samples were gently ground and then mounted on a flat Kapton sample holder. The data collection involved acquisition of two different sections with increasing angular position,

giving two different 2D frames. These frames were integrated and combined to produce the final 1D X-ray diffraction powder pattern. Calculated X-ray powder diffraction patterns were generated from the structural data in corresponding CIF resulting from single-crystal analyses, the calculation was performed using Mercury software of the Cambridge Crystallographic Data Centre.[59] A unique value of the FWHM for the diffraction peaks was adjusted in order to get a better match between the resolution of the experimental and the calculated patterns. The determination of the total carbon, hydrogen, nitrogen, and sulphur (C, H, N, S) content in the compounds was performed using EA 1108 Fisons CHNS Element analyzer with the quantitative '*dynamic flash combustion*' method. UV-visible spectra were recorded on a Cary 5000. The ATR-FTIR spectra were observed with a Nicolet iS 10 Smart FT-IR Spectrometer within 600-4000 cm^{-1}. The thermogravimetry analysis was performed using Mettler Toledo TGA1. The samples were studied from 25 to 800 °C with a heating rate of 10 °C/min.

5.3. Electrochemical measurements of compounds 12-14

Electrochemical measurements were performed in pure dimethylformamide purged with argon at room temperature with a BAS SP-50 potentiostat. Glassy carbon electrode was used as a working electrode, the counter electrode was a Pt wire and silver wire were the pseudo-reference electrode. The reference of electrochemical potential was set using 1 mM ferrocene as an internal standard and the values of potentials are reported vs SCE.[60] The concentrations of samples were 1mM. Tetrabutylammonium hexafluorophosphate (TBAP) (0.1 M) was used as supporting electrolyte. Cyclic voltammograms were obtained at a scan rate of 100 mV/s and current amplitude of 100 μA.

5.4. Photocatalytic Experiments

A PerkinElmer Clarus-480 gas chromatograph (GC) was used to measure hydrogen gas evolved from the reaction. The assembly of the chromatograph consists of a thermal conductivity detector, a 7-inch HayeSep N 60/80 pre-column, a 9-inch molecular sieve 13*45/60 column, a 2 mL injection loop and argon gas as carrier and eluent. DMF was the solvent of choice for our experiments. Three separate solutions of 1) sacrificial donor and proton source, 2) photosensitizer [Ru(bpy)$_3$] (PF$_6$)$_2$ and 3) catalyst were prepared in order to obtain 5 mL of sample solutions in standard 20 mL headspace vials. In DMF, the resulting molar concentration of photocatalytic components were: 1 M for triethanolamine (TEOA), 0.1 M for (HBF$_4$), 0.56 M for water, 0.1 mM for the photosensitizer [Ru(bpy)$_3$] (PF$_6$)$_2$ and 1 mM catalyst (**12-14**) (pH apparent = 8-9). The resulting mixture was placed on a panel of blue LED 10 W center at 445 nm in a thermostatic bath set at 20°C which was sealed with a rubber septum and two stainless-steel tubes pierced in it. Argon was carried in the first tube at a flow rate of 10 ml min^{-1} (flow rate adjusted with a manual flow controller (Porter, 1000) and referenced with a digital flowmeter (Perkin Elmer Flow Mark)). The second stainless steel tube carried the flow to the GC sample loop passing through a 2 ml overflow protection vial and an 8-port stream select valve (VICCI). Timed injections were done by a microprocessor (Arduino Uno) coupled with a custom PC interface. Corresponding to a specific argon flow, H$_2$ production rate was calibrated. For calibration of H$_2$ production rate at a specific argon flow, a syringe pump (New Era Pump) equipped with a gas-tight syringe (SGE) and a 26s-gauge needle (Hamilton) was used to bubble different rates of pure hydrogen gas into the sample, to a minimum of 0.5 μL/minute. This gave a linear fit for peak area for H$_2$ versus the flow rates of H$_2$. For calibration testing, stock cylinders of known concentration of H$_2$ in argon replaced the argon flow (inserted at the pre-bubbler, to keep the same vapor matrix). The measured results independent of flow rate (under same pressure) can be easily converted into the rate of hydrogen using equation 1. The errors associated to the TON and TOF are estimated to be 10 %.[61]

Equation 1

Rate of production of H_2 (μL min^{-1}) = [H_2 standard] (ppm) x Ar flow rate (L min^{-1})

6. Conflicts of Interest

There are no conflicts to declare.

7. Acknowledgments

8. Supporting information available

The supporting Information is available free of charge via the internet at RSC Publications website at DOI: https://doi.org/10.1039/C9RA04303A

Additional crystallographic details (including thermal atomic displacement ellipsoid plots), TGA curves, IR and CV data (PDF)

9. Accession Codes

CCDC 1919278-1919280 contain the supplementary crystallographic data for this paper. These data can be obtained free of charge via www.ccdc.cam.ac.uk/data_request/cif, of by email data_request@ccdc.cam.ac.uk, or by contacting The Cambridge Crystallographic Data Centre, 12 Union Road Cambridge CB2 1EZ, UK; fax: +44 1223 336033.

10. AUTHOR INFORMATION

Corresponding Author

*E-mail: adam.duong@uqtr.ca.

ORCID

Thierry Maris: 0000-0001-9731-4046

Adam Duong: 0000-0002-4927-3603

Prabhjyot Kaur: 0000-0001-9339-1247

11. Notes

The authors declare no competing financial interest.

12. References

1 P. Pachfule, T. Panda, C. Dey and R. Banerjee, *Cryst. Eng. Comm*, 2010, **12**, 2381-2389.

2 E. D. Bloch, D. Britt, C. Lee, C. J. Doonan, F. J. Uribe-Romo, H. Furukawa, J. R. Long and O. M. Yaghi, *J. Am. Chem. Soc.*, 2010, **132**, 14382-14384.

3 A. Peter, M. Mohan, T. Maris, J. D. Wuest and A. Duong, *Cryst. Growth Des.*, 2017, **17**(10), 5242-5248.

4 C. M. A. Ollagnier, D. Nolan, C. M. Fitchett and S. M. Draper, *Supramol. Chem.*, 2012, **24**(8), 563-571.

5 A. Duong, S. Rajak, A. A. Tremblay, T. Maris and J. D. Wuest, *Cryst. Growth Des.*, 2019, **19**(2), 1299-1307.

6 D. Xiao, Y. Hou, E. Wang, J. Lu, Y. Li, L. Xu and C. Hu, *Inorg. Chem. Commun.*, 2004, **7**, 437-439.

7 S. Rajak, M. Mohan, A. A. Tremblay, T. Maris, S. Leal do Santos, E. C. Venancio, S. F. Santos and A. Duong, *ACS Omega*, 2019, **4**, 2708-2718.

8 D. B. D. Amico, F. Calderazzo, M. Curiardi, L. Labella and F. Marchetti, *Inorg. Chem. Commun.*, 2005, **8**, 673-675.

9 A. Duong, T. Maris and J. D. Wuest, *Cryst. Growth Des.*, 2011, **11**, 287-294.

10 A. K. Pal, A. Duong, J. D. Wuest and G. S. Hanan, *Polyhedron*, 2016, **108**, 100-103.

11 A. Duong, M.-A. Dubois, T. Maris, V. Metivaud, J.-H. Yi, A. Nanci, A. Rochefort and J. D. Wuest, *J. Phys. Chem. C*, 2011, **115**(26), 12908-12919.

12 A. Duong, V. Metivaud, T. Maris and J. D. Wuest, *Cryst. Growth Des.*, 2011, **11**(5), 2026-2034.

13 D. Braga, L. Brammer and N. R. Champness, *Cryst. Eng. Comm*, 2005, **7**, 1-19.

14 A. Duong, T. Maris and J. D. Wuest, *Inorg. Chem.*, 2011, **50**(12), 5605-5618.

15 D. Salazar-Mendoza, S. A. Baudron and M. W. Hosseini, *Chem. Commun.*, 2007, 2252-2254.

16 D. Braga, S. L. Giaffreda, F. Grepioni, L. Maini and M. Polito, *Coord. Chem. Rev.*, 2006, **250**, 1267-1285.

17 D. A. McMorran, *Inorg. Chem.*, 2008, **47**, 592-601.

18 S. G. Telfer and J. D. Wuest, *Chem. Commun.*, 2007, 3166-3168.

19 E. C. Constable, Prog. *Inorg. Chem.*, 1994, **42**, 67.

20 M. Mascal, Contemp. *Org. Synth.*, 1994, **31**.

21 T. Hasegawa, Y. Furusho, H. Katagiri and E. Yashima, *Angew. Chem.*, 2007, **119**, 5989.

22 F. Cardinalli, H. Mamlouk, Y. Rio, N. Armaroli and J.-F. Nierengarten, *Chem. Commun.*, 2004, 1582.

23 T. Hasegawa, Y. Furusho, H. Katagiri and E. Yashima, *Angew. Chem.*, Int. Ed., 2007, **46**, 5885-5888.

24 G. I. Pascu, A. C. G. Hotze, C. Sanchez-Cano, B. M. Kariuki and M. J. Hannon, *Angew. Chem.,* Int. Ed., 2007, **46**, 4374-4378.

25 J.-M. Lehn, *Angew. Chem., Int. Ed. Engl.*, 1990, **29**, 1304-1319.

26 J. L. Serrano and T. Sierra, *Coord. Chem. Rev.*, 2003, **242**, 73-85.

27 A.-M. Stadler, N. Kyritsakas, G. Vaughan and J.-M. Lehn, *Chem. -Eur. J.*, 2007, **13**, 59-68.

28 N. S. Lewis, D. G. Nocera and P. Natl, Proc. Natl. Acad. Sci. U. S. A., 2006, **103**, 15729-15735.

29 M. Wang, L. Chen and L. C. Sun, *Energy Environ. Sci.*, 2012, **5**, 6763-6778.

30 M. Serra, J. Albero and H. Garc, *Chem. Phys. Chem*, 2015, **16**, 1842-1845.

31 J. A. Turner, Sustainable hydrogen production, *Science*, 2004, **305**, 972-974.

32 M. G. Pfeffer, T. Kowacs, M. W¨achtler, J. Guthmuller, B. Dietzek, J. G. Vos and S. Rau, *Angew. Chem., Int. Ed.*, 2015, **54**, 6627-6631.

33 P. L. Catherine and M. J. M. Alexander, *ACS Catal.*, 2014, **4**, 2727-2733.

34 P. N. Curtin, L. L. Tinker, C. M. Burgess, E. D. Cline and S. Bernhard, *Inorg. Chem.*, 2009, **48**, 10498-10506.

35 T. M. McCormick, B. D. Calitree, A. Orchard, N. D. Kraut, F. V. Bright, M. R. Detty and R. Eisenberg, *J. Am. Chem. Soc.*, 2010, **132**, 15480-15483.

36 M. Nippe, R. S. Khnayzer, J. A. Panetier, D. Z. Zee, B. S. Olaiya, M. Head-Gordon, C. J. Chang, F. N. Castellano and J. R. Long, *Chem. Sci.*, 2013, **4**, 3934-3945.

37 M. A. Gross, A. Reynal, J. R. Durrant and E. Reisner, *J. Am. Chem. Soc.*, 2014, **136**, 356-366.

38 L. Li, S. Zhu, R. Hao, J.-J. Wang, E.-C. Yang and X.-J. Zha, *Dalton Trans.*, 2018, **47**, 12726-12733.

39 Q. Liu, C. Chen, M. Du, Y. Wu, C. Ren, K. Ding, M. Song and C. Huang, *ACS Appl. Nano Mater.*, 2018, **1**, 4566-4575.

40 A. Duong, T. Maris, O. Lebel and J. D. Wuest, *J. Org. Chem.*, 2011, **76**, 1333-1341.

41 V. W. Henke, S. Kremer and D. Reinen, Z. Anorg. *Allg. Chem.*, 1982, **491**, 124-136.

42 E. C. Constable, S. M. Elder, J. Healy and D. A. Tocher, *J. Chem. Soc., Dalton Trans.*, 1990, 1669.

43 B. Murphy, M. Aljabri, A. M. Ahmed, G. Murphy, B. J. Hathaway, M. E. Light, T. Geilbrich and M. B. Hursthouse, *Dalton Trans.*, 2006, **2**, 357-367.

44 A. Meyer, G. Schnakenburg, R. Glaum and O. Schiemann, *Inorg. Chem.*, 2015, **54**, 8456-8464.

45 C.-W. Chan, T.-F. Lai and C.-M. Che, J. Chem. Soc., *Dalton Trans.*, 1994, **6**, 895-899.

46 V. Kalsani, M. Schmittel, A. Listorti and N. Armaroli, *Inorg. Chem.*, 2006, **45**, 2061.

47 A. Adamski, M. Walesa-Chorab, M. Kubicki, Z. Hnatejko and V. Patroniak, *Polyhedron*, 2014, **81**, 188-195.

48 K.-M. Lam, K.-Y. Wong, S.-M. Yang and C.-M. Che, J. Chem. Soc., *Dalton Trans.*, 1995, **7**, 1103-1107.

49 E. C. Constable, S. M. Elder, M. J. Hannon, A. Martin, P. R. Raithby and D. A. Tocher, *J. Chem. Soc., Dalton Trans.*, 1996, 2423-2433.

50 Z. Guo, F. Yu, Y. Yang, C.-F. Leung, S.-M. Ng, C.-C. Ko, C. Cometto, T.-C. Lau and M. Robert, *ChemSusChem*, 2017, **10**, 4009-4013.

51 Z. Guo, S. Cheng, C. Cometto, E. Anxolabehere-Mallart, S.-M. Ng, C.-C. Ko, G. Liu, L. Chen, M. Robert and T.-C. Lau, *J. Am. Chem. Soc.*, 2016, **138**(30), 9413-9416.

52 S. C.-F. Leung, S.-M. Ng, C.-C. Ko, W.-L. Man, J.-S. Wu, L.-J. Chen and T.-C. Lau, *Energy Environ. Sci.*, 2012, **5**, 7903-7907.

53 E. Rousset, D. Chartrand, I. Ciofini, V. Marvaud and G. S. Hanan, *Chem. Commun.*, 2015, **51**, 9261.

54 R. W. Hogue, O. Schott, G. S. Hanan and S. Brooker, *Chem.– Eur. J.*, 2018, **24**, 9820-9832.

55 B. Probst, C. Kolano, P. Hamm and R. Alberto, *Inorg. Chem.*, 2009, **48**, 1836-1843.

56 V. Artero, M. Chavarot-Kerlidou and M. Fontecave, *Angew. Chem.*, 2011, **50**(32), 7238-7266.

57 G. M. Sheldrick, *Acta Crystallogr., Sect. C: Struct. Chem.*, 2015, **71**, 3-8.

58 G. M. Sheldrick, *Acta Crystallogr., Sect. A: Found. Adv.*, 2015, **71**, 3-8.

59 C. F. Macrae, P. R. Edgington, P. McCabe, E. Pidcock, G. P. Shields, R. Taylor, M. Towler and J. Streek, *J. Appl. Crystallogr.*, 2006, **39**, 453-457.

60 N. G. Connelly and W. E. Geiger, *Chem. Rev.*, 1996, **96**, 877-910.

61 C. Lentz, O. Schott, T. Auvray, G. S. Hanan and B. Elias, *Inorg. Chem.*, 2017, **56**(18), 10875-10881.

4.4. Conclusion

The present project serves a dual purpose, (i) facile synthesis of functionalized quarterpyridine complexes **12-14** and (ii) efficient catalysts for hydrogen evolution reaction (HER). To the best of our knowledge, this is the premier investigation on the coordination chemistry of ligand **6**. Three novel -NH$_2$ functionalized qtpy complexes **12-14** have been synthesized with high yield, high purity and easy synthetic procedure. All complexes involve distorted octahedral geometry and typical hydrogen-bonding networks of the DAT groups. Low cost transition metals salts like Co (II), Ni (II) and Cu (II) were chosen for coordination instead of expensive noble metals (Pt, Pd and Ir). Complexes **12-14** display good catalytic activities and produce H$_2$ with the turnover numbers of 56, 174 and 47 moles of H$_2$ per mole of PS respectively. Our work provides a remedy to the lack of straight forward and efficient synthesis of functionalized 2,2':6',2'':6'',2'''-quaterpyridine (qtpy) ligands and their complexes.

4.5. Supporting Information

X-ray Crystallographic data

Fig. S1. Thermal atomic displacement ellipsoid plot of the structure of **12** grown from DMSO/ EtOAc. The ellipsoids of non-hydrogen atoms are drawn at 50% probability level, and hydrogen atoms are represented by a sphere of arbitrary size.
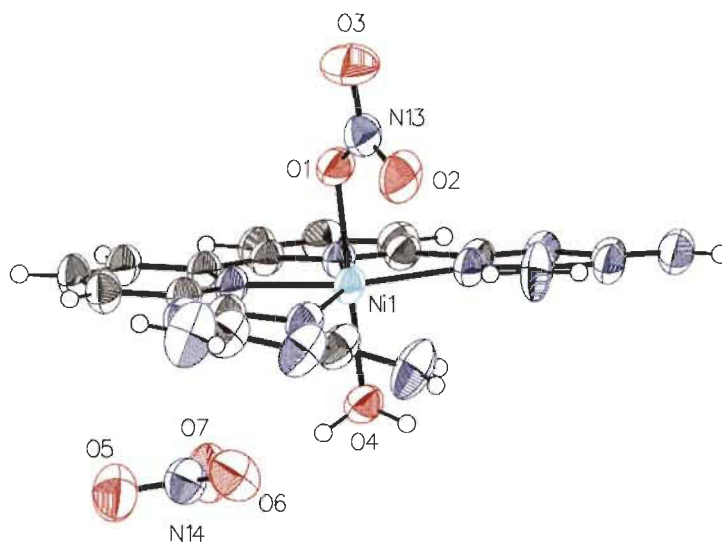
Fig. S2. Thermal atomic displacement ellipsoid plot of the structure of **13** grown from DMSO/EtOAc. The ellipsoids of non-hydrogen atoms are drawn at 50% probability level, and hydrogen atoms are represented by a sphere of arbitrary size.
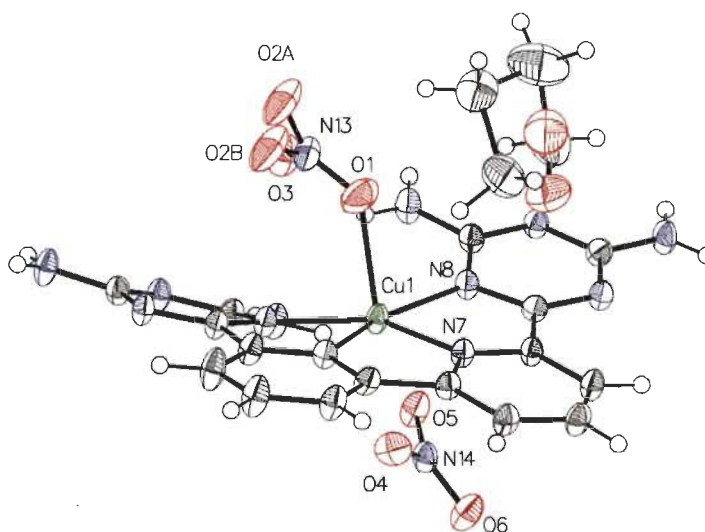
Fig. S3. Thermal atomic displacement ellipsoid plot of the structure of **14** grown from DMSO/THF. The ellipsoids of non-hydrogen atoms are drawn at 50% probability level, and hydrogen atoms are represented by a sphere of arbitrary size.

Table S1. Hydrogen-bond geometry (Å, °) in structure of **12**

D—H$\cdots A$	D—H	H$\cdots A$	$D\cdots A$	D—H$\cdots A$
O1—H1$A\cdots$O2	0.88	2.46	3.165 (3)	138
O1—H1$A\cdots$O4	0.88	1.93	2.789 (3)	164
O1—H1$A\cdots$N7	0.88	2.55	3.403 (3)	167
O1—H1$B\cdots$S1	0.88	2.94	3.6667 (18)	142
O1—H1$B\cdots$O5	0.88	1.86	2.727 (3)	167
N5—H5$A\cdots$N3^{i}	0.88	2.24	3.059 (3)	156
N5—H5$B\cdots$O2	0.88	2.16	2.811 (3)	131
N6—H6$A\cdots$O2^{i}	0.88	2.09	2.962 (3)	173
N6—H6$B\cdots$O5^{ii}	0.88	2.03	2.878 (3)	162

Symmetry codes: (i) $-x+1$, $-y+2$, $-z+1$; (ii) $-x+1$, $-y+1$, $-z+1$.

Table S2. Hydrogen-bond geometry (Å, °) in structure of **13**

D—H$\cdots A$	D—H	H$\cdots A$	$D\cdots A$	D—H$\cdots A$
N11—H11$A\cdots$O5	0.83 (4)	2.17 (4)	2.998 (3)	172 (3)
N11—H11$B\cdots$O5^{i}	0.88 (5)	2.59 (4)	3.180 (3)	125 (3)
N11—H11$B\cdots$O6^{i}	0.88 (5)	2.19 (5)	3.051 (3)	165 (4)
N5—H5$A\cdots$O2	0.85 (4)	2.24 (4)	2.957 (3)	142 (3)
N5—H5$A\cdots$N11	0.85 (4)	2.54 (4)	3.153 (3)	129 (3)
N5—H5$B\cdots$O9	0.79 (4)	2.19 (4)	2.954 (4)	161 (4)
N6—H6$A\cdots$O10	0.87 (4)	2.06 (4)	2.926 (3)	173 (3)
N6—H6$B\cdots$O4^{ii}	0.81 (4)	2.25 (4)	3.040 (3)	165 (4)
N12—H12$A\cdots$O8	0.80 (4)	2.11 (4)	2.903 (4)	170 (4)
N12—H12$B\cdots$O7	0.79 (4)	2.23 (4)	2.994 (4)	162 (4)

Symmetry codes: (i) $-x+1$, $-y+1$, $-z+1$; (ii) $-x$, $-y+1$, $-z+1$.

Table S3. Hydrogen-bond geometry (Å, $^\circ$) in structure of **14**

D—H$\cdots A$	D—H	H$\cdots A$	$D\cdots A$	D—H$\cdots A$
N5—H5$A\cdots$O20A^{i}	0.88	2.01	2.822 (7)	153
N5—H5$A\cdots$O20B^{i}	0.88	1.97	2.826 (16)	163
N5—H5$B\cdots$O5	0.88	2.14	2.941 (4)	151
N6—H6$A\cdots$O6$^{\text{ii}}$	0.88	2.10	2.966 (4)	169
N6—H6$B\cdots$N9$^{\text{iii}}$	0.88	2.17	3.023 (4)	163
N11—H11$A\cdots$N4$^{\text{i}}$	0.88	2.25	3.129 (4)	176
N11—H11$B\cdots$O3	0.88	2.25	2.972 (5)	140
N11—H11$B\cdots$N5	0.88	2.56	3.130 (5)	124
N12—H12$A\cdots$O4$^{\text{iv}}$	0.88	2.12	2.936 (4)	154
N12—H12$B\cdots$O21A^{iv}	0.88	1.96	2.800 (6)	158

Symmetry codes: (i) $-x+1/2, y-1/2, -z+3/2$; (ii) $x-1, y, z$; (iii) $-x+1/2, y+1/2, -z+3/2$; (iv) $-x+3/2, y-1/2, -z+3/2$.

Thermal analysis
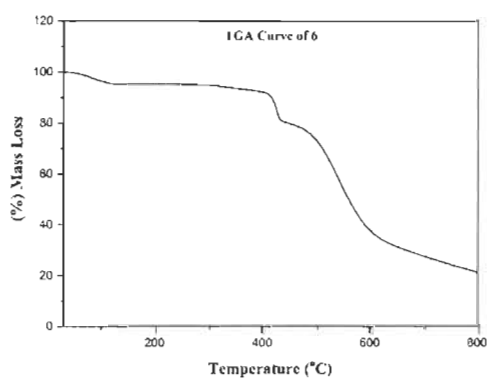
a
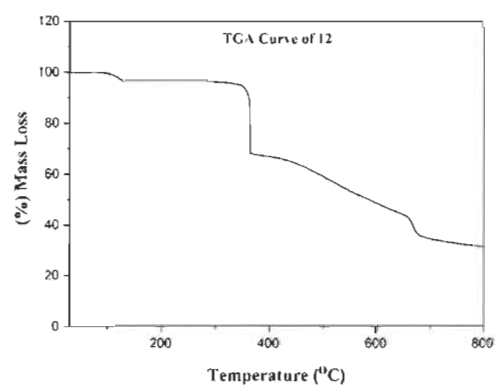
b
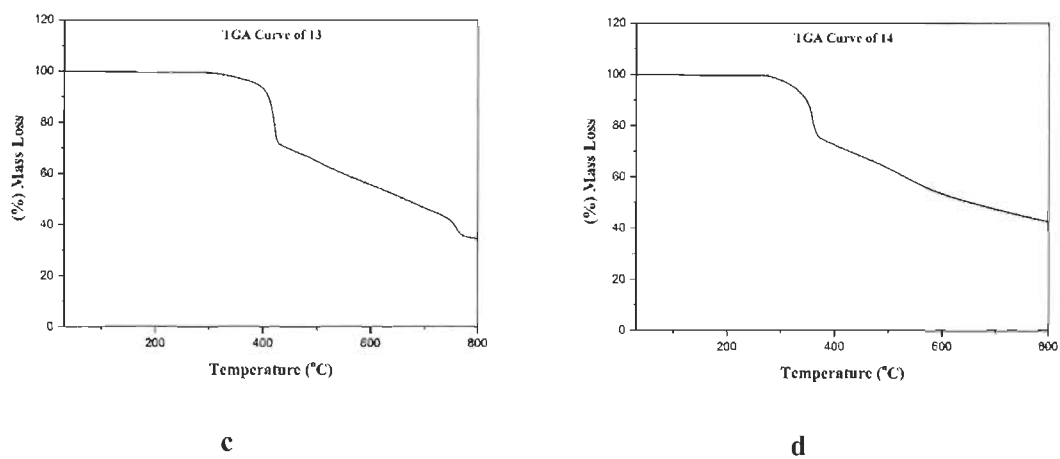
Fig. S4. Thermogravimetric analysis (TGA) curves of **6** and **12-14**

Infrared spectroscopy
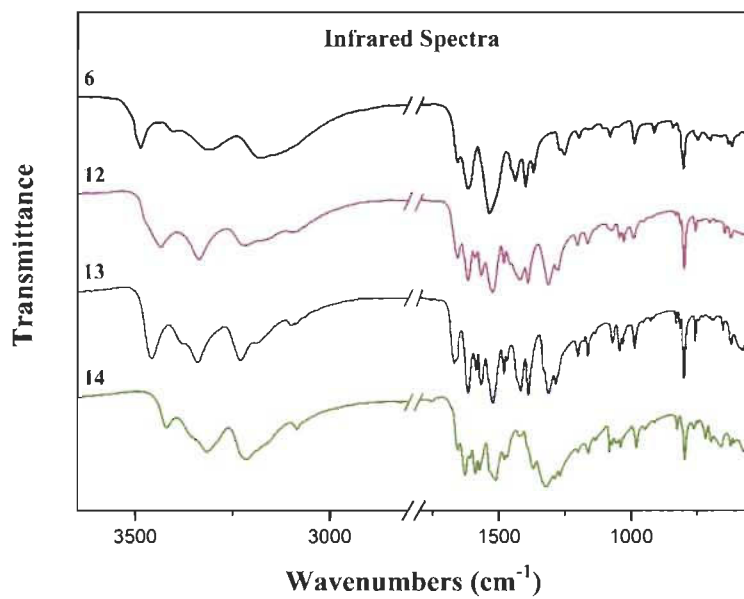
Fig. S5. Infrared spectra of **6** and **12-14**

Table S4. IR data and assignments of vibrations for ligand **6** and complexes **12-14**

$\tilde{\nu}/cm^{-1}$				Assignment***
6	**12**	**13**	**14**	
594w	572w	579w	611w	τ (NO$_3^-$)
621w	625w	623w	625w	Triazine as well as bipyridine ring out-of-plane
635w	648w	654w	660w	def. γ(C-N), γ(C-C)
702w	705vw	705vw	700w	Triazine ring out-of-plane def. γ(C-N), ω(NH$_2$)
711sh		729vw	720w	
750w	742vw	745vw	749w	ω(NH$_2$)
761sh	758w	758w	765w	
803m	800m	800s	799m	
820sh	817w	816w	827w	Triazine ring out-of-plane def. γ(C-N), ω(C-H)
843w	832w	831w		
914w		917w	912w	
		927w		Ring breathing both triazine as well as bipyridine
	955vw	955vw	951w	
989w	991w	987w	981w	
	1029w	1032w		
	1045w	1044w	1040w	
		1058w		τ(NH$_2$)
	1077w	1071w	1074w	
1080w			1083w	
1108sh		1136w	1134w	Bipyridine ring breathing, ρ(NH$_2$), ρ(C-H)
1157sh	1165w	1164w	1163w	ω(NH$_2$), δ(C-H), ρ(NH$_2$)
1198w	1203w	1201w	1201w	Triazine ring def., τ(NH$_2$)
1254w	1276m	1284m	1270w	
1275w			1288w	ν(C-N) aromatic amines

	1313s	1313s	1323s	v(NO$_3^-$)
1370w	1390s	1388s	1371m	ρ(C-H)
1401m				
1439m	1423s	1418s	1417w	
1456w	1454sh	1470w	1470w	ρ(C-H)
	1482w	1481w	1480w	
1537s	1525s	1523s	1513s	Bipyridine ring breathing v(C-C), δ(NH$_2$)
			1522sh	
	1567m	1568m	1574m	δ(NH$_2$)
	1591w	1588w	1590m	
1618s	1617s	1616s	1609w	Triazine ring breathing v(C-N), δ(NH$_2$)
			1629m	
1657w	1661m	1658w	1655w	Triazine ring breathing v(C-N)
		1668m		
			3066sh	
	3084w	3083w	3085w	v(C-H)
3137s	3099w	3100w		
3178s	3165sh	3185w	3154sh	v$_s$(NH$_2$)
3312s	3219m	3230s	3214s	v$_{as}$(NH$_2$)
3405w	3338s	3340s	3316s	v$_s$(NH$_2$), v$_{as}$(NH$_2$)
		3381w	3360sh	
3487m	3436m	3458s	3420m	v$_{as}$(NH$_2$)

***Abbreviation used for the type of vibration mode. def.: deformation; δ, γ, ρ, τ, ω: bending vibrations; v: stretching vibration

Cyclic Voltammetry

a

b

c
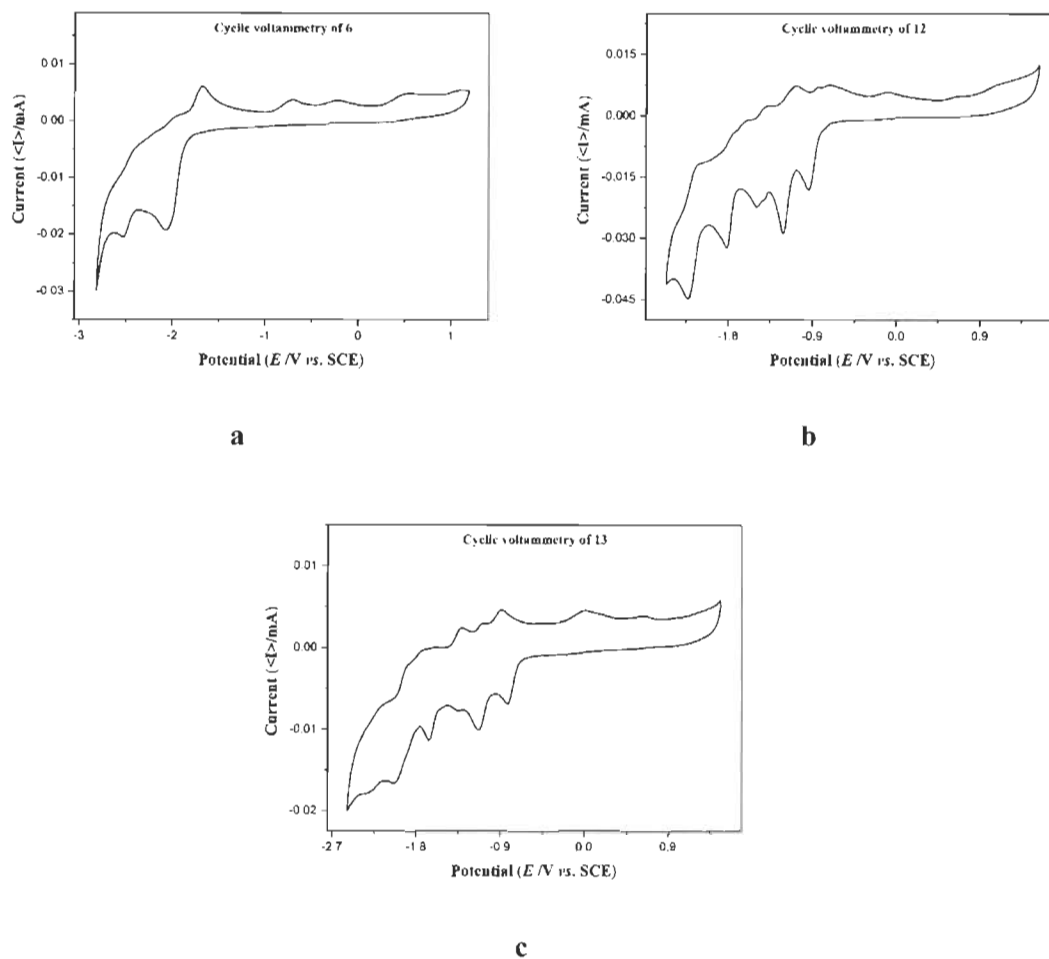
Fig. S6. Cyclic voltammetry of **6, 12** and **13** in full scale

Table S5. Cyclic voltammetry data of 2, 2':6', 2":6", 2"'-quaterpyridine complexes reported in literature

Compound	Solvent	Eox1$_{1/2}$ [V]	Ered1$_{1/2}$ [V]	Ered2$_{1/2}$ [V]	Ered3$_{1/2}$ [V]	Ered4$_{1/2}$ [V]
Co(qtpy)(H$_2$O)$_2$(ClO$_4$)$_2$ [1]	MeCN		-0.65	-1.15	---	---
Ni(qtpy)(ClO$_4$)$_2$ [1]	DMF		-0.79	-1.13	-1.90	---
Cu(qtpy)(PF$_6$)$_2$ [2]	MeCN	0.13 (nr)	-0.24 (nr)	---	---	---

qtpy = 2, 2':6', 2":6", 2"'-quaterpyridine, nr = non-reversible

207
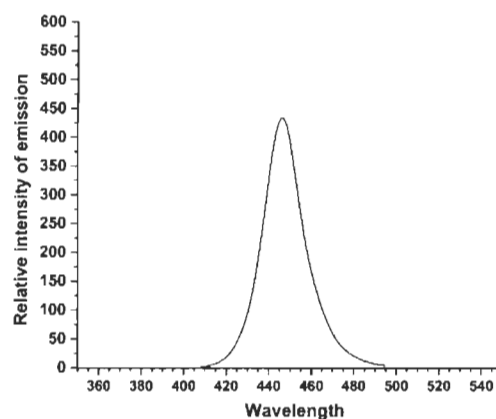
Fig. S7 Emission spectrum of blue LED.

Table S6. Emission maxima and amplitude of LED light.

Light source[a]	Blue
$\lambda_{max,em}$ (nm)	445
$\Delta\lambda$ (nm)	90
Photon flux in $\mu mol_{photons}.min^{-1}.cm^{-2}$ [b]	20

[a] blue LED 445 nm.

[b] an analog power-meter PM100A (THORLABS) associated with a compact photodiode power head with silicon detector S120C is used to evaluate the photon flux for the LEDs. Photo-diode detector is placed at the same distance from the LED surface than the bottom of illuminated vial.

HER Curves of Co(II), Ni(II) and Cu(II) nitrates
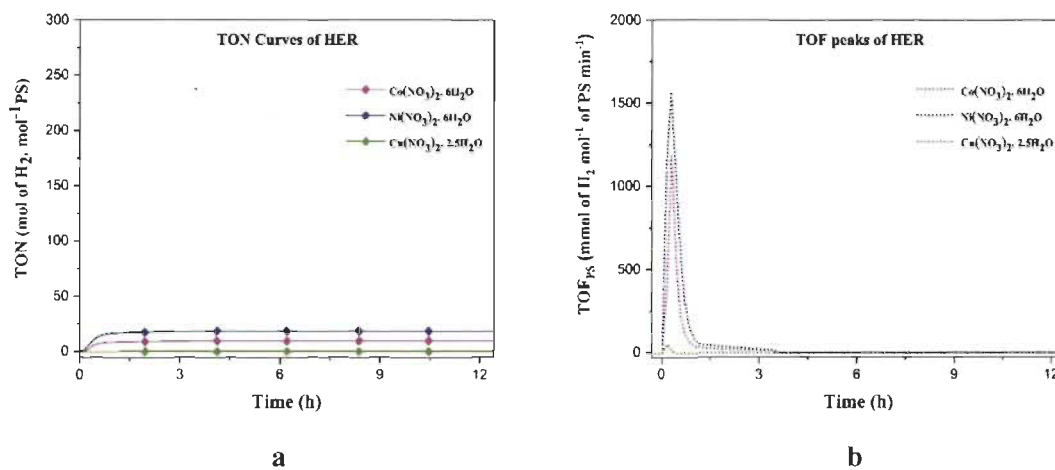
Fig. S8. Hydrogen evolution reaction of Co(NO₃)₂. 6H₂O, Ni(NO₃)₂. 6H₂O and Cu(NO₃)₂. 2.5H₂O (1 mM each) under blue light. (a) TON's and (b) TOF's.

Mechanism of hydrogen evolution reactions

The mechanism of the hydrogen evolution reaction may occur by two important steps; (I) Activation of the molecular catalyst by the photosensitizer and (II) Redox photocatalytic hydrogen evolution.
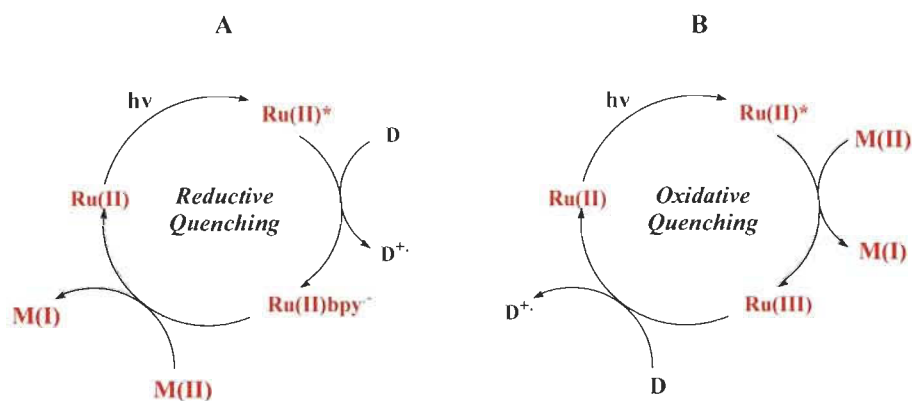
Step I

Fig. S9. Photosensitizer based processes in light-driven hydrogen evolution reaction

In step I, activation of the molecular photocatalyst can take place either by reductive or oxidative quenching pathways from the excited photosensitizer (PS*). Visible light is used to for the excitation of the photosensitizer where, in the process of reductive quenching (A), the excited PS* accept an electron from the sacrificial electron donor (SED) and shares it with the molecular catalyst, during this course, the oxidation state of Ru(II) does not change. In the process of oxidative quenching (B), the excited PS* oxidizes and donates its electron to the molecular catalysts and then abstracts an electron from the SED, this process involves redox changes in Ru(II) PS.

In step II, at the photocatalytic centre, the hydrogen evolution can occur by two different mechanisms.

Step II

Fig. S10. Heterolytic and homolytic mechanisms of hydrogen evolution reaction catalysed by molecular photocatalyst

In heterolytic mechanism (C), H_2 is evolved by the protonation of the intermediate metal hydride. In the catalytic cycle, the two electrons are transferred either consecutively or alternatively. The H_2 evolution in the alternative homolytic pathway (D) happens by the reductive elimination of two metal hydride intermediates. In both the mechanisms, the metal salts of +II oxidation state undergoes one electron reduction before protonation takes place.[3]

References

1. K-M. Lam, K-Y. Wong, S-M. Yang and C-M. Che, *J. Chem. Soc. Dalton Trans.*, 1995, **7**, 1103-1107.

2. E. C. Constable, S. M. Elder, M. J. Hannon, A. Martin, P. R. Raithby and D. A. Tocher, *J. Chem. Soc. Dalton Trans.*, 1996, **12**, 2423-2433.

3. Artero, V.; Chavarot-Kerlidou, M.; Fontecave, M., *Angew. Chem.* 2011, 50 (**32**), 7238-7266.

Chapter 5

Design of a [FeFe] Macrocyclic Metallotecton

for Light-Driven Hydrogen Evolution Reaction

5.1. Introduction

Numerous efforts have been put forward by scientists towards the discovery of novel and efficient materials having potential applications in the field of energy. Sometimes, these efforts involve amalgamation of different branches of chemistry into one another to produce the desired results. Macrocyclic chemistry and metallotectons are two such fields of supramolecular chemistry which have been rarely brought together. Their converging can result in the formation of a macrocyclic metallotectons which can have the advantages of a macrocycle as well as a metallotecton. As the name suggests, macrocyclic metallotecton is a macrocyclic complex with incorporated sticky sites for hydrogen bond formation and one or more metal ions. Such complexes are fascinating due to their intriguing molecular structures and supramolecular architectures dictated by both coordination and hydrogen bonds and their utility for catalytic applications such as light-driven hydrogen evolution reaction (HER).

5.2. *Article 4*

Design of a [FeFe] Macrocyclic Metallotecton for Light-Driven Hydrogen Evolution Reaction

Sanil Rajak, Olivier Schott, Prabhjyot Kaur, Thierry Maris, Garry S. Hanan and Adam Duong*

5.3. Author's Contribution

Sanil Rajak: Investigation, conceptualization, methodology, synthesis and characterization, photo catalytic testing, electrochemical analysis, interpretation of results, writing of the article.

Olivier Schott: Mentoring, conceptualization, methodology.

Dr. Prabhjyot Kaur: Writing- review and editing.

Dr. Thierry Maris: Crystallographic data analysis.

Prof. Garry S. Hanan: Co-supervision, conceptualization, methodology.

Prof. Adam Duong: Supervision, finding financial supports, project administration, conceptualization, interpretation of results, writing- review and editing.

1. Abstract

Combining the two most fascinating fields of chemistry in the development of novel metal-organic architectures *viz.* macrocyclic chemistry and metallotectons, herein, we report the one-pot synthesis of a binuclear Fe(II) macrocyclic metallotecton **2** *via* coordination-driven assembly in excellent yield and purity. The single crystal structure of **2** indicates two units of cationic iron complex with ligand **1** (6- pyridin-2-yl-[1,3,5]-triazine-2,4-diamine) acting as metallotectons connected to each other by two $[\mu\text{-PHO}_3\text{CH}_3]^-$ bridges forming a [FeFe] macrocycle embedded in two metallotectons. The pyridine and DAT rings of both ligands **1** are nearly coplanar in **2** and each iron(II) has a distorted octahedral geometry. Diaminotriazine groups incorporated in **2** direct multiple hydrogen bonding according to predictable motifs **II** to produce a final three-dimensional structure. Thermal stability, electronic properties, and redox properties of **2** have been studied by thermogravimetric analysis, UV-Vis, and cyclic voltammetry respectively. The hydrogen evolution reaction (HER) study of **2** reveals it as an efficient photocatalyst displaying a high turnover number (TON) and turnover frequency (TOF), which is much higher than other Fe based molecular catalysts reported in literature. Also, its photocatalytic activity outperforms the most reported standard reference cobaloxime catalyst ($Co^{III}(dmgH)_2(py)Cl$). This is by far, the only report showcasing a macrocyclic metallotecton for photocatalytic HER. In addition, complex **2** can be regarded as the next level in supramolecular chemistry as it bridges the gap between macrocycles and metallotectons as well as it can be a future option for our deteriorating environment.

Keywords

2. Introduction

In 1873, the existence of van der Waals interactions between particles to understand phase transitions was proposed by Johannes Diderik [1]. Subsequently, this hypothesis gave rise to the concept of supramolecular chemistry that relies on non-covalent interactions to explain the molecular organization in the solid state. Jean-Marie Lehn summarises this phenomenon as *"chemistry beyond the molecule, the science of non-covalent interactions"* [2]. A major break through in the field of supramolecular chemistry occurred by the discovery of crown ethers- the simplest macrocycles, in 20th century by Charles Pederson [3,4]. Due to their ability to act as host molecules, the research on them continued and eventually different classes of macrocycles came into existence [5,6]. Macrocyclic ligands are known to form metal complexes with higher thermodynamic stability and kinetic inertness because of the "macrocyclic effect" as it was later known [7]. Consequently, they are attractive scaffolds for assembling metal complexes for a multitude of applications including catalysis, ion transport, magnetic resonance imaging, molecular sensing, diagnostic tools and therapeutic agents [8-11]. Although in chemistry there are many methods to synthesize sophisticated compounds, macrocyclic molecules of purely organic and organometallic nature are still very complicated to prepare.

Currently, supramolecular chemistry represents a multidisciplinary field targeted towards the construction of diverse materials [12-14]. Towards the end of 20th century, Wuest and co-researchers introduced molecules that could self-assemble by hydrogen bonds as *tectons* giving scientists a new terminology in the field of crystal engineering that focuses on crystalline materials [15-17]. Pre-programming the molecular components and controlling their environment allows to some degree to predict the structural outcome. As tecton was mainly identified for organic molecules, Constable describe the coordination complexes as *metallotectons*, meaning simply that the ligands are bonded to metal ions which doesn't includes the concept of hydrogen bonds [18]. The term metallotecton [19-28] is now much more referred to complexes that contain hydrogen bonding sticky sites to direct their self-assembly. Controlling the molecular organization over the

coordination bond has several advantages: (i) it allows to create a wide range of metallo-supramolecular architectures with topologies that don't exist in ''pure'' organic chemistry, (ii) the synthesis of sophisticated molecules can be simplified and (iii) it gives rise to unique properties that come from both organic and inorganic components. Because of these advantages, the field of metallo-supramolecular chemistry is now highly extensive [18,29].

Herein, we propose to form a macrocyclic metallotecton. These are macrocyclic complexes with incorporated sticky sites for hydrogen bond formation and one or more metal ions which makes them interesting candidates for catalytic applications [30,31]. Besides, these are interesting due to their intriguing molecular structure and supramolecular architectures dictated by both coordination and hydrogen bonds. In this work, we have three challenges: 1) design and synthesis of a bimetallic macrocyclic metallotecton, 2) to study its supramolecular chemistry and physicochemical properties and 3) its application in light-driven hydrogen evolution reaction (HER).

Based on the structures of complexes reported in the past, we expect 6-pyridin-2-yl-[1,3,5]-triazine-2,4-diamine **1** to bind iron metal ions with well established coordination modes and to further associate in the solid-state by hydrogen bonding of DAT groups to produce crystalline molecular materials (Chart 1) [25,32,33]. We also described in previous work the condition to properly fix the number of ligands coordinated to metal ions [23]. According to known structures, the coordination number of iron can be up to six. By integrating this knowledge, it is possible to envisage the preparation of a cationic iron complex with two ligands **1**. By using the phosphorate monomethyl ester dianionic ligands, we also expect to bridge the cationic iron complexes to produce cyclic or polymeric multi-metallic complexes. As the formation of cyclic or polymeric structures depends mainly on the experimental conditions, we first investigated on the synthesis and the characterization of macrocyclic metallotecton **2**.

As part of our ongoing research in energy application, we investigated the catalytic activity of **2** for hydrogen production. The current situation of our environment with increasing global warming and green house effect demands the necessity of using clean fuels and renewable energy resources

instead of fossil fuels [34-36]. Hydrogen is a clean fuel and one of the greatest energy carriers with the potential to be used as a future alternative to fossil fuels. This is because of its numerous advantages such as high energy density by combustion, recyclability and pollution-free use. Currently, the best methods to produce hydrogen are based on platinum metal catalyst such as photoelectrochemical cells or proton-exchange-membrane fuel-cells and electrolysers [37]. However, these technologies are economically not viable because of the cost of platinum metal catalyst. To replace platinum, considerable effort has been expended by chemists to develop efficient catalysts based on transition metal complexes for HER. There are numerous reports in literature using transition metal complexes, nanosheets, nanoparticles and nanorods as efficient electro and photocatalysts for HER [38-49]. Inspired by the catalytic active site of hydrogenases that contains first row transition metals of Ni-Fe or Fe-Fe, several research groups have also focused on the development of artificial enzymes/catalysts [50-56]. Indeed, major drawbacks of the current biomimetic catalysts prepared so far are their accessibilities, sensitivities to oxygen and often the efficiency. Because **2** is a cyclic [FeFe] dinuclear complex, we envisaged this compound to lead to an interesting catalytic activity, particularly for hydrogen production. Hence, we tested the catalytic activity of **2** for HER.
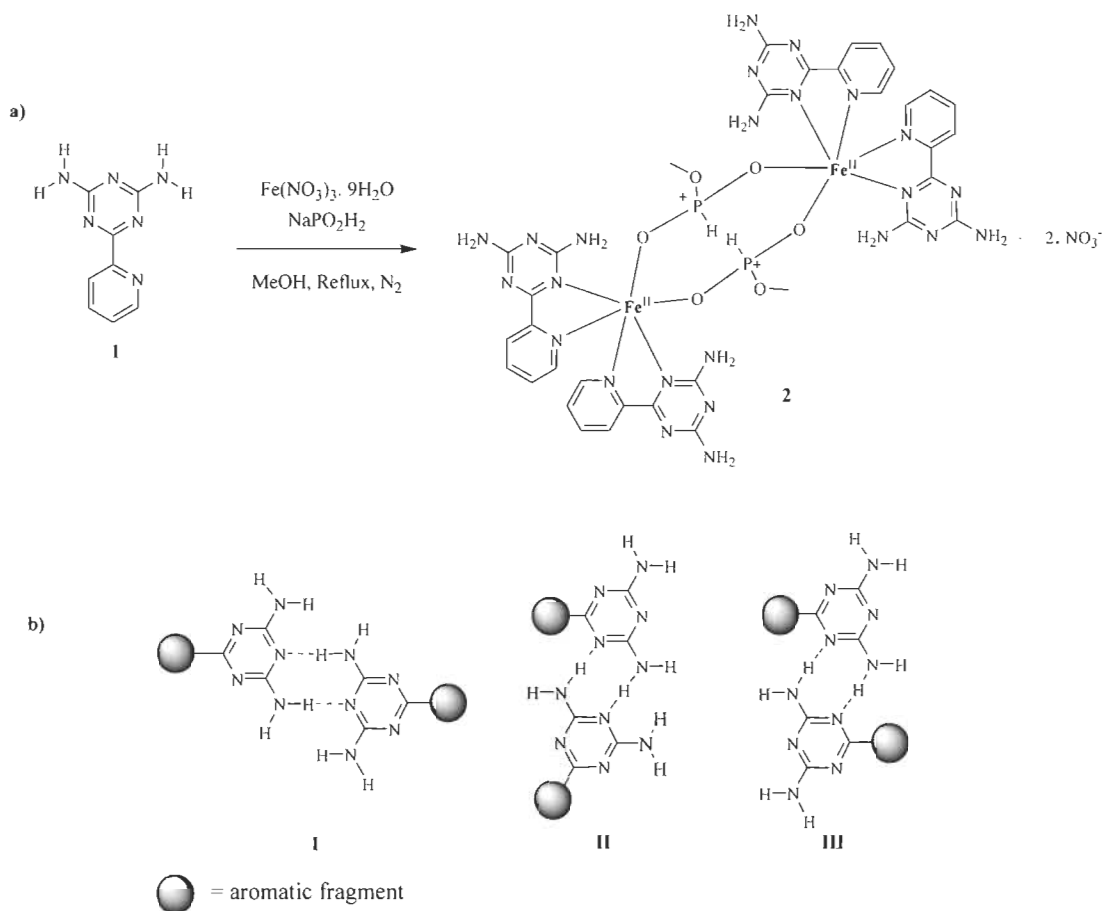
Chart 1 (a) Synthetic route for [FeFe] macrocyclic metallotecton **2** and (b) Cyclic hydrogen bonding motifs **I-III** of diamino-1,3,5-triazinyl group (DAT).

3. Experimental section

A. General Notes and Procedures for the Synthesis of 1 and 2

6-(Pyridin-2-yl)-1,3,5-triazine-2,4-diamine **1** was synthesized by reported methods. The [FeFe] bimetallic complex **2** was prepared following the experimental procedure described below. All the chemicals used were commercially available and used without additional purification.

A.1. Synthesis of compound 2

Sodium hypophosphite ($NaPO_2H_2$, 0.0211g, 0.1992 mmol, 1.5 equiv) was added at 25 °C to the stirred solutions of $Fe(NO_3)_3 \cdot 9H_2O$ (0.053g, 0.1328 mmol, 1 equiv) in MeOH (30 mL). The mixture was refluxed for 15 minutes and then 6-(pyridin-2-yl)-1,3,5-triazine-2,4-diamine ligand (0.05g, 0.265 mmol, 2 equiv) was added. After 12h of reflux the resulting homogeneous solutions was cooled to room temperature and subjected to crystallization by slow diffusion with diethyl ether (82% yield). FTIR (ATR): 3404.39, 3320.60, 3209.48, 3157.23, 2974.24, 1660.45, 1625.51, 1585.36, 1561.50, 1511.06, 1484.56, 1464.37, 1444.39, 1397.43, 1369.73, 1329.37, 1261.81, 1164.21, 1144.32, 1083.20, 1050.13, 1018.77, 992.13, 910.70, 882.18, 823.94, 791.21, 752.74, 681.84 cm^{-1}. Anal. calcd for $C_{38}H_{56}Fe_2N_{26}O_{16}P_2$: C, 34.93; H, 4.32; N, 27.87. Found: C, 34.69; H, 3.91; N, 27.84.

B) Instrumentation

The crystallographic data was collected using a Bruker Venture Metaljet diffractometer with Ga Kα radiation and Bruker APEX2 diffractometer equipped with Cu Kα radiation from a microfocus source. The structures were solved by direct methods using SHELXT [57], and non-hydrogen atoms were refined anisotropically with least-squares minimization [58]. Hydrogen atoms were served by first locating them from different Fourier maps, recalculating their positions using standard values for distances and angles, and then refining them as riding atoms. Microcrystalline powders were analysed in transmission-mode geometry using a Bruker D8-Discover instrument (θ–θ geometry) equipped with a XYZ platform and a HI-STAR gas detector. X-rays were generated using a conventional sealed-tube source with a copper anode producing Cu Kα radiation (λ = 1.54178 Å). The samples were grounded gently and then mounted on a flat Kapton sample holder. The data collection involved acquisition of two different sections with increasing angular position, giving two different 2D frames. These frames were integrated and combined to produce the final one-dimensional powder X-ray diffraction pattern. Calculated powder X-ray diffraction

patterns were generated from the structural data in the corresponding CIF resulting from single crystal analyses. The calculation was performed using MERCURY [59] software of the Cambridge Crystallographic Data Center. A unique value of the full width at half maximum for the diffraction peaks was adjusted to get a better match between the resolution of the experimental and the calculated patterns. The UV–Vis spectra were recorded on a Cary 5000 spectrometer. The ATR–FTIR spectra were collected with a Nicolet iS 10 Smart FT-IR Spectrometer within 600-4000 cm^{-1}. The thermogravimetric analyses were performed simultaneously using Mettler Toledo TGA1. The samples were loaded and heated from 25 to 800 °C with a heating rate of 10 °C/min under N_2 gas. Electrochemical measurements were performed in pure dimethylformamide purged with argon at room temperature with a BAS SP-50 potentiostat. Glassy carbon electrode was used as a working electrode, the counter electrode was a Pt wire and silver wire was the pseudo-reference electrode. The reference was set using 1mM ferrocene. The concentrations of samples were 1mM. Tetrabutylammonium hexafluorophosphate (TBAP) (0.1 M) was used as supporting electrolyte. Cyclic voltammograms were obtained at a scan rate of 100 mV/s and current amplitude of 100 μA.

C) Electrochemical measurements

A BAS SP-50 potentiostat were used to perform the electrochemical measurements in pure dimethylformamide purged with nitrogen at room temperature. Glassy carbon electrode was used as a working electrode, the counter electrode was a Pt wire and silver wire were the pseudo-reference electrode. 1 mM ferrocene was used as an internal standard to set the reference of the electrochemical potential and the values of the potentials are reported vs SCE. The concentrations of sample were 1mM. Tetrabutylammonium hexafluorophosphate (TBAP) (0.1 M) was used as supporting electrolyte. Cyclic voltammograms were obtained at a scan rate of 100 mV/s and current amplitude of 100 μA.

D) Photocatalytic experiments

All photocatalytic experiments were performed with a PerkinElmer Clarus-480 gas chromatograph (GC) with a thermal conductivity detector, argon carrier and eluent gas, a 7 inch HayeSep N 60/80 pre-column, a 9 inch molecular sieve 45/60 column, and a 2 mL injection loop was used to measure hydrogen evolution. All the experiments were performed in DMF, three separate solutions of (i) the photosensitizer (PS) [Ru(bpy)$_3$] (PF$_6$)$_2$, (ii) catalyst, and (iii) triethanolamine (TEOA) and an acid source (48% HBF$_4$ in water) were prepared. A 5 mL solution in a standard headspace vial (20 mL) was formed by mixing these three solutions. 1M TEOA, 0.1 M HBF$_4$, 0.56M water, 0.1 mM PS [Ru(bpy)$_3$] (PF$_6$)$_2$ and 1 mM catalyst were the final molar concentration of each photocatalytic components. The vials were then placed on a panel of 90 x 1 W LEDs (λ_{max} = 452 nm, $\Delta\lambda$ = 150 nm, 20.5 µEinstein min^{-1} cm^{-2} flux) in a thermostatic bath set at 20°C. A rubber septum was used to seal the vials and two stainless-steel tubes were pierced. Argon was carried in the first tube at a flow rate of 10 mL min^{-1} pre-bubbled in spectroscopic grade solvent. A manual flow controller (Porter, 1000) was used to adjust the flow rate and a digital flow meter (PerkinElmer Flow Mark) was used to test it. The second tube caused the flow to go to the GC sample loop through a 2 mL overflow protection vial, and finally to the GC sample loop through an 8-port stream select valve (VICCI). Timed injections were allowed by a microprocessor (Arduino Uno) coupled with a custom PC interface. H$_2$ production rate was calibrated at a specific argon flow. A syringe pump equipped with a gas tight syringe and a 26 s gauge needle was used to bubble different rates of pure hydrogen gas into the GC sample loop, to a minimum of 0.5 µL/minute. This gave a linear fit for peak area for H$_2$ versus the flow rates of H$_2$. Stock cylinders of known concentration of H$_2$ in argon replaced the argon flow (inserted at the pre-bubbler, to keep the same vapour matrix) for calibration testing. The equation below was used to convert the measured results into rate of hydrogen. The estimated errors with TONs and TOFs values were about 10% [60].

Equation 1

H_2 rate (μL min^{-1}) = [H_2 standard] (ppm) x Ar flow rate (L min^{-1})

4. Results and discussion

### A. Synthesis and characterization of [FeFe] macrocyclic metallotecton 2

Ligand **1** was obtained following the reported method [61]. It consists of a pyridine and a diamino-1,3,5-triazinyl group (DAT) that are used as building blocks to prepare many biological molecules and organometallic materials [62-66]. [FeFe] macrocycle **2** was prepared in a one-pot reaction by mixing $Fe(NO_3)_3.9(H_2O)$ (1 equiv.), ligand **1** (2 equiv.) and sodium hypophosphite (1.5 equiv.) in methanol (30 mL) under reflux. Compound **2** was crystallized by slow diffusion of ether into the above reaction mixture. The infrared spectrum of **2** indicated the presence of [μ-PHO_3CH_3]$^-$ with P-O-P stretches observed at 1164, 1146 and 1097 cm^{-1} (Fig. S3). The medium peak at 2358 cm^{-1} can be assigned to the C-O group from the [μ-PHO_3CH_3]$^-$. Bands of ligand **1** were observed at 3209, 3320 and 3209 cm^{-1} which are attributed to the symmetric and asymmetric -NH_2 vibrations. The band at 1329 cm^{-1} is of NO_3^- group. The peak positions for **2** are listed in Table S3 along with their proposed assignments. The atomic composition of **2** was determined by elemental analysis (EA). The general chemical formula found corresponds to $Fe_2(C_8H_8N_6)_4(PHO_3CH_3)_2(NO_3)_2$•4(MeOH) which is matching with the anticipated molecular structure (see experimental section).

B. Crystal structure and phase purity of 2

Crystals of **2** were grown from MeOH/Ether and proved to belong to the monoclinic space group $P2_1/n$. Views of the structure of [FeFe] macrocyclic metallotecton **2** are shown in Fig. 1, and other crystallographic data are given in Table 1. The X-ray analysis of **2** revealed the presence of a cyclic bimetallic complex with chemical formula of [$Fe_2(1)_2(\mu$-$PHO_3CH_3)_2$]($NO_3)_2$ (Fig. 1a). Each iron(II) is in a distorted octahedral geometry. The first coordination sphere consists of four

nitrogen atoms from ligand **1** and two oxygen atoms from the bridging $[\mu\text{-}PHO_3CH_3]^-$. In the structure, the two iron complexes are doubly linked by the $[\mu\text{-}PHO_3CH_3]^-$ which form the dicationic [FeFe] macrocyclic metallotecton. Each phosphorous atom is tetravalent with a global charge +1. Table S1 gives geometrical parameters including selected bond lengths and interatomic distances. The size of the macrocycle is represented by the Fe⋯Fe separation of 5.511 Å and the P⋯P distance of 3.666 Å. The pyridine and DAT rings of both ligands **1** are nearly coplanar with angles of 7.6° and 3.1°. The bond lengths and angles of the iron complex are normal (average $d_{Fe\text{-}Npy}$ = 2.178 Å, $d_{Fe\text{-}NDAT}$ = 2.220 Å and $d_{Fe\text{-}O}$ = 2.096 Å) [67,68]. The distance Fe-N of the closest nitrate counterion is of 5.432 Å. Average carbon-carbon and carbon-nitrogen bond lengths are similar to those reported for the free pyridine-substituted diaminotriazine molecule [69].

As expected, the cyclic bimetallic complex engages in multiple hydrogen bonding directed by the DAT groups according to type **II** (average distance = 3.126 Å) to produce the three-dimensional structure (Fig. 1b). Selected hydrogen bonds and angles are provided in Table S2. The ligands also interact *via* π-π interactions with a separation of 3.687 Å to strengthen the supramolecular network. Additionally, intramolecular hydrogen bonding between the free hydrogen of the $-NH_2$ and the closest oxygen atom of the $[\mu\text{-}PHO_3CH_3]^-$ reinforce the configuration of the macrocycle. It is noteworthy that the structures contain disordered methanol molecules and nitrates. The presence of methanol in the structure is reinforced by the elemental analysis and thermogravimetry analysis (discussed below).
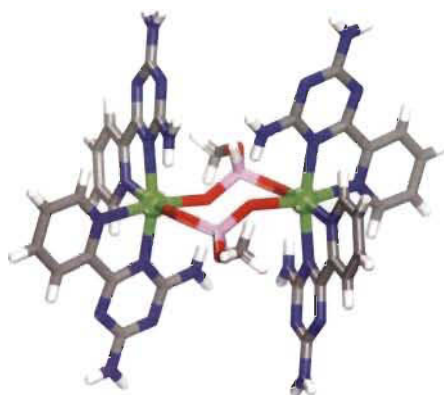
a
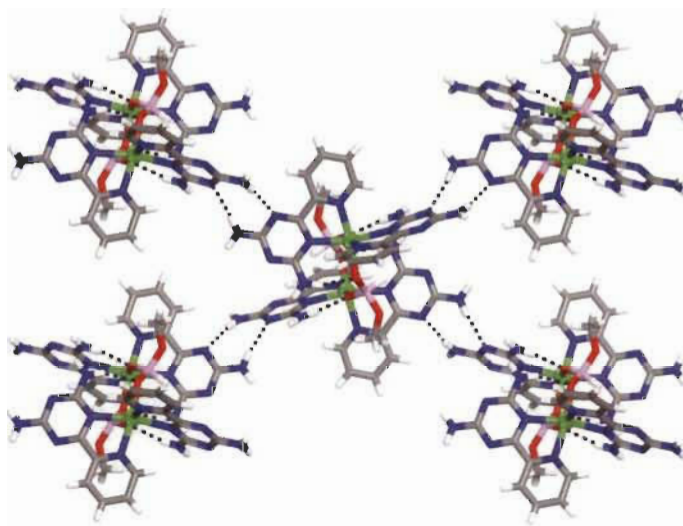
b

Fig. 1 - Crystal structure of **2** grown from MeOH/Ether. Hydrogen bonds are represented by broken lines. Unless stated otherwise, carbon atoms are shown in grey, hydrogen atoms in white, oxygen atoms in red, nitrogen atoms in blue, phosphorus atoms in pink and iron atoms in green. (a) View of the molecular structure of **2**. (b) View showing the hydrogen bonding between macrocycles. For more clarity, methanol and nitrates are omitted.

B.1. Table 1. Crystallographic Data for **2**

Compound	2
Formula	$C_{36.25}H_{50}Fe_2N_{26}O_{14.25}P_2$
Mr	1251.66
Crystal system	Monoclinic
Radiation	GaKα
λ (Å)	1.34139
F(000)	1291
Space group	P21/n
a (Å)	10.6206(3)
b (Å)	14.3962(4)
c (Å)	19.5412(6)
α (deg)	90
β (deg)	100.6870(10)
γ (deg)	90
V (Å^3)	2935.95(15)
Z	2
ρ_{calcd} (g/cm^3)	1.416
T (K)	150
μ (mm^{-1})	3.524
measured reflections	62514
independent reflections	6753
R_{int}	0.0370
Observed reflns	6096
R_1 $[I > 2\sigma (I)]$	0.0564
R_1 (all data)	0.0603

ωR_2 [I >2σ (I)]	0.1691
ωR_2 (all data)	0.1739
GoF	1.08

The phase purity of the crystalline sample of **2** was determined by powder X-ray diffraction (PXRD). Fig. S2 show the comparison of the collected PXRD (in black) and the simulated patterns (in red) obtained from the SCXRD data. The two patterns are matching well which confirm the phase homogeneity of the bulk sample of **2**.

C. Thermal Stability and Degree of Solvation

The thermogravimetric analysis (TGA) was recorded to investigate the thermal stability and the degree of solvation of **2**. Single-crystals of **2** were heated from 25 to 800 °C at a rate of 10 °C/min under N_2 atmosphere. The TG curve of **2** is shown in Fig. 2. The first step with mass loss of ~ 11% at around ~ 65 °C is indicative of the loss of ~ 4 methanol molecules that are included in the structure. This result is in good agreement with the EA data and reinforces that the disordered species observed in the SCXRD corresponds to methanol molecules. Multistage decompositions of **2** without defined steps are observed starting at ca. ~ 180 °C.
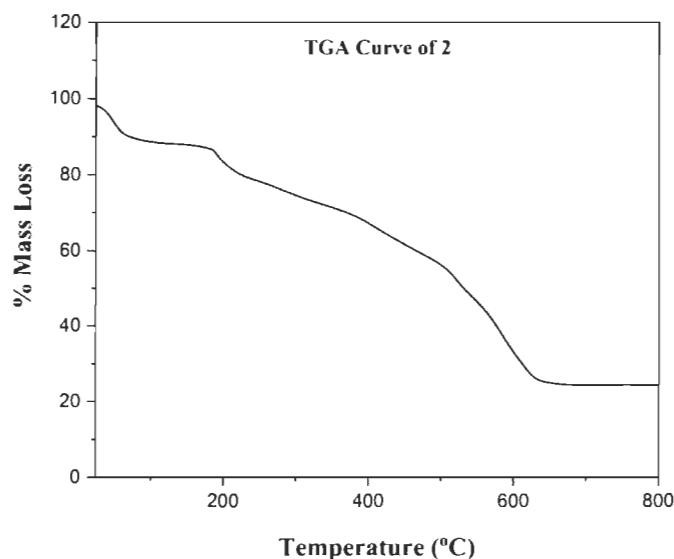
Fig. 2 - TG curve of **2**.

D. Electronic properties

Liquid UV-Vis absorption spectra of **1** and **2** were recorded in DMF solution at concentration 8.8 x 10^{-6} M and at 8 x 10^{-3} M at room temperature (Fig. 3). The electronic absorption spectrum of free ligand **1** displays an absorption band at 267 nm and a small shoulder at 296 nm that are attributed to the n-π^* and π-π^* transitions. The UV-Vis spectrum of **2** shows an intense band that can be attributed to the intraligand transition with maximum absorbance value at 270 nm. In the visible region (350-900 nm) three absorption bands appeared at λ_{max} 487 nm, 394 nm and 368 nm which are attributed to three transitions $^1T_1(I) \leftarrow {}^1A_1(D)$ and $^1T_2(I) \leftarrow {}^1A_1(D)$ and $^1E(I) \leftarrow {}^1A_1(D)$, respectively, typical for an octahedral coordination geometry. Selected data (wavelengths (λ_{max}), molar absorptivity (ε)) are summarized in Table 2.

D.1. Table 2. UV-Vis spectroscopy data of **1** and **2** in DMF solution

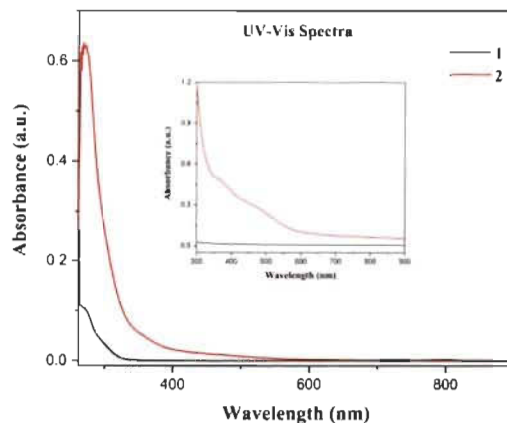| Parameters	In DMF solution			
	Conc = 8.8 x 10^{-6} M		Conc = 8 x 10^{-3} M	
Sample	From 250 to 900 nm		From 300 to 900 nm	
	λ_{max} (nm)	ε (mol^{-1} dm^3 cm^{-1})	λ_{max} (nm)	ε (mol^{-1} dm^3 cm^{-1})
1	267	1.26 x 10^4		
	296sh	0.44 x 10^4		
2	270	7.13 x 10^4	368	0.6 x 10^2
			394	0.52 x 10^2
			487	0.32 x 10^2

Fig. 3 - UV-Vis spectra of **1** and **2** in DMF solution at room temperature at a concentration of 8.8 x 10^{-6} M. Inset is showing the visible region (300-900 nm) at a concentration 8 x 10^{-3} M.

E. Cyclic Voltammetric Studies

Cyclic voltammograms (CV) of free ligand **1** and complex **2** were measured in degassed and anhydrous DMF solutions at concentration of compound at 1 mmol/dm^3 with 0.1 M TBA-PF$_6$ (tetrabutylammonium hexafluorophosphate) as a supporting electrolyte at scan rate 100 mV/s. To facilitate the discussion about the electrochemical properties, we summarized succinctly the CV data of **1** reported in our previous work. As can be seen in Fig. 4a, the free ligand did not show any reversible redox waves in the range -3 to -2 V. CV of **2** exhibited quasi reversible redox peaks at -1.94 V and -1.47 V (Fig. 4b) which are attributed to the reduction of the ligand **1**. The peak at -2.14 V is irreversible and it ascribed as the redox state of Fe$^{III/II}$. Table 3 summarizes the redox data of **1** and **2**.

E.1. Table 3. Redox data of ligand **1** and [FeFe] bimetallic complex **2** in DMF solution

Compound	Ered1$_{1/2}$ |V|	Ered2$_{1/2}$ |V|	Ered3$_{1/2}$ |V|	Ered4$_{1/2}$ |V|
1	-2	-2.22		
2	-0.24(56)	-1.47(11)	-1.94(79)	-2.14(76)

a   b
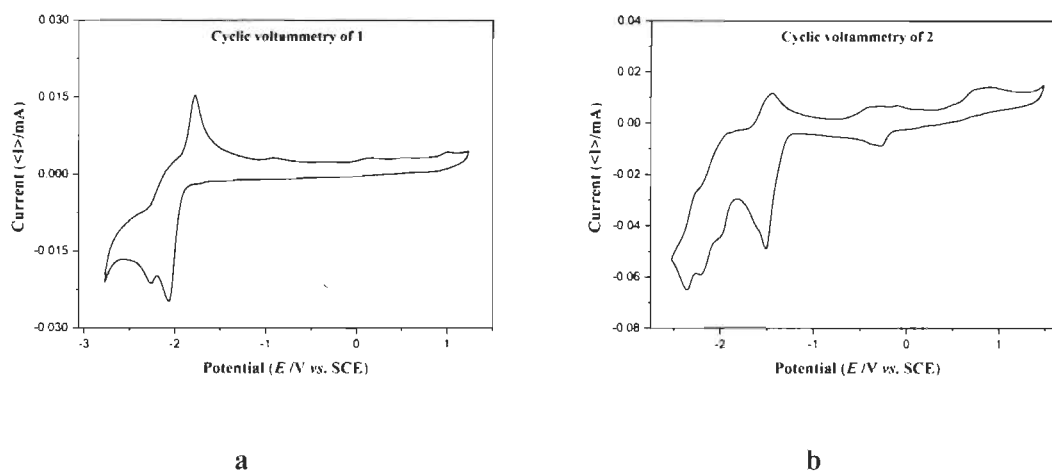
Fig. 4 - Cyclic voltammograms in DMF solution of 1 mM of **1** and **2**. Conditions: 0.1 M Tetrabutylammonium hexafluorophosphate (TBAP) as supporting electrolyte, scan rate: 100 mV/s, glassy carbon working electrode (1 mm diameter), Pt wire counter electrode, Ag wire was the pseudo-reference electrode.

F. Hydrogen Evolution Reaction Study

Under blue irradiation (452 nm) cyclic bimetallic complex **2** is an active catalyst for photocatalytic HER in DMF solution. The photocatalytic activity for hydrogen production by **2** was performed using 1 mM catalyst (complex **2**),1M triethanolamine (TEOA) as the sacrificial electron donor, 0.1 mM $Ru(bpy)_3(PF_6)_2$ as the photosensitizer (PS) and 0.1 M aqueous HBF_4 as the proton source at 452 nm. The experiment was conducted for 25 hours. The hydrogen production rate, turnover number (TON) and turnover frequency (TOF) have been reported in millimoles of hydrogen per hour, moles of hydrogen per mole of PS and mmol of hydrogen per mole of PS per minute respectively. Control experiments were conducted in the presence of PS/TEOA alone with and without light and no H_2 production was recorded which was consistent with the previous results and which proved that complex **2** is responsible for the H_2 production [70]. **2** displays a hydrogen production rate of 1.30 mmoles H_2 per hour; TON of 326 moles of H_2 per mole of PS and TOF of 4189 mmol of H_2 per mole of PS per minute (Fig. 5). Blank experiment was conducted with Fe

(NO)$_3$.9H$_2$O which gave a TON of 12.52 moles of H$_2$ per mole of PS proving that the salt alone cannot function as a photocatalyst (Fig. S6). We have also compared the TON and TOF of **2** with standard reference (Co^{III}(dmgH)$_2$(py)Cl) and observed an ~ 5 times better performance for **2** compared to standard reference (Fig. S7). The general mechanism for the photocatalysis process has been shown in the supporting information.

There are no reports in the literature related to TON or TOF of macrocyclic metallotectons. However, we have compared our value with some Fe based molecular photocatalysts for H$_2$ production. DeKrafft and coworkers synthesized Fe$_2$O$_3$@TiO$_2$ composite nanoparticles and observed its photocatalytic activity in combination with K$_2$PtCl$_4$ using xenon lamp, triethylamine (TEA) as sacrificial donor. 0.26 μmol/h was the observed H$_2$ production rate [71]. Sasan and coresearchers synthesized a heterogeneous photocatalyst ([FeFe]@ZrPF). Its photocatalytic activity was observed to be 1.75 μmol/h in visible light in the presence of ascorbic acid as sacrificial electron donor [72]. Xu and fellow researchers prepared FeO$_{3.3}$C$_{0.2}$H$_{1.0}$ photocatalyst which showed a H$_2$ production rate of 28.3 μmol/h in white light LED in the presence of TEA as sacrificial donor and eosin Y as photosensitizer [73]. Pham and researchers synthesized Fe$_2$O$_3$-TiO$_2$-PtO$_x$ photocatalyst for visible light H$_2$ generation. This catalyst displayed a H$_2$ production rate of 22 μmol/h in the presence of lactic acid as a sacrificial reagent [74].
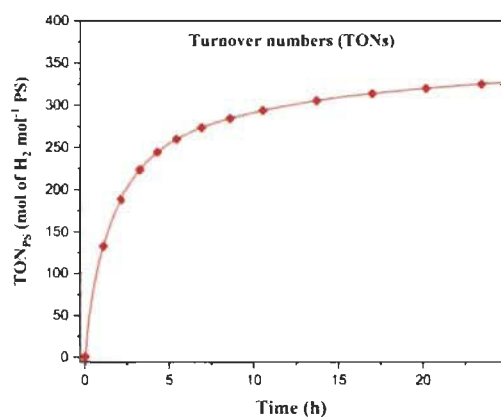
a
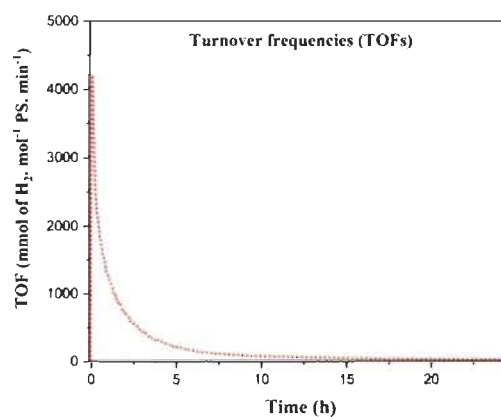
b

Fig. 5 - Hydrogen evolution reaction of **2**. (a) TONs and (b) TOFs

5. Conclusion

Converging two enthralling branches of supramolecular chemistry, we have synthesized a binuclear Fe(II) complex $[Fe_2(1)_2(\mu\text{-PHO}_3CH_3)_2]^{2+}$ **2** which is partly a macrocycle and partly a metallotecton. The interior of **2** is the macrocyclic part consisting of iron, oxygen and phosphorous atoms which is surrounded on both sides by a metallotecton exterior. Iron(II) atoms have a distorted octahedral geometry and are a part of both the macrocycle as well as the metallotecton. The photocatalytic activity for hydrogen production by **2** was performed in DMF using triethanolamine (TEOA) as the sacrificial electron donor, $Ru(bpy)_3(PF_6)_2$ as the photosensitizer (PS) and aqueous HBF_4 as the proton source. Complex **2** proves to be a promising candidate for hydrogen production from water, displaying a TON of 324 mol H_2. mol$_{PS}^{-1}$ and TOF of 4189 mmol of H_2. mol$_{PS}^{-1}$.min^{-1}. To the best of our knowledge, this is the only report displaying the TON and TOF of a macrocyclic metallotecton. Thereby **2** not only amalgamates two versatile chemical branches but also has prospects as a possible future substitute for fossil fuels.

6. Acknowledgements

7. Appendix A. Supplementary data

A. Supporting Information

The supporting Information is available free of charge via the internet at ACS Publications website at DOI: https://doi.org/10.1016/j.ijhydene.2019.11.141

Additional crystallographic details (including thermal atomic displacement ellipsoid plots), Mass spectrum, ORTEP diagrams and other crystallographic data, Powder X-ray diffraction, Infrared, Thermogravimetry analysis and Photographs of the crystalline samples (PDF).

B. Accession Codes

CCDC 1921972 contain the supplementary crystallographic data for this paper. These data can be obtained free of charge via www.ccdc.cam.ac.uk/data_request/cif, of by email data_request@ccdc.cam.ac.uk, or by contacting The Cambridge Crystallographic Data Centre, 12 Union Road Cambridge CB2 1EZ, UK; fax: +44 1223 336033.

C. Author Information

Corresponding Author

*E-mail: adam.duong@uqtr.ca.

ORCID

Adam Duong : 0000-0002-4927-3603

D. Conflicts of interest

There are no conflicts to declare.

8. References

[1] Van der Waals JD. On the Continuity of the Gaseous and Liquid States. Ph.D. thesis Leiden, The Netherlands 1873.

[2] Lehn JM. Cryptates: the chemistry of macropolycyclic inclusion complexes. Chem Res 1978;11:49-57.

[3] Pedersen CJ. Cyclic polyethers and their complexes with metal salts. *J Am Chem Soc* 1967;89:7017-7036.

[4] Pedersen CJ. Cyclic polyethers and their complexes with metal salts. *J Am Chem Soc* 1967;89:2495-2496.

[5] Yudin AK. Macrocycles: lessons from the distant past, recent developments, and future directions. Chem Sci 2015;6:30-49.

[6] Wessjohann LA, Ruijter E, Garcia-Rivera D, Brandt W. What can a chemist learn from nature's macrocycles? A brief, conceptual view. Mol Diversity 2005;9:171-186.

[7] Gloe K. Macrocyclic Chemistry Current Trends and Future Perspectives. Springer: Dordrecht, the Netherlands 2005.

[8] Lindoy LF, Park K-M, Lee SS. Metals, macrocycles and molecular assemblies – macrocyclic complexes in metallo-supramolecular chemistry. Chem Soc Rev 2013; 42:1713-1727.

[9] Geduhn J, Walenzyk T, Konig B. Transition Metal Complexes of Some Azamacrocycles and Their Use in Molecular Recognition. Curr Org Synth 2007;4:390-412.

[10] Shinoda S. Dynamic cyclen–metal complexes for molecular sensing and chirality signaling. Chem Soc Rev 2013;42:1825-1835.

[11] Joliat E, Schnidrig S, Probst B, Bachmann C, Spingler B, Baldridge KK, *et al.* Cobalt complexes of tetradentate, bipyridine-based macrocycles: their structures, properties and photocatalytic proton reduction. Dalton Trans 2016;45:1737-1745.

[12] Maspoch D, Ruiz-Molina D, Veciana J. Old materials with new tricks: multifunctional open-framework materials. Chem Soc Rev 2007;36:770-818.

[13] Wang L, Hu Y, Xu W, Pang Y, Liu F, Yang Y. Investigation of hydrogen bonding patterns in a series of multi-component molecular solids formed by tetrabromoterephthalic acid with selected N-heterocycles. RSC Adv 2014;4:56816-56830.

[14] Xing P, Li. Q, Li Y, Wang K, Zang Q, Wang L. Organic salts formed by 2,4,6-triaminopyrimidine and selected carboxylic acids via a variety of hydrogen bonds: Synthons cooperation, and crystal structures. J Mol Struct 2017;1136:59-68.

[15] Simard M, Su D, Wuest JD. Use of hydrogen bonds to control molecular aggregation. Self-assembly of three-dimensional networks with large chambers. J Am Chem Soc 1991;113:4696-4698.

[16] Wuest JD. Engineering crystals by the strategy of molecular tectonics. Chem Commun 2005;47:5830-5837.

[17] Hosseini MW. Molecular Tectonics: From Simple Tectons to Complex Molecular Networks. Acc Chem Res 2005;38:313-323.

[18] Constable EC. Higher Oligopyridines as a Structural Motif in Metallosupramolecular Chemistry. Prog Inorg Chem 1994;42:67-138.

[19] Telfer SG, Wuest JD. Metallotectons: Comparison of Molecular Networks Built from Racemic and Enantiomerically Pure Tris(dipyrrinato)cobalt(III) Complexes. Cryst Growth Des 2009;9:1923-1931.

[20] Constable EC, Housecroft CE, Neuberger M, Schaffner S, Schaper F. Preparation and structural characterisation of bis(4′-(3-pyridyl)-2,2′:6′,2″-terpyridine)ruthenium(II) hexafluorophosphate. Inorg Chem Commun 2006;9:433-436.

[21] Braga D, Brammer L, Champness NR. New trends in crystal engineering. CrystEngComm 2005;7:1-19.

[22] McCleverty JA, Meyer TJ, Lever ABP. Comprehensive coordination chemistry II: from biology to nanotechnology. Vol. 2, Fundamentals: physical methods, theoretical analysis, and cases studies. Amsterdam, Elsevier Pergamon 2004.

[23] Duong A, Maris T, Wuest JD. Using Pyridinyl-Substituted Diaminotriazines to Bind Pd(II) and Create Metallotectons for Engineering Hydrogen-Bonded Crystals. Inorg Chem 2011;50:5605-5618.

[24] Santillan GA, Carrano CJ. Self assembly of silver(I) coordination polymers formed through hydrogen bonding with a new ditopic heteroscorpionate ligand. Dalton Trans 2009;33:6599-6605.

[25] Duong A, Métivaud V, Maris T, Wuest JD. Surrogates of 2,2'-Bipyridine Designed to Chelate Ag(I) and Create Metallotectons for Engineering Hydrogen-Bonded Crystals. Cryst Growth Des 2011; 11:2026-2034.

[26] McMorran DA. Ag(I)-Based Tectons for the Construction of Helical and meso-Helical Hydrogen-Bonded Coordination Networks. Inorg Chem 2008;47:592-601.

[27] Salazar-Mendoza D, Baudron SA, Hosseini MW. Beyond classical coordination: silver–π interactions in metal dipyrrin complexes. Chem Commun 2007;22:2252-2254.

[28] Braga D, Giaffreda SL, Grepioni F, Maini L, Polito M. Design, synthesis, characterization and utilization of hydrogen bonded networks based on functionalized organometallic sandwich compounds and the occurrence of crystal polymorphism. Coord Chem Rev 2006;250:1267-1285.

[29] Mascal M. Noncovalent design principles and the new synthesis. Contemp Org Synth 1994;1:31-46.

[30] Takano S, Takeuchi Y, Takeuchi D, Osakada K. Selective Formation of Ethyl- and/or Propyl-branched Oligoethylene Using Double-decker-type Dinuclear Fe Complexes as the Catalyst. Chem Lett 2014;43:465-467.

[31] Wang Z, Martell AE, Motekaitis RJ, Reibenspies JH. Dinuclear Fe(II) macrocyclic complexes as catalysts for the oxidation of hydrocarbons by molecular oxygen. Inorganica Chimica Acta 2000;300–302:378-383.

[32] Duong A, Maris T, Wuest JD. Structural Similarity of Hydrogen-Bonded Networks in Crystals of Isomeric Pyridyl-Substituted Diaminotriazines. Cryst. Growth Des 2011;11:287-294.

[33] Rajak S, Schott O, Kaur P, Maris T, Hanan GS, Duong A. Mimicking 2,2':6',2'':6'',2'''-quaterpyridine complexes for the light-driven hydrogen evolution reaction: synthesis, structural, thermal and physicochemical characterizations. RSC Adv 2019;9:28153-28164.

[34] Lewis NS, Nocera DG. Powering the planet: Chemical challenges in solar energy utilization. Proc Natl Acad Sci 2006;103:15729-15735.

[35] Wang M, Chen L, Sun L. Recent progress in electrochemical hydrogen production with earth-abundant metal complexes as catalysts. Energy Environ Sci 2012;5: 6763-6778.

[36] Cook TR, Dogutan DK, Reece SY, Surendranath Y, Teets TS, Nocera DG. Solar Energy Supply and Storage for the Legacy and Nonlegacy Worlds. Chem Rev 2010;110:6474-6502.

[37] Khaselev O, Turner JA. A Monolithic Photovoltaic-Photoelectrochemical Device for Hydrogen Production via Water Splitting. Science 1998;280:425-427.

[38] Liu T, Wang K, Du G, Asiric AM, Sun X. Self-supported CoP nanosheet arrays: a nonprecious metal catalyst for efficient hydrogen generation from alkaline $NaBH_4$ solution. J Mater Chem A 2016;4:13053-13057.

[39] Tang C, Pu Z, Liu Q, Asiri AM, Luo Y, Sun X. Ni_3S_2 nanosheets array supported on Ni foam: A novel efficient three-dimensional hydrogen evolving electrocatalyst in both neutral and basic solutions. Int J Hydrog Energy 2015;40:4727-4732.

[40] Xie L, Qu. F,Liu Z, Ren X, Hao S, Ge R, Du G, Asiri AM, Sun X, Chen L. In situ formation of a 3D core/shell structured $Ni_3N@Ni$–Bi nanosheet array: an efficient nonnoble-metal bifunctional electrocatalyst toward full water splitting under near-neutral conditions. J Mater Chem A 2017;5:7806-7810.

[41] Li G, Yu J, Jia J, Yang L, Zhao L, Zhou W, Liu H. Development of cobalt–cobalt phosphide nanoparticles@nitrogen-phosphorus doped carbon/graphene derived from cobalt ions adsorbed saccharomycete yeasts as an efficient, stable, and large-current-density electrode for hydrogen evolution reactions. Adv Funct Mater 2018;28:1801332.

[42] Yang L, Zeng L, Liu H, Deng Y, Zhou Z, Yu J, Liu H, Zhou H. Hierarchical microsphere of MoNi porous nanosheets as electrocatalyst and cocatalyst for hydrogen evolution reaction. Appl Catal B 2019;249:98-105.

[43] Jia J, Zhou W, Wei Z, Xiong T, Li G, Zhao L, Zhang X, Liu H, Zhou J, Chen S. Molybdenum carbide on hierarchical porous carbon synthesized from $Cu-MoO_2$ as efficient electrocatalysts for electrochemical hydrogen generation. Nano Energy 2017;41:749–757.

[44] Zhou LL, Fu LZ, Tang LZ, Zhang YX, Zhan SZ. Electrochemical and photochemical-driven hydrogen evolution catalyzed by a dinuclear cobalt(II)etriazenido complex with high turnover number. Int J Hydrog Energy 2015;40:5099-5105.

[45] Tang LZ Lin CN, Zhang YX, Zhan SZ. Electrocatalytic and photocatalytic hydrogen generation from water by a water-soluble cobalt complex supported by 2-ethyl-2-(2-hydroxybenzylideneamino)propane-1,3-diol. Int J Hydrog Energy 2016;41:14676-14683.

[46] Maheu C, Puzenat E, Geantet C, Cardenas L, Afanasiev P. Titania-supported transition metals sulfides as photocatalysts for hydrogen production from propan-2-ol and methanol. Int J Hydrog Energy 2019;44:18038-18049.

[47] Xu J, Gao J, Wang W, Wang C, Wang L. Noble metal-free NiCo nanoparticles supported on montmorillonite/MoS$_2$ heterostructure as an efficient UV-visible light-driven photocatalyst for hydrogen evolution. Int J Hydrog Energy 2018;43:1375-1385.

[48] Shi Y, Yang AF, Cao CS, Zhao B. Applications of MOFs: Recent advances in photocatalytic hydrogen production from water. Coordin Chem Rev 2019;390:50-75.

[49] Gao F, Huang X, Zhang L, Zhao Y, Feng W, Liu P. Crafty design of chemical bonding to construct MoO$_2$/CdS nanorod photocatalysts for boosting hydrogen evolution. Int J Hydrog Energy 2019;44:24228-24236.

[50] Surawatanawong P, Tye JW, Darensbourg MY, Hall MB. Mechanism of electrocatalytic hydrogen production by a di-iron model of iron–iron hydrogenase: A density functional theory study of proton dissociation constants and electrode reduction potentials. Dalton Trans 2010;39:3093-3104.

[51] Borg SJ, Ibrahim SK, Pickett CJ, Best SP. Electrocatalysis of hydrogen evolution by synthetic diiron units using weak acids as the proton source: Pathways of doubtful relevance to enzymic catalysis by the diiron subsite of [FeFe] hydrogenase. C R Chimie 2008;11:852-860.

[52] Chong D, Georgakaki IP, Mejia-Rodriguez R, Sanabria-Chinchilla J, Soriaga MP, Darensbourg MY. Electrocatalysis of hydrogen production by active site analogues of the iron hydrogenase enzyme: structure/function relationships. Dalton Trans 2003;21:4158-4163.

[53] Song L-C, Hong D-J, Guo Y-Q, Wang X-Y. Dinuclear FeIIFeII Biomimetics for the Oxidized State Active Site of [FeFe]-Hydrogenases: Synthesis, Characterization, and Electrocatalytic H_2 Production. Organometallics 2018;37:4744-4752.

[54] Yen T-H, Chu K-T, Chiu W-W, Chien Y-C, Lee G-H, Chiang M-H. Synthesis and characterization of the diiron biomimics bearing phosphine borane for hydrogen formation. Polyhedron 2013;64:247-254.

[55] Martell AE, Perutka J, Kong D. Dinuclear metal complexes and ligands: stabilities and catalytic effects. Coord Chem Rev 2001; 216-217:55-63.

[56] Fu L-Z, Zhou L-L, Tang L-Z, Zhang Y-X, Zhan S-Z. A molecular iron(III) electrocatalyst supported by amine-bis(phenolate) ligand for water reduction. Int J Hydrogen Energy 2015;40:8688-8694.

[57] Sheldrick GM. SHELXT-Integrated space-group and crystal-structure determination. Acta Cryst A 2015;71:3-8.

[58] Sheldrick GM. Crystal structure refinement with SHELXL. *Acta Cryst C* 2015;71, 3-8.

[59] Macrae CF, Bruno IJ, Chisholm JA, Edgington PR, McCabe P, Pidcock E, *et al.* Mercury CSD 2.0 – new features for the visualization and investigation of crystal structures. J Appl Crystallogr 2008;41:466-470.

[60] Lentz C, Schott O, Auvray T, Hanan GS, Elias B. Photocatalytic Hydrogen Production Using a Red-Absorbing Ir(III)–Co(III) Dyad. Inorg Chem 2017:56(18):10875–10881.

[61] Case FH, Koft E. The Synthesis of Certain Substituted 1,3,5-Triazines Containing the Ferroin Group. J Am Chem Soc 1959;81:905-906.

[62] Li K, Tong GS, Wan Q, Cheng G, Tong W-Y, Ang W-H, Kwong W-L, Che C-M. Highly phosphorescent platinum(II) emitters: photophysics, materials and biological applications. Chem Sci 2016;7:1653-1673.

[63] Singla P, Luxami V, Paul K. Triazine as a promising scaffold for its versatile biological behavior. Eur J Med Chem 2015;102:39-57.

[64] Corbo R, Georgiou DC, Wilson DJ, Dutton JL. Reactions of $[PhI(pyridine)_2]^{2+}$ with Model Pd and Pt II/IV Redox Couples. Inorg Chem 2014;53:1690-1698.

[65] Mooibroek TJ, Gamez P. The s-triazine ring, a remarkable unit to generate supramolecular interactions. Inorg Chim Acta 2007;360:381-404.

[66] Gamez P, Reedijk J. 1,3,5-Triazine-Based Synthons in Supramolecular Chemistry. Eur J Inorg Chem 2006;2006:29-42.

[67] Ye W, Staples RJ, Rybak-Akimov EV. Oxygen atom transfer mediated by an iron(IV)/iron(II) macrocyclic complex containing pyridine and tertiary amine donors. J Inorg Biochem 2012;115:1-12.

[68] Drahoš B, Herchel R, Trávníček Z. Single-Chain Magnet Based on 1D Polymeric Azido-Bridged Seven-Coordinate Fe(II) Complex with a Pyridine-Based Macrocyclic Ligand. Inorg Chem 2018;57:12718-12726.

[69] Rajak S, Mohan M, Tremblay AA, Maris T, Santos S, Venancio EC, *et al.* Programmed Molecular Construction: Driving the Self-Assembly by Coordination and Hydrogen Bonds Using 6-(Pyridin-2-yl)-1,3,5-triazine-2,4-diamine with $M(NO_3)_2$ Salts. ACS Omega 2019;4:2708-2718.

[70] Hogue RW, Schott O, Hanan GS, Brooker S. A Smorgasbord of 17 Cobalt Complexes Active for Photocatalytic Hydrogen Evolution. Chem Eur J 2018;24:9820-9832.

[71] deKrafft KE, Wang C, Lin W. Metal-Organic Framework Templated Synthesis of Fe_2O_3/TiO_2 Nanocomposite for Hydrogen Production. Adv Mater 2012;24:2014-2018.

[72] Sasan K, Lin, QP, Mao CY, Feng PY. Incorporation of iron hydrogenase active sites into a highly stable metal–organic framework for photocatalytic hydrogen generation. Chem Commun 2014;50:10390-10393.

[73] Xu JY, Zhai XP, Gao LF, Chen P, Zhao M, Yang HB, Cao DF, Wang Q, Zhang HL. In situ preparation of a MOF-derived magnetic carbonaceous catalyst for visible-light-driven hydrogen evolution. RSC Adv 2016;6:2011-2018.

[74] Pham MH, Dinh CT, Vuong GT, Ta ND, Do TO. Visible light induced hydrogen generation using a hollow photocatalyst with two cocatalysts separated on two surface side. Phys Chem Chem Phys 2014;16:5937-5941.

5.4. Conclusions

We have synthesized a binuclear Fe(II) complex $[Fe_2(1)_2(\mu\text{-}PHO_3CH_3)_2]^{2+}$ **2** by combining the two interesting branches of supramolecular chemistry namely, macrocyclic chemistry and metallotectons. The structure of [FeFe] macrocyclic metallotecton includes a macrocyclic part consisting of iron, oxygen and phosphorous atoms surrounded by a metallotecton exterior on two sides. The diaminotriazine (DAT) based ligand **2** directs multiple hydrogen-bonding according to motifs II to produce a final three-dimensional structure. HER study of **2** reveals it as an efficient photocatalyst displaying a high TON and turnover frequency (TOF), which is much higher than other Fe based molecular catalysts reported in literature. Besides, the photocatalytic activity of **2** outperforms that of the most widely reported standard reference cobaloxime catalyst $(Co^{III}(dmgH)_2(py)Cl)$ by ~ 4.8 times. To the best of our knowledge, this is the only report displaying the photocatalytic activity for hydrogen evolution reaction by a macrocyclic metallotecton. Based on its high catalytic activity, **2** can be used to produce hydrogen, which can serve as a possible substitute for fossil fuels. Inspired by the naturally occurring hydrogenases enzymes present in nature, this project not only integrates two versatile branches of chemistry but also adds a biological spice to it.

5.5. Supporting Information

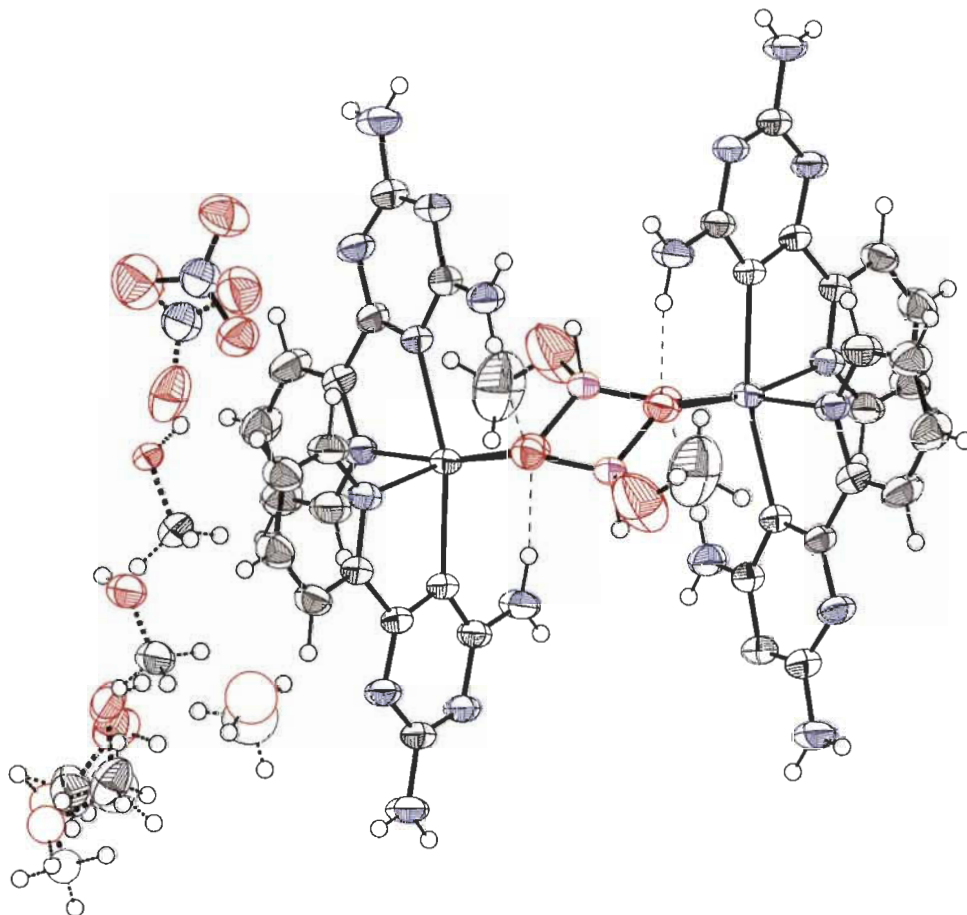| Contents		Page

Fig. S1 - Thermal atomic displacement ellipsoid plot of the structure of **2** grown from MeOH/ Ether. The ellipsoids of non-hydrogen atoms are drawn at 50% probability level, and hydrogen atoms are represented by a sphere of arbitrary size.
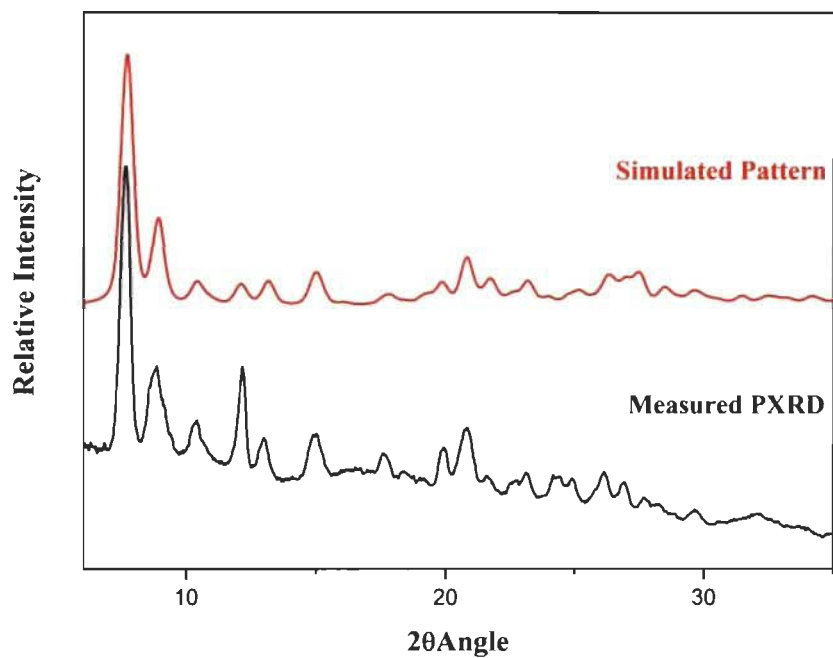
Fig. S2- Comparison of the measured PXRD (in black) with simulated patterns (in red) calculated from single-crystal structures of **2**.
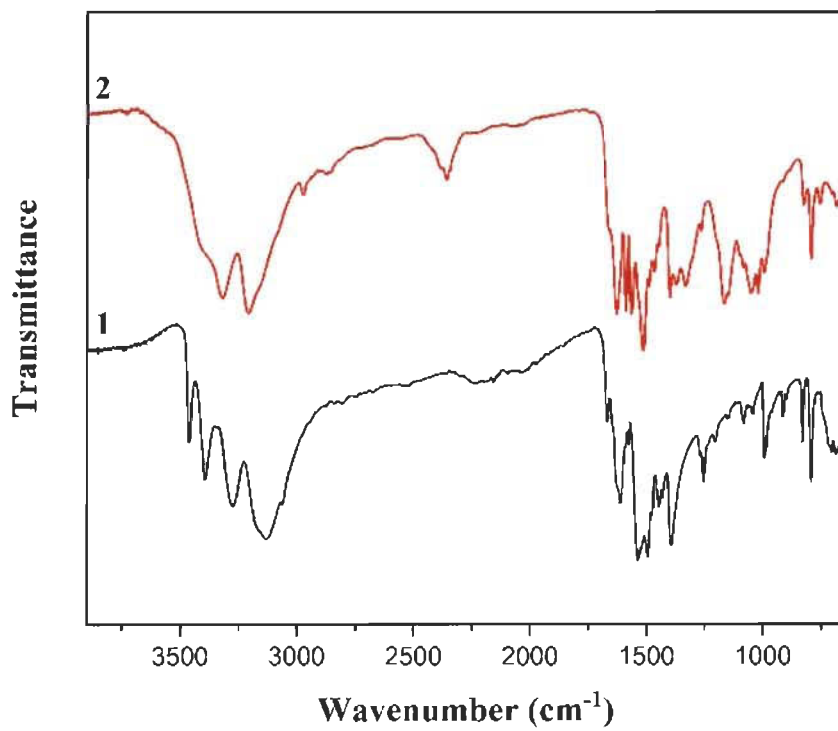
Fig. S3- Infrared spectra of ligand **1** and complex

Fig. S4- Optical microscopy image of crystals of **2**

Fig. S5- Thermogravimetric analysis (TGA) curves of ligand **1**

Table S1 Geometrical parameters including selected bond lengths and interatomic distances of complex **2**.

Atoms	Distance (Å)	Atoms	Angle (º)
Fe1 N1	2.172(2)	Fe1 O1 P1 O2	129.56(16)

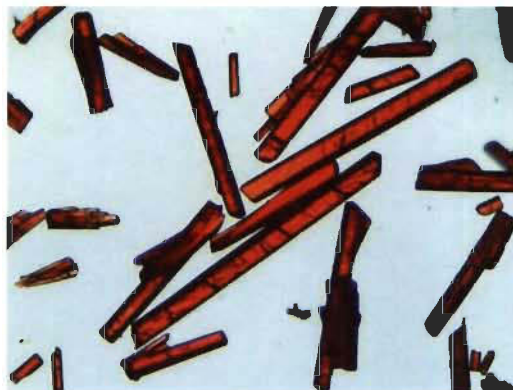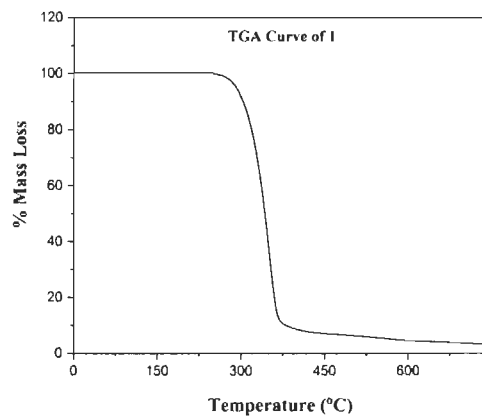|			
Fe1 N2	2.2165(19)	Fe1 O1 P1 O3	-100.5(5)
Fe1 N7	2.228(2)	Fe1¹ O2 P1 O1	-86.67(16)
Fe1 N8	2.190(2)	Fe1¹ O2 P1 O3	146.1(4)
Fe1 O1	2.0923(18)	N3 C7 N2 Fe1	-173.47(19)
Fe1 O2	2.1010(18)	N4 C6 N2 Fe1	177.6(2)
		N5 C7 N2 Fe1	5.7(4)
		N9 C14 N7 Fe1	-170.6(2)
		N10 C16 N7 Fe1	168.43(19)
		N11 C16 N7 Fe1	-11.9(4)
		N1 Fe1 N2	75.49(8)
		N1 Fe1 N7	98.07(8)
		N1 Fe1 N8	92.61(9)
		N2 Fe1 N7	164.12(8)
		N8 Fe1 N2	91.64(8)
		N8 Fe1 N7	73.96(8)
		O1 Fe1 N1	169.17(8)
		O1 Fe1 N2	94.60(7)
		O1 Fe1 N7	92.62(7)
		O1 Fe1 N8	92.02(8)
		O1 Fe1 O2¹	87.94(8)
		O2¹ Fe1 N1	88.96(8)
		O2¹ Fe1 N2	97.05(7)
		O2¹ Fe1 N7	97.33(7)

O2^i Fe1 N8	171.29(7)
C1 N1 Fe1	125.02(17)
C5 N1 Fe1	116.28(17)
C6 N2 Fe1	114.92(16)
C7 N2 Fe1	130.93(16)
C14 N7 Fe1	116.18(16)
C16 N7 Fe1	129.38(17)
C9 N8 Fe1	124.82(18)
C13 N8 Fe1	117.19(17)
P1 O1 Fe1	136.46(11)
P1 O2 Fe1^i	129.96(11)

Table S2 Hydrogen-bond geometry (Å, °) in structure of **2**

D—H$\cdots A$	D—H	H$\cdots A$	$D\cdots A$	D—H$\cdots A$
N5—H5$A\cdots$O3B^i	0.88	2.30	3.038 (9)	141
N5—H5$A\cdots$O1C^i	0.88	2.05	2.881 (4)	156
N5—H5$B\cdots$O1	0.88	1.98	2.826 (3)	162
N6—H6$A\cdots$N9^{ii}	0.88	2.28	3.146 (3)	169
N6—H6$B\cdots$O2^{iii}	0.88	2.49	3.251 (3)	145
N6—H6$B\cdots$O2A^{ii}	0.88	2.37	3.034 (12)	133
N6—H6$B\cdots$O2B^{ii}	0.88	2.37	3.017 (12)	131
N11—H11$A\cdots$O3B^{iv}	0.88	2.25	3.021 (9)	147
N11—H11$A\cdots$O1C^{iv}	0.88	2.08	2.948 (4)	170
N11—H11$B\cdots$O2^v	0.88	2.07	2.889 (3)	154
N11—H11$B\cdots$O2B^{iv}	0.88	2.55	2.949 (12)	109
N12—H12$A\cdots$O1F^{iv}	0.88	2.41	3.288 (11)	176
N12—H12$B\cdots$N3^{vi}	0.88	2.24	3.103 (4)	166

Symmetry codes: (i) $x-1/2$, $-y+1/2$, $z-1/2$; (ii) $x+1/2$, $-y+1/2$, $z-1/2$; (iii) $x+1$, y, z; (iv) $-x+3/2$, $y+1/2$, $-z+3/2$; (v) $-x+1$, $-y+1$, $-z+1$; (vi) $x-1/2$, $-y+1/2$, $z+1/2$.

Table S3 IR data and assignments of ligand **1** and complex **2**

$\tilde{\nu}$/cm⁻¹		Assignment
1	**2**	
686m	683w	Ring out-of-plane def., $\delta(NH_2)$
705w	700vw	
	752w	Ring out-of-plane def., $\delta(CH)$
792s	791m	
830m	823w	$\delta(CH)$
913w	910vw	$\nu(C\text{-}N)$, $\nu(C=N)$, $\nu(C\text{-}NH_2)$ DAT Ring
993m	992m	
1043w	1018m	$\delta(NH_2)$
	1050m	
1082w	1081w	$\delta(NH_2)$
	1097vw	
1153w	1146w	$\delta(P\text{-}O)$
	1164m	
1203w	1196vw	Ring out-of-plane def., $\delta(NH_2)$
1253m	1262w	Ring out-of-plane def., $\delta(NH_2)$
	1299w	
	1329m	$\nu(NO_3^-)$
	1369m	
	1397m	
1446w	1444w	DAT Ring breathing, $\nu(C\text{-}NH_2)$
	1464w	$\nu(C\text{-}C)$, $\nu(C=N)$, $\delta(CH)$ py Ring

1494s	1487w	ν(C-N), ν(C=N), DAT Ring, δ(CH)
	1511m	
	1532vw	ν(C-C), ν(C=C) py Ring
1576s	1561m	
	1585m	
1612m	1625m	ν(C-C), ν(C-N), ν(C=N) py Ring, ν(C-N),
1668w	1660w	ν(C=N), DAT Ring, δ(NH$_2$),
	2358w	ν(P-H)
	2385w	
3063vw	2974w	ν(CH)
3131s	3147w	
3274m	3209m	ν(NH)
3394m	3320m	
3461m	3409w	

***Abbreviation used for the type of vibration mode. def.: deformation; δ, γ, ρ, τ, ω: bending vibrations; ν: stretching vibration.

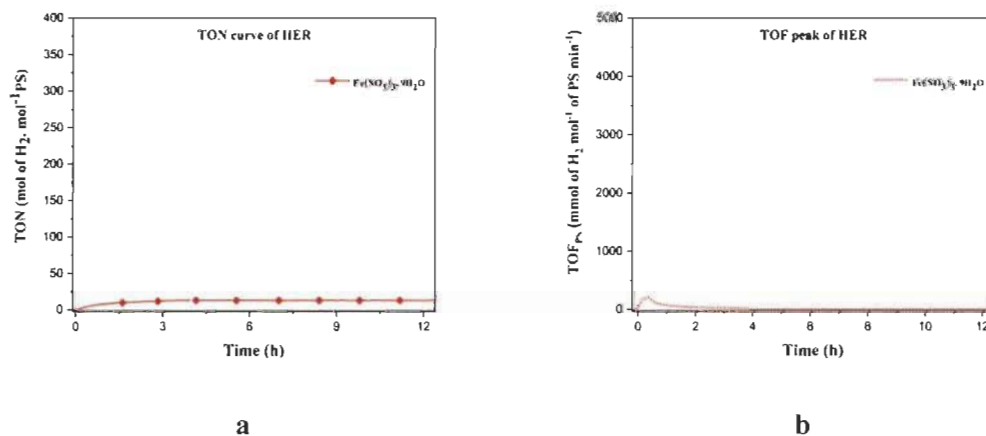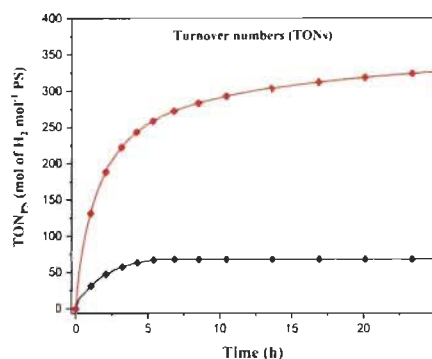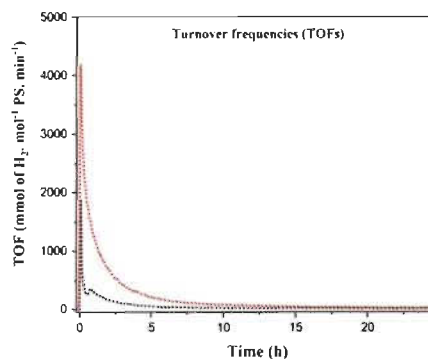a   b

Fig. S6 – (a) TON and (b) TOF for Fe(NO)$_3$.9H$_2$O

a   b

Fig. S7 – (a) TONs and (b) TOFs of **2** compared with the standard reference $(Co^{III}(dmgH)_2(py)Cl)$

General mechanism of hydrogen evolution reactions

The mechanism of the hydrogen evolution reaction may occur by two important steps; (I) Activation of the molecular catalyst by the photosensitizer and (II) Redox photocatalytic hydrogen evolution.
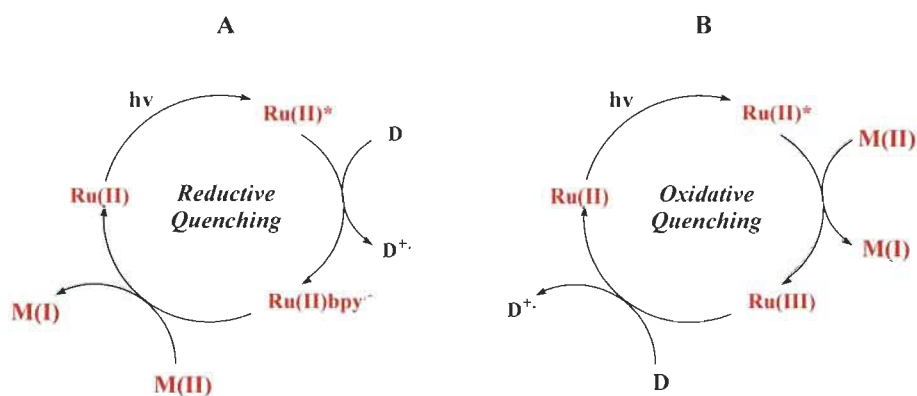
Step I

Fig. S8- Photosensitizer based processes in light-driven hydrogen evolution reaction

252

In step I, activation of the molecular photocatalyst can take place either by reductive or oxidative quenching pathways from the excited photosensitizer (PS*). Visible light is used to for the excitation of the photosensitizer where, in the process of reductive quenching (A), the excited PS* accept an electron from the sacrificial electron donor (SED) and shares it with the molecular catalyst, during this course, the oxidation state of Ru(II) does not change. In the process of oxidative quenching (B), the excited PS* oxidizes and donates its electron to the molecular catalysts and then abstracts an electron from the SED, this process involves redox changes in Ru(II) PS.

In step II, at the photocatalytic centre, the hydrogen evolution can occur by two different mechanisms.
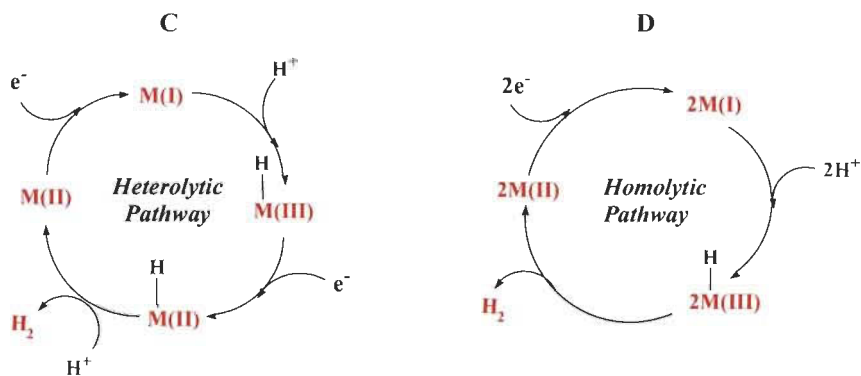
Step II

Fig. S9- Heterolytic and homolytic mechanisms of hydrogen evolution reaction catalysed by molecular photocatalyst

In heterolytic mechanism (C), H_2 is evolved by the protonation of the intermediate metal hydride. In the catalytic cycle, the two electrons are transferred either consecutively or alternatively. The H_2 evolution in the alternative homolytic pathway (D) happens by the reductive elimination of two metal hydride intermediates. In both the mechanisms, the metal salts of +II oxidation state undergoes one electron reduction before protonation takes place.[1]
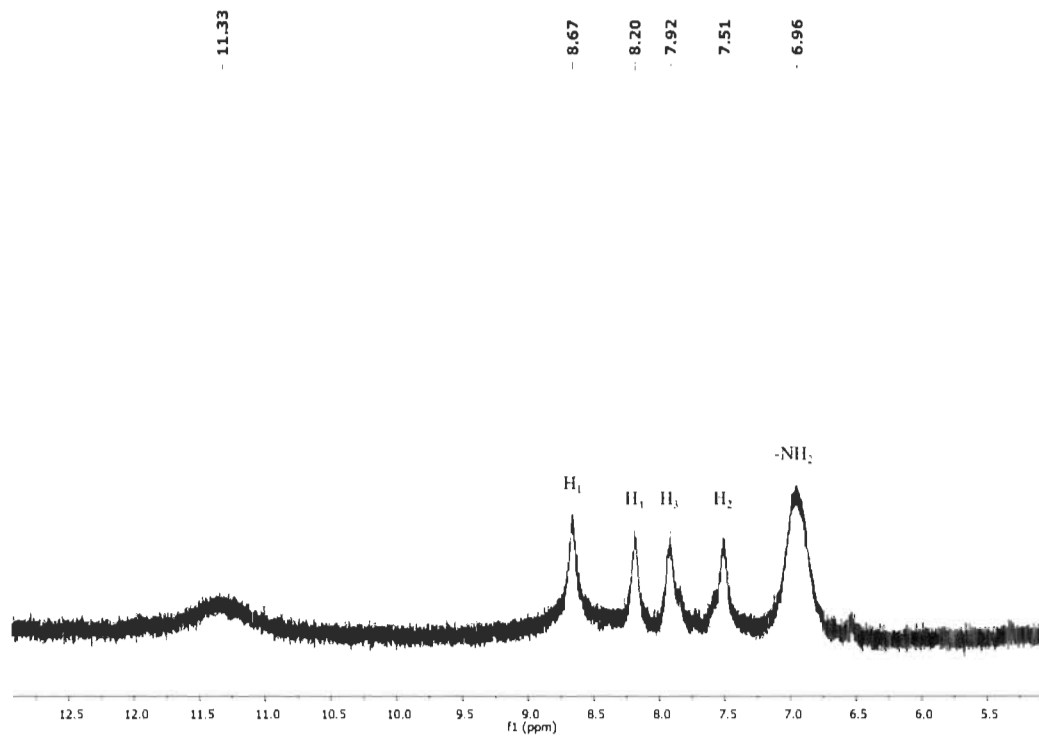
253

Fig. S10 - ¹H NMR of **2.**

References

4. Artero, V.; Chavarot-Kerlidou, M.; Fontecave, M., *Angew. Chem.* 2011, 50 (**32**), 7238-7266.

Chapter 6

Amidine/Amidinate Cobalt Complexes: One-Pot Synthesis, Mechanism and Photocatalytic Application for Hydrogen Production

6.1. Introduction

In this project, studies based on the synthesis of coordinatively saturated amidine/amidinate cobalt complexes *via* the one-pot introduction of amidine/amidinate groups into pyridinyl-substituted diaminotriazine cobalt complex have been reported. Single-crystal X-ray diffraction has been used to investigate and propose the formation mechanism of amidine/amidinate complexes. Cobalt complexes prepared herein utilize a renewable energy resource *viz.* sunlight to produce hydrogen which has much higher catalytic activity than that reported for previously synthesized pyridinyl-substituted diaminotriazine cobalt complex.

6.2. Article 5

Amidine/Amidinate Cobalt Complexes: One-Pot Synthesis, Mechanism and Photocatalytic Application for Hydrogen Production.

Sanil Rajak, Khaoula Chair, Lovekaran Rana, Prabhjyot Kaur, Thierry Maris, Adam Duong*

6.3. Author's Contribution

Sanil Rajak: Investigation, conceptualization, methodology, synthesis and characterization, photo catalytic testing, electrochemical analysis, interpretation of results, writing of the article.

Dr. Khaoula Chaiir: Some synthesis, characterization and photo catalytic testing.

Dr. Lovekaran Rana: Crystallographic data interpretation.

Dr. Prabhjyot Kaur: Writing- review and editing.

Dr. Thierry Maris: Crystallographic data analysis.

Prof. Adam Duong: Supervision, finding financial supports, investigation, conceptualization, interpretation of results, writing- review and editing.

1. Abstract

A new synthetic route *via* a one-pot reaction was carried out to prepare a novel series of amidine/amidinate cobalt complexes **8-10** obtained by mixing ligand **2** (6-pyridin-2-yl-[1,3,5]-triazine-2,4-diamine) with Co(II) in acetonitrile or benzonitrile. We observed that a change of solvent from methanol (in complex **7**, previously reported) to nitrile solvents (MeCN and PhCN) leads to the *in-situ* incorporation of amidine group forming ultimately **8-10**. So far, this is the unique method reported to introduce amidine/amidinate groups into pyridinyl-substituted diaminotriazine complex. Remarkably, Single-crystal X-ray diffraction study of these new compounds reveals associations involving Janus- DAT amidine and DAT amidinate. A mechanism is proposed to explain the formation of amidine/amidinate groups by investigating the single-crystal structures of the possible intermediates **11** and **12** where the cobalt ion acts as a template. These amidine/amidinate cobalt complexes have been used as a model to assess the photocatalytic activity for the hydrogen evolution reaction (HER). Complexes **9** and **10** show a 74% and 86% enhancement respectively, of catalytic activity towards hydrogen evolution reaction (HER) compared to complex **7**. This highlights the structure-property relationship. By examining the novel cobalt complexes described here we discovered (i) a method to introduce amidine group into pyridine DAT based complex; (ii) the efficiency of amidine complexes to form multiple hydrogen bonds to direct the molecular organization (iii) the plausible mechanism of formation of amidines based on the SCXRD study (iv) modification of the final structure and hence the final properties by varying the reaction conditions and (v) the utility of amidine complexes towards photocatalytic HER activity.

2. Introduction

The development and synthesis of novel ordered materials with well controlled chemical compositions and tailored properties for their utility in diverse fields like catalysis, ion-exchange, batteries, non-linear optics, medicine, photovoltaics, energy storage, gas absorption, magnetism and so forth is a predominant part of chemistry.[1] A continuously evolving and never-ending exploration in this prospect has led to the discovery of numerous innovative materials with sundry applications and an upsurge in advancement of knowledge leading to a better understanding of the structure-property relationship. Crystal engineering plays a pivotal role in the synthesis of such ordered materials as it provides a platform to amalgamate different organic molecules having requisite topologies with inorganic components (metal ions) to produce ordered materials with predictable structures.[2] This strategy also provides an opportunity to vary the metal ions which allows tuning properties of materials. It is well known that the properties of a complex depend upon its structure which in turn depends on the reaction conditions such as precursors, counterions, solvents, temperature, etc. Thus, in crystal engineering, ligand, metal ion and reaction conditions play a crucial role in determining the final structure of the materials and hence its properties.

One of the ligands widely used in coordination chemistry, is 2,2'-bipyridine (2,2'-bipy) whose good chelating ability has led to its extensive utilization in conjunction with the metal ions to engineer crystalline complexes suitable for a wide range of applications.[3] However, the lack of straightforward and efficient synthetic route to functionalize 2,2'-bipy severely limits any prospects of their use to create versatile coordination complexes. Fortunately, the design of pyridinyl- and pyrazinyl-substituted diaminotriazines (DAT) derivatives **2-4** (Scheme 1) called tectoligands has resulted in the elimination of the most drawbacks concerning 2,2'-bipy derivative synthesis.[4] DAT group is easy to prepare and can be incorporated in any organic fragment. Due to its presence, **2-4** have the ability to bind to metal ions with the same ligating mode as 2,2'-bipy and to undergo self-assembly by multiple hydrogen bonds with reliable patterns.[5] Complexes

prepared with tectoligands are so called metallotectons.[6] So far, metallotectons have been mainly studied to advance knowledge in crystal engineering that is focusing on the organization of molecules *via* intermolecular interactions. To adapt these compounds for the various applications to which they have been designed additional functional groups must be integrated.

Through a literature survey, we found that amidine functional group is facile to prepare and has several applications. Amidine groups can be formed by reaction of nitrile (RCN) with amine (R'NH$_2$) in presence of Lewis acids. They are a class of organic compounds having a – C(=NH)NH$_2$ group homologous to a carboxamide in which the oxygen atom of the oxo has been replaced by the N-H group. They are present in numerous complexes which find applications in medicinal chemistry, pharmacology, catalyst design, material science and so forth.[7] Besides substituted amidines have a significant role in several biological activities due to which their synthesis has been of interest for many research groups. In principle, it should be viable to incorporate amidine functionality into DAT substitution-based complexes. However, no report has been presented so far on the synthesis of amidine compounds using -NH$_2$ of DAT group.

Herein, combining the self-assembly provided by DAT groups with the versatile properties associated to amidines, we have developed a new facile synthetic route to prepare amidine cobalt complexes **8-10** by reacting **2** with Co(II) salt in acetonitrile (MeCN) or benzonitrile (PhCN) under reflux *via* a one-pot reaction (Scheme 2a). This work is the unique report on the synthesis of amidine using -NH$_2$ of DAT group. In our previous work, we have shown the synthesis of complex **7** by mixing **2**[8] with Co(II) salt in MeOH under reflux (Scheme 1).[4c] We observed that a change of solvent from MeOH to MeCN or PhCN leads to the formation of **8-10**. Interestingly, by analyzing diverse reaction conditions (Scheme 3) and the crystallographic structure of complexes **8-12** a plausible mechanism for amidine/amidinate formation has been proposed. Based on the principles of organic/inorganic chemistry, **11** could be the reactive intermediate to form **8**. We have also shown that **9** and **10** are catalytically efficient towards light driven hydrogen evolution reaction

(HER) and show a far more improved activity compared to complex **7** (prepared under different reaction conditions). HER is one of the best possible solution to control the currently deteriorating situation of our environment with increased global warming and greenhouse effect.[9] During the past decade, cobalt complexes have been widely used as catalysts for H_2 generation that are driven photochemically. Especially, cobalt complexes based on polypyridine have attracted considerable attention for photocatalytic proton reduction.[10] To this regard, design of functionalized polypyridyl complexes still represents one of the most important challenges in the field of catalysis. The results obtained in the present work demonstrated an enhanced HER activity with the presence of amidine/amidinate groups in **9** and **10** as compared to **7**.[11] Hence, a modification in the preparatory strategy leads to novel complexes with different structures and improved hydrogen evolution emphasizing the relationship between a compound's structure and its properties.
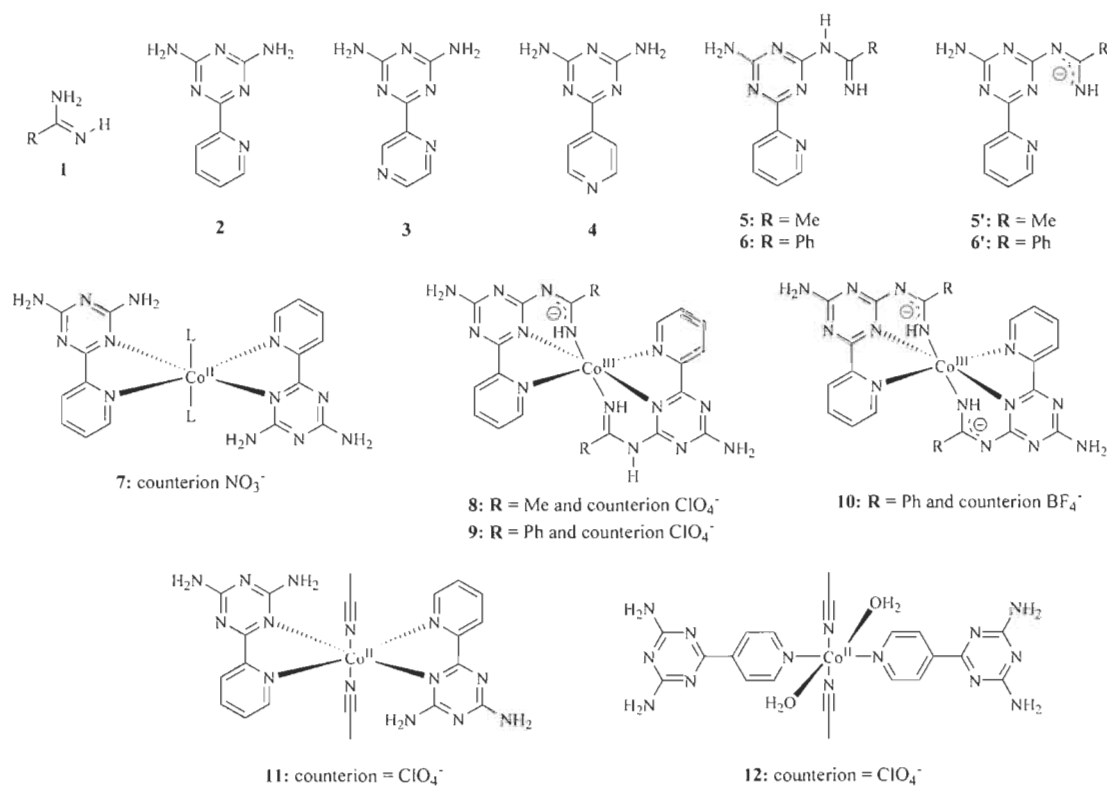
Scheme 1. Molecular structures of amidine **1**, ligands **2-6** and cobalt complexes **7-12**.

3. Results and Discussions

In a previous study, we have described the design, synthesis and characterization of **7** and investigated its catalytic activity for light driven hydrogen evolution reaction (HER).[4c, 11] To develop a new method to functionalize complexes with amidine/amidinate functional groups and to potentially improve the catalytic activities for HER, we have prepared **8-10** (Scheme 2a). Our method to synthesize amidine/amidinate cobalt complexes is advantageous because the coordination and the formation of **5** and **5'**, and **6** and **6'** is *in situ*, and no further purification step is required (Scheme 1). **5** and **5'**, and **6** and **6'** were never isolated but simply were the initial intermediates which led to the formation of ultimate intermediates (**11, 12**) followed by the final complexes (**8-10**). A similar kind of analogous *in situ* reaction has been observed in the hydration of nitrile group into carboxamide with ferrous centre as the Lewis acid reaction site.[12] We have also examined the effect of counterions by using $Co(ClO_4)_2$ and $Co(BF_4)_2$ salts. Our results showed that the change of counterion did not prevent the formation of amidine/amidinate group. In addition, we found that the incorporation of amidine/amidinate group and a change of counterion, results in greater stability of **9** and **10** in HBF_4 compared to **7**. In this work, we have laid an emphasis on studying the mechanism of amidine/amidinate formation. Furthermore, as **9** and **10** have shown a good stability in acid condition, we tested their catalytic activity for HER.

3.1. Synthesis and structural characterization

Complexes **8-12** were characterized by electrospray ionization mass spectrometry (ESI-MS), infrared (IR) spectroscopy, elemental analysis (EA) and single-crystal X-ray diffraction (SCXRD). Their thermal stability was investigated by thermogravimetry analysis (TGA) (Figure S1). Compounds **8-11** are thermally stable up to ~270 °C and **12** up to ~200 °C. Analyses by ESI-MS measurements confirm the presence of the metal ions for all complexes (see experimental section). The IR of **8-12** indicates the presence of typical broad bands characteristic of symmetric

and asymmetric N-H stretching in the range 3100-3500 cm^{-1} (Figure S2). In the case of **8-10**, the presence of the C=N bond of the C(=NH)NH group is mainly diagnosed with the bands at ~1522 cm^{-1}. The bands at ~ 2270 cm^{-1} in the spectra of **11** and **12** could be attributed to -C≡N of coordinated acetonitrile molecules. For **8, 9, 11** and **12**, the bands corresponding to perchlorate (ClO$_4^-$) are observed between 1000-1100 cm^{-1}. For **10**, the band at 1020 cm^{-1} is ascribed to tetrafluoroborate (BF$_4^-$). SCXRD was performed to confirm the obtention of **8-12** and to study the self-assembly by hydrogen bonds involving Janus- DATamidine and DATamidinate (Scheme 2b). Figure 1 shows the structures of these compounds. General formulas of **8-12** determined by EA (see experimental section) are in good agreement with their crystallographic data (Table S1 and S5).
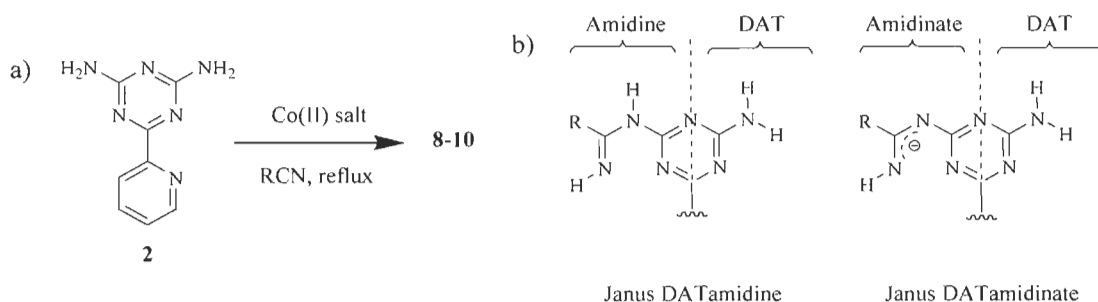
Scheme 2. (a) *In situ* synthetic route to prepare amidine/amidinate cobalt complexes **8-10**. (b) Representation of the molecular structure of Janus- DATamidine and DATamidinate.
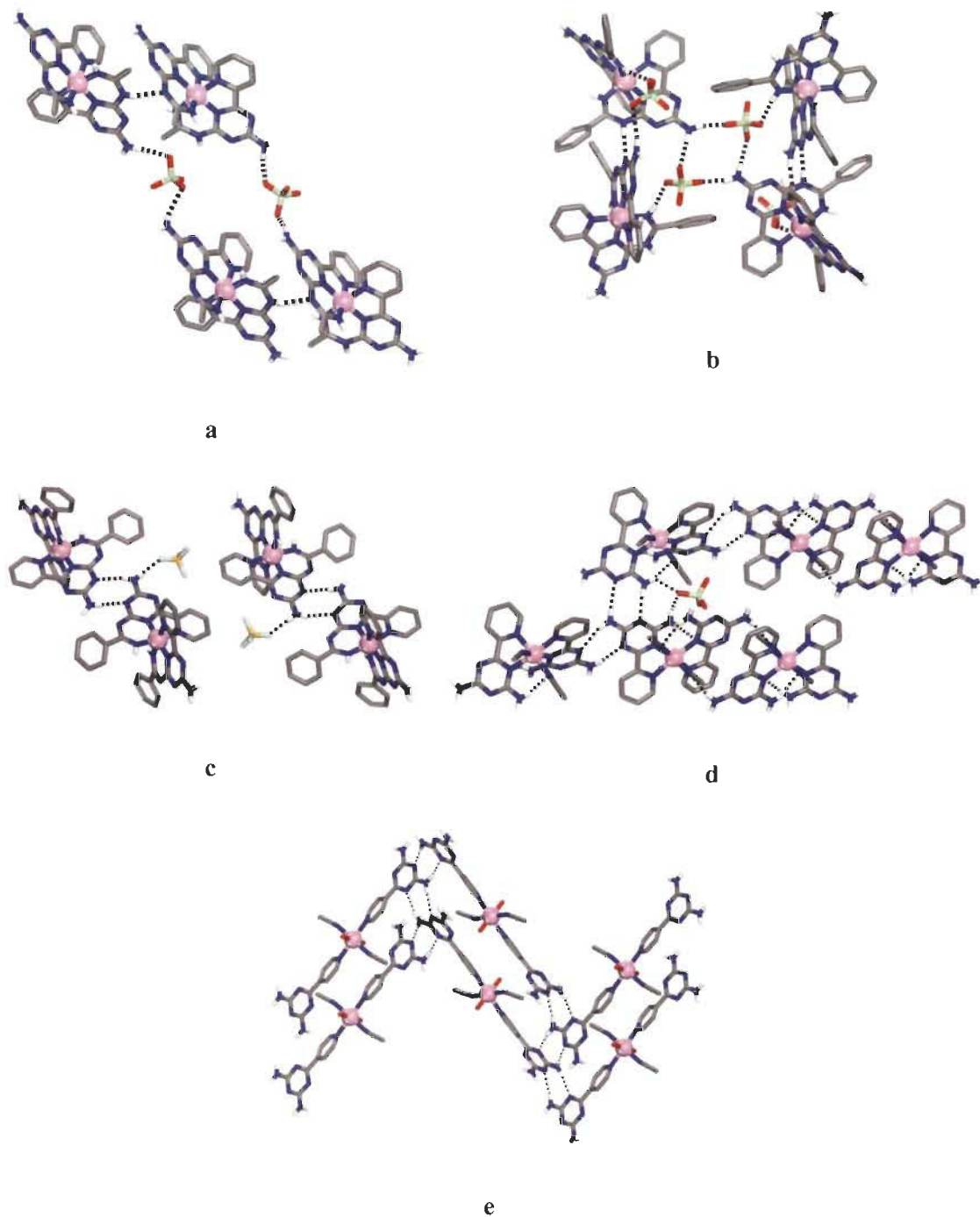
Figure 1. (a)-(e) View of the main hydrogen bonding interactions in the structures of **8-12** respectively. Hydrogen bonds are represented by dashed lines. Carbon atoms are shown in grey, hydrogen atoms in white, oxygen atoms in red, nitrogen atoms in blue, chlorine atoms in green, boron atoms in orange, fluorine atoms in cyan and cobalt atoms in pink. Hydrogen attached to carbon atom have been omitted for clarity.

Structure of **8** is shown in Figures 1a, S3 and S4. In the structure, Co(III) ion is bounded by ligands **5** and **5'** oriented perpendicular to each other (dihedral angle, $\delta = 87.98°$ between triazinyl rings), with each molecule coordinated *via* (NNN) set using triazine, pyridine and amidine/amidinate nitrogen atoms to form a distorted octahedral dication complex $[Co(\mathbf{5})(\mathbf{5'})]^{2+}$. The charge of the complex is balanced by an amidinate ligand **5'** and two disordered perchlorate ions. In the structure, complexes with λ and Δ configurations are alternately linked by N-H···N hydrogen bonds according to motif **I** to form chains (Chart 1a). Chains are further joined by N-H···O hydrogen bonds involving bridging of perchlorate to generate a 2D sheet (Figure 1a). It is noted that the change of oxidation state from Co(II) to Co(III) due to the experimental condition is also described in several other reports.[13] Selected hydrogen bonds and angles are given in Table S2.
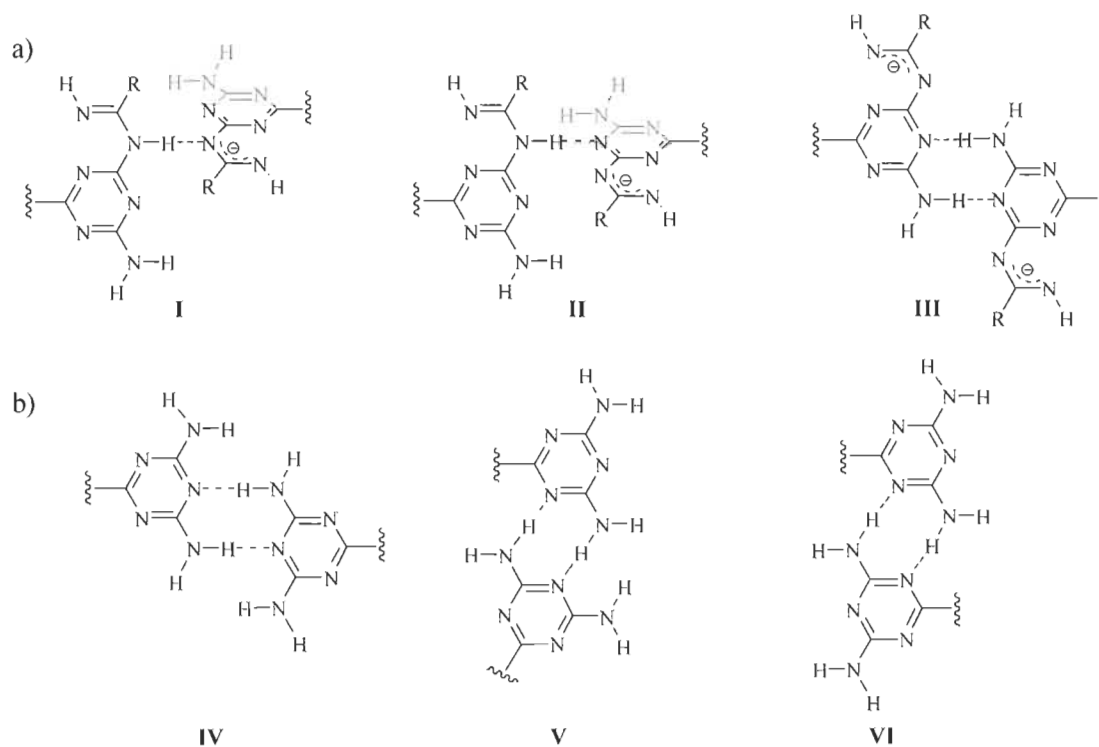

Chart 1. Hydrogen bonding motifs (a) **I-III** of amidine/amidinate and (b) **IV-VI** of diamino-1,3,5-triazinyl group (DAT).
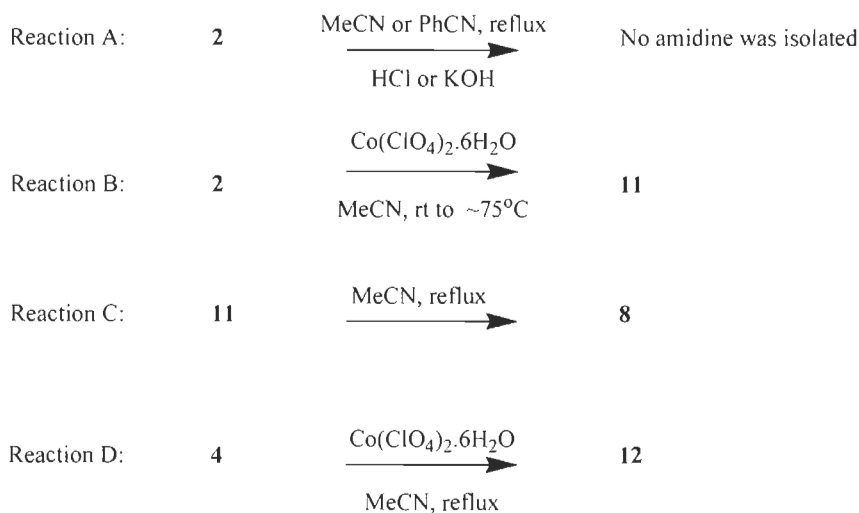
To evaluate the effect of the R substituent, several nitrile compounds (RCN) with electron donating (R = -CH$_3$, -Phenyl) and withdrawing groups (R = -PhNO$_2$ and -PhCF$_3$) were utilized to prepare amidine/amidinate cobalt complexes. The synthesis with 4-trifluoromethyl-benzonitrile and 4-nitro-benzonitrile in MeOH or DMF (as solvents) did not deliver amidine/amidinate compounds. However, with benzonitrile, **9** was successfully obtained in good yield. The complex **9** is structurally analogous to **8** with unique mononuclear [Co(**6**)(**6'**)]$^{2+}$ in the crystal lattice (Figures 1b, S5 and S6). These two compounds differ only in the substituent present on amidine/amidinate moiety (methyl in ligands **5** and **5'** vs phenyl ring in **6** and **6'**). Dication complex **9** is connected by N-H···N hydrogen bonds according to motif **II** (Chart 1a) to form chains which are then joined by bridging involving ClO$_4^-$ to generate a 2D sheet (Figure 1b). It is noteworthy that **9** is solvated with ethyl acetate and benzonitrile molecules. Details of hydrogen bonds and angles are provided in Table S3.

To determine if counterion plays a key role in the formation of amidine/amidinate, we also synthesized **10** using **2** and Co(BF$_4$)$_2$.6H$_2$O. Cationic complex **10** with chemical formula of [Co(**6'**)$_2$]$^+$ has identical coordination geometry around the Co(III) ion as that of **8** and **9** (Figures 1c and S7). In the structure, two amidinate ligands **6'** and one BF$_4^-$ balance the charge of the Co(III). Adjacent complexes (λ and Δ) self-assemble by N-H···N hydrogen bonds according to motif **III** (Chart 1a) to form 1D chains running along the *c*-axis. These chains are packed together to produce the final structure (Figure S8). Crystal of **10** is a solvate incorporating one diethyl ether and four benzonitrile molecules. Summary of hydrogen bonds and angles are given in Table S4.

3.1.1. Mechanism

Our study demonstrates that concomitant addition of Co(II) salts (Co(ClO$_4$)$_2$.6H$_2$O or Co(BF$_4$)$_2$.6H$_2$O) and **2** in RCN solvent (R = methyl/phenyl) under reflux offers a novel one pot

synthesis of **8-10**. To determine the sequence of steps involved in the mechanism of amidine/amidinate formation, we performed reactions A-D (Scheme 3).

Reaction A:	2	MeCN or PhCN, reflux → HCl or KOH	No amidine was isolated
Reaction B:	2	$Co(ClO_4)_2.6H_2O$ → MeCN, rt to ~75°C	11
Reaction C:	11	MeCN, reflux →	8
Reaction D:	4	$Co(ClO_4)_2.6H_2O$ → MeCN, reflux	12

Scheme 3. Reactions performed to elucidate the mechanism of amidine/amidinate formation.

Usually, when nitrile (RCN) and amino (R'NH$_2$) compounds are mixed in acidic solution amidine product **1** can be obtained. However, the reaction A of free ligand **2** with MeCN or PhCN at reflux in acidic or basic conditions did not result in **5**. This shows that in our case the -NH$_2$ of DAT groups are not ''normal'' amino groups. We believe that the lone pair of nitrogen atom of -NH$_2$ group is in resonance with the triazinyl ring which is no longer available for nucleophilic attack. Besides, it also indicates that metal ion governs the reaction between RCN and **2** by providing the necessary coordination sites for the binding to allow the formation of amidine. Reaction B was also achieved to assess the importance of temperature. In all reactions below the temperature of boiling point of MeCN, only **11** is isolated. Molecular structure of **11** shows a Co(II) ion surrounded by two ligands **2** and two MeCN in *cis*-position forming a distorted octahedral complex (Figures 1d and S9). Ligands **2** are dispositioned in two different planes as apparent from dihedral angle (δ = 71.54°) between triazine rings. Neighbouring complexes (λ and Δ) are associated by N-H···N hydrogen bonding in accordance to motifs **IV** and **VI** (Chart 1b) to produce a tridimensional network (Figures 1d and S10). The complex is further strengthened by hydrogen

bonding interactions involving hydrogen atom of free -NH₂ group and nitrogen atom of coordinated MeCN. N-H⋯O hydrogen bonds involving bridging ClO_4^- also reinforce the network (Figure S10b). Summary of hydrogen bonds and angles are given in Table S6.

From a structural point of view, compound **11** could be the reactive intermediate to generate **8**. Indeed, in the crystal structure shorter distance of ~3 Å between inner -NH₂ of DAT group and carbon atom of coordinated MeCN is thought to enable the formation of **8**. To validate our hypothesis, we conducted the reaction C by refluxing compound **11** in MeCN. Without surprise, we managed to isolate **8**. From the crystallographic study of **8-11**, we believe that only the -NH₂ near to the coordinated MeCN can contribute to the formation of amidine/amidinate functional groups. Moreover, we also think that this reaction happens intramolecularly since outer -NH₂ of DAT group has not generated amidine/amidinate unit as can be seen from molecular structures of **8-10**. To verify these assumptions, we performed the reaction D by mixing **4** with $Co(ClO_4)_2.6H_2O$ salt in MeCN under reflux and obtained **12**. SCXRD analysis shows that Co(II) ion is bound by two ligands **4**, two H₂O and two MeCN molecules in *trans*-positions to generate an octahedral coordination geometry (Figures 1e and S11). Adjacent complexes are linked by N-H⋯N hydrogen bonds following the motif **V** (Chart 1b) to form a 2D sheet (Figure 1e). Sheets are interlinked by bridging of ClO_4^- to generate a 3D hydrogen bonded network (Figure S12). Summary of hydrogen bonds and angles are given in Table S7.

Molecular structure of **12** shows that although MeCN is coordinated to cobalt ion, the formation of amidine/amidinate does not occur because -NH₂ and -CN groups are too far from each other. It also demonstrates that intermolecular nucleophilic attack from -NH₂ of one complex to the other does not happen. After isolation of **12** by filtration, the filtrate was also analyzed by ESI-MS to exclude the presence of amidine/amidinate cobalt complex in solution. The unique recognizable peak detected corresponds to the free ligand **4**.

From reactions of schemes 2 and 3, we concluded that the formation of amidine/amidinate only occurs under the following conditions (i) both ligand **2** and nitrile compounds should be coordinated to the cobalt ion, (ii) only the -NH$_2$ group closer to the coordinated nitrile group can participate in the reaction, (iii) the reaction is intramolecular and (iv) counterions don't affect the formation of amidine/amidinate. Using these results, we proposed a mechanism for the formation of **8-10** (Scheme 4). The mechanism involves four elementary steps I-IV. In step I, ligand **2** chelates cobalt ion with simultaneous coordination of two nitrile compounds to form an intermediate complex. In step II, the lone pair of N atom from inner -NH$_2$ group attacks the carbon atom of nitrile group to form charge separated $^+$N-C=N$^-$ intermediate. The step III corresponds to a switch proton. The last elemental step IV is a single and double deprotonation to form **8** and **9**, and **10** respectively.
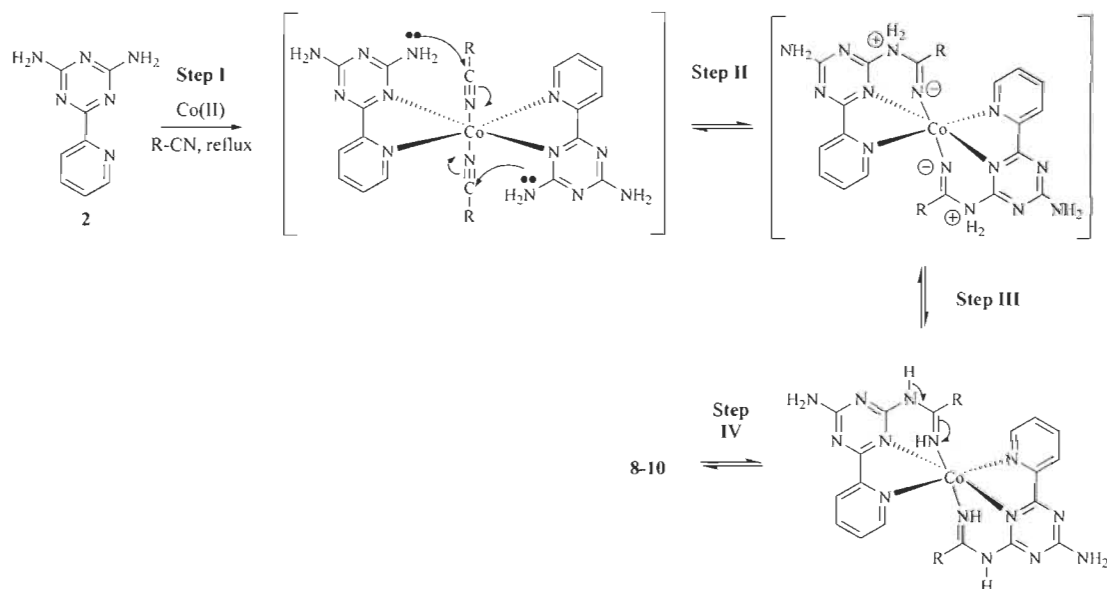
Scheme 4. Proposed mechanism for the formation of amidine cobalt complexes **8-10**.

3.2. Hydrogen evolution reaction

The optical and electrochemical properties along with the photocatalytic activity for H_2 evolution reaction (HER) have been investigated for **9** and **10**. Figure S13 shows the UV-Vis spectra for **2**, **9** and **10** measured at room temperature in DMF solution at concentration 8.8 x 10^{-6} M while the inset shows the graphs corresponding to concentration of 8.8 x 10^{-3} M. The absorption band at 265 nm observed for the free ligand **2** and a shoulder at ~260 nm in **9** corresponds to ligand centered π-π* electronic transition. A sharp band at 330 nm for **9** and a shoulder at 310 nm for **10** is ascribed to intra-ligand n-π* electronic transition. Characteristic weak d-d transition bands are observed for **9** and **10** at around 500 nm and at 600 nm, respectively. Selected data (wavelengths (λ_{max}), absorbance (A) and molar absorptivity (ε)) are summarized in Table S8.

The electrochemical behavior of **9** and **10** was recorded using cyclic voltammetry in DMF solutions at a concentration of 1 mM of complexes with 1 M tetrabutylammonium hexafluorophosphate (TBA-PF$_6$) as supporting electrolyte at a scan rate 100 mV/s (Figure S14). Cyclic voltammograms of **9** and **10** show quasi- and partially reversible oxidation and reduction peaks (Table S9) versus saturated calomel electrode (SCE), respectively. The peaks in the range -0.14 to -0.78 V correspond to $Co^{III/II}$ redox couple, those in the range -1.10 to -1.83 V correspond to $Co^{II/I}$ redox couple while those in the range -2.0 to -2.50 V correspond to reduction of ligand.[14] The possibility of multiple redox states of these two complexes indicates their potential application as catalysts especially for HER.

Intrigued by the potential application of amidine/amidinate complexes, we studied the catalytic activity of **9** and **10** for HER. The HER experiment was conducted for 22 hours in DMF solution of **9** and **10**, under blue light (452 nm) using triethanolamine (TEOA) as the sacrificial electron donor, Ru(bpy)$_3$(PF$_6$)$_2$ as the photosensitizer (PS) and aqueous HBF$_4$ as the proton source. TON and TOF curves of **9** and **10** are shown in Figure 2 and Table 1. Complex **9** displays HER properties

with a TON and TOF of 50 mol_{H2} mol_{PS}^{-1} and 786 $mmol_{H2}$ $mol_{PS}^{-1}min^{-1}$ respectively. For **10**, TON of 179 mol_{H2} mol_{PS}^{-1} and TOF of 878 $mmol_{H2}$ $mol_{PS}^{-1}min^{-1}$ were recorded. These values are much higher compared to **7** which exhibits a TON and TOF of 16 mol_{H2} mol_{PS}^{-1} and 307 $mmol_{H2}$ $mol_{PS}^{-1}min^{-1}$ respectively. The hydrogen production rate of **9** and **10** is enhanced by 74% and 86% compared to **7**. Control experiments conducted using the metal salts illustrated that the metal ion has negligible contribution towards photocatalytic activity in comparison to complexes (Figure S15). The control experiments conducted in the presence of PS/TEOA alone with and without light show no H_2 production.[15]

To the best of our knowledge, no amidine/amidinate complex has been previously utilized as a photocatalyst for HER. However, we have compared the photocatalytic efficiency with other cobalt based photocatalysts reported in literature whose HER has been carried out under similar conditions as ours. Brooker and coworkers screened 17 cobalt complexes which are 11 dinuclear, three tetranuclear and three mononuclear complexes for photocatalytic hydrogen evolution in presence of 0.1 mM $[Ru(bpy)_3]^{2+}$ as photosensitizer (PS), 1 M triethanolamine as a sacrificial electron donor and 0.1 M fluoroboric acid (HBF_4) as a proton source in DMF solvent. Among the 17 cobalt complexes, a dinuclear cobalt complex with the molecular formula $[Co^{II}(^{t\text{-}BuPh}Trz_{Me/Me})(\mu\text{-}BF_4)](BF_4)_3$ (where **Trz** = 1,2,4-triazole used as central bridging moiety, $^{t\text{-}BuPh}Trz_{Me/Me}$ = an example of bis-tetradentate ligands) produced H_2 with the TON of 150 moles of H_2 per mole of PS. In addition, the three mononuclear cobalt complexes $[Co^{II}(M_{Et})]^+$, $[Co^{II}(^{Br}M_{Et})]^+$ and $[Co^{II}(M_{pr})]^+$ (where **M** ligands are three different tetradentate diimine macrocycles featuring a diphenylamine head unit) respectively, produced H_2 with the TON of 130, 94 and 25 moles of H_2 per mole of PS, respectively.[15] Furthermore, the most widely reported standard reference cobaloxime catalyst ($[Co^{III}(dmgH)_2(py)Cl]$) produces H_2 with the TON of 68 moles of H_2 per mole of PS.[11] Comparatively, the hereby studied complex **10** produces higher amount of H_2.
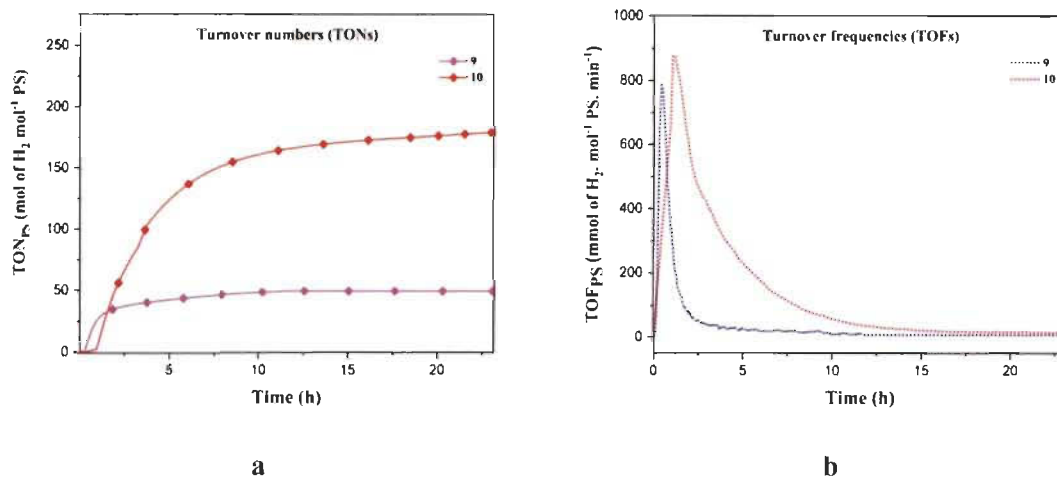
a   b

Figure 2. Hydrogen evolution reaction of **9** and **10** in blue light (Conc: 1mM). (a) TONs and (b) TOFs.

Table 1. Turnover number and Turnover frequency maxima for **9** and **10**

Sample	H_2 production (mmol/h)	TON_{max}	TOF_{max} (min^{-1})
7	0.11	16	307
9	0.43	50	786
10	0.78	179	878

*TON is reported in moles of hydrogen per mole of PS and TOF in mmol of hydrogen per mole of PS per minute.

4. Conclusions

We have reported the synthesis of a new series of crystalline amidine/amidinate cobalt complexes **8-10** obtained by a one-pot reaction of **2** with Co(II) in MeCN and PhCN under reflux. Their structures were confirmed, and the self-assemblies studied by SCXRD. In solid-state Janus-DATamidine and DATamidinate groups are the main sticky sites by hydrogen bonds that dictated the supramolecular organization in the case of **8-10**. For **11** and **12**, as expected DAT groups form

273

predictable hydrogen bond patterns to produce the three-dimensional network. The mechanism of amidine/amidinate formation was elucidated by analyzing the crystal structures of **8-12**. Mainly, four elemental steps are involved to form amidine cobalt complexes. HER performed on **9** and **10** demonstrated an improvement in photocatalytic efficiency as compared to a previously reported cobalt complex **7** that differs in terms of amidine/amidinate groups and counterion. Our work uncovered three principles of chemistry involving (i) the effect of variation of reactants/ reaction conditions on the chemical reaction and hence the product formation, (ii) a reaction may occur if molecules are in proximity and in suitable conformations and (iii) a small modification of the structure can alter drastically the properties of materials. This current study opens a door to prepare a large number of amidine/amidinate complexes with various metal ions and tectoligands that promise to be interesting candidates owing to their potential applications.

5. Experimental Section

5.1. General notes and procedures for the synthesis of 8-12.

6-(Pyridin-2-yl)-1,3,5-triazine-2,4-diamine **2** and 6-(Pyridin-4-yl)-1,3,5-triazine-2,4-diamine **4** were synthesized according to the reported methods.[11] Complexes **8-12** were prepared following the method below. All the other chemicals were commercially available and were purchased and used without any additional purification.

5.1.1. General procedure for preparing 8-12

A stirred suspension of $Co(ClO_4)_2.6H_2O$ or $Co(BF_4)_2.6H_2O$ (1.0 equiv) and the ligand (2.0 equiv) was heated at reflux in nitrile solvent (25 mL) for 16 h. In the case of **11**, the reaction is conducted at room temperature. The resulting homogeneous mixture was cooled and were subjected to crystallization.

A. Complex 8

The reaction of **2** (0.05 g, 0.2656 mmol) with $Co(ClO_4)_2 \cdot 6H_2O$ (0.049 g, 0.1328 mmol) in MeCN according to the general procedure yielded **8** (83 mg, 0.1159 mmol, 87%). Orange-red crystals of composition $[Co(\mathbf{5})(\mathbf{5'})](ClO_4)_2 \cdot 4(CH_3CN)$ were grown by allowing Et_2O to diffuse slowly into a solution in MeCN. FTIR (ATR): 3445, 3344, 3238, 2935, 2851, 1622, 1604, 1569, 1526, 1494, 1470, 1455, 1401, 1289, 1270, 1216, 1058, 1032, 1001, 956, 928, 843, 812, 782, 757, 700, 620 cm^{-1}. HRMS (ESI) calcd for $[C_{20}H_{22}CoN_{14}]^+$ m/e, 517.1484 found 517.1433. Anal. Calcd for $C_{20}H_{21}Cl_2CoN_{14}O_8$: C, 33.58; H, 2.96. Found: C, 33.26; H, 2.90.

B. Complex 9

The reaction of **2** (0.05 g, 0.2656 mmol) with $Co(ClO_4)_2 \cdot 6H_2O$ (0.049 g, 0.1328 mmol) in PhCN according to the general procedure yielded **9** (95 mg, 0.1130 mmol, 84%). Orange-red crystals of composition $[Co(\mathbf{6})(\mathbf{6'})](ClO_4)_2 \cdot 2(C_2H_5COOCH_3)(PhCN)$ were grown by layering EtOAc over solution in PhCN. FTIR (ATR): 3449, 3336, 3239, 3090, 1622, 1596, 1584, 1569, 1541, 1522, 1494, 1483, 1464, 1447, 1397, 1367, 1308, 1284, 1242, 1160, 1086, 1067, 1057, 1027, 1001, 990, 929, 875, 812, 781, 756, 727, 699, 671, 644, 619 cm^{-1}. HRMS (ESI) calcd for $[C_{30}H_{26}CoN_{14}]^{2+}$ m/e 320.5898, found 320.5901. Anal. Calcd for $C_{30}H_{25}Cl_2CoN_{14}O_8$: C, 42.92; H, 3.00. Found: C, 42.25; H, 2.96.

C. Complex 10

The reaction of **2** (0.05 g, 0.2656 mmol) with $Co(BF_4)_2 \cdot 6H_2O$ (0.045 g, 0.1328 mmol) in PhCN according to the general procedure yielded **10** (95 mg, 0.1165 mmol, 88%). Orange-red crystals of composition $[Co(\mathbf{6'})_2](BF_4)_2 \cdot (C_2H_5OC_2H_5) \cdot 4(Ph\text{-}CN)_4$ were grown by layering Et_2O over solution in PhCN. FTIR (ATR): 3476, 3445, 3359, 3305, 3237, 3154, 3088, 1672, 1621, 1595, 1582, 1565, 1541, 1524, 1481, 1448, 1434, 1394, 1371, 1339, 1277, 1235, 1161, 1053, 1020, 984, 923, 876, 820, 785, 763, 699, 674, 659, 648, 631 cm^{-1}. HRMS (ESI) calcd for $[C_{30}H_{26}CoN_{14}]^+$ m/e

641.1797, found 641.1734. Anal. Calcd for $C_{30}H_{24}BCoF_4N_{14}$: C, 49.61; H, 3.33. Found: C, 49.09; H, 3.15.

D. Complex 11

The reaction of **2** (0.05 g, 0.2656 mmol) with $Co(ClO_4)_2.6H_2O$ (0.049 g, 0.1328 mmol) in MeCN according to the general procedure yielded **11** (82 mg, 0.1144 mmol, 86%). Pink crystals of composition $[Co(2)_2(CH_3CN)_2](ClO_4)_2$ were grown by allowing Et_2O to diffuse slowly into a solution in MeCN. FTIR (ATR): 3481, 3460, 3349, 3230, 3119, 3084, 2930, 1678, 1620, 1584, 1563, 1515, 1488, 1463, 1448, 1400, 1367, 1300, 1283, 1269, 1197, 1159, 1091, 1057, 1022, 992, 930, 914, 824, 790, 756, 703, 684 cm^{-1}. HRMS (ESI) calcd for $[C_{16}H_{16}CoN_{12}]^{2+}$ m/e 217.5476, found 217.5470. Anal. Calcd for $C_{20}H_{22}Cl_2CoN_{14}O_8$: C, 33.53; H, 3.10. Found: C, 33.33; H, 3.23.

E. Complex 12

The reaction of **4** (0.05 g, 0.2656 mmol) with $Co(ClO_4)_2.6H_2O$ (0.049 g, 0.1328 mmol) in MeCN according to the general procedure yielded **12** (91 mg, 0.1184 mmol, 89%). Pink crystals of composition $[Co(4)_2(H_2O)_2(CH_3CN)_2](ClO_4)_2 \cdot 2(CH_3CN)$ were grown by allowing Et_2O to diffuse slowly into a solution in MeCN. FT-IR (ATR): 3445, 3363, 3338, 3207, 3152, 2934, 1643, 1622, 1579, 1533, 1448, 1414, 1399, 1322, 1260, 1218, 1080, 1059, 985, 930, 857, 809, 792, 748, 697, 621 cm^{-1}. HRMS (ESI) calcd for $[C_{16}H_{16}CoN_{12}]^{2+}$ m/e, 217.5476 found. 217.5444. Anal. Calcd for $C_{20}H_{26}Cl_2CoN_{14}O_{10}$: C, 31.93; H, 3.86. Found: C, 31.53; H, 3.63.

5.2. Characterization studies of 8-12

Crystallographic data were collected at 100 K using a Bruker Microstar diffractometer with Cu Kα radiation (λ = 1.54178 Å) for compounds **9-11** and at 150 K using a Bruker Venture Metaljet diffractometer with Ga Kα radiation (λ = 1.3413) for **8** and **12**. The structures were solved by

intrinsic phasing using SHELXT or direct methods using SHELXS, and non-hydrogen atoms were refined anisotropically with SHELXL-2018 for **8** and **12**.[16] Hydrogen atoms attached to carbon atoms were treated by first locating them from difference Fourier maps, recalculating their positions using standard values for distances and angles, and then refining them as riding atoms. Hydrogen atoms attached to nitrogen or oxygen atoms were found by Fourier difference map and fully refined. UV-Vis spectra were performed on a Cary 5000. The ATR-FTIR spectra were recorded with a Nicolet iS 10 Smart FT-IR Spectrometer within 600–4000 cm^{-1}. The thermogravimetric analysis was measured using Perkin Elmer TGA. The samples were heated from 25 to 800 °C with a rate of 10 °C/min.

Electrochemical measurements were achieved in pure dimethylformamide purged with argon at room temperature with a BAS SP-50 potentiostat. The counter electrode was a Pt wire, glassy carbon electrode was used as a working electrode and silver wire was the pseudo-reference electrode. The reference of electrochemical potential was set using 1 mM ferrocene as an internal standard and the values of potentials are reported vs SCE.[17] The concentrations of samples were 1mM. Tetrabutylammonium hexafluorophosphate (TBA-PF$_6$) (0.1 M) was used as supporting electrolyte. Cyclic voltammograms were performed at a scan rate of 100 mV/s and current amplitude of 100 µA.

A PerkinElmer Clarus-480 gas chromatograph (GC) was used to measure hydrogen gas evolved from the reaction. The assembly of the chromatograph consists of a thermal conductivity detector, a 7-inch HayeSep N 60/80 pre-column, a 9-inch molecular sieve 13*45/60 column, a 2 mL injection loop and argon gas as carrier and eluent. DMF was used as the solvent in our experiments. Three separate solutions of 1) photosensitizer [Ru(bpy)$_3$] (PF$_6$)$_2$, 2) sacrificial donor and proton source and 3) catalyst were prepared in order to obtain 5 mL of sample solutions in standard 20 mL headspace vials. In DMF, the resulting molar concentration of photocatalytic components were: 0.1 M for (HBF$_4$), 0.56 M for water, 1 M for triethanolamine (TEOA), 0.1 mM for the

photosensitizer [Ru(bpy)$_3$] (PF$_6$)$_2$ and 1 mM catalyst (**9** and **10**) (pH ~ 8-9). The resulting mixture was placed on a panel of blue LED 10 W center at 445 nm in a thermostatic bath set at 20°C which was sealed with a rubber septum and two stainless-steel tubes pierced in it. Argon was carried in the first tube at a flow rate of 10 ml min^{-1} (flow rate adjusted with a manual flow controller (Porter, 1000) and referenced with a digital flowmeter (Perkin Elmer Flow Mark)). The second stainless steel tube carried the flow to the GC sample loop passing through a 2 ml overflow protection vial and an 8-port stream select valves (VICCI). Timed injections were done by a microprocessor (Arduino Uno) coupled with a custom PC interface. Corresponding to a specific argon flow, H$_2$ production rate was calibrated. For calibration of H$_2$ production rate at a specific argon flow, a syringe pump (New Era Pump) equipped with a gas-tight syringe (SGE) and a 26s-gauge needle (Hamilton) was used to bubble different rates of pure hydrogen gas into the sample, to a minimum of 0.5 μL/minute. This gave a linear fit for peak area for H$_2$ versus the flow rates of H$_2$. For calibration testing, stock cylinders of known concentration of H$_2$ in argon replaced the argon flow (inserted at the pre-bubbler, to keep the same vapor matrix). The measured results independent of the flow rate (under same pressure) can be easily converted into the rate of hydrogen using equation 1. The errors associated to the TON and TOF are estimated to be 10 %.[18]

Equation 1

Rate of production of H$_2$ (μL.min^{-1}) = [H$_2$ standard] (ppm) x Ar flow rate (L.min^{-1})

6. Associated Content

6.1. Supporting Information. The supporting Information is available free of charge via the internet at ACS Publications website at DOI:

Additional crystallographic details (including thermal atomic displacement ellipsoid plots), FT-IR and TGA of **8-12** and HER curves of cobalt salts (PDF)

6.2. Accession Codes

CCDC 1996216-1996220 contain the supplementary crystallographic data for this paper. These data can be obtained free of charge via www.ccdc.cam.ac.uk/data_request/cif, of by email data_request@ccdc.cam.ac.uk, or by contacting The Cambridge Crystallographic Data Centre, 12 Union Road Cambridge CB2 1EZ, UK; fax: +44 1223 336033.

6.3. Author Information

Corresponding Author

*E-mail: adam.duong@uqtr.ca.

ORCID

Adam Duong : 0000-0002-4927-3603

6.4. Notes

The authors declare no competing financial interest.

6.5. Acknowledgment

7. References

(1) (a) Serrano, D. P.; Coronado, J. M.; Víctor, A.; Pizarro, P.; Botas, J. Á. Advances in the design of ordered mesoporous materials for low-carbon catalytic hydrogen production. *J. Mater. Chem. A.* **2013**, *1*, 12016-12027. (b) Hausbrand, R.; Cherkashinin, G.; Ehrenberg, H.; Gröting, M.; Albe, K.; Hess, C.; Jaegermann, W. Fundamental degradation mechanisms of layered oxide Li-ion battery cathode materials: Methodology, insights and novel approaches. *Mater. Sci. Eng. B.* **2015**, *192*, 3-25.

(2) (a) Han, Y.-F.; Yuan, Y.-X; Wang, H.-B. Porous hydrogen-bonded organic frameworks. *Molecules.* **2017**, *22*, 266. (b) Brunet, P.; Simard, M.; Wuest, J. D. Molecular tectonics. Porous hydrogen-Bonded networks with unprecedented structural integrity. *J. Am. Chem. Soc.* **1997**, *119*, 2737-2738. (c) Rigby, N.; Jacobs, T.; Reddy, J. P.; Hardie, M. J. Metal complexes of 2,2'-bipyridine-4,4'-diamine as metallo-tectons for hydrogen bonded networks. *Cryst. Growth Des.* **2012**, *12*, 1871-1881. (d) Stefanou, V.; Matiadis, D.; Tsironis, D.; Igglessi-Markopoulou, O.; McKee, V.; Markopoulos, J. Synthesis and single crystal X-ray diffraction studies of coumarin-based Zn(II) and Mn(II) complexes, involving supramolecular interactions. *Polyhedron.* **2018**, *141*, 289-295. (e) Chen, P.; Du, L.; Zhou, J.; Qiao, Y.; Li, B.; Zhao, Q. Four complexes with triazine derivative and terephthalate: synthesis, structures, and luminescent, magnetic properties. Chin. *Inorg. Chem.* **2014**, *30*, 1038-1044.

(3) (a) Kawahara, R.; Fujita, K.-I.; Yamaguchi, R. Dehydrogenative oxidation of alcohols in aqueous media using water-soluble and reusable Cp*Ir catalysts bearing a functional bipyridine ligand. *J. Am. Chem. Soc.* **2012**, *134*, 3643-3646. (b) Bindra, G. S.; Schulz, M.; Paul, A.; Soman, S.; Groarke, R.; Inglis, J.; Pryce, M. T.; Browne, W. R.; Rau, S.; Maclean, B. J.; Vos, J. G. The effect of peripheral bipyridine ligands on the photocatalytic hydrogen production activity of Ru/Pd catalysts. *Dalton Trans.* **2011**, *40*, 10812-10814. (c) Kaes, C.; Katz, A.; Hosseini, M. W. Bipyridine: The most widely used ligand. A review of molecules comprising at least two 2,2'-

bipyridine units. *Chem. Rev.* **2000**, *100*, 3553–3590. (d) Malkov, A. V.; Pernazza, D.; Bell, M.; Bella, M.; Massa, A.; Teplý, F.; Meghani, P.; Kocovský, P. Synthesis of new Chiral 2,2'-bipyridine ligands and their application in copper-catalyzed asymmetric allylic oxidation and cyclopropanation. *J. Org. Chem.* **2003**, *68*, 4727-4742.

(4) (a) Pal, A. K.; Duong, A.; Wuest, J. D.; Hanan, G. S. Long-lived, red-emitting excited state of a Ru(II) complex of a diaminotriazine ligand, *Polyhedron*, **2016**, *108*, 100-103. (b) Duong, A.; Dubois, M.-A.; Maris, T.; Métivaud, V.; Yi, J.-H.; Nanci, A.; Rochefort, A.; Wuest, J. D. Engineering Homologous Molecular Organization in 2D and 3D. Cocrystallization of Pyridyl-Substituted Diaminotriazines with Alkanecarboxylic Acids.

J. Phys. Chem. C **2011**, *115*, 12908-12919. (c) Rajak, S.; Mohan, M.; Tremblay, A. A.; Maris, T.; Leal do Santos, S.; Venancio, E. C.; Santos, S. F.; Duong, A. Programmed molecular construction: Driving the self-assembly by coordination and hydrogen bonds using 6-(Pyridin-2-yl)-1,3,5-triazine-2,4-diamine with $M(NO_3)_2$ Salts. *ACS Omega.* **2019**, *4*, 2708-2718. (d) Duong, A.; Maris, T.; Wuest, J. D. Using pyridinyl-substituted diaminotriazines to bind Pd(II) and create metallotectons for engineering hydrogen-bonded crystals. *Inorg. Chem.* **2011**, *50*, 5605-5618. (e) Li, J.-Y.; Xie, M.-J.; Jiang, J.; Chang, Q.-W.; Ye, Q.-S.; Liu, W.-P.; Chen, J.-L.; Ning, P. Synthesis and Ccystal structure of two polydimensional molecular architectures from cobalt(II), copper(II) complexes of 2,4-diamino-6-pyridyl-1,3,5-triazine. *Asian J. Chem.* **2014**, *26*, 419-422.

(5) (a) Duong, A.; Métivaud, V.; Maris, T.; Wuest, J. D. Surrogates of 2,2'-bipyridine designed to chelate Ag(I) and create metallotectons for engineering hydrogen-bonded crystals. *Cryst. Growth Des.* **2011**, *11*, 2026-2034. (b) Telfer, S. G.; Wuest, J. D. Metallotectons: Comparison of molecular networks built from racemic and enantiomerically pure tris(dipyrrinato)cobalt(III) complexes. *Cryst. Growth Des.* **2009**, *9*, 1923–1931.

(6) (a) Maly, K. E.; Gagnon, E.; Maris, T.; Wuest, J. D. Engineering hydrogen-bonded molecular crystals built from derivatives of hexaphenylbenzene and related compounds. *J. Am. Chem. Soc.* **2007**, *129*, 4306-4322. (b) Rajak, S.; Schott, O.; Kaur, P.; Maris, T.; Hanan, G. S.; Duong, A. Mimicking 2,2':6',2'':6'',2'''-quaterpyridine complexes for the light-driven hydrogen evolution reaction: Synthesis, structural, thermal and physicochemical characterizations. *RSC Adv.* **2019**, *9*, 28153-28164. (c) Rajak, S.; Schott, O.; Kaur, P.; Maris, T.; Hanan, G. S.; Duong, A. Design of a [FeFe] macrocyclic metallotecton for light-driven hydrogen evolution reaction. *Int. J. Hydrog. Energy.* **2020**, *45*, 2699-2708.

(7) (a) Aly, A. A.; Bräse, S.; Gomaa, M. A.-M. Amidines: their synthesis, reactivity, and applications in heterocycle synthesis. *Arkivoc.* **2018**, *part vi*, 85-138. (b) Rezler, M.; Z.ołek, T., Wolska, I.; Maciejewska, D. Structural aspects of intermolecular interactions in the solid state of 1,4-dibenzylpiperazines bearingnitrile or amidine groups research papers. *Acta Cryst. B.* **2014**, *70*, 820-827. (c) Coles, M. P. Application of neutral amidines and guanidines in coordination chemistry. *Dalton Trans.* **2006**, 985-1001. (d) Taylor, J. E.; Bull, S. D.; Williams, J. M. J. Amidines, isothioureas, and guanidines as nucleophilic catalysts. *Chem. Soc. Rev.* **2012**, *41*, 2109-2121. (e) Edwards, P. D.; Albert, J. S.; Sylvester, M.; Aharony, D.; Andisik, D.; Callaghan, O.; Campbell, J. B.; Carr. R. A.; Chessari, G.; Congreve, M.; Frederickson, M.; Folmer, R. H. A.; Geschwindner, S.; Koether, G.; Kolmodin, K.; Krumrine, J.; Mauger, R. C.; Murray, C. W.; Olsson, L-L.; Patel, S.; Spear, N.; Tian. G. Application of fragment-based lead generation to the discovery of novel, cyclic amidine β-secretase inhibitors with nanomolar potency, cellular activity, and high ligand efficiency. *J. Med. Chem.* **2007**, *50*, 5912-5925. (f) Z. Li, D. K. Lee, M. Coulter, L. N. J. Rodriguez and R. G. Gordon. Synthesis and characterization of volatile liquid cobalt amidinates. *Dalton Trans.* **2008**, 2592-2597. (g) Pálinkás, N., Kollár, L., & Kégl, T. Palladium-Catalyzed Synthesis of Amidines via tert-Butyl isocyanide Insertion. *ACS Omega.* **2018**, *3*, 16118–16126. (h) Youn, S. W., & Lee, E. M. Metal-Free One-Pot Synthesis of N,N'-

Diarylamidines and N-Arylbenzimidazoles from Arenediazonium Salts, Nitriles, and Free Anilines. *Org Lett.* **2016**, *18(21)*, 5728–5731. (i) Conde-Guadano, S., Hanton, M., Tooze, R. P., Danopoulos, A. A., & Braunstein, P. Amidine- and amidinate-functionalised N-heterocyclic carbene complexes of silver and chromium. *Dalton Trans.* **2012**, *41*, 12558. (j) Tolpygin, A. O., Cherkasov, A. V., Fukin, G. K., & Trifonov, A. A. Synthesis of new bulky bis(amidine) with the conformationally rigid meta-phenylene bridge and its dilithium derivative [1,3-$C_6H_4\{NC(Ph)N(2,6\text{-iso-}Pr_2C_6H_3)\}_2]Li_2(TMEDA)_2$. *Russ. J. Coord. Chem.* **2019**, *45*, 288–294.

(8) Case, F. H.; Koft, E. The synthesis of certain substituted 1,3,5- triazines containing the ferroin group. *J. Am. Chem. Soc.* **1959**, *81*, 905-906.

(9) (a) Lewis, N. S.; Nocera, D. G. Powering the planet: chemical challenges in solar energy utilization. *Proc. Natl. Acad. Sci.* **2006**, *103*, 15729-15735. (b) Serra, M.; Albero, J.; García, H. Photocatalytic activity of Au/TiO_2 photocatalysts for H_2 evolution: Role of the Au nanoparticles as a function of the irradiation wavelength. *ChemPhysChem.* **2015**, *16*, 1842-1845. (c) Barber, Photosynthetic energy conversion: natural and artificial. *J. Chem. Soc. Rev.* **2009**, *38*, 185-196. (d) Cook, T. R.; Dogutan, D. K; Reece, S. Y.; Surendranath, Y.; Teets, T. S.; Nocera, D. G. Solar energy supply and storage for the legacy and nonlegacy worlds. *Chem. Rev.* **2010**, *110*, 6474-6502. (e) Sun, Y.; Bigi, J. P.; Piro, N.A.; Tang, M. L.; Long, J. R.; Chang, C. J. Molecular cobalt pentapyridine catalysts for generating hydrogen from water. *J. Am. Chem. Soc.* **2011**, *133*, 9212-9215.

(10) (a) Deponti, E.; Luisa, A.; Natali, M.; Iengo, E.; Scandola, F. Photoinduced hydrogen evolution by a pentapyridine cobalt complex: elucidating some mechanistic aspects. *Dalton Trans.* **2014**, *43*, 16345-16353. (b) Sun, Y.; Sun, J.; Long, J. R.; Yang, P.; Chang, C. Photocatalytic generation of hydrogen from water using a cobalt pentapyridine complex in combination with molecular and semiconductor nanowire re photosensitizers. *J. Chem. Sci.* **2013**, *4*, 118-124. (c) Stubbert, B. D.; Peters, J. C.; Gray, H. B. Rapid water reduction to H2 catalyzed by a cobalt

bis(iminopyridine) complex. *J Am. Chem. Soc.* **2011**, *133*, 18070-18073. (d) Wang, Z. Q.; Tang. L. Z.; Zhang, Y. X.; Zhan, S. Z.; Ye, J. S. Electrochemical-driven water splitting catalyzed by a water soluble cobalt(II) complex supported by N,N'-bis(2'-pyridinecarboxamide)-1,2-benzene with high turnover frequency. *J Power Sources.* **2015**, *287*, 50-57.

(11) Rajak, S.; Schott, O.; Kaur, P.; Maris, T.; Hanan, G. S.; Duong, A. Synthesis, crystal structure, characterization of pyrazine diaminotriazine based complexes and their systematic comparative study with pyridyldiaminotriazine based complexes for light-driven hydrogen production. *Polyhedron.* **2020**, *180*, 114412.

(12) Thallaj, N. K.; Przybilla, J.; Welter, R.; Mandon, D. A ferrous center as reaction site for hydration of a nitrile group into a carboxamide in mild conditions. *J. Am. Chem. Soc.* **2008**, *130* (8), 2414-2415.

(13) (a) Martin, C.; Whiteoak C. J.; Martin, E.; Escudero-Adán, E. C.; Galán-Mascarós, J. R.; Kleij, A. W. Synthesis and Structural Features of Co(II) and Co(III) Complexes Supported by Aminotrisphenolate Ligand Scaffolds. *Inorg. Chem.* **2014**, *53*, 11675-11681. (b) Luo, J.; Rath, N. P.; Mirica, M. Dinuclear Co(II)Co(III) Mixed-Valence and Co(III)Co(III) Complexes with N- and O-Donor Ligands: Characterization and Water Oxidation Studies. *Inorg. Chem.* **2011**, *50*, 6152-6157.

(14) Ferreira, H.; Conradie, M. M.; Conradie, J. Cyclic voltammetry data of polypyridine ligands and Co(II)-polypyridine complexes. *Data in Brief.* **2019**, *22*, 436-445.

(15) Hogue, R. W.; Schott, O.; Hanan, G. S.; Brooker, S. A smorgasbord of 17 cobalt complexes active for photocatalytic hydrogen evolution. *Chem. Eur. J.* **2018**, *24*, 9820-9832.

(16) (a) Sheldrick, G. M. SHELXT- Integrated space-group and crystal structure determination. *Acta Crystallogr., Sect. A: Found. Adv.* **2015**, *71*, 3-8. (b)   Sheldrick, G. M. Crystal structure refinement with SHELXL. *Acta Crystallogr., Sect. C: Struct. Chem.* **2015**, *71*, 3-8.

(17) Connelly, N. G.; Geiger, W. E. Chemical redox agents for organometallic chemistry. *Chem. Rev.* **1996**, *96*, 877-910.

(18) Lentz, C. D.; Schott, O.; Auvray, T.; Hanan, G. S.; Elias, B. Photocatalytic hydrogen production using a red-absorbing Ir(III)-Co(III) dyad. *Inorg. Chem.* **2017**, *56*, 10875-10881.

6.4. Conclusions

In this project we have reported the synthesis of novel amidine/amidinate cobalt complexes via a new synthetic procedure through a one-pot reaction. The structure of all the complexes were characterized by single-crystal X-ray diffraction. The formation mechanism of amidine/amidinate cobalt complexes was investigated and proposed by analysing the single crystals structures of **8-12**. Numerous partially and completely reversible oxidation and reduction peaks shown by complex **9** and **10** versus saturated calomel electrode (SCE) proved that they can be suitable photo catalysts for hydrogen evolution reaction prior to their catalytic testing. HER performed on **9** and **10** demonstrated an improvement in photocatalytic efficiency as compared to a previously reported cobalt complex **7** that differs in terms of amidine/amidinate groups and counterion. This proves that the physical and chemical modifications of pyridinyl-substituted diaminotriazine cobalt (II) complexes led to the synthesis of more efficient amidine/amidinate cobalt complexes for hydrogen production. Complex **10** proved out to be the best cobalt catalyst as compared to other cobalt catalysts for hydrogen evolution reaction reported under identical reaction conditions. Interestingly, complex **10** produced hydrogen about 2.63 times more than the standard reference cobaloxime catalyst (as indicated by TON). All the synthesized photo catalysts were thermally stable and were very active and stable towards catalyzing the hydrogen evolution reaction, which can be observed from their TON and TOF curves.

6.5. Supporting Information

Contents		Page

Figure S1. Thermogravimetric analysis (TGA) curves of **8-12**.

Figure S2. Infrared spectra of ligands **2** and **4**, and **8-12**.

Table S1. Crystallographic data of **8-10**

Compound	8	9	10
Empirical formula	$C_{28}H_{33}Cl_2CoN_{18}O_8$	$C_{83}H_{87}Cl_4Co_2N_{29}O_{24}$	$C_{62}H_{54}BCoF_4N_{18}O$
Formula weight	879.55	2134.47	1212.97
Crystal system	monoclinic	monoclinic	monoclinic
Radiation	CuKα	GaKα	GaKα
Temperature (K)	150 K	150	150
λ (Å)	1.54178	1.34139	1.34139
$F(000)$	1808	2204.0	2512.0

| Space group	P2$_1$/c	P2$_1$/c	P2$_1$/c
Z	4	2	4
a (Å)	11.9086(5)	12.5415(3)	12.3280(3)
b (Å)	21.6399(8)	16.9560(4)	20.9629(5)
c (Å)	14.8958(6)	23.1839(6)	23.1256(5)
α (deg)	90	90	90
β (deg)	102.158(2)	105.140(1)	90.3080(10)
γ (deg)	90	90	90
V (Å^3)	3752.6(3)	4759.0(2)	5976.3(2)
Crystal size /mm^3	0.1 x 0.06 x 0.06	0.3 × 0.11 × 0.04	0.24 × 0.13 × 0.12
ρ_{calcd} (g cm^{-3})	1.557	1.490	1.348
μ (mm^{-1})	5.539	3.092	1.955
Reflections collected	74962	67565	128409
Independent reflections	7032	10955	13741
R_{int}	0.0646	0.0330	0.0288
Observed reflections	5876	10228	12869
2θ range for data collection/°	7.32 to 139.20	5.69 to 121.498	4.95 to 121.454
Data/restraints/parameters	7032/36/596	10955/222/754	13741/0/830
R_1 [$I>=2\sigma(I)$]	0.0528	0.0474	0.0330
ωR_2 [$I>=2\sigma(I)$]	0.1422	0.1298	0.0864
R_1 (all data)	0.0642	0.0501	0.0356
ωR_2 (all data)	0.1521	0.1326	0.0886
Goodness-of-fit on F^2	1.026	1.053	1.052
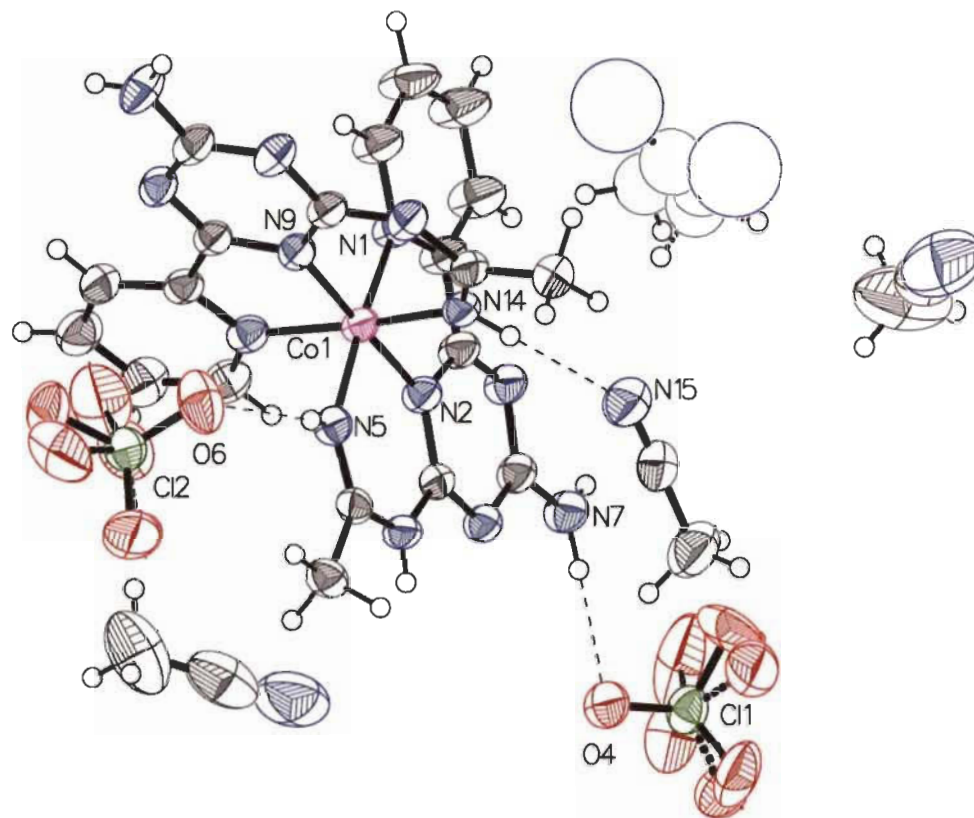
Figure S3. Thermal atomic displacement ellipsoid plot of the structure of **8** grown from MeCN/Et$_2$O. The ellipsoids of non-hydrogen atoms are drawn at 50% probability level, and hydrogen atoms are represented by a sphere of arbitrary size.
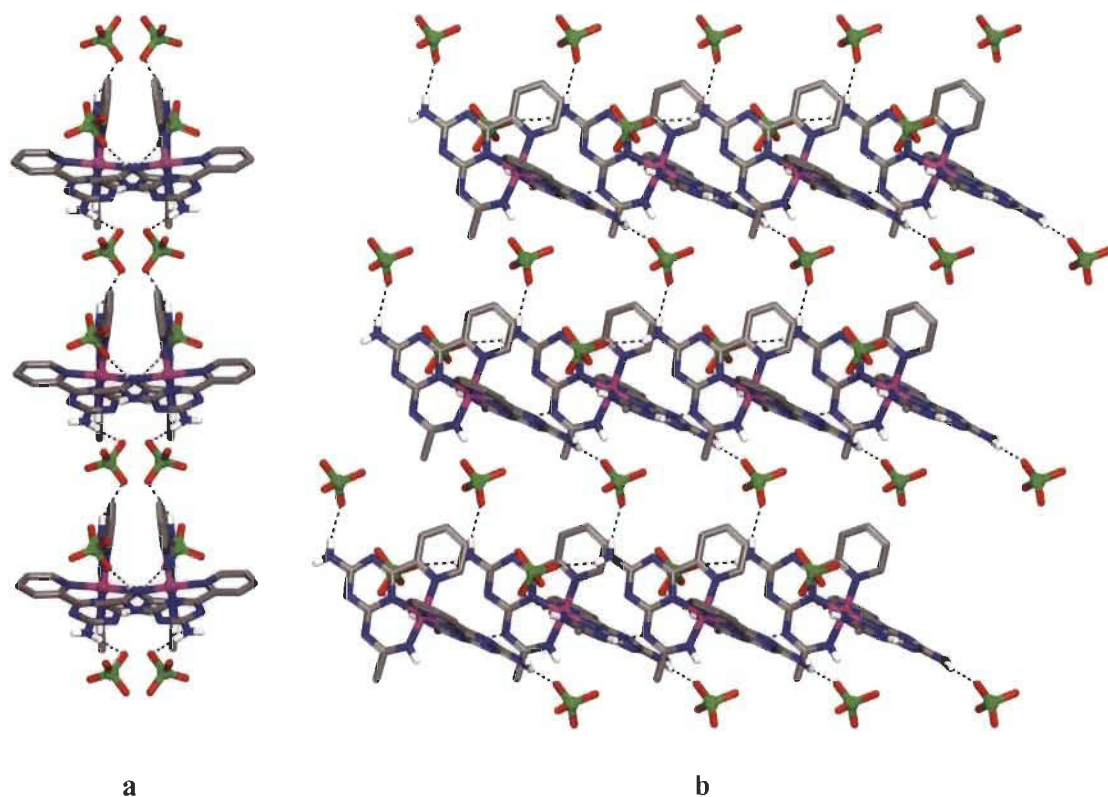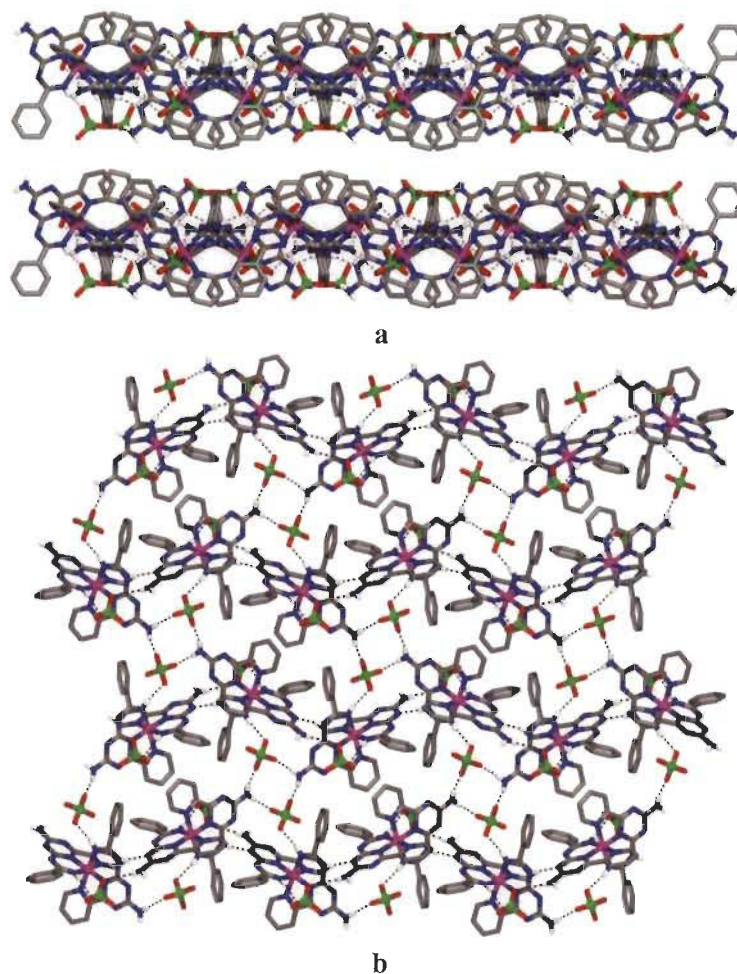
Figure S4. Structure of **8**. (**a**) Side view of one hydrogen-bonded layer along the *c* axis and (**b**) View showing the hydrogen bonded layer in the (*a*, *c*) plane. Hydrogen bonds are represented by dashed lines. Carbon atoms are shown in grey, hydrogen atoms in white, oxygen atoms in red, nitrogen atoms in blue, chlorine atom in green and cobalt atoms in pink. Hydrogen attached to carbon atom have been omitted for clarity.

Table S2. Hydrogen-bond geometry (Å, °) in structure of **8**

D—$H \cdots A$	D—H	$H \cdots A$	$D \cdots A$	D—$H \cdots A$
N7—H7$A \cdots$N17^i	0.78(4)	2.44(5)	3.167(7)	156(4)
N7—H7$B \cdots$O4	0.92(4)	2.12(5)	3.018(4)	167(4)
N12—H12$A \cdots$O7^{ii}	0.77(6)	2.26(6)	2.960(7)	151(5)
N12—H12$A \cdots$O5B^{ii}	0.77(6)	2.60(6)	3.34(3)	161(5)

N12—H12B···O2^{iii}	0.77(5)	2.38(5)	3.085(11)	152(4)
N12—H12B···O2B^{iii}	0.77(5)	2.17(5)	2.906(13)	160(5)
N14—H14···N15	0.86(4)	2.31(5)	3.148(5)	164(4)
N6—H6···N13^{i}	0.81(4)	2.05(4)	2.824(4)	159(3)
N5—H5···O6	0.70(4)	2.39(4)	3.072(4)	165(4)

Symmetry codes: (i) x, $-y+1/2$, $z+1/2$; (ii) x, $-y+1/2$, $z-1/2$; (iii) $x-1$, y, $z-1$.
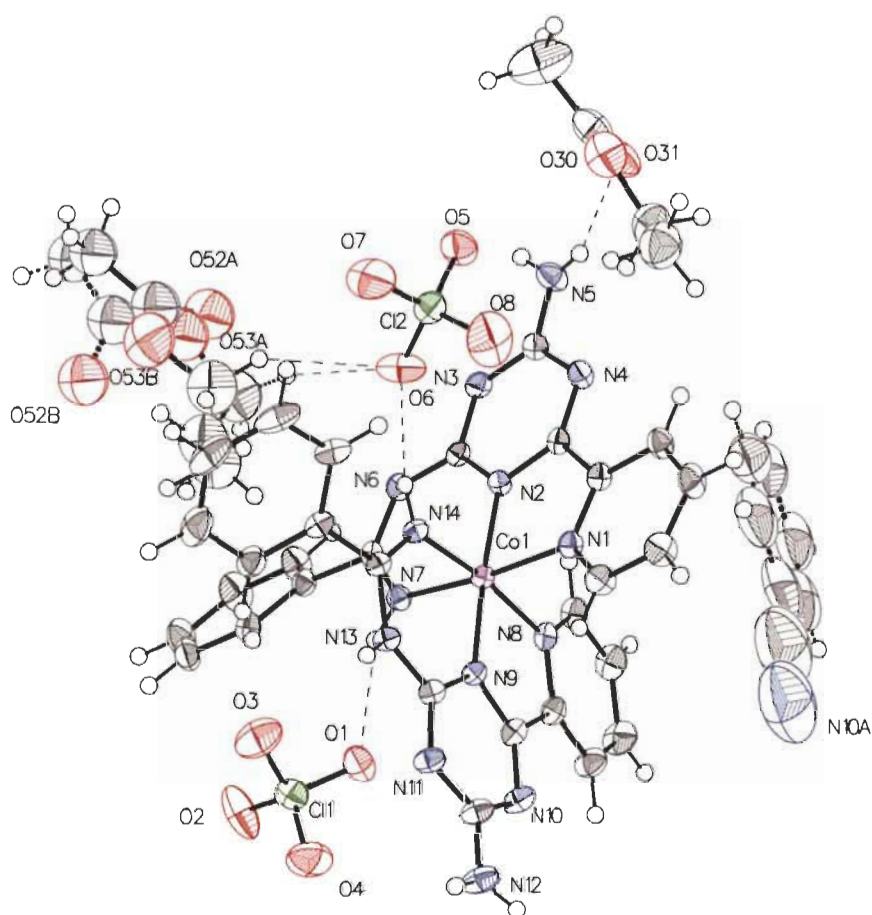
Figure S5. Thermal atomic displacement ellipsoid plot of the structure of **9** grown from PhCN/EtOAc. The ellipsoids of non-hydrogen atoms are drawn at 50% probability level, and hydrogen atoms are represented by a sphere of arbitrary size.

Figure S6. Structure of **9.** (**a**) Side view of two hydrogen-bonded layers along the *c* axis and (**b**) View showing one hydrogen bonded layer in the (*b*, *c*) plane. Hydrogen bonds are represented by dashed lines. Carbon atoms are shown in grey, hydrogen atoms in white, oxygen atoms in red, nitrogen atoms in blue, chlorine atom in green and cobalt atoms in pink. Hydrogen atoms attached to carbon atoms and solvent guest molecules have been deleted for clarity.

Table S3. Hydrogen-bond geometry (Å, °) in structure of **9**

D—H$\cdots A$	D—H	H$\cdots A$	$D\cdots A$	D—H$\cdots A$
N14—H14$\cdots$O6	0.85(3)	2.13(3)	2.959(2)	166(3)
N13—H13$\cdots$N3^{i}	0.83(3)	1.92(3)	2.745(2)	173(3)
N7—H7$\cdots$O1	0.85(3)	2.23(3)	3.034(2)	158(3)
N5—H5A$\cdots$O31	0.76(3)	2.18(3)	2.901(3)	157(3)
N5—H5B$\cdots$O3^{iv}	0.81(3)	2.53(3)	3.246(3)	149(3)
N12—H12A$\cdots$O7^{v}	0.88(4)	2.07(4)	2.924(3)	163(3)
N12—H12B$\cdots$Cl2^{i}	0.81(4)	2.96(4)	3.721(2)	157(3)
N12—H12B$\cdots$O5^{i}	0.81(4)	2.22(4)	3.027(3)	175(3)

Symmetry codes: (i) 1-x, 1/2+y, 1/2-z; (iv) 1-x, -1/2+y, 1/2-z; (v) +x, 3/2-y, 1/2+z.
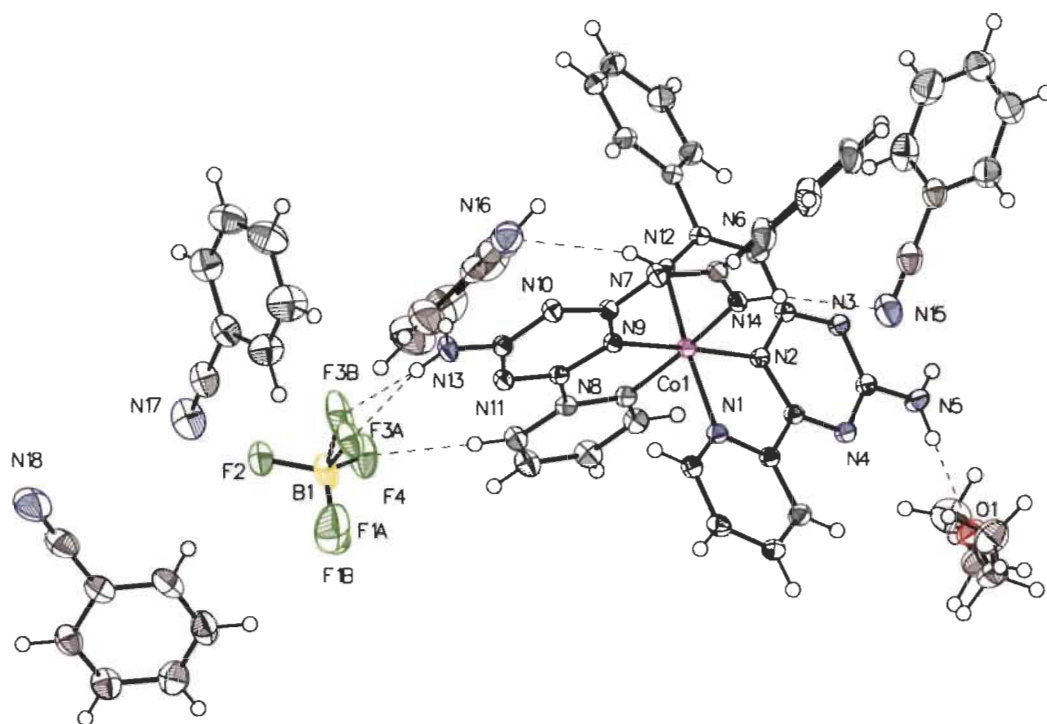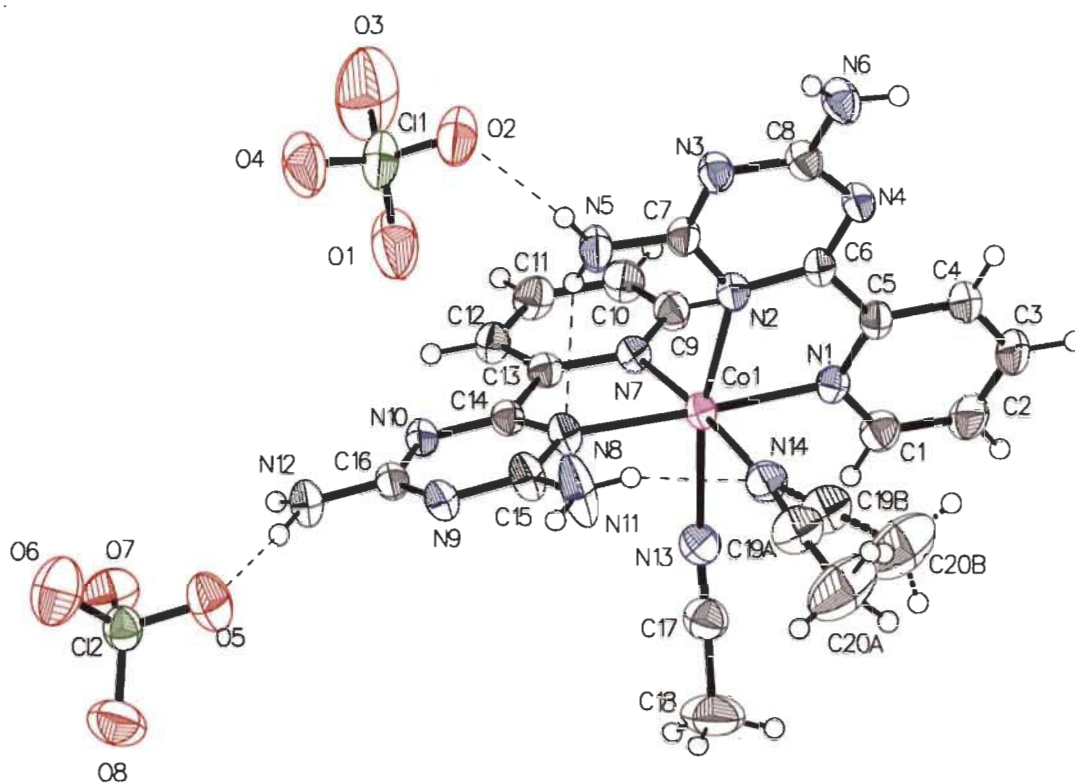
Figure S7. Thermal atomic displacement ellipsoid plot of the structure of **10** grown from PhCN/Et$_2$O. The ellipsoids of non-hydrogen atoms are drawn at 50% probability level, and hydrogen atoms are represented by a sphere of arbitrary size.

a

b

c
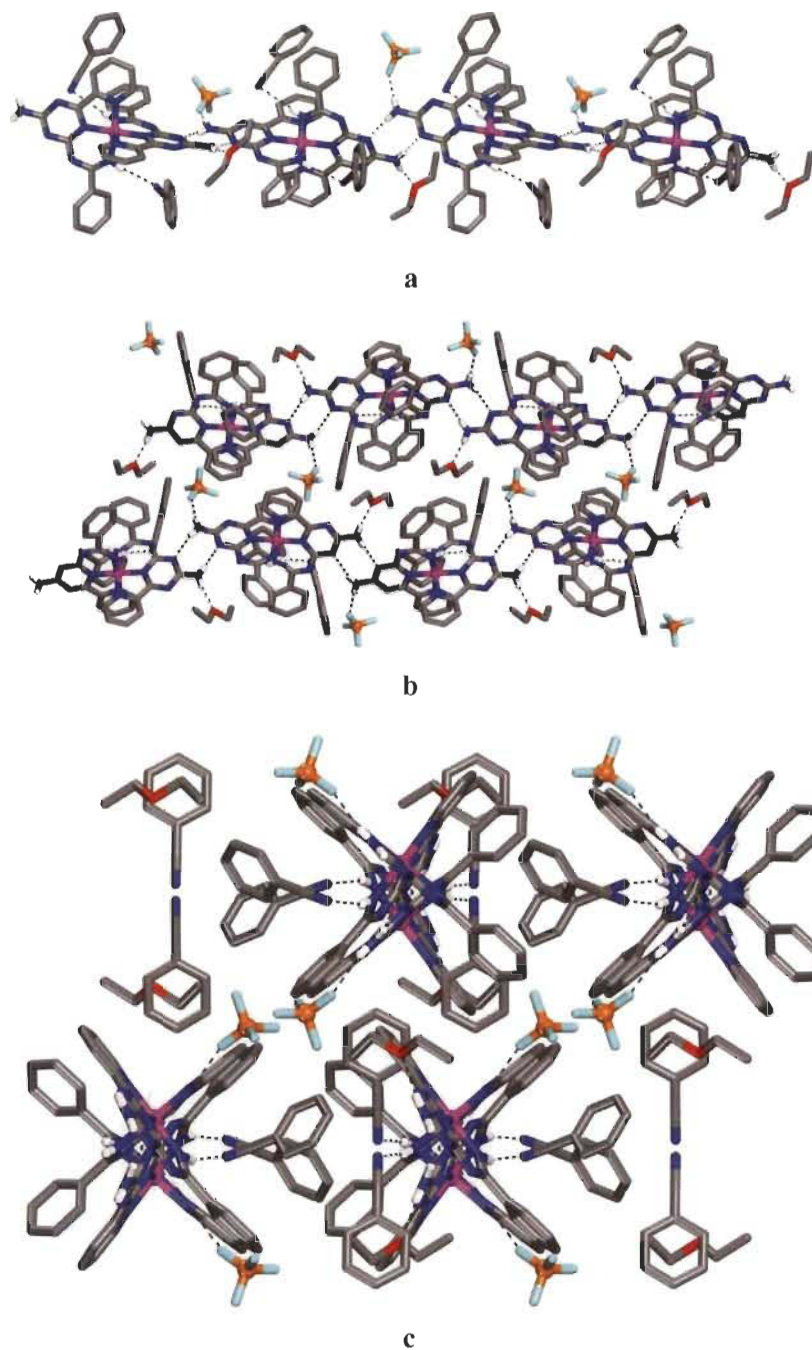
Figure S8. Structure of **10**. (a) View of the main hydrogen bonding interactions of **10** generating one chain running along the c-axis. (b) View in the (b, c) plane showing the stacking between two chains. (c) Projection along the c-axis showing the side view of the chains with interacting counter ions and included solvent molecules. Hydrogen bonds are represented by dashed lines. Carbon atoms are shown in grey, hydrogen atoms in white, nitrogen atoms in blue, boron atoms in orange,

fluorine atom in cyan and cobalt atoms in pink. Hydrogen atoms attached to carbon atoms and some non-interacting solvent guest molecules have been deleted for clarity.

Table S4. Hydrogen-bond geometry (Å, °) in structure of **10**

D—H$\cdots A$	D—H	H$\cdots A$	$D \cdots A$	D—H$\cdots A$
N13—H13A$\cdots$F3A	0.825(17)	2.082(18)	2.897(4)	169.2(15)
N13—H13A$\cdots$F3B	0.825(17)	2.035(19)	2.858(7)	174.5(18)
N5—H5A$\cdots$O1	0.833(18)	2.096(18)	2.9228(14)	171.7(16)
N13—H13B$\cdots$N3^{iii}	0.809(18)	2.292(19)	3.0817(14)	165.6(16)
N5—H5B$\cdots$N10^{iv}	0.845(18)	2.107(18)	2.9490(14)	174.5(16)
N7—H7$\cdots$N16	0.813(18)	2.594(18)	3.3801(16)	163.1(16)
N14—H14$\cdots$N15	0.882(16)	2.376(16)	3.2338(16)	164.1(13)

Symmetry codes: (iii) +x, 3/2-y, 1/2+z; (iv) +x, 3/2-y, -1/2+z.

Table S5. Crystallographic data of **11** and **12**

Compound	**11**	**12**
Empirical formula	$C_{20}H_{22}Cl_2CoN_{14}O_8$	$C_{24}H_{32}Cl_2CoN_{16}O_{10}$
Formula weight	716.34	834.48
Crystal system	monoclinic	monoclinic
Radiation	GaKα	CuKα
Temperature (K)	150	100

λ (Å)	1.34139	1.54178
$F(000)$	2920.0	858
Space group	C2/c	P2$_1$/c
Z	8	2
a (Å)	24.4834(7)	11.5878(6)
b (Å)	9.8021(3)	7.4968(4)
c (Å)	24.8817(7)	21.0318(11)
α (deg)	90	90
β (deg)	101.8220(10)	100.942(3)
γ (deg)	90	90
V (Å^3)	5844.7(3)	1793.85(16)
Crystal size/mm^3	0.17 x 0.16 x 0.1	0.08 x 0.08 x 0.005
ρ_{calcd} (g cm^{-3})	1.628	1.545
μ (mm^{-1})	4.750	
Reflections collected	6883	25653
Independent reflections	6883	3220
R_{int}	0.0499	0.0865
Observed reflections	6371	
2θ range for data collection/°	8.82 to 121.37	8.13 to 135.56
Data/restraints/parameters	6883/2/450	3220/60/278
R_1 [$I>=2\sigma(I)$]	0.0452	0.0444
ωR_2 [$I>=2\sigma(I)$]	0.1251	0.1037
R_1 (all data)	0.0482	0.0784
ωR_2 (all data)	0.1289	0.1136

| Goodness-of-fit on F^2 | 1.074 | 0.944 |
| Largest diff. peak/hole/e Å^{-3} | 0.77/-0.48 | 0.47/-0.44 |

Figure S9. Thermal atomic displacement ellipsoid plot of the structure of **11** grown from MeCN/Et$_2$O. The ellipsoids of non-hydrogen atoms are drawn at 50% probability level, and hydrogen atoms are represented by a sphere of arbitrary size.
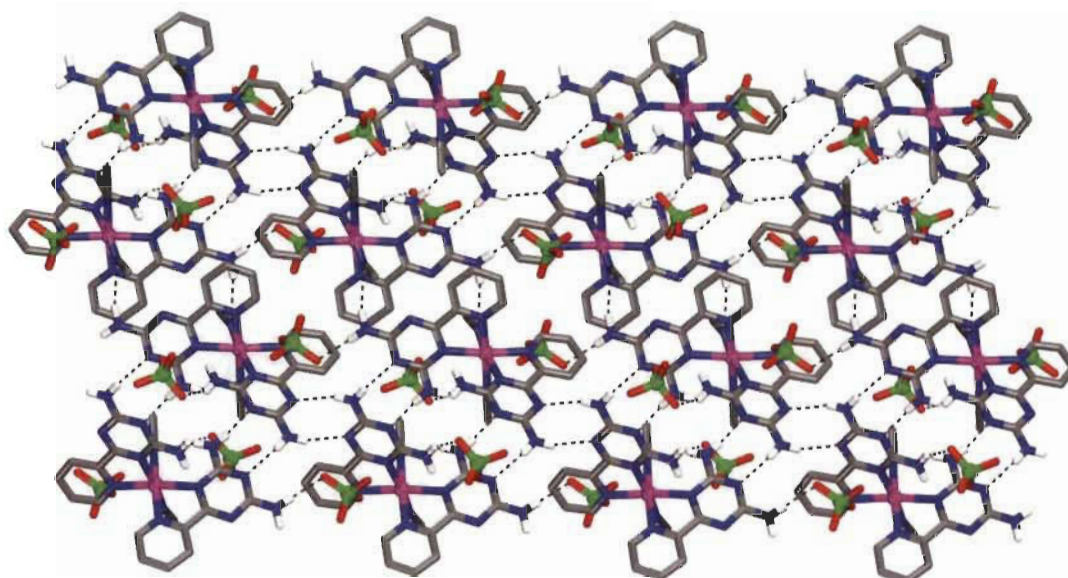
Figure S10. Structure of **11**. View of the (*a*, *c*) plane showing array of hydrogen bonded cations and perchlorate anions. Hydrogen bonds are represented by dashed lines. Carbon atoms are shown in grey, hydrogen atoms in white, oxygen atoms in red, nitrogen atoms in blue, chlorine atom in green and cobalt atoms in pink. Hydrogen atoms attached to carbon atoms have been omitted for clarity.

Table S6. Hydrogen-bond geometry (Å, °) in structure of **11**

D—H···*A*	*D*—H	H···*A*	*D*···*A*	*D*—H···*A*
N5—H5A···N8	0.81(3)	2.38(3)	3.090(3)	147(3)
N12—H12A···N13[i]	0.89(3)	2.48(3)	3.355(3)	165(3)
N12—H12B···O5	0.90(4)	2.10(4)	2.996(3)	177(4)
N5—H5B···O2	0.87(3)	2.11(3)	2.920(3)	155(3)
N11—H11A···N3[iv]	0.87(5)	2.04(5)	2.906(3)	171(4)
N6—H6A···N4[v]	0.86(3)	2.52(3)	3.333(3)	158(2)

N6—H6A···O5^{vi}	0.86(3)	2.51(3)	2.954(3)	112(2)
N6—H6B···N9^{vi}	0.82(4)	2.42(4)	3.241(3)	174(3)
N11—H11B···N14	0.82(6)	2.26(6)	3.028(4)	157(5)
N11—H11B···O2^{iv}	0.82(6)	2.54(5)	2.954(4)	113(4)

Symmetry codes: (i) 1/2-x, 3/2-y, 1-z; (iv) 1/2-x, 1/2+y, 1/2-z; (v) 1-x, +y, 1/2-z; (vi) 1/2-x, -1/2+y, 1/2-z.
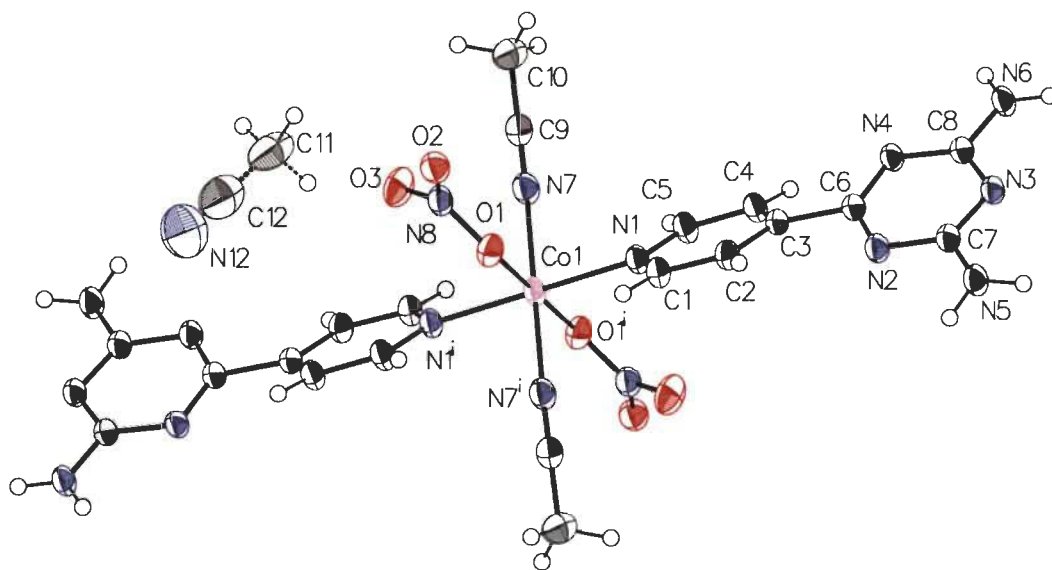
Figure S11. Thermal atomic displacement ellipsoid plot of the structure of **12** grown from MeCN/Et$_2$O. The ellipsoids of non-hydrogen atoms are drawn at 50% probability level, and hydrogen atoms are represented by a sphere of arbitrary size.
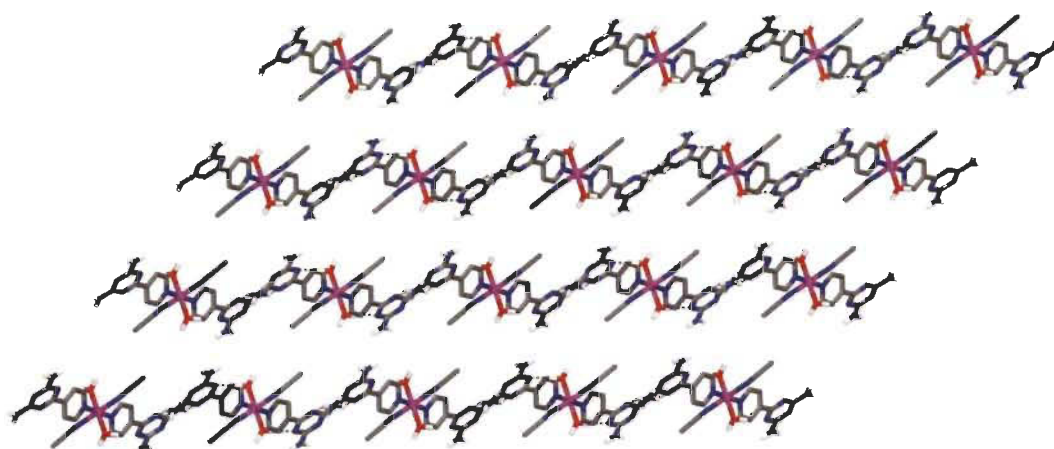
a
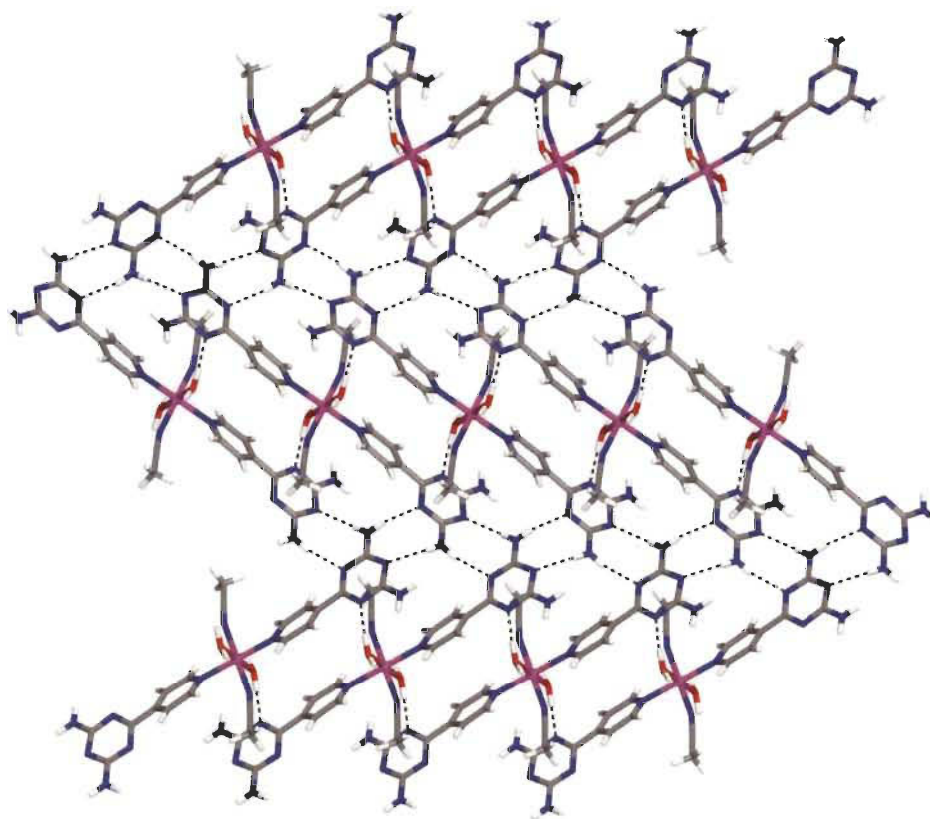
b

Figure S12. Structure of **12.** (a) Pictorial presentation of 2D hydrogen bonded sheet in (*a, c*) plane

of **12** and (b) 3D hydrogen bonded framework. Hydrogen bonds are represented by dashed lines.

Carbon atoms are shown in grey, hydrogen in white, oxygen atoms in red, nitrogen atoms in blue

and cobalt atoms in pink. Hydrogen atoms attached to carbon atoms and acetonitrile guest molecules have been deleted for clarity.

Table **S7.** Hydrogen-bond geometry (Å, °) in structure of **12**

D—$H \cdots A$	D—H	$H \cdots A$	$D \cdots A$	D—$H \cdots A$
N12—H12$A \cdots$N7[i]	0.87(4)	2.14(4)	3.003(5)	174(4)
N12—H12$B \cdots$N9[ii]	0.88(4)	2.33(5)	3.191(5)	166(4)
N13—H13$A \cdots$O2A[iii]	0.83(4)	2.55(4)	3.179(5)	134(3)
N13—H13$A \cdots$O3A[iii]	0.83(4)	2.56(4)	3.390(7)	174(4)
N13—H13$A \cdots$O3B[iii]	0.83(4)	1.80(4)	2.584(14)	156(4)
N13—H13$B \cdots$O2A[iv]	0.84(4)	2.21(4)	3.028(6)	164(4)
N13—H13$B \cdots$O2B[iv]	0.84(4)	2.29(4)	3.066(16)	153(4)
O17—H17$A \cdots$N11[v]	0.97(1)	1.743(4)	2.711(4)	176(3)
O17—H17$B \cdots$Cl1[vi]	0.97(1)	2.65(2)	3.500(2)	147(3)
O17—H17$B \cdots$O1A[vi]	0.97(1)	1.834(5)	2.802(3)	175(3)
O17—H17$B \cdots$O2A[vi]	0.97(1)	2.53(3)	3.065(4)	115(3)

Symmetry codes: (i) $-x+3/2$, $y+1/2$, $-z+1/2$; (ii) $-x+3/2$, $y-1/2$, $-z+1/2$; (iii) x, $y+1$, z; (iv) $-x+1/2$, $y+1/2$, $-z+1/2$; (v) x, $y-1$, z; (vi) $-x+1/2$, $y-1/2$, $-z+1/2$.
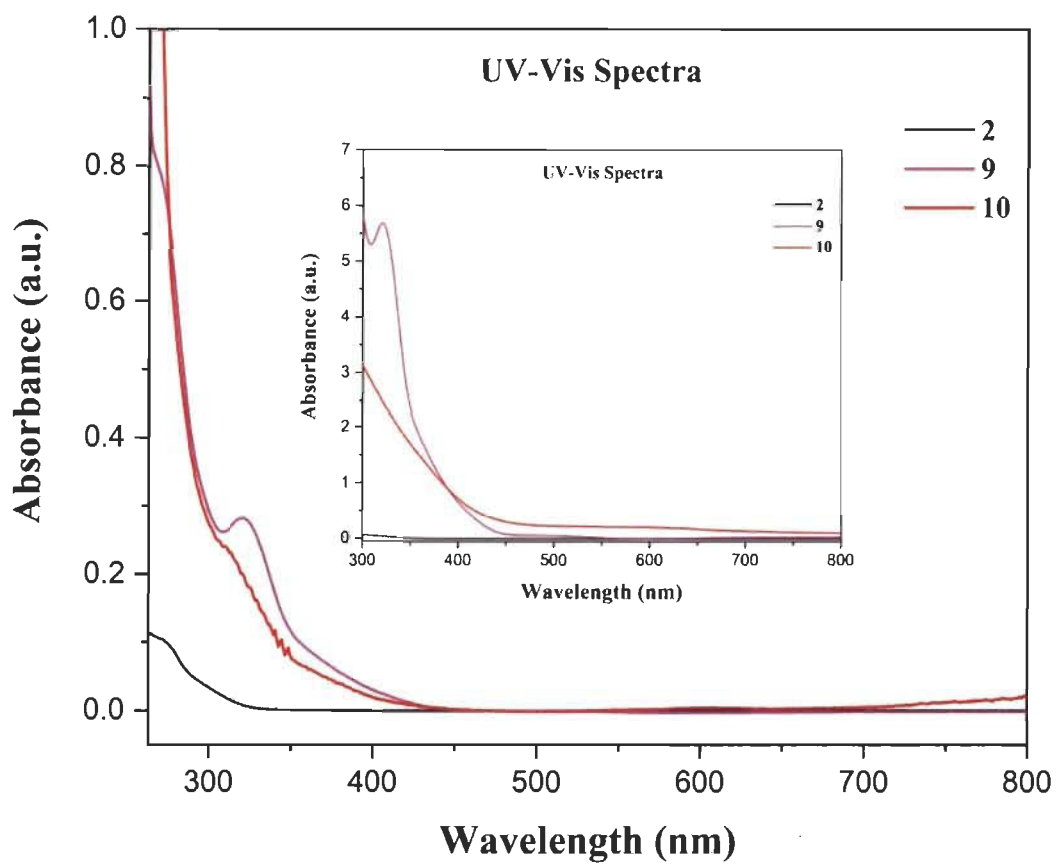
Figure S13. UV-Vis spectra of **2**, **9** and **10** in DMF solution at room temperature at a concentration of 8.8 x 10^{-6} M. Inset shows the spectra at a concentration of 8.8 x 10^{-3} M.

Table S8. Solution state UV-Vis data of **2**, **9** and **10** ^{a}

Parameters	DMF					
	Conc = 8.8 x 10^{-6} M			Conc = 8.8 x 10^{-3} M		
	From 263 to 800 nm			From 263 to 800 nm		
Sample	λ_{max} (nm)	A	ε (mol^{-1} dm^3 cm^{-1})	λ_{max} (nm)	A	ε (mol^{-1} dm^3 cm^{-1})
2	265	0.1067	1.212 x 10^4	281	9.40	1.06 x 10^3

	262	0.8264	9.39×10^4	301	3.001	0.34×10^3
9	330	0.2815	3.19×10^3			
	502	1.6977	1.929×10^5			
10	310	0.2485	2.82×10^3	317	2.6156	0.29×10^3
	608(sh)	0.0058	0.65×10^3	609(sh)	0.1963	0.22×10^2

[a] λ: wavelength; A: absorbance and ε: molar absorptivity
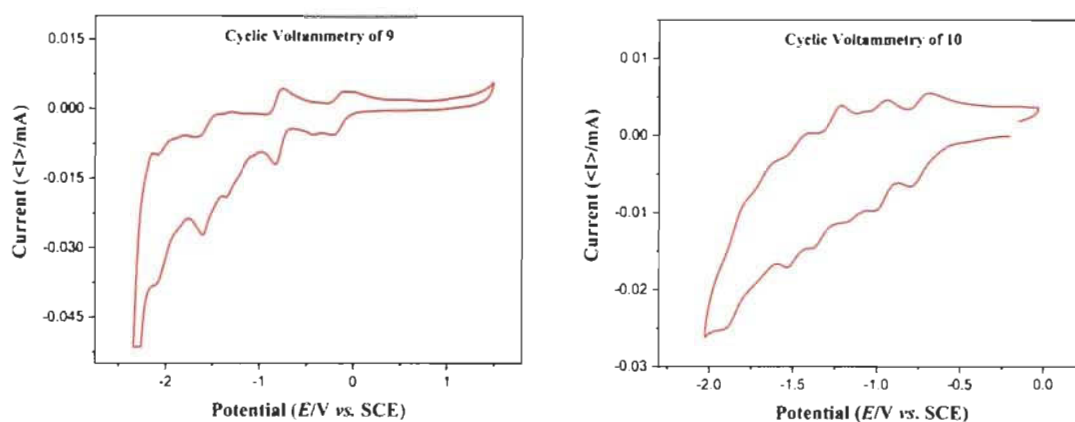
Figure S14. Cyclic voltammograms of **9** and **10.**

Table S9. Cyclic voltammetry data of **9** and **10** in DMF solution

Sample	$Ered1_{1/2}$ [V]	$Ered2_{1/2}$ [V]	$Ered3_{1/2}$ [V]	$Ered4_{1/2}$ [V]	$Ered5_{1/2}$ [V]	$Ered6_{1/2}$ [V]	$Ered7_{1/2}$ [V]	$Ered8_{1/2}$ [V]	$Ered9_{1/2}$ [V]
9	-0.14 (22)	-0.38 (93)	-0.78 (58)	-1.20 (51)	-1.33 (08)	-1.56 (36)	-1.83 (86)	-2.0(25)	-2.31(95)
10	-0.72 (79)	-0.94 (80)	-1.10 (53)	-1.33 (21)	-1.48 (95)	-1.63 (54)	-1.83 (03)	-2.21 (45)	-2.50(41)

307
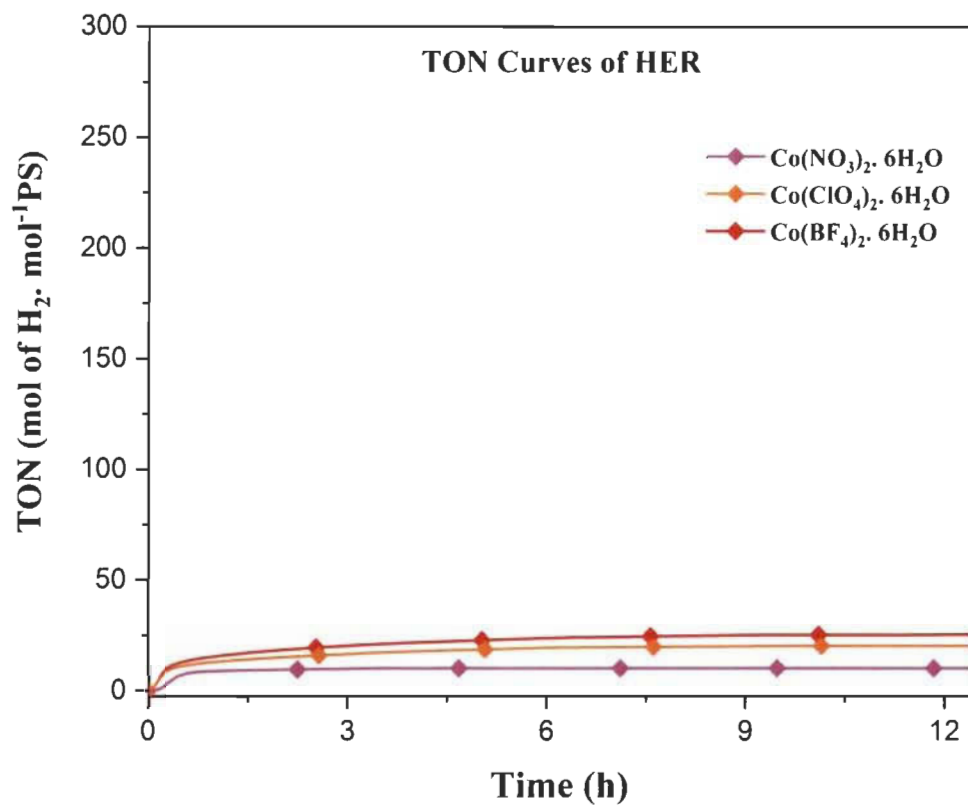
Figure S15. HER curves of $Co(NO_3)_2$. $6H_2O$ (pink), $Co(ClO_4)_2$. $6H_2O$ (orange) and $Co(BF_4)_2$. $6H_2O$ (red).

Chapter 7
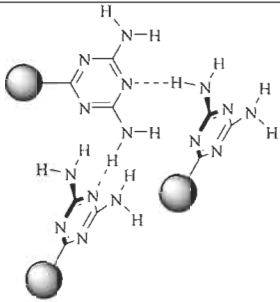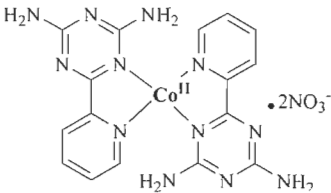
Conclusions and perspectives
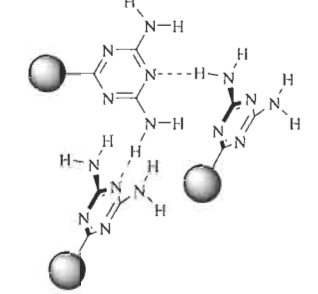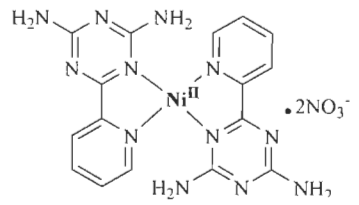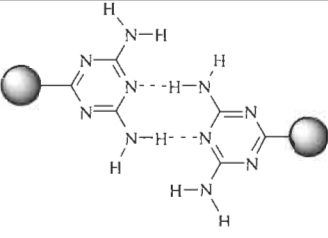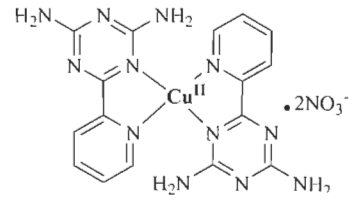
1. Conclusions and perspectives
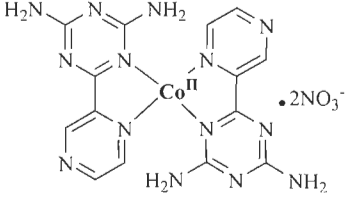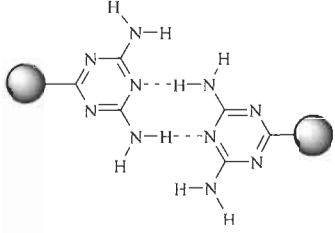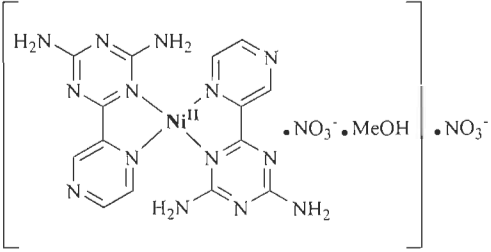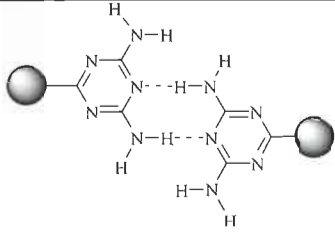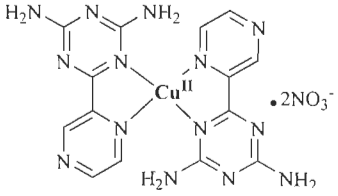
Studies based on **16** novel molecular complexes have been demonstrated in the present thesis. All the ligands and their complexes were synthesized as per the Ph. D objectives. The first row transition metals Fe (II), Co (II), Ni (II), Cu (II) and Zn (II) were mainly chosen due to their inexpensiveness, high abundance and their ability to undergo change in the oxidation states. All the complexes, except $Zn(Py-2-DAT)_2(NO_3)_2$ possessed efficient redox properties which were identified by cyclic voltammetry prior to their photocatalytic testing. Our work provides a remedy to the lack of straight forward and efficient synthesis of functionalized 2,2'-bypyridine (bpy), [2,2';6',2"]-terpyridine (tpy), 2,2':6',2'':6'',2'''-quaterpyridine (qtpy) ligands and their complexes. All the synthesized molecular complexes were pure, crystalline, homogeneous and showed a single phase. They were also thermally stable. All the molecular complexes were tested for visible light-driven hydrogen evolution reactions in organic medium i.e. by using DMF as a solvent. By comparing the photo catalytic activities for HER under similar conditions with the literature reports, our complexes [6,6'-(2,2'-bipyridine-6,6'-diyl)bis(1,3,5-triazine-2,4-diamine)](nitrato-O)nickel(II) (complex **13** article 3), [FeFe] macrocyclic metallotecton (complex **2** article 4) and $Co(py-2-DAT)_2(phCNH)_2BF_4$ (complex **10** article 5) proved to be the best reported catalysts, producing hydrogen with TON of 174, 326 and 179 moles of H_2 per mole of the photosensitizer, respectively. Furthermore, research based on the functionalization of bpy, tpy and qpy ligands and the synthesis of their molecular complexes is under progress. In addition, the hydrogen evolution reactions under aqueous conditions are also being studied. Results based on the utility of the synthesized complexes as photocatalysts for carbon dioxide reduction reactions are in their preliminary stages and currently an optimization of their reaction conditions is being carried out. Efforts are also being undertaken to immobilize these molecular photo catalysts on the surface of some heterogeneous supports to prepare heterogeneous photocatalysts.

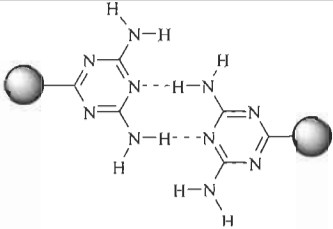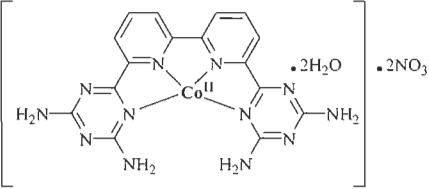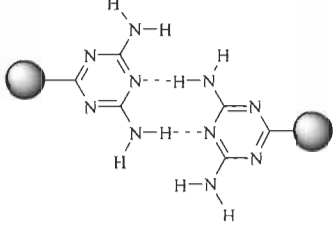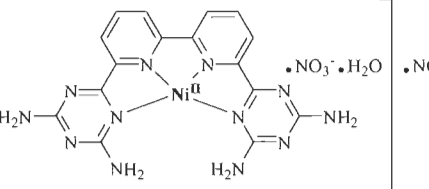## 2. Summary table of all the complexes for hydrogen evolution reaction (HER)

Chapter 3: Synthesis, Crystal Structure, Characterization of Pyrazine Diaminotriazine based Complexes and their Systematic Comparative Study with Pyridyl Diaminotriazine based Complexes for Light-Driven Hydrogen Production
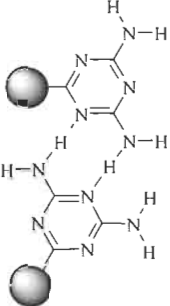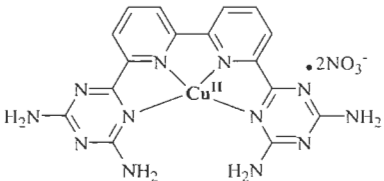
Reactants	Reaction Conditions	H-Bond Motifs	Chemical Structure	TON
1. $Co(NO_3)_2 \cdot 6(H_2O)$ (1 equiv) 2. 6-Pyridin-2-yl-[1,3,5]-triazine-2,4-diamine (2 equiv) 3. MeOH (Solvent)	Reflux	Type IV		16.15

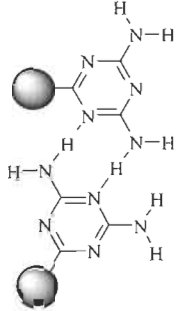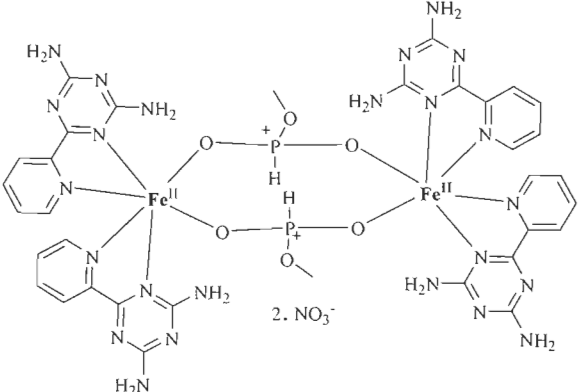|				
1. Ni(NO₃)₂. 6(H₂O) (1 equiv) 2. 6-Pyridin-2-yl-[1,3,5]-triazine-2,4-diamine (2 equiv) 3. MeOH (Solvent)	Reflux	 Type IV		21.32
1. Cu(NO₃)₂. 6(H₂O) (1 equiv) 2. 6-Pyridin-2-yl-[1,3,5]-triazine-2,4-diamine (2 equiv) 3. MeOH (Solvent)	Reflux	 Type I		71.81
1. Co(NO₃)₂. 6(H₂O) (1 equiv)	Reflux	Only powder X-ray diffraction was obtained for this complex		

2. 6-pyrazin-2-yl-[1,3,5]-triazine-2,4-diamine (2 equiv) 3. MeOH (Solvent)				36.44
1. Ni(NO$_3$)$_2$. 6(H$_2$O) (1 equiv) 2. 6-pyrazin-2-yl-[1,3,5]-triazine-2,4-diamine (2 equiv) 3. MeOH (Solvent)	Reflux	 Type I		9.17
1. Cu(NO$_3$)$_2$. 6(H$_2$O) (1 equiv) 2. 6-pyrazin-2-yl-[1,3,5]-triazine-2,4-diamine (2 equiv) 3. MeOH (Solvent)	Reflux	 Type I		2.16

Chapter 4: Mimicking 2, 2':6', 2'':6'', 2'''-Quaterpyridine Complexes for the Light-Driven Hydrogen Evolution Reaction: Synthesis, Structural, Thermal and Physicochemical Characterizations

Reactants	Reaction Conditions	H-Bond Motifs	Chemical Structure	TON
1. Co(NO$_3$)$_2$. 6(H$_2$O) (1 equiv) 2. 6,6'-(2,2'-Bipyridine-6,6'-diyl)bis(1,3,5-triazine-2,4-diamine) (1 equiv) 3. MeOH (Solvent)	Reflux	Type I		56.03
1. Ni(NO$_3$)$_2$. 6(H$_2$O) (1 equiv) 2. 6,6'-(2,2'-Bipyridine-6,6'-diyl)bis(1,3,5-triazine-2,4-diamine) (2 equiv) 3. MeOH (Solvent)	Reflux	Type I		174.14

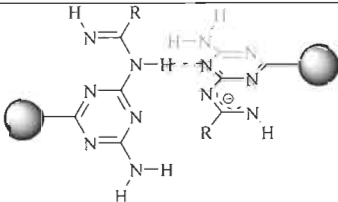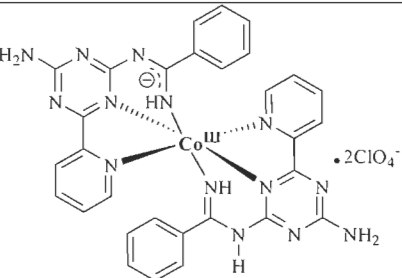| Reactants	Reaction Conditions	H-Bond Motifs	Chemical Structure	TON
1. $Cu(NO_3)_2 \cdot 6(H_2O)$ (1 equiv) 2. 6,6'-(2,2'-Bipyridine-6,6'-diyl)bis(1,3,5-triazine-2,4-diamine) (2 equiv) 3. MeOH (Solvent)	Reflux	 Type II		47.14

Chapter 5: Design of a [FeFe] Macrocyclic Metallotecton for Light-Driven Hydrogen Evolution Reaction

Reactants	Reaction Conditions	H-Bond Motifs	Chemical Structure	TON
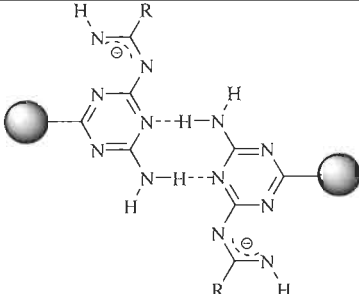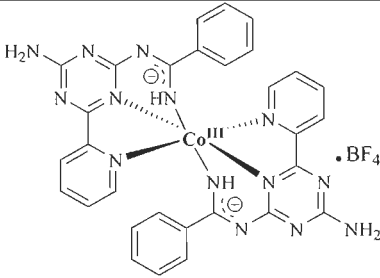
Reactants	Reaction Conditions	H-Bond Motifs	Chemical Structure	TON
1. Fe(NO₃)₃. 9(H₂O) (1 equiv) 2. 6-Pyridin-2-yl-[1,3,5]-triazine-2,4-diamine (2 equiv) 3. NaPO₂H₂ (1.5 equiv) 4. MeOH (Solvent)	Reflux	 Type II		325.38

Chapter 6: Amidine/Amidinate Cobalt Complexes: One-Pot Synthesis, Mechanism and Photocatalytic Application for Hydrogen Production

Reactants	Reaction Conditions	H-Bond Motifs	Chemical Structure	TON
1. Co(ClO₄)₂. 6(H₂O) (1 equiv) 2. 6-Pyridin-2-yl-[1,3,5]-triazine-2,4-diamine (2 equiv) 3. phCN (Solvent)	Reflux	 Amidine/Amidinate Motif II		49.97

1. Co(BF$_4$)$_2$. 6(H$_2$O) (1 equiv) 2. 6-Pyridin-2-yl-[1,3,5]-triazine-2,4-diamine (2 equiv) 3. phCN (Solvent)	Reflux	 Amidine/Amidinate Motif III		179.46